Felix Selim Göküzüm

Fast Solvers for Homogenization Problems: Fast Fourier Transform- and Neural Network-Based Approaches

Fast Solvers for Homogenization Problems: Fast Fourier Transform- and Neural Network-Based Approaches

Von der Fakultät Bau- und Umweltingenieurwissenschaften der Universität Stuttgart
zur Erlangung der Würde eines Doktor-Ingenieurs (Dr.-Ing.)
genehmigte Abhandlung

von

Felix Selim Göküzüm

aus Stuttgart

Institut für Mechanik (Bauwesen) der Universität Stuttgart

2022

Organisation und Verwaltung:

Institut für Mechanik (Bauwesen)
Lehrstuhl für Materialtheorie
Universität Stuttgart
Pfaffenwaldring 7
70569 Stuttgart
Tel.: +49 (0)711 685-66378
Fax: +49 (0)711 685-66347

Danksagung

Die hier vorliegende Arbeit entstand während meiner Tätigkeit als wissenschaftlicher Mitarbeiter am Institut für Mechanik der Universität Stuttgart.

Hohe Anerkennung verdient mein Doktorvater Prof. Dr.-Ing. Marc-André Keip, dessen Expertise auf dem Feld der Multiskalen- und der Homogenisierungsmethoden mir den Weg zu einigen der hier präsentierten Lösungen aufzeigte. Auch schätzte ich immer die offene akademische Atmosphäre, in der es keine „falschen" Fragen gibt. In bester Erinnerung werde ich immer Prof. Dr.-Ing. Christian Miehe behalten, meinen ersten Doktorvater (April - August 2016), der durch seine Vorlesungen früh mein Interesse für die Kontinuumsmechanik weckte und mir meine weitere akademische Laufbahn ebnete. Danken möchte ich auch meinen beiden Mitberichtern Prof. Dr.-Ing. Dennis Kochmann und Prof. Dr.-Ing. Stephan Wulfinghoff. Da beide einen prägenden Einfluss auf mich hatten, schließt sich mit ihrem Koreferat für mich ein Kreis: Prof. Dr.-Ing. Dennis Kochmann ermöglichte mir im Rahmen meiner Masterarbeit einen Forschungsaufenthalt in seiner Forschungsgruppe am California Institute of Technology im Jahr 2015. Hier wurde ich in die Thematik der Fourier-basierten Löser eingeführt. Die fruchtbaren Diskussionen mit ihm und Vidyasagar Ananthan haben meine Forschung ein gutes Stück vorangebracht. Prof. Dr.-Ing. Stephan Wulfinghoff bestärkte mich nach der Präsentation meiner ersten Forschungsergebnisse in Bad-Herrenalb und damit außerhalb des Lehrstuhls in meiner Tätigkeit und meinen Fähigkeiten.

Meine Wertschätzung möchte ich auch gegenüber meinen Mitdoktoranden und den Postdoktoranden am Institut für Mechanik aussprechen, insbesondere für die gegenseitige Unterstützung und die Zeit für die Fragen des anderen. Ich profitierte davon ganz besonders mit meiner teils ausgeprägten Hartnäckigkeit, wenn sich mir eine Lösung nicht erschließt. Meine Kollegen verloren aber nie die Geduld mit mir und das rechne ich ihnen hoch an. Danken möchte ich in diesem Zusammenhang Stephan Teichtmeister, Aref Nateghi, Daniel Kienle, Elten Polukhov, Matthias Rambausek, Omkar Nadgir, Ashish Sridar, Fadi Aldakheel und Daniel Vallicotti. In diesem Personenkreis darf auch Lu Trong Khiem Nguyen nicht unerwähnt bleiben, dessen mathematische Methodik und Präzision großen Eindruck bei mir hinterließen. Des Weiteren möchte ich mich bei Lukas Böger und Steffen Mauthe für ihre jeweilige Unterstützung während meiner Bachelor- bzw. Masterarbeit bedanken. Auch die folgenden ehemaligen und aktuellen Mitarbeiter und Mitarbeiterinnen machten meine Zeit am Institut zu etwas Besonderem: Nadine Steinecke, Leonie Fischer, Jan Lukas Eurich, Nadine Kijanski, David Krach, Andreas Krischok, Siddharth Nirupama Sriram, Matthias Ruf, Arndt Wagner, Linda Werneck, Basavesh Yaraguntappa und viele mehr.

Ein riesiges Dankeschön geht an meine (Schwieger-)Familie für die Bestärkung meines akademischen Lebensabschnitts und an meine Freunde für die von Zeit zu Zeit durchaus notwendige und willkommene Ablenkung und Zerstreuung vom verkopften Tagesgeschäft.

Die Promotion ist eine bereichernde Zeit, die aber auch geprägt ist von einigen Selbstzweifeln - zumindest erging es mir manchmal so. Am Zuspruch meiner wundervollen Frau Amelie Hoppe musste ich jedoch nie zweifeln und sie war und ist die große Konstante in meinem Leben, an der ich mich festhalten kann.

Stuttgart, September 2022   Felix Selim Göküzüm

Glossary of most important quantities

symbol	description	unit
$\mathfrak{F}$	force vector	N
ϵ_0	vacuum permittivity	F/m
q/Q	electric point charge/overall charge in a specific volume	C
$\boldsymbol{e}/\boldsymbol{E}$	electric field in current/reference configuration	V/m
λ	volume charge density	C/m^3
ϕ	scalar electric potential	V
ψ	elastic energy density function describing the energy per unit reference volume	J/m^3
$\mathfrak{p}$	electric dipole moment	Cm
$\boldsymbol{p}/\boldsymbol{P}$	polarization or electric dipole moment density in current/reference configuration	Cm/m^3
$\boldsymbol{d}/\boldsymbol{D}$	electric displacement in current/reference configuration	C/m^2
χ	electric susceptibility of dielectric matter	-
$\boldsymbol{g}/\boldsymbol{G}$	metric tensor in current/reference configuration	-
$\mathcal{S}/\mathcal{B}$	embedded current/reference body	-
$\boldsymbol{\varphi}$	deformation map that maps from reference configuration $\mathcal{B}$ to current configuration $\mathcal{S}$	-
$\boldsymbol{v}/\boldsymbol{V}$	velocity vector parameterized in current/reference coordinates	m/s
$T_X\mathcal{S}/T_X\mathcal{B}$	current/referential tangent space or space of current/referential contravariant vectors	-
$\boldsymbol{F}$	deformation gradient $\nabla_{\boldsymbol{X}}\boldsymbol{\varphi}$ that maps referential contravariant vectors onto current contravariant vectors $T_X\mathcal{B} \to T_X\mathcal{S}$	-
$T_X^*\mathcal{S}/T_X^*\mathcal{B}$	current/referential normal space or space of current/referential covariant vectors	-
$\mathrm{cof}[\boldsymbol{F}]$	cofactor $\det[\boldsymbol{F}]\boldsymbol{F}^{-T}$ of the deformation gradient that maps referential covariant vectors onto current covariant vectors $\boldsymbol{A} \mapsto \boldsymbol{a} = \mathrm{cof}[\boldsymbol{F}]\boldsymbol{A}$	-
J	determinant $\det[\boldsymbol{F}]$ of the deformation gradient that maps referential volume elements onto current volume elements $V \mapsto v = JV$	-
ρ/ρ_0	mass density in the current/reference configuration	kg/m^3
$\boldsymbol{C}$	right Cauchy-Green tensor, which is the referential representation of the current metric $\boldsymbol{g}$	-
$\boldsymbol{c}$	inverse left Cauchy-Green tensor, which is the current representation of the referential metric $\boldsymbol{G}$	-

symbol	description	unit
$\boldsymbol{t}$	current traction vector, which is force over the current deformed area of a body	N/m^2
$\boldsymbol{\sigma}$	Cauchy stress tensor that relates a current unit normal of a surface to the current traction vector $\boldsymbol{n} \mapsto \boldsymbol{t} = \boldsymbol{\sigma n}$	N/m^2
$\boldsymbol{t}^0$	current traction vector, which is force per reference unit area of a body	N/m^2
$\widetilde{\boldsymbol{T}}$	first Piola-Kirchhoff stress tensor that relates a reference unit normal of a surface to the current traction vector $\boldsymbol{N} \mapsto \boldsymbol{t}^0 = \widetilde{\boldsymbol{T}} \boldsymbol{N}$	N/m^2
Π	energetic potential	J
$\boldsymbol{\gamma}$	volume body forces such as gravitational forces	N/m^3
$\boldsymbol{t}^{\#}/q^{\#}$	prescribed surface tractions/charges within a boundary value problem; quantities can be parametrized in reference or current configuration depending on the integral they are used in	N/m^2|C/m^2
$\boldsymbol{F}^{\#}/\boldsymbol{E}^{\#}$	deformation gradient/electric field in physical equilibrium, either macroscopic or microscopic, i.e., fields that emerge from solving equilibrium equations such as the balance of linear momentum or Maxwell's equations	- |V/m
$\boldsymbol{T}$	first Piola-Kirchhoff stress tensor that emerges from $\partial \psi / \partial \boldsymbol{F}$ with one contra- and one covariant basis and that relates to $\widetilde{\boldsymbol{T}}$ through the metric $\boldsymbol{T} = \boldsymbol{g}\widetilde{\boldsymbol{T}}$	N/m^2
$\mathcal{P}$	power performed by mechanical and electrical fields	J/s
$\mathcal{D}$	dissipation rate for a mechanical or electrical process with $\mathcal{D} \geq 0$	J/s
$\diamond$	generic contraction operator that contracts the tensor corresponding to their degree, i.e., single, double, triple, ... contraction	-
$\mathfrak{d}$	dissipation potential describing the dissipative power per volume	J/sm^3
$\Pi^{\Delta t}$	time-discrete incremental variational potential obtained from the time integration of a rate-type variational potential $\Pi(\dot{\boldsymbol{\varphi}}, \dot{\phi})$	J
$\mathbb{G}$	generalized strain field incorporating all primary fields such as $\mathbb{G} = [\boldsymbol{F}; \boldsymbol{E}]$ for example	-
$\mathbb{S}$	generalized stress field incorporating all primary dual fields such as $\mathbb{S} = [\boldsymbol{T}; \boldsymbol{D}]$ for example	-
$\partial_{\mathbb{G}}\widetilde{\mathbb{G}}$	generalized fluctuation sensitivities; equivalent to the expression $\frac{\partial \widetilde{\mathbb{G}}}{\partial \mathbb{G}}$	-
$\overline{\mathbb{C}}^{algo}$	homogenized generalized macroscopic tangent operator emerging from microscopic boundary value problem	-
$\widehat{(\bullet)}$	a quantity in Fourier space; in the discrete form, it might emerge from a discrete or fast Fourier transform of a real-space quantity $\widehat{(\bullet)} = \text{fft}\{(\bullet)\}$	-
$\boldsymbol{\omega}$	discrete Fourier transform matrix as defined for the one-dimensional transform in Equation (5.4)	-
$\boldsymbol{k}/\boldsymbol{K}$	n-dimensional vector of wave numbers reflecting the frequency of the approximative sine and cosine functions in the current/reference configuration	1/m

symbol	description	unit
$\mathbf{\Gamma}^0/\widehat{\mathbf{\Gamma}}^0$	Green operator in real/Fourier space that that can be used to solve boundary value problems	-
$\boldsymbol{\tau}$	polarization tensor, which is the difference of the generalized stresses and the geberalized stresses of a linear reference material	-
$\mathbb{F}$	assembled generalized fluctuation sensitivities	-
$\boldsymbol{a}$	electric vector potential	C/m
d	fracture phase-field parameter, where $d = 0$ indicates the unbroken and $d = 1$ the broken state	-
l_c	length scale parameter for the regularization of the fracture interface	m
g_c	Griffith constant determining fracture toughness; energy per area that is released when a crack occurs	J/m^2
$\mathfrak{z}$	crack surface density	1/m
$\mathcal{H}$	local crack-driving-force, which is calculated as the local maximum of energy density over all time-steps including the current one	J/m^2
$\mathfrak{r}$	vector of all weights and biases of an artificial neural network	-
$N(\boldsymbol{x}, \mathfrak{r})$	artificial neural network output that takes $\boldsymbol{x}$ as input and has weights and biases $\mathfrak{r}$	-

Table of Contents

II   Fourier Transform-based Solvers

Abstract

The goal of numerics based science is the replication of our tangible reality within computer-aided simulations with as little deviation from relevant experiments as possible. Although the vision of a 'fully simulated world' might still lie in the distant future, simulation methods have still undergone an amazing development in the recent decades and found entry into a wide variety of research areas in engineering and other scientific disciplines. An ever-growing hardware capability have led to an ever-growing resolution of simulations. This increase starts to enable the simulation of material behavior on several length scales and their interaction in computational solid mechanics. From a material physics point of view, the analysis of several lengths scales is of high interest, as many macroscopically observable effects are of microscopic origin. One example is the material class of electroactive polymers: Electrodes that are strapped on a soft polymer attract each other due to electrostatic forces between them and lead to a polymer's deformation. One can now observe that one can manipulate the type and strength of said deformation by mixing in high-electric-permittivity particles. In such scenario, the amount, the size and the distribution of the particles play a crucial role. However, these particles' size is usually of much lower length scale compared with the overall component. A further example is given by microcracks which localize at grain boundaries or preexisting microscopic voids. In the presence of such localization points, the macroscopic component might break under much lower loads than one would expect from a purely macroscopically continuous description. Ideally, one would refine a solution up to the degree that all microscopic effects are considered. However, despite the massive increase in computational power, full-field simulations across several scales are still uneconomic and time-consuming, preventing them from being applied to a wide range of realistic engineering problems. To relieve said problem, researchers developed homogenization methods and the concept of representative volume elements. In doing so, one chooses a statistically representative volume of the material at hand and determines either analytically or numerically effective material properties of said volume. These effective properties should be computed to describe as accurately as possible a macroscopically homogeneous body that acts under load the same way the inhomogeneous material with microstructure would. The present work deals with such numerical homogenization approaches and applies them to several material effects. We put emphasis on the computation of effective properties as well as their embedding into multiscale simulations.

As this work mainly deals with the homogenization of the already mentioned electroactive polymers, the electrostatics theory will be discussed a little deeper. The basic governing differential equations of electric fields in vacuum are motivated by using Coulomb's law for the attractive and repulsive forces between charges. The theory is then extended to fields in the presence of solid dielectric matter. Although the differential equations emerging for electrostatics appear to be similar to the mechanical ones in their structure, there are still massive differences in the underlying physics they represent. These differences one needs to consider when interpreting stresses and applying boundary conditions. Next, we introduce the fundamental theory of continuum mechanics. In the framework of large strains, we put a particular focus on the mapping of tangents, area, and volume elements between the undeformed and the deformed configuration of the solid body under a given load. Additionally, different stress measures are considered. The introduced mappings are then applied to the electric quantities, whose relation between the undeformed reference con-

figuration and the deformed current configuration are of relevance for the construction of coupled energy potentials. The representation of electro-mechanically coupled differential equations as a minimization of a coupled energy potential belongs to the field of variational methods. This variational structure allows for an elegant formulation of the scale transition in the form of the famous Hill-Mandel macrohomogeneity conditions. We, therefore, condense the representative volume element to a point problem on the macroscopic scale. In doing so, the information on the boundary conditions for the representative volume element is lost. The Hill-Mandel conditions fill this emerging gap by postulating an integral average rule between the macroscopically observable energy density and the microscopic one. From this integral relation, appropriate boundary conditions can be recovered. As this work is mainly concerned with fast Fourier transform-based solution schemes, we will be exclusively using periodic boundary conditions.

fast Fourier transform-based solution schemes have found increased application over the past years in the field of homogenization of continuum mechanics related boundary value problems. They are based on the trigonometric approximation of solution fields and Green operators' construction in Fourier space. Amongst others, this approach leads to the famous Lippmann-Schwinger equation for solving the mechanical equilibrium equation. It is an equation formally already known from the field of quantum scattering theory.

The scale transition and the computation of adjacent macroscopic tangent operators are of special interest to this work. We, therefore, present a novel approach by calculating so-called fluctuation derivatives from the Lippmann-Schwinger equation. Similar approaches are already known from finite element-based approaches but have, to the best knowledge of the author, not been carried over to the field of fast Fourier transform-based methods. In doing so, a new Lippmann-Schwinger-type equation emerges for the fluctuation sensitivities.

This approach is then extended to the field of electro-mechanically coupled systems and numerically tested. Numerical experiments are performed to investigate the coupled Green operator's preconditioning properties, and the convergence behavior is tested for a multiscale problem. The multiscale boundary value problem is an electroactive gripper made of soft polymer in which stiff particles of high electric permittivity are embedded.

One further application on the field of phase-field-based fracture mechanics is investigated. Therefore, a time-discrete incremental variational potential is used that incorporates the evolution of a fracture phase-field. Said incremental variational potential in combination with an operator split for the displacement and phase-field variables grant a fast and robust computation of fracture processes on the microscale and their homogenization.

The last part of the present work deals with the, in continuum mechanics, rather new field of machine learning. More specifically, a new discretization method based on artificial neural networks is motivated and tested. The artificial neural networks are constrained in a way that they automatically always fulfill the periodic boundary conditions prescribed by the Hill-Mandel conditions. An electrostatic potential serves as a minimization functional. This method's goal is to reduce memory storage by reducing the number of unknowns to solve for. This is done by solving for the neural network's weight parameters instead of the nodal degrees of freedom.

Zusammenfassung

Ziel der numerischen Wissenschaft ist die Replikation unserer erfahrbaren Realität innerhalb computergestützter Simulationen unter möglichst geringer Abweichung relevanter Experimente. Auch wenn sich die Vision der 'simulierten Welt' vermutlich noch in weiter Ferne befindet, so haben Simulationsmethoden in den letzten Jahrzehnten dennoch eine rasante Entwicklung durchlaufen und Einzug in verschiedenste Teilgebiete der Physik und des Ingenieurwesens gehalten. Immer leistungsfähigere Computerkomponenten führen hierbei zu immer hochauflösenderen Simulationen. Auf dem Gebiet der numerischen Festkörpermechanik ermöglicht dieser Anstieg an Rechenkraft zunehmends die Simulation von Materialverhalten auf mehreren Längenskalen und deren Interaktion. Materialtheoretisch ist die Betrachtung mehrerer Skalen hochinteressant, da viele makroskopisch beobachtbare Effekte mikroskopischen Ursprung oder Einfluss haben. Ein Beispiel sind elektroaktive Polymere: Elektroden, die an weiche Polymere angebracht werden, führen über elektrostatische Anziehungen zu Deformationen des Polymers. Es zeigt sich nun, dass man die Art und Stärke der Deformation durch das Beifügen von Partikeln hoher elektrischer Durchlässigkeit beeinflussen kann. Hierbei spielt sowohl die Menge, als auch die Form und Verteilung der Partikel eine entscheidende Rolle. Die Partikel sind jedoch meistens deutlich kleiner als das Gesamtbauteil. Ein weiteres Beispiel sind Mikrorisse, die an Korngrenzen kristalliner Materialien lokalisieren oder an bereits bestehenden Mikroeinschlüssen. Sind solche Lokalisationspunkte vorhanden, bricht das makrosopische Bauteil unter Umständen unter deutlich niedrigeren Lasten, als es von einer makroskopisch rein kontinuierlichen Betrachtung aus zu erwarten sei. Idealerweise würde man eine Simulation so stark verfeinern, dass sie solche Effekte abdeckt. Doch trotz der gestiegenen Rechenleistung sind Vollfeldsimulationen über mehrere Skalen hinweg noch immer unökonomisch und zeitintensiv, um sie in der Breite auf realistische, ingenieurstechnische Problemstellungen anzuwenden. Um dieses Problem zu umgehen wurden die Homogenisierungsmethoden und das Konzept der repräsentativen Volumenelemente entwickelt. Hierbei sucht man sich einen statistisch repräsentativen Bereich des zu simulierenden Materials aus und bestimmt entweder analytisch oder numerisch effektive Materialeigenschaften für diesen Bereich. Diese effektiven Eigenschaften sollten so beschaffen sein, dass sie möglichst akkurat ein makroskopisch homogenes Material beschreiben, dass aber auf Belastungen dieselbe Materialantwort wie das tatsächliche mit Mikrostrukturen versehene Material zeigt. Die vorliegende Arbeit beschäftigt sich mit dieser numerischen Homogenisierung und wendet sie auf verschiedene Materialeffekte an. Ein besonderer Fokus liegt hierbei auf der Berechnung effektiver Eigenschaften sowie deren Einbettung in Multiskalensimulationen.

Da sich diese Arbeit in großen Teilen mit der Homogenisierung von den bereits oben erwähnten elektroaktiven Polymeren befasst, wird zunächst etwas ausführlicher auf die Theorie der Elektrostatik eingegangen. Hierbei werden die Grundgleichungen der Elektrostatik im Vakuum aus Coulombs Kraftgesetz für Ladungen motiviert und dann auf Felder in dielektrischer fester Materie erweitert. Obgleich die Differentialgleichungen, die hieraus hervorgehen, den mechanischen Grundgleichungen sehr ähneln, so unterscheidet sich die zugrundelegende Physik doch massiv. Dies gilt es vor allem bei der Interpretation von Spannungen und dem Aufbringen von Randbedingungen zu beachten. Weiters wird die grundlegende Theorie der Kontinuumsmechanik eingeführt. Im Rahmen der Theorie großer Verzerrungen werden wir hier besondere Aufmerksamkeit auf die Abbildungen von

Tangentenvektoren, Flächen- und Volumenelementen zwischen der undeformierten und der deformierten Lage eines festen Körpers unter Last legen, sowie verschiedene Spannungsmaße besprochen. Die Abbildungseigenschaften werden dann auf elektrische Felder übertragen, deren Beziehungen zwischen der undeformierten Referenzlage und der aktuellen Lage von Bedeutung für die Konstruktion von gekoppelten Energiepotentialen sind. Die Darstellung elektro-mechanisch gekoppelter Differentialgleichungen als Minimierung eines gekoppelten Energiepotentials gehört zu den Methoden der Variationsrechnung. Diese variationelle Struktur erlaubt dann eine elegante Formulierung des Skalenübergangs in Form der berühmten Hill-Mandel-Homogenitätsbedingungen. Hierbei wird das repräsentative Volumenelement der Mikroskale zu einem Punkt auf der Makroskale kondensiert. Durch die Kondenstation auf einen Punkt gehen zwangsläufig die Randbedingungsinformationen für das repräsentative Volumenelement verloren. Die Hill-Mandel-Bedingungen füllen diese entstandene Lücke, indem sie eine integrale Mittelungsbeziehung zwischen der makroskopisch beobachtbaren Energiedichte und der mikroskopischen Energiedichte postulieren. Aus ihr lassen sich verschiedene Randbedingungen gewinnen. Da sich diese Arbeit hauptsächlich mit Fourier-basierten Lösungsmethoden befasst, werden hier ausschließlich periodische Randbedingungen verwendet.

Fourier-Transformation-basierte Lösungsmethoden haben in den letzten Jahren vermehrt Anwendung in der Homogenisierung von kontinuumsmechanischen Randwertproblemen gefunden. Sie basieren auf der trigonometrischen Approximation von Lösungsfeldern und der Konstruktion Greenscher Operatoren im Fourierraum. Dieser Ansatz führt unter anderem zur berühmten Lippmann-Schwinger Gleichung zur Lösung des mechanischen Gleichgewichts. Hierbei handelt es sich um eine Gleichung, die bereits aus der Quantenmechanik bekannt ist.

In dieser Arbeit liegt ein besonderes Augenmerk auf dem Multiskalenübergang und der Berechnung der dafür notwendigen makroskopischen Tangentenoperatoren. Hierbei wird ein neuartiger Ansatz gewählt, indem sogenannte Fluktuationsableitungen aus den Lippmann-Schwinger-Gleichungen gewonnen werden. Ähnliche Vorgehensweisen sind bereits aus Finite-Elemente-basierten Multiskalensimulationen bekannt, wurden nach dem besten Wissen des Autors bisher jedoch noch nicht auf Fouriermethoden erweitert. Hierbei ergibt sich eine neue Lippmann-Schwinger-artige Gleichung für die Lösung der Fluktuationsableitungen.

Die oben genannte Theorie wird dann auf elektromechanisch gekoppelte Systeme erweitert und numerisch getestet. Hierbei werden numerische Experimente zu Vorkonditionierungseigenschaften des gekoppelten Greenschen Operators durchgeführt und das Konvergenzverhalten anhand folgendes Multiskalenproblems getestet: Ein elektroaktiver Greifer aus weichem Plastik mit eingebetten starren, elektrisch permittiven Partikeln öffnet sich unter Anlegen eines elektrischen Feldes und der daraus resultierenden Deformation.

Eine weitere Anwendung wird im Bereich der phasenfeldbasierten Rissmodellierung untersucht. Hierbei wird ein inkrementelles energetisches Ratenpotential, dass die Evolution eines Rissphasenfeldes beinhaltet, verwendet. Dieses Ratenpotential in Kombination mit einem sogenannten Operatorsplit zwischen den Verschiebungs- und der Phasenfeldvariable erlaubt die schnelle und robuste Berechnung von Bruchvorgängen auf der Mikroskale sowie deren Homogenisierung.

Im letzten Teil der Arbeit wird das im Bereich der Kontinuumsmechanik vergleichsweise neue Feld des maschinellen Lernens behandelt. Im Detail wird eine neuartige Diskretisierungsmethode basierend auf künstlichen neuronalen Netzen motiviert und getestet. Die

künstlichen neuronalen Netze werden hierbei auf eine Art eingeschränkt, sodass sie die durch die Hill-Mandel-Bedingungen vorgegebenen periodischen Randbedingungen a priori erfüllen. Als Minimierungsfunktional dient ein elektrostatisches variationelles Potential. Ziel der Methode ist die Reduktion des Speicherbedarfs durch Reduktion der unbekannten Variablen, indem nach den Netzgewichten anstelle der Knotenfreiheitsgrade gelöst wird.

<div align="right">

Chapter 1

</div>

Introduction and motivation

This work deals with the computational homogenization of materials that have a distinct microstructure and the embedding of the computational homogenization into a multiscale framework. Homogenization allows for the prediction of effective material properties of such materials and, thus, a smart design of microstructures. These so-called metamaterials are mainly known from electromagnetism [13, 88, 112], where they can be used to obtain negative refractive indices and invisibility cloaking. However, they are recently finding their way into classical mechanics [8], where they can be used for applications such as unfeelability cloaks [18] or ultralight materials [170]. To understand the interaction of such structures in multi-component machines such as an airplane or car at much larger scales, embedding computational homogenization schemes into a multiscale framework is of great use. This work will present the homogenization and multiscale framework for different material models at small and large strains, such as viscoelasticity and electro-mechanical coupling. This framework is numerically tested within fast Fourier transform-(FFT) and artificial neural network (ANN)-based schemes.

1.1. Homogenization of composites

Homogenization in physics deals with the description of properties based on physical effects appearing on far smaller length scales. First thoughts on this sort of problem have been conducted by MAXWELL [121]: How could one describe the electric field in the matter, while it is build of atoms that are assembled in heterogeneous lattices and are moving chaotically? Describing such behavior on scales far larger than the atomic lattice demands accurate averaging methods, which are not always trivial [157].

Similar problems arise when predicting the mechanical behavior of matter. The ideas of analytical homogenization in *solid mechanics* trace back to only a few years later, when VOIGT thought of the possibilities of expressing partially heterogeneous microscopic moduli through effective macroscopic moduli. His work led to the so-called Voigt-bound [198]. Much later, REUSS proposed an averaging of Hooke's law in the inverse form, giving the so-called Reuss-bound [159]. While these two models were widely used for composites, TAYLOR [187] and SACHS [167] derived the corresponding models for polycrystals under

plastic deformation, assuming constant stress or constant strain in the microstructure respectively, see also GEERS ET AL. [53] for a more detailed discussion. It was HILL who proved that under the assumption of uncorrelated stress and strain fields, those two bounds form the most general upper and lower bounds of a given composite [75]. In the following years, the theory of bounds was massively improved, inter alia, by HASHIN & SHTRIKMAN [70] and WILLIS [204]. For statistical approaches, see KRÖNER [102]. Even though the continous and the statistical approach follow different variational principles, they share the same underlying Euler equation. It is the form of the celebrated Lippmann-Schwinger equation, which is already known from quantum mechanical scattering theory [113]. Therefore, solution strategies such as Fourier-transform-based approaches were already available. Further contributions for analytically predicting the effective properties of heterogeneous materials are, among others, the self-consistent method (BUDIANSKY [19], HILL [77]), the Mori-Tanaka method (MORI & TANAKA [135]), and the differential method (NORRIS [142]). For a more general and deeper background on analytical methods for homogenization, the reader is referred to HILL [78], SUQUET [185], PONTE CASTAÑEDA [151] and MILTON [133].

1.2. Physical homogenization problems

The present work is concerned with physical problems of material nonlinearity such as viscoelasticity and phase-field-induced fracture, geometrical nonlinearity within the framework of large strains, and coupled problems for electroactive polymers (EAP). A short overview of these frameworks will be given in the following subsections.

1.2.1. Materially and geometrically non-linear problems

Many materials in engineering and natural processes exhibit non-linear behavior. The reasons of this non-linearity can be manifold. In general, we distinguish between geometrical non-linearity and material non-linearity. Geometrical non-linearity concerns deformation processes that are so large that the simplifications made in the linear theory are not valid anymore. These large deformations happen quite often in soft materials such as polymers but are also observed in the failure of stiffer materials such as steel. The theoretical foundation of large-strains' fundamental framework can be found among others in CIARLET [27] and MARSDEN & HUGHES [117]. In the present work, the geometrical non-linearity is necessary to model large deformation in electro-mechanically coupled polymers, as described in the next section.

Material non-linearity, on the other hand, includes a large variety of material effects such as viscoelasticity, plasticity, and fracture. Quite often, these non-linear effects are time-dependent, which calls for distinct mathematical treatments. In this work, we will use the concept of incremental variational potentials to model time-dependent material behavior where we refer to existing works of HACKL & FISCHER [68], ORTIZ & REPETTO [143], MAUGIN [119], MIEHE [125] and LAHELLEC & SUQUET [105]. These variational formulations will then allow for an elegant way of formulating physical problems and their scale transition.
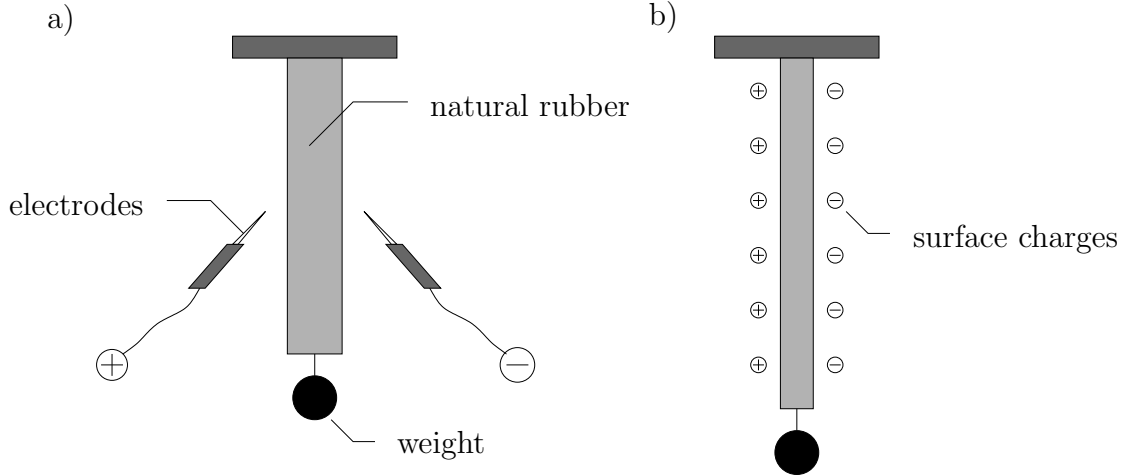
Figure 1.1: Experiment suggested by RÖNTGEN [162] to demonstrate electrically driven deformation of a polymer. The natural rubber strip is clamped on top and elongated, utilizing a weight attached to the strip's bottom. In a second step, the positive electrode of a Holtz electrostatic generator is rubbed to one side, and the negative electrode is rubbed to the other side, see a). One then observes a further elongation of the rubber strip, which grows as the area grows, which was in contact with the electrodes. The electrostatic attractive Coulomb forces between the surface charges lead to a contraction in the strip's horizontal direction and thus due to the incompressibility of rubber to elongation in the vertical direction.

1.2.2. Electro-mechanical coupling phenomena

One main focus of this work is the computational homogenization of a specific type of electro-mechanically coupled materials: electroactive polymers (EAPs). These kinds of polymers exhibit possibly large deformations when being subjected to an electric field. The first experiments on that field were already conducted in 1880 by RÖNTGEN [162]. In his work, he proposes an experimental set-up in which a rubber band is strapped on top and is loaded with weights at its bottom end as shown in Figure 1.1. After deformation due to gravitational forces, an assistant is supposed to electrify the rubber on both sides using a Holtz electrostatic generator's positive and negative electrodes. One then observes a further elongation of the rubber band, which grows as the electrified area grows[1].

EAPs can be roughly categorized into two subgroups, electronic and ionic EAPs. *Electronic EAPs* are polymers that react mainly due to the Coulomb attractive or repulsive forces generated between opposite or same sign charges. The rubber experiment of RÖNTGEN falls into this category, as the charges of different sign on the surface of the natural rubber follow Coulomb's law and attract each other. Due to the incompressibility of the natural rubber, it extends into the perpendicular direction. Electronic EAPs demand for a high voltage for deformation, but have low response times [209]. This drawbacks has recently been overcome by the molecular design of the polymers and special geometric architectures, see Figure 1.2. The second kind is *ionic EAPs*. In contrast to the first kind, ionic EAPs do not only deform due to the attraction of electrodes but due to the movement of the electrically induced diffusion of ionic liquids within the polymer.

This work focuses on electronic EAPs. The theoretical foundations of electro-mechanically

---

[1]In this work, RÖNTGEN also vigorously attacks the idea of another scientist who carried out similar experiments but came to the conclusion that the electric field must change the elastic properties of the material.

Free-standing diaphragm actuator
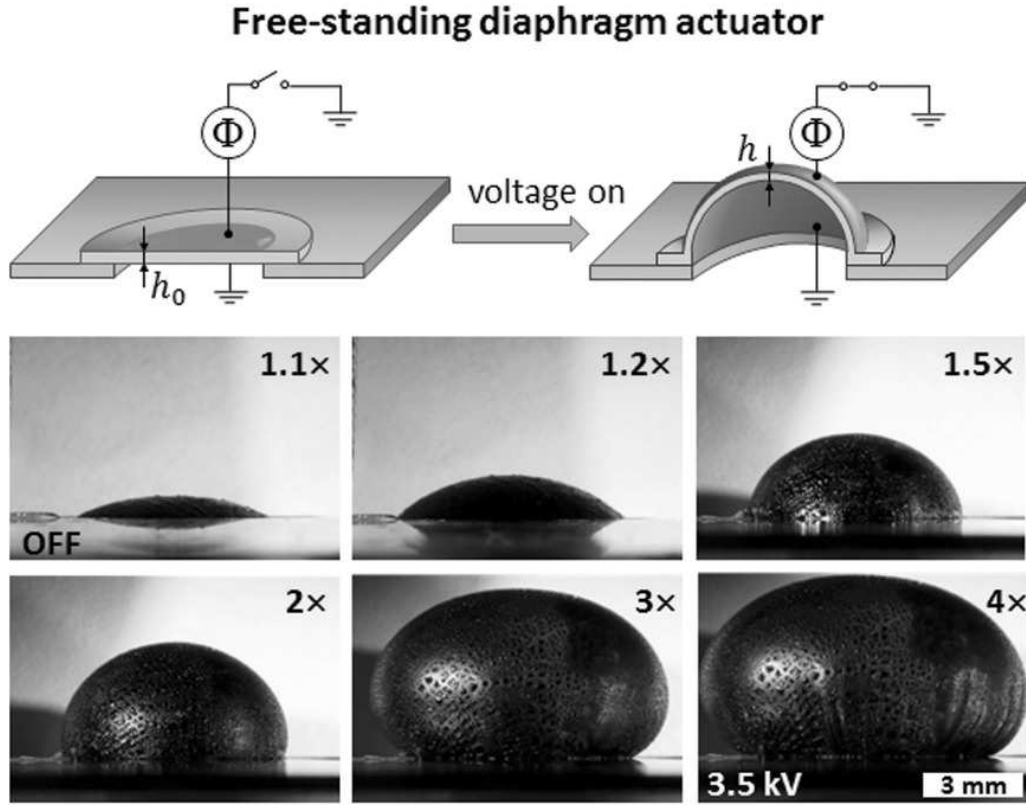
Figure 1.2: A Polydimethylsiloxan bottlebrush elastomer film of height h_0 is subjected to a voltage of up to 3.5 kV. The film then shows an increase in the surface area of up to four times the undeformed area before electrical breakdown. Image courtesy of Vatankhah-Varnoosfaderani et al. [197] ©2016 WILEY-VCH Verlag GmbH & Co. KGaA, Weinheim.

coupled material response were built by Toupin [192], Eringen [42] as well as Tiersten [191], see also Maugin [120] and Kovetz [100] for more recent fundamental works. In this work, we will mainly use constitutive continuum approaches of finite elasticity to model electronic EAPs. The framework for these implementations at finite strains can be found among others in Dorfmann & Ogden [39] and McMeeking & Landis [123], see also Vu et al. [202] for a non-dissipative and Miehe et al. [128] for a dissipative variational framework. Amongst recent analytical homogenization schemes for EAP composites, we mention the references [21, 34, 110, 152, 164, 178, 179].

1.2.3. Micromechanically induced fracture

Fracture mechanics and the prediction of materials' failure have been a vivid field of continuum mechanics for decades. Naturally, many engineering tasks are concerned with how long a component or building lasts under given loads and under which condition failure occurs. Simultaneously, it is a challenging field as it touches many fields such as stability analysis or singularity treatment in numerical methods. Early works lead back to the seminal works of Griffith [66], Irwin [84], and Rice [160] who derived critical parameters which characterize when a material locally fails. There are several methods to implement such failure behavior. In this work, we will employ a phase-field-based approach to fracture, which has become quite popular in the mechanics' community in

the past few years. The idea for phase separations using said phase-field models originate from the field of image segmentation [139] and was carried over to computational mechanics by FRANCFORT & MARIGO [50], who reformulated the fracture process into an energetic minimization framework. The numerical treatment was further specified by BOURDIN [14]. Later, MIEHE ET AL. [126, 132] formulated a variational potential together with an irreversibility constraint for the crack evolution to avoid nonphysical crack-healing processes. The said formulation comes along with the introduction of a history field of maximum energy and a pass-forward scheme, which is the backbone of the formulation used in this work.

1.3. Numerical solvers for homogenization problems

Analytic solution schemes provide fast and accurate solutions to physical boundary value problems. However, they are usually limited to strict restrictions on the microstructure topology or material law. In cases where the complexity of the microstructure significantly exceeds those restriction, *computational homogenization methods* can numerically compute effective responses based on discretized microscopic boundary value problems. There are different numerical methods to carry out these computations. In the field of continuum mechanics, most of these numerical computations are performed through the finite element method (FEM). However, more recently, the use of alternative solution schemes has risen in popularity. This work will focus on two relatively new methods in the field of computational mechanics: Fast Fourier transform-based solvers and artificial neural network-based solvers. The characteristics and development of these solvers will be briefly introduced below, where the introduction to the fast Fourier transform-based solvers is partially taken from [64].

1.3.1. Fast Fourier transform-based solvers

In 1994, MOULINEC & SUQUET presented an iterative algorithm to numerically compute the effective response of periodic representative volume elements (RVEs) based on discrete Fourier transforms (DFTs), including the analysis of the plastic behavior. They implemented a *fixed-point method* as the main solver, often referred to as the *basic scheme* [136, 137]. This method is fastly converging for small phase contrasts and can be efficiently implemented by using *fast Fourier transforms*[2] (FFTs), but shows only slow convergence rates when the phase contrast is high. Recently, many modifications to this scheme have been investigated. EYRE & MILTON [45] developed a faster version of the fixed-point version, often referred to as the *accelerated scheme.* Later, BRISARD & DORMIEUX [15] and ZEMAN ET AL. [211] simultaneously suggested the use of *conjugate gradient methods* as the primary solver, see also VONDŘEJC [199] for recent applications. Conjugate gradient methods usually compare favorably with the fixed-point method regarding convergence rates [54, 86]. However, for nonlinear material models, the conjugate gradient method demands a linearization of the Lippmann-Schwinger equation, and thus a higher

---

[2]The fast Fourier transform is a highly efficient implementation of the discrete Fourier transform that traces back to Gauss's seminal work [72]. The Cooley-Tukey algorithm is the most common one used [29]. A very powerful code for computing the FFT exists in the form of the FFTW-library [51], which is also used in the present paper.

amount of Fourier transforms. More recently, the use of FFT-based approaches for pre-conditioning an FEM-solution has been researched [111, 172]. On the side of material modeling, FFT-based homogenization methods for a variety of phenomenon such as viscoplasticity [41, 55, 109, 124], fracture [108, 182] including phase-field models [26, 115], and microstructure evolution [25, 177, 203] have been implemented.

1.3.2. Artificial neural network-based solvers

Artificial neural networks (ANNs) were first introduced as a mathematical concept to mimic the learning processes in real human neural networks [71, 122]. They attracted great attention when it was shown that they indeed reproduce some aspects of human learning, such as wrong grammatical conjugation in language learning. With the rise in computational power and GPU parallelization, artificial neural networks are nowadays used for a broad range of applications such as image and speech recognition [101, 183], and predictive modeling of user behavior on social and media websites. These tasks are usually defined by a vast amount of accessible data in combination with complex underlying interactions and relations of said data. The use of statistical approaches such as ANNs or additional machine learning algorithms such as *support vector machines* [184] or *anomaly detection* [37] enable the fitting of machine-learning-based models to such complex behavior in the data without having to explicitly formulate complex mathematical laws. Recently, advances in machine learning point to a combination of well-known mathematical laws and statistic machine learning approaches by physically constraining the output of ANNs, see RAISSI ET AL. [154], for example.

The aforementioned properties and strengths of machine learning algorithms paved the way for continuum mechanics and material modeling applications. First research approaches in this area were concerned with predicting a material response based on machine learning through experimental stress-strain data [56, 83, 107]. In the field of homogenization, the prediction of effective properties based on RVE information is a task that might be realized through machine learning concepts, as demonstrated, for example, in LE ET AL.[107] and YAN ET AL. [207], see also BOCK ET AL. [11] for a recent review. In such approaches, the training process's data is usually generated numerically, employing a discrete solver such as FEM- or FFT-based schemes. This kind of homogenization procedure, where machine learning predictions replace computationally costly microscopic boundary value problems, have the possibility to speed up multiscale simulations [32, 52]. In the field of microstructure pattern recognition, we want to highlight the works of LIU ET AL. [114], BESSA ET AL. [9], and CAVALIERE ET AL. [24]. In these works, areas of constant stress are detected by means of cluster analysis and the mechanical response is then approximated by Hashin-Shtrikman-bounds.

In this thesis, we analyze a method to numerically solve boundary value problems through artificial neural networks. We now focus on the work of LAGARIS ET AL. [103], which suggested the construction of ANNs that fulfill some given boundary value problems a priori and use them as trial functions for the differential equation at hand. The constraining is performed utilizing constraining functions that are multiplied with the original ANN. The optimization is then performed using the squared error of the differential equation as the objective function. The construction of such constraining functions might be challenging, so BERG & NYSTRÖM [7] suggested a generalization of constraining functions to complex geometries using additional trained ANNs. For our purpose, we adopt the method
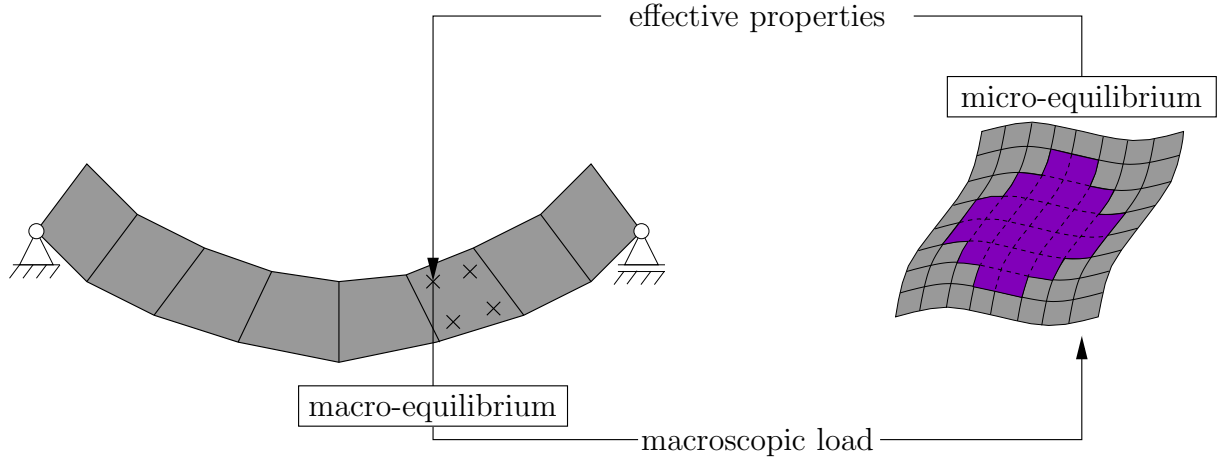
Figure 1.3: Schematic layout of a multiscale simulation. A macroscopic problem is discretized employing finite elements, for example. At the integration points, the macroscopic load, i.e., the deformation gradient, is passed to a microscale simulation. A volume element with a distinct microstructure represents the microscale. Effective properties such as macroscopic stress and stiffness are computed on the microscale under appropriate boundary conditions and are passed back to the macroscale. In contrast, a one-scale solution would simply evaluate a given constitutive law using the macroscopic deformation gradient instead of calling a microscopic simulation.

to solve homogenization problems with *periodic boundary conditions*. For such boundary conditions, the ANN can be explicitly constructed so that periodicity is always fulfilled. Additionally, the method is performed within an *integral variational framework* or *weak form* to easily treat the inhomogeneities that appear in homogenization problems. See also NABIAN & MEIDANI [140] for a recent application using the differential equation's strong form.

1.4. Multiscale approach for first-order homogenization

Multiscale simulations aim for the consequent usage of homogenization results within a macroscopic boundary value problem. Namely, the *effective properties* obtained from the homogenization procedure are used as a material law. In doing so, one can assume isotropic materials on the microscale and still observe anisotropy on the macroscale due to *geometrically anisotropic effects* as it is the case for laminates, for example. The extraction of the effective properties and their embedding into a macroscopic computation is called *scale transition* and is the major task of multiscale homogenization. Depending on the microstructure's size and structure, there are different approaches for realizing this scale transition. In this work, we will follow the *first-order homogenization* ideas, which assumes a strict scale separation between the macro- and the microscale. An asymptotic expansion of the microscopic kinematic fields is performed [6, 168], and an energetic criterion, the Hill-Mandel conditions [76] is employed as a macro-micro-energy transition rule. One is then able to derive *microscopically compatible* boundary conditions and perform a microscopic simulation for a discretized RVE, whose effective response is upscaled to a macroscopically discretized boundary value problem, see Figure 1.3 for a conceptual sketch. According to the reviews on multiscale simulations [89, 144], the idea of numerically implementing such a multiscale procedure by means of a finite element

discretized microstructure goes back to RENARD & MARMONIER [158]. The method was then further generalized, refined, and extended among others by SMIT ET AL. [181], FEYEL & CHABOCHE [47], TERADA ET AL. [189], TERADA & KIKUCHI [190] MIEHE ET AL. [129], KOUZNETSOVA [98], see also SCHRÖDER [175] for a review. Recently, the extension of the homogenization and multiscale framework to coupled problems such as thermo-elasticity [145, 146], magneto-elasticity [33, 85, 90, 91], and similarly in the area of electro-elasticity [92, 138, 174, 176] has drawn the attention of researchers. The embedding of the latter homogenization schemes within an FE-FFT multiscale framework was performed inter alia by SPAHN ET AL.[182], KOCHMANN ET AL. [95, 96], GÖKÜZÜM ET AL. [62, 64], and RAMBAUSEK ET AL. [155].
The research conducted in this work is built on the results mentioned above and focuses on four major points:

1. An FE-FFT multiscale framework, including a consistent scale-bridging technique, is presented, where a particular focus lies on the derivation of the effective properties of a RVE [62]. It serves as an alternative to finite difference-based approaches [182, 95] and is tested for materially and geometrically nonlinear problems.

2. Motivated by recent research efforts and new fields of application for electroactive polymers (EAPs) [4, 22, 93, 99, 149], the FE-FFT multiscale framework derived in the previous part is extended for the computational homogenization of *electroelastic effects in heterogeneous composites* [64]. Recently, it could be shown that for elastomers a *smart design of composite structure* allows for the enhancement of electromechanical coupling. The overall electroactivity can be enhanced by enriching the elastomeric matrix with particles of high electric permittivity [23, 82, 212]. In doing so, the strength of the electric field that needs to be applied to achieve a certain deformation can be reduced.

3. Fracture within materials plays a huge role in their material response, where crack initiations and paths are often highly dependent on the material's underlying microstructure [69]. Therefore, we establish an incremental variational framework for phase-field fracture on the microscale [139, 50, 14, 126]. The variational structure then allows for the identification of macroscopic material properties in the presence of a microscopic fracture phase-field. The FFT-based implementation is first tested for three-dimensional RVEs. An FE-FFT multiscale simulation is carried out to demonstrate microstructurally induced anisotropic crack behavior in a second step. Codes are provided in open repositories [60, 61].

4. Driven by recent breakthrough developments in the field of machine learning, an artificial neural network-based solution scheme [103] for periodic homogenization problems is presented [63]. It is numerically tested for electrostatic problems for different microstructure realizations with a focus on the training behavior of the ANN. Furthermore, a Tensorflow code [1] used to generate some of the results is provided.

— Part I —

Fundamentals of Electro-Mechanics and Homogenization

Chapter 2

Foundations of electrostatics and continuum mechanics

This chapter lays out the basic concepts of electrostatics and continuum mechanics at large strains. The electrostatic theory section is mainly motivated using basic experimental observations on the attractive and repulsive forces of charges. In general, the theory of electrostatics is well developed, and there are several works an author can draw inspiration from when incorporating the theory in his work. In the case of the present work, the derivations mainly follow the way the theory is outlined by REBHAN [157](©Elsevier B.V.). When outlining the concepts of continuum mechanics, a particular focus is set on the mapping properties of tensors as well as on stress relations [130].

2.1. Fundamentals of electrostatics

In this section, the fundamental governing equations of electrostatics are motivated. Historically, the effect of electricity was first observed in amber (ancient greek. electron = amber). Much later, the research on electro- and magnetostatic forces accelerated in the 18th century, leading to the discovery of two different charges - positive and negative - and Coulomb's law. In the 19th century, Faraday discovered electric fields' induction through the magnetic field changing in time. It was Maxwell who integrated those intermediate results into its final form, which we nowadays call the Maxwell equations. To motivate the Maxwell equations, we will recapitulate Coulomb's law and the superposition principle to derive the static version of the Maxwell equations in vacuum. The equations are then considered in an energetic context and are appended for the presence of polarizing material. Both the historical and mathematical elaborations are kept relatively short, for a more detailed discussion on the fundamental theory of electrostatics and -dynamics, the reader is referred to REBHAN [157], see also FEYNMAN [48].
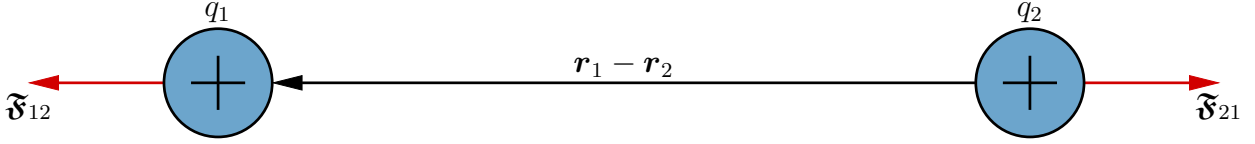
Figure 2.1: Coulomb's law: Two charges causing an equal force acting on both charges in opposite directions. The axis of the forces lies on the connecting line between the two charges.

2.1.1. Maxwell equations of electrostatics

Given one charge q_1 at location $\boldsymbol{r}_1$ and a second charge q_2 at location $\boldsymbol{r}_2$, it can be observed that for charges of the same sign, a repelling force is acting on the charges, while charges of different signs attract each other. As shown in Figure 2.1, the forces on the charges point in opposite directions. The axis of forces lies on the connecting line between the two charges. *Coulomb's law* gives the forces' strength and direction

$$\boldsymbol{\mathfrak{F}}_{12} = \frac{1}{4\pi\epsilon_0} q_1 q_2 \frac{\boldsymbol{r}_1 - \boldsymbol{r}_2}{|\boldsymbol{r}_1 - \boldsymbol{r}_2|^3} = -\boldsymbol{\mathfrak{F}}_{21}, \tag{2.1}$$

where $\epsilon_0 \approx 8.854187 \cdot 10^{-12}$ [As/Vm] is the free space permittivity. Interestingly, the inner structure of electrons and protons, the carriers of negative and positive charges, does not affect the electric field they induce. Otherwise, it would not be possible to describe the charges with a scalar value. The fact that the forces then lie on a connecting line between the charges is a consequence of the isotropy of space. Furthermore, it can be experimentally observed that a *superposition principle* governs the interaction of several charges

$$\boldsymbol{\mathfrak{F}}(\boldsymbol{r}_i) = \frac{q_i}{4\pi\epsilon_0} \sum_{k \neq i} q_k \frac{\boldsymbol{r}_i - \boldsymbol{r}_k}{|\boldsymbol{r}_i - \boldsymbol{r}_k|^3}. \tag{2.2}$$

Dividing the force by the charge q_i gives the *total electric field*, emerging from all other charges at location $\boldsymbol{r}_i$

$$\boldsymbol{e}(\boldsymbol{r}_i) = \frac{1}{4\pi\epsilon_0} \sum_{k \neq i} q_k \frac{\boldsymbol{r}_i - \boldsymbol{r}_k}{|\boldsymbol{r}_i - \boldsymbol{r}_k|^3}. \tag{2.3}$$

The definition of electric field and force allows us to measure the charge's value. We combine Equation (2.2) with (2.3) and write

$$\boldsymbol{\mathfrak{F}}(\boldsymbol{r}_i) = q_i \boldsymbol{e}(\boldsymbol{r}_i). \tag{2.4}$$

Taking into account that the point charge q_i can take any location in space, the latter equation can be formulated as

$$\boldsymbol{\mathfrak{F}}(\boldsymbol{r}) = q \boldsymbol{e}(\boldsymbol{r}). \tag{2.5}$$

Due to the superposition principle, we can now measure the force acting on a test charge in order to determine the strength of the electric field as shown in Figure 2.2. Next, we move to a continuous description of the electric field as visualizied in Figure 2.3. We, therefore, introduce a *volume charge density*

$$q_l = \lambda(\boldsymbol{r}_l) v_l^{\Delta}. \tag{2.6}$$

Absolute electric field   Measured electric field
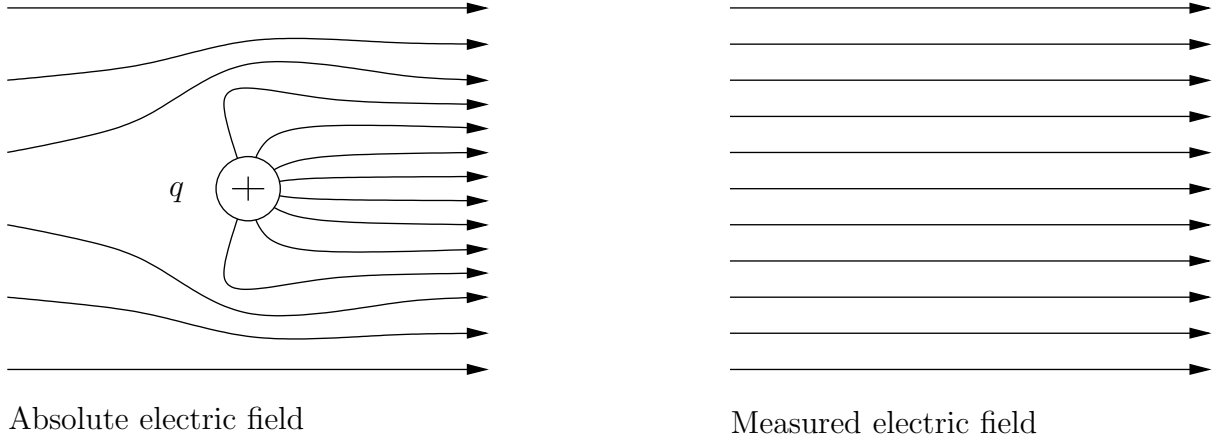
Figure 2.2: The absolute electric field emerges from the test charge q and the reference electric field. The force acting on the test charge allows for the measurement of the reference field.
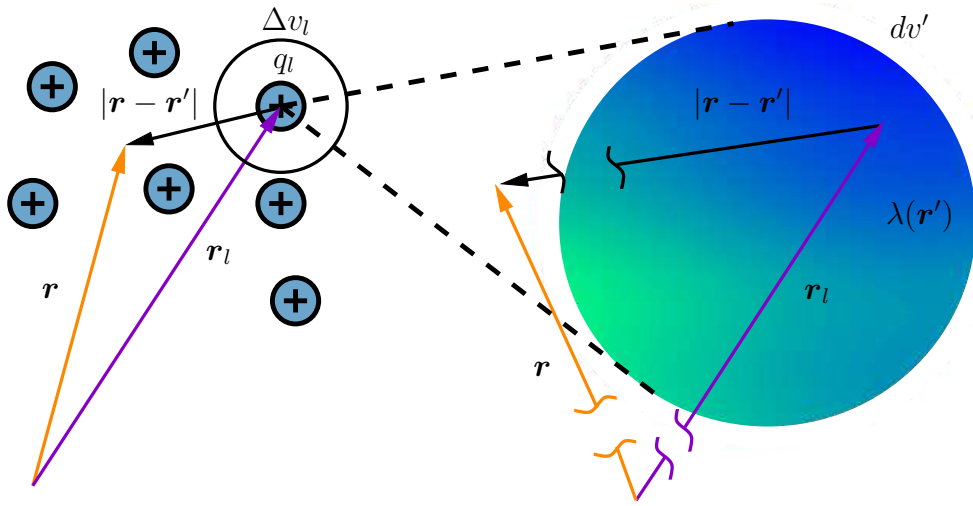
Figure 2.3: Transition from a point charge based description on the left to a charge density based desription visualized on the right: A volume charge density $\lambda(\boldsymbol{r}_l)$ is introduced that fulfills the relation $q_l = \lambda(\boldsymbol{r}_l)\Delta v_l$. Localization to the infinitesimal volume dv' then allows for the computation of the electric field using an integral according to Equation (2.7).

Inserting the latter equation into the definition of the electric field (2.3) and localizing gives the integral form

$$\boldsymbol{e}(\boldsymbol{r}) = \frac{1}{4\pi\epsilon_0}\sum_{l=1}^{N}\frac{\lambda(\boldsymbol{r}_l)(\boldsymbol{r}-\boldsymbol{r}_l)}{|\boldsymbol{r}-\boldsymbol{r}_l|^3}v_l^\Delta \to \frac{1}{4\pi\epsilon_0}\int_{\mathbb{R}^3}\frac{\lambda(\boldsymbol{r}')(\boldsymbol{r}-\boldsymbol{r}')}{|\boldsymbol{r}-\boldsymbol{r}'|^3}dv'. \tag{2.7}$$

Having the identity $\nabla\frac{1}{|\boldsymbol{r}-\boldsymbol{r}'|} = -\frac{\boldsymbol{r}-\boldsymbol{r}'}{|\boldsymbol{r}-\boldsymbol{r}'|^3}$ at hand, the latter equation can be further simplified

$$\boldsymbol{e}(\boldsymbol{r}) = -\frac{1}{4\pi\epsilon_0}\nabla\int_{\mathbb{R}^3}\frac{\lambda(\boldsymbol{r}')}{|\boldsymbol{r}-\boldsymbol{r}'|}dv', \tag{2.8}$$

where we could pull the gradient operator out of the integral, as it acts on $\boldsymbol{r}$ and not on $\boldsymbol{r}'$. We now define the *scalar electric potential* ϕ as follows

$$\phi(\boldsymbol{r}) = \frac{1}{4\pi\epsilon_0}\int_{\mathbb{R}^3}\frac{\lambda(\boldsymbol{r}')}{|\boldsymbol{r}-\boldsymbol{r}'|}dv' \tag{2.9}$$
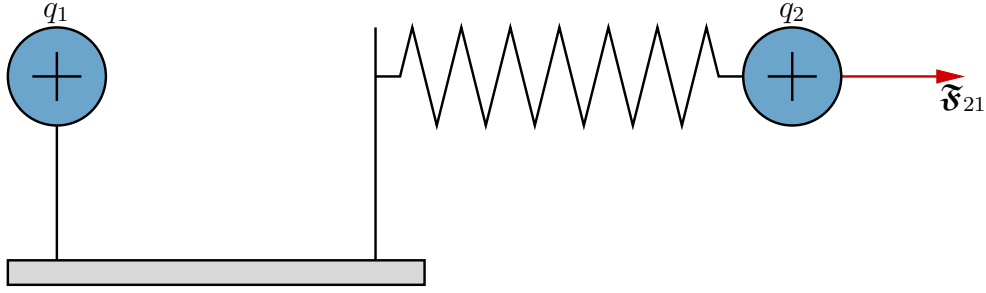
Figure 2.4: Measuring the work done between two charges. One charge is kept fixed while the other charge pulls a spring [157].

and see that the electric field is the gradient of the latter scalar-valued function

$$\boxed{\boldsymbol{e} = -\nabla\phi.} \tag{2.10}$$

It thus always fulfills the condition

$$\operatorname{curl}\boldsymbol{e} = \boldsymbol{0}, \tag{2.11}$$

which is also known as the *static Faraday's law*. We can now further use the property of the Dirac delta function

$$\delta(\boldsymbol{r} - \boldsymbol{r}') = -\Delta\frac{1}{4\pi}\frac{1}{|\boldsymbol{r} - \boldsymbol{r}'|} = -\frac{1}{4\pi}\Delta\frac{1}{|\boldsymbol{r} - \boldsymbol{r}'|} \tag{2.12}$$

in order to reformulate Equation (2.8). Applying the divergence operation on both sides then leads to

$$\operatorname{div}\epsilon_0\boldsymbol{e} = \int_{\mathbb{R}^3}\lambda(\boldsymbol{r}')\delta(\boldsymbol{r} - \boldsymbol{r}')dv' = \lambda(\boldsymbol{r}). \tag{2.13}$$

We see that an electric field caused by an arbitrary volume charge density $\lambda(\boldsymbol{r})$ is governed by the two equations

$$\boxed{\operatorname{curl}\boldsymbol{e} = \boldsymbol{0} \quad \text{and} \quad \operatorname{div}\epsilon_0\boldsymbol{e} = \lambda(\boldsymbol{r}),} \tag{2.14}$$

which in combination are called the *Maxwell equations of electrostatics*. These can be transformed into a useful integral form

$$\oint_c \boldsymbol{e}\cdot d\boldsymbol{s} = 0 \quad \text{and} \quad \int_a \epsilon_0\boldsymbol{e}\cdot d\boldsymbol{a} = \int_g \lambda\,dv = Q, \tag{2.15}$$

where c and a are closed curves and areas respectively, and Q is the integration of the charge density over a volume g being enclosed by the area a. Localization of the latter equation would recover the differential equations again.

2.1.2. Energy of charges

One can define the work performed by two charges on each other by the thought experiment shown in Figure 2.4: The charge q_1 is kept at its place while the force $\mathfrak{F}_{21}$ acting

on charge q_2 pulls an attached spring. In line with Equation (2.5), an extension from location r_2 to r'_2 results in the overall work

$$
\begin{aligned}
A &= q_2 \int_{r_2}^{r'_2} e_1(\boldsymbol{r}) ds = -q_2 \int_{r_2}^{r'_2} \nabla \phi_1(\boldsymbol{r}) ds \\
&= q_2(\phi_1(\boldsymbol{r}_2) - \phi_1(\boldsymbol{r}'_2)) = \frac{q_1 q_2}{4\pi\epsilon_0} \left(\frac{1}{|\boldsymbol{r}_2 - \boldsymbol{r}_1|} - \frac{1}{|\boldsymbol{r}'_2 - \boldsymbol{r}_1|} \right),
\end{aligned}
\tag{2.16}
$$

where we inserted Equation (2.9) for the scalar electric potential. As the spring is only moving in x_1-direction, we only used the x_1-component of the electric field in the latter equation, denoted as $e_1 = \nabla \phi_1$. The maximum work performed by this system appears for $\boldsymbol{r}'_2 \to \infty$ and gives

$$
A_{max} = \frac{q_1 q_2}{4\pi\epsilon_0} \frac{1}{|\boldsymbol{r}_2 - \boldsymbol{r}_1|} = q_2 \phi_1(\boldsymbol{r}_2),
\tag{2.17}
$$

which can be regarded as the potential energy stored in the system of charges before the displacement. With this explanation, we can interpret the energy

$$
W_e = q_2 \phi_1(\boldsymbol{r}_2) = \frac{q_1 q_2}{4\pi\epsilon_0} \frac{1}{|\boldsymbol{r}_2 - \boldsymbol{r}_1|} = q_1 \phi_2(\boldsymbol{r}_1) = \frac{1}{2}(q_1 \phi_2(\boldsymbol{r}_1) + q_2 \phi_1(\boldsymbol{r}_2))
\tag{2.18}
$$

as the *electric interaction energy* of two charges. Having a system of N point charges, the overall interaction energy of the system is

$$
W_e = \frac{1}{4\pi\epsilon_0} \sum_{i=1}^{N-1} \sum_{j>i}^{N} \frac{q_i q_j}{|\boldsymbol{r}_i - \boldsymbol{r}_j|} = \frac{1}{2} \frac{1}{4\pi\epsilon_0} \sum_{\substack{i,j=1 \\ i\neq j}}^{N} \frac{q_i q_j}{|\boldsymbol{r}_i - \boldsymbol{r}_j|}.
\tag{2.19}
$$

Analogously to the previous section, we perform a transition to a continuous description in terms of charge densities. With relation (2.9) at hand, we arrive at

$$
W_e = \frac{1}{8\pi\epsilon_0} \int_{\mathbb{R}^3} \int_{\mathbb{R}^3} \frac{\lambda(\boldsymbol{r})\lambda(\boldsymbol{r}')}{|\boldsymbol{r} - \boldsymbol{r}'|} dv dv' = \frac{1}{2} \int_{\mathbb{R}^3} \lambda(\boldsymbol{r})\phi(\boldsymbol{r}) dv.
\tag{2.20}
$$

Using the Gauss equation $\lambda = \operatorname{div} \epsilon_0 \boldsymbol{e} = -\epsilon_0 \operatorname{div} \nabla \phi$ and integration by parts, the latter equation can be recast into

$$
W_e = -\frac{\epsilon_0}{2} \int_{\mathbb{R}^3} \phi \operatorname{div} \nabla \phi \, dv = -\frac{\epsilon_0}{2} \oint_{\mathbb{R}^2} \phi \nabla \phi \cdot \boldsymbol{n} \, da + \frac{\epsilon_0}{2} \int_{\mathbb{R}^3} \nabla \phi \cdot \nabla \phi \, dv.
\tag{2.21}
$$

For the thought experiment as visualized in Figure 2.4, the scalar electric potential is described through Equation (2.9). From Equation (2.9), we obtain the following dependencies of the scalar potential $\phi \sim 1/r$ and its gradient $|\nabla \phi| \sim 1/r^2$ and thus $\phi \nabla \phi \sim 1/r^3$. As the area integral only scales quadratically in terms of the radius $\oint_{\mathbb{R}^2} \boldsymbol{n} \, da \sim r^2$, for $r \to \infty$, the boundary integral vanishes and we identify the energy

$$
W_e = \int_{\mathbb{R}^3} \frac{\epsilon_0}{2} \boldsymbol{e} \cdot \boldsymbol{e} \, dv,
\tag{2.22}
$$

where the integrand is the well-known *energy density function for the electric field in vacuum*

$$
\boxed{\psi_e = \frac{\epsilon_0}{2} \boldsymbol{e} \cdot \boldsymbol{e}.}
\tag{2.23}
$$
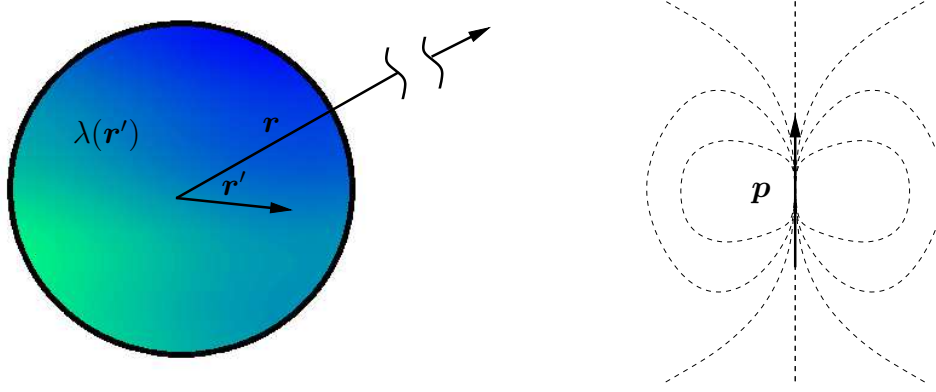
Figure 2.5: Anisotropic charge density $\lambda(\boldsymbol{r}')$ leading to an infinitesimal polarizing momentum, which influences the outer electric field in $r \gg r'$.

2.1.3. The electric field in matter

So far, the previous sections have covered the electric fields emerging from point charges or charge density distributions in vacuum. Next, the electric field in matter is explored. The matter is composed of atoms which compose molecules or crystal lattices. Despite some of those material having zero average charge, the distribution of charges within the latices might be highly anisotropic. This microscopic anisotropy can have a major impact on an external macroscopic field, as shown for *dielectrics* in the subsequent sections. We will therefore first perform a dipole expansion of the electric field. Next, the outer and the inner electric field of a sphere with charge density distribution is investigated. Focus lies in materials that are able to polarize, i.e. will change their charge distribution when being exposed to an electric field. The Maxwell equations in matter will therefore be modified compared to the ones in vacuum. Finally, an energy density function for dielectric matter is derived.

Dipole expansion of the electric field. Recalling our definition of the scalar electric potential

$$\phi = \frac{1}{4\pi\epsilon_0} \int_{\mathbb{R}^3} \frac{\lambda(\boldsymbol{r}')}{|\boldsymbol{r} - \boldsymbol{r}'|} dv', \tag{2.24}$$

we know from experiments that the volume charge density $\lambda(\boldsymbol{r}')$ can have nonlinear distributions as visualized in Figure 2.5. This nonlinearity results in effective fields in distances far more extensive than the length scales of the individual molecules. We now want to investigate this effect for the case of dielectrics by applying a dipole expansion to the scalar electric potential (2.24). Introducing the definition of the unit direction vectors $\mathfrak{e}_r = \frac{\boldsymbol{r}}{r}$ and $\mathfrak{e}_r' = \frac{\boldsymbol{r}'}{r'}$ and the scale relation $\epsilon = \frac{r'}{r}$, we can rewrite the term

$$\frac{1}{|\boldsymbol{r} - \boldsymbol{r}'|} = \frac{1}{\sqrt{r^2 + r'^2 - 2rr'\mathfrak{e}_r \cdot \mathfrak{e}_r'}} = \frac{1}{r} \frac{1}{\sqrt{1 + \epsilon^2 - 2\epsilon\mathfrak{e}_r \cdot \mathfrak{e}_r'}}. \tag{2.25}$$

In distances far away from the charge density distribution $r \gg r'$, ϵ becomes very small in comparison. We thus can perform a Taylor series on x as

$$\frac{1}{\sqrt{1 + x}} = 1 - \frac{x}{2} + \frac{3}{8}x^2 - \mathcal{O}(x^3) \tag{2.26}$$

Along with $x = \epsilon^2 - 2\epsilon \mathbf{e}_r \cdot \mathbf{e}_r$, we obtain

$$\frac{1}{|\boldsymbol{r} - \boldsymbol{r}'|} = \frac{1}{r}(1 + \epsilon \mathbf{e}_r \cdot \mathbf{e}'_r + \epsilon^2 (\frac{3}{2}(\mathbf{e}_r \cdot \mathbf{e}'_r)^2 - \frac{1}{2} + \mathcal{O}(\epsilon^3)). \tag{2.27}$$

In line with the previous argumentation, if $r \gg r'$, ϵ becomes very small. We therefore truncate the latter equation for order of $\epsilon \geq 2$. Reinserting the definition of ϵ then gives

$$\frac{1}{|\boldsymbol{r} - \boldsymbol{r}'|} = \frac{1}{r} + \frac{1}{r^2}(\mathbf{e}_r \cdot \boldsymbol{r}'). \tag{2.28}$$

Inserting this expression into the scalar electric field (2.24) gives the dipole form

$$\phi = \frac{1}{4\pi\epsilon_0}(\frac{Q}{r} + \frac{\mathfrak{p} \cdot \mathbf{e}_r}{r^2}) = \phi^{(1)} + \phi^{(2)}, \tag{2.29}$$

where Q is the overall charge computed from the charge distribution and $\mathfrak{p}$ is the dipole momentum defined as

$$Q = \int_{\mathbb{R}^3} \lambda(\boldsymbol{r}')dv' \quad \text{and} \quad \mathfrak{p} = \int_{\mathbb{R}^3} \lambda(\boldsymbol{r}')\boldsymbol{r}'dv', \tag{2.30}$$

and where we define the scalar electric potential emerging from the overall charge $\phi^{(1)} = \frac{1}{4\pi\epsilon_0}\frac{Q}{r}$ and the scalar electric potential emerging from the dipole momentum $\phi^{(2)} = \frac{1}{4\pi\epsilon_0}\frac{\mathfrak{p} \cdot \mathbf{e}_r}{r^2}$.

The outer electric field. According to the dipole expansion, the contribution of the scalar potential related to the polarisation within matter of a molecule m that is able to polarizeis

$$\phi_{p,m} = \frac{1}{4\pi\epsilon_0} \left(\frac{Q_m}{|\boldsymbol{r} - \boldsymbol{r}_m|} + \frac{\mathfrak{p}_m \cdot (\boldsymbol{r} - \boldsymbol{r}_m)}{|\boldsymbol{r} - \boldsymbol{r}_m|^3} \right), \tag{2.31}$$

where $\boldsymbol{r}_m$ is the center of mass of the molecule at hand. A material that can polarize is also often called an isolator, as the *polarization field* $\boldsymbol{e}_p$ in the isolator is adjusting against the *external electric field* $\boldsymbol{e}_{ext}$. As a consequence of the superposition principle, the overall electric field can be split as follows

$$\boldsymbol{e} = \boldsymbol{e}_{ext} + \boldsymbol{e}_p. \tag{2.32}$$

Here, $\boldsymbol{e}_p$ is the field that emerges from the superposition of all single fields of the molecules

$$\boldsymbol{e}_p = \sum_m \boldsymbol{e}_{p,m}. \tag{2.33}$$

The electric field that appears at the place of a particular molecule as the result of a superposition of external fields and fields of all other molecules arises as to

$$\boldsymbol{e}_m = \boldsymbol{e}_{ext} + \sum_n (\boldsymbol{e}_{p,n}) - \boldsymbol{e}_{p,m}. \tag{2.34}$$

This electric field that acts on the molecule m, emerges from the superposition principle as the addition of the external field plus the electric field created by all other molecules

n. It can be seen as an overall external field that acts on the molecule n. Along with the relations (2.32) and (2.33), we obtain

$$\boldsymbol{e}_m = \boldsymbol{e} - \boldsymbol{e}_{p,m}. \tag{2.35}$$

For calculating the outer field we now take a closer look at the scalar electric potential (2.31). We see that the integral term (2.30)$_2$ accounting for the dipole momentum depends on the choice of coordinate system. We thus first define a point of reference for each molecule, where we choose its center of charge $\boldsymbol{r}_m(t)$. We split this location into the time-independent time average

$$\overline{\boldsymbol{r}}_m = \lim_{t \to \infty} \frac{1}{2t} \int_{-t}^{+t} \boldsymbol{r}_m(t') dt' \tag{2.36}$$

and the time-dependent fluctuations $\boldsymbol{r}_m^\Delta(t)$ around the average. In summation, the center of mass is then described through

$$\boldsymbol{r}_m(t) = \overline{\boldsymbol{r}}_m + \boldsymbol{r}_m^\Delta(t). \tag{2.37}$$

To a certain extent, this split resembles the decomposition of the mechanical strains into macroscopic constant and fluctuating contribution, which we will see in the subsequent sections. Analogously to the location, the dipole momentum is decomposed

$$\mathfrak{p}_m(t) = \overline{\mathfrak{p}}_m + \mathfrak{p}_m^\Delta(t). \tag{2.38}$$

By definition (2.36), the time average of the fluctuating contributions of $\boldsymbol{r}_m(t)$ and $\mathfrak{p}_m(t)$ must vanish

$$\overline{\mathfrak{p}_m^\Delta(t)} = \boldsymbol{0} \quad \text{and} \quad \overline{\boldsymbol{r}_m^\Delta(t)} = \boldsymbol{0}. \tag{2.39}$$

The time-dependent scalar electric potential differentiates from the static electric potential (2.31) only in a correction term that is negligibly small at speeds much slower than light. For a detailed proof, the reader is referred to REBHAN [157]. We thus can write

$$\phi_{p,m}(\boldsymbol{r}, t) = \frac{1}{4\pi\epsilon_0} \left(\frac{Q_m}{|\boldsymbol{r} - \boldsymbol{r}_m(t)|} + \frac{\mathfrak{p}_m(t) \cdot (\boldsymbol{r} - \boldsymbol{r}_m(t))}{|\boldsymbol{r} - \boldsymbol{r}_m(t)|^3} \right). \tag{2.40}$$

Using the decomposition of the molecule location (2.37) and performing the dipole expansion analogously to the previous section, we obtain

$$\begin{aligned}
\frac{1}{|\boldsymbol{r} - \boldsymbol{r}_m(t)|} &= \frac{1}{|\boldsymbol{r} - \overline{\boldsymbol{r}}_m - \boldsymbol{r}_m^\Delta(t)|} \\
&= \frac{1}{|\boldsymbol{r} - \overline{\boldsymbol{r}}_m|} + \frac{(\boldsymbol{r} - \overline{\boldsymbol{r}}_m) \cdot \boldsymbol{r}_m^\Delta(t)}{|\boldsymbol{r} - \overline{\boldsymbol{r}}_m|^3} + \mathcal{O}\left(\frac{1}{|\boldsymbol{r} - \overline{\boldsymbol{r}}_m|^3} \right).
\end{aligned} \tag{2.41}$$

Using this relation and inserting it into the relation

$$\frac{\boldsymbol{r} - \boldsymbol{r}_m(t)}{|\boldsymbol{r} - \boldsymbol{r}_m(t)|^3} = \frac{\boldsymbol{r} - \overline{\boldsymbol{r}}_m}{|\boldsymbol{r} - \overline{\boldsymbol{r}}_m|^3} + \mathcal{O}\left(\frac{1}{|\boldsymbol{r} - \overline{\boldsymbol{r}}_m|^3} \right) \tag{2.42}$$

allows us to write the time-dependent scalar electric potential (2.40) as

$$\begin{aligned}
\phi_{p,m}(\boldsymbol{r}, t) = \frac{1}{4\pi\epsilon_0} \Bigg(&\frac{Q_m}{|\boldsymbol{r} - \overline{\boldsymbol{r}}_m|} + \frac{\overline{\mathfrak{p}}_m \cdot (\boldsymbol{r} - \overline{\boldsymbol{r}}_m)}{|\boldsymbol{r} - \overline{\boldsymbol{r}}_m|^3} \\
&+ \frac{Q_m(\boldsymbol{r} - \boldsymbol{r}_m) \cdot \boldsymbol{r}_m^\Delta(t)}{|\boldsymbol{r} - \overline{\boldsymbol{r}}_m|^3} + \frac{\mathfrak{p}_m^\Delta(t) \cdot (\boldsymbol{r} - \overline{\boldsymbol{r}}_m)}{|\boldsymbol{r} - \overline{\boldsymbol{r}}_m|^3} \Bigg) + \mathcal{O}\left(\frac{1}{|\boldsymbol{r} - \overline{\boldsymbol{r}}_m|^3} \right).
\end{aligned} \tag{2.43}$$
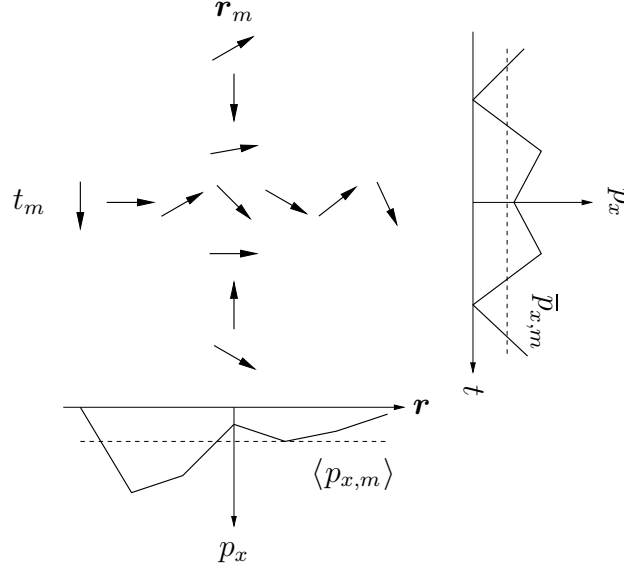
Figure 2.6: The spatial average $\langle p_{x,m} \rangle$ of the fluctuating polarizations in a spatial neighborhood of $\boldsymbol{r}_m$ at time t_m is equivalent to the time average $\overline{p}_{x,m}$ over $t_i, ..., t_M$ for a specific molecule at location $\boldsymbol{r}_m$. Consequently, the averaging of the fluctuations over time as visualized on the top-bottom axis can be exchanged by the averaging over space on the left-right axis.

Next, we want to follow another homogenization concept, and by doing so, we will eliminate the time-dependent terms in the latter equation. Therefore, we consider the neighboring area of a molecule and the spatial distribution of the polarization $\mathfrak{p}_m$. We assume that the fluctuations in space and in time are independent of each other and purely statistical. This independence means the spatial distribution in the neighborhood of $\mathfrak{p}_m$ is the same as the one in time $t_1, ..., t_m$ for a single molecule m, see Figure 2.6. Assuming so, for a given quantity f_m, the average can be either taken in time or space

$$\overline{f}_m = \lim_{t \to \infty} \frac{1}{2t} \int_{-t}^{t} f_m(t')dt' = \frac{1}{M} \sum_{m=1}^{M} f_m = \langle f_m \rangle , \tag{2.44}$$

where in this context $\overline{f}_m$ denotes the time average of f_m and $\langle f_m \rangle$ its spatial average. Here, we set $t_1 = -t$, $t_M = t$ and equidistant time steps $t_i^{\Delta} = t_{i+1} - t_i = \frac{2t}{M}$ and used

$$\overline{f}_m = \sum_{i=1}^{M} f_m(t_i) = \frac{1}{2t} \sum_{i=1}^{M} f_m(t_i) t_i^{\Delta} \approx \lim_{t \to \infty} \frac{1}{2t} \int_{-t}^{t} f_m(t')dt'. \tag{2.45}$$

The independence of space and time regarding the fluctuations and the consequent *equivalence of space and time average* been proved experimentally. We now make use of this equivalence by taking the spatial average of the scalar electric potential without terms of $\mathcal{O}\left(1/|\boldsymbol{r} - \overline{\boldsymbol{r}}_m|^3\right)$

$$\phi_p = \sum_{i=1}^{M} \phi_{p,m} = \frac{1}{4\pi\epsilon_0} \left(\frac{Q_m}{|\boldsymbol{r} - \overline{\boldsymbol{r}}_m|} + \frac{\overline{\mathfrak{p}}_m \cdot (\boldsymbol{r} - \overline{\boldsymbol{r}}_m)}{|\boldsymbol{r} - \overline{\boldsymbol{r}}_m|^3} \right)$$
$$+ \frac{M}{4\pi\epsilon_0} \overline{\left(\frac{Q_m(\boldsymbol{r} - \boldsymbol{r}_m) \cdot \boldsymbol{r}_m^{\Delta}(t)}{|\boldsymbol{r} - \overline{\boldsymbol{r}}_m|^3} + \frac{\mathfrak{p}_m^{\Delta}(t) \cdot (\boldsymbol{r} - \overline{\boldsymbol{r}}_m)}{|\boldsymbol{r} - \overline{\boldsymbol{r}}_m|^3} \right)}, \tag{2.46}$$

where we used the equivalence of space and time average $\sum_{m=1}^{M} f_m = M \langle f_m \rangle = M \overline{f}$ only for the last term. Here, only the quantities $\boldsymbol{r}_m^{\Delta}(t)$ and $\mathfrak{p}^{\Delta}(t)$ are time-dependent. Conse-

quently, the averaging operation that was shifted to time only applies to $\boldsymbol{r}_m^\Delta(t)$ and $\mathfrak{p}^\Delta(t)$, while the other variables are only scaling the average. According to definition (2.39), the averages vanish, leaving the potential in the outer space of the isolater as

$$\phi_p = \sum_{i=1}^M \phi_{p,m} = \frac{1}{4\pi\epsilon_0}\left(\frac{Q_m}{|\boldsymbol{r}-\overline{\boldsymbol{r}}_m|} + \frac{\overline{\mathfrak{p}}_m\cdot(\boldsymbol{r}-\overline{\boldsymbol{r}}_m)}{|\boldsymbol{r}-\overline{\boldsymbol{r}}_m|^3}\right). \tag{2.47}$$

Next, we assume that all molecules have the same charge Q_m. It allows us to write down the average of the charge density as

$$\langle\lambda\rangle = \frac{\sum_{m=1}^M Q_m}{v} = \frac{MQ_m}{v} = \overline{\lambda}, \tag{2.48}$$

where v is the volume occupied by the M molecules. Further assuming that the molecules are macroscopically not moving or rather saying that their only movement is the fluctuating contribution, the charge of molecule m appears as

$$Q_m = \overline{\lambda}v_m^\Delta, \tag{2.49}$$

where $v_m^\Delta = v/M$ is the average neighborhood volume of one molecule. As the fluctuations of the dipole momentum are small compared to macroscopic fields, it is valid to assume that the average dipole momentum $\overline{\mathfrak{p}}_m$ in v is constant, leading to the simplification

$$\overline{\boldsymbol{p}} = \frac{M\overline{\mathfrak{p}}_m}{v} = \frac{M\langle\mathfrak{p}_m\rangle}{v} = \frac{\sum_{m=1}^M \mathfrak{p}_m}{v} = \langle\boldsymbol{p}\rangle, \tag{2.50}$$

which corresponds to an *average dipole density*, from which we can state

$$\overline{\mathfrak{p}}_m = \overline{\boldsymbol{p}}v_m^\Delta. \tag{2.51}$$

Using the averages (2.49) and (2.51) along with (2.47) gives us the potential of the outer electric field

$$\phi_p = \frac{1}{4\pi\epsilon_0}\int \frac{\overline{\lambda}(\boldsymbol{r}')}{|\boldsymbol{r}-\boldsymbol{r}'|} + \frac{\overline{\boldsymbol{p}}(\boldsymbol{r}')\cdot(\boldsymbol{r}-\boldsymbol{r}')}{|\boldsymbol{r}-\boldsymbol{r}'|^3}dv'. \tag{2.52}$$

The electric field of a sphere. In order to have the overall field in the matter, we now want to take a closer look at the inner field of a region with a charge density distribution. As a simplification, we consider a sphere of radius R with a constant charge density λ_0 inside the sphere and zero charge density outside of it

$$\lambda = \begin{cases} \lambda_0 & |r| \leq R \\ 0 & |r| > R \end{cases} \tag{2.53}$$

Having the symmetry of the problem in mind, we can choose an ansatz as follows

$$\boldsymbol{e} = E(r)\frac{\boldsymbol{r}}{r}, \tag{2.54}$$

which automatically satisfies $\mathrm{curl}\,\boldsymbol{e} = \boldsymbol{0}$. Inserting this ansatz into the integral form of the Maxwell equation (2.15)

$$\oint_f \epsilon_0\boldsymbol{e}\cdot d\boldsymbol{f} = \int_A \epsilon_0\boldsymbol{e}\cdot\boldsymbol{n}\,da = \int_g \lambda\,dv, \tag{2.55}$$

and exploiting that $\boldsymbol{n}$ and $\frac{\boldsymbol{r}}{r}$ for a spherical surface always point in the same direction allows writing

$$\int_A \epsilon_0 E(r) \frac{\boldsymbol{r}}{r} \cdot \boldsymbol{n} \, da = \int_A \epsilon_0 E(r) \, da = \int_G \lambda \, dv. \tag{2.56}$$

As the radius r is constant over the surface of the sphere and as λ_0 is contant inside the sphere, we can directly use the sphere surface $A = 4\pi r^2$ and volume $G = \frac{4}{3}\pi r^3$ for the integration and obtain

$$\begin{aligned} \epsilon_0 4\pi r^2 E &= \tfrac{4\pi}{3} r^3 \lambda_0 \quad \text{for} \quad r \le R \\ \epsilon_0 4\pi r^2 E &= Q \qquad \text{for} \quad r \ge R \end{aligned} \tag{2.57}$$

where $Q = \frac{4}{3}\pi R^3 \lambda_0$ satisfies the transition condition. The electric field then appears as

$$E(r) = \begin{cases} \frac{Q}{4\pi\epsilon_0 R^3} r & r \le R \\[2mm] \frac{Q}{4\pi\epsilon_0 r^2} & r \ge R \end{cases}. \tag{2.58}$$

The mean value theorem for harmonic functions. Functions $\phi(\boldsymbol{r})$ that satisfy the Laplace equation $\Delta\phi(\boldsymbol{r}) = 0$ are called harmonic functions. For these functions, we can derive the mean value theorem, which will be needed in subsequent calculations of average values. We, therefore, start with Green's theorem, which states

$$\int_g U\Delta V - V\Delta U \, dv = \int_F U\,\boldsymbol{n}\cdot\nabla V - V\,\boldsymbol{n}\cdot\nabla U \, df. \tag{2.59}$$

Next, we set the terms in the Green's theorem as

$$U(r') = \frac{1}{|\boldsymbol{r}-\boldsymbol{r}'|} \quad \text{and} \quad V(\boldsymbol{r}') = \phi(\boldsymbol{r}'). \tag{2.60}$$

As we know that $\phi(\boldsymbol{r}')$ satisfies the Laplace equation, we see from the latter equation that the same holds true for $V(\boldsymbol{r}')$ and thus $\Delta'V(\boldsymbol{r}') = \Delta'\phi(\boldsymbol{r}') = 0$, where $\Delta' = \operatorname{div}'\nabla'$ is the Laplace operator. Furthermore, we write $\rho = |\boldsymbol{r}-\boldsymbol{r}'|$, which becomes $\rho = R$ on the surface of the sphere f_k, Green's theorem gives

$$\begin{aligned} -\int_k \phi(\boldsymbol{r}')\Delta'\frac{1}{|\boldsymbol{r}-\boldsymbol{r}'|} \, dv' &= \int_{f_k} \frac{1}{\rho}\frac{\partial\phi}{\partial\rho} - \phi(\boldsymbol{r}')\frac{\partial}{\partial\rho}\frac{1}{\rho} \, df' \\ &= \frac{1}{R}\int_{f_k} \frac{\partial\phi(\boldsymbol{r}')}{\partial\rho} \, df' + \frac{1}{R^2}\int_{f_k} \phi(\boldsymbol{r}') \, df'. \end{aligned} \tag{2.61}$$

With the definition of the Dirac delta function (2.12) at hand

$$\delta(\boldsymbol{r}-\boldsymbol{r}') = -\frac{1}{4\pi}\Delta'\frac{1}{|\boldsymbol{r}-\boldsymbol{r}'|}, \tag{2.62}$$

the left-hand side can now be written as

$$\int_k 4\pi\phi(\boldsymbol{r}')\delta(\boldsymbol{r}-\boldsymbol{r}') \, dv = 4\pi\phi(\boldsymbol{r}). \tag{2.63}$$

Regarding the right-hand side of Equation (2.61), the first term must vanish as the harmonic function must fulfill the Laplace equation $\Delta\phi(\boldsymbol{r}') = 0$ and thus

$$\int_{f_k} \frac{\partial\phi(\boldsymbol{r}')}{\partial\rho}\,df' = \int_{f_k} \nabla'\phi(\boldsymbol{r}')\cdot\boldsymbol{n}\,df' = \int_k \mathrm{div}'\nabla'\phi(\boldsymbol{r}')\,dv' = \int_k \Delta'\phi(\boldsymbol{r}')\,dv' = 0, \quad (2.64)$$

must be also fulfilled in its integral form. Comparing the left-hand side of Equation (2.61) as reformulated in Equation (2.63) and the right-hand side of Equation (2.61) using Equation (2.64) finally yields the mean value theorem

$$\boxed{\phi(\boldsymbol{r}) = \frac{1}{4\pi R^2}\int_{f_k}\phi(\boldsymbol{r}')df'.} \qquad (2.65)$$

It states that the value of a harmonic function $\phi(\boldsymbol{r})$ at location $\boldsymbol{r}$ is equal to the average value over the surface f_k of an arbitrary sphere of radius R at location $\boldsymbol{r}$.

The average electric field of a sphere. We will now need these expressions to calculate the average

$$\langle\boldsymbol{e}\rangle = \frac{1}{v}\int_k \boldsymbol{e}(\boldsymbol{r})\,dv \qquad (2.66)$$

of the electric field over the sphere k of radius R at location $\boldsymbol{r}_0$. We further need to distinguish two cases. One where there is no charge density distribution in the sphere and one where there is a charge density distribution in the sphere.

Case 1: No charge density inside sphere

In the case of no charge density, we are allowed to apply the mean value theorem. As $\boldsymbol{e} = -\nabla\phi$ and $\mathrm{div}(\epsilon_0\boldsymbol{e}) = -\epsilon_0\Delta\phi = 0$, we see that

$$\mathrm{div}\,\boldsymbol{e} = -\mathrm{div}\,\nabla\phi = -\Delta\phi = 0 \qquad (2.67)$$

the electric field also satisfies the Laplace equation and thus is a harmonic function. According to the mean value theorem (2.65), we can state

$$\int_{f_k}\boldsymbol{e}(\boldsymbol{r})\,df = 4\pi\rho^2\boldsymbol{e}(\boldsymbol{r}_0) \qquad (2.68)$$

where $\rho = |\boldsymbol{r} - \boldsymbol{r}_0|$ is the radius of the sphere. With the latter equation at hand, the volume average can be split and appears as

$$\int_k \boldsymbol{e}(\boldsymbol{r})\,dv = \int_0^R d\rho \int_{f_k}\boldsymbol{e}(\boldsymbol{r})\,df = \frac{4\pi R^3}{3}\boldsymbol{e}(\boldsymbol{r}_0). \qquad (2.69)$$

With $v = 4\pi R^3/3$ as the volume of the sphere, the volume average can then be computed as

$$\boxed{\langle\boldsymbol{e}\rangle = \frac{1}{v}\int_k \boldsymbol{e}(\boldsymbol{r})\,dv = \boldsymbol{e}(\boldsymbol{r}_0) \quad \text{for} \quad \lambda = 0 \text{ in } k} \qquad (2.70)$$

Case 2: Nonzero charge density inside sphere

For the case of nonzero charge density inside the sphere, expression (2.8) for the electric field is averaged according to Equation (2.66)

$$\langle \boldsymbol{e} \rangle = -\frac{1}{4\pi\epsilon_0}\frac{1}{v}\int_k\int_k \nabla \frac{\lambda(\boldsymbol{r}')}{|\boldsymbol{r}-\boldsymbol{r}'|}\, dv'\, dv$$
$$= -\frac{1}{4\pi\epsilon_0}\frac{1}{v}\int_k\int_k \lambda(\boldsymbol{r}')\nabla \frac{1}{|\boldsymbol{r}-\boldsymbol{r}'|}\, dv'\, dv. \tag{2.71}$$

Using the latter equation along with the relation $\nabla\frac{1}{|\boldsymbol{r}-\boldsymbol{r}'|} = -\nabla'\frac{1}{|\boldsymbol{r}-\boldsymbol{r}'|}$, the average can be formulated as

$$\langle \boldsymbol{e} \rangle = \frac{1}{4\pi\epsilon_0}\frac{1}{v}\int_k \lambda(\boldsymbol{r}')\nabla'\int_k \frac{1}{|\boldsymbol{r}-\boldsymbol{r}'|}\, dv\, dv'. \tag{2.72}$$

We now want to evaluate the second integral of the latter equation. We therefore revisit the result for the electric field in a sphere with zero charge density (2.58) with $Q = \frac{4\pi R^3 \lambda_0}{3}$ and insert it in the ansatz (2.54)

$$\boldsymbol{e} = \frac{\lambda_0 \boldsymbol{r}}{3\epsilon_0}. \tag{2.73}$$

Comparison of this expression with the representation of the electric field through the scalar potential according to Equation (2.8) yields

$$\boldsymbol{e}(\boldsymbol{r}) = -\frac{1}{4\pi\epsilon_0}\nabla\int_k \frac{\lambda_0}{|\boldsymbol{r}-\boldsymbol{r}'|}\, dv' = \frac{\lambda_0}{3\epsilon_0}\boldsymbol{r}. \tag{2.74}$$

Omitting ϵ_0 and λ_0, we obtain the relation

$$-\frac{1}{4\pi}\nabla\int_k \frac{dv'}{|\boldsymbol{r}-\boldsymbol{r}'|} = \frac{1}{4\pi}\int_k \frac{(\boldsymbol{r}-\boldsymbol{r}')}{|\boldsymbol{r}-\boldsymbol{r}'|^3}\, dv' = \frac{1}{3}\boldsymbol{r}. \tag{2.75}$$

Renaming $\boldsymbol{r}$ into $\boldsymbol{r}'$ and inserting this expression into Equation (2.72) gives

$$\langle \boldsymbol{e} \rangle = -\frac{1}{\epsilon_0}\frac{1}{v}\int_k \frac{\lambda(\boldsymbol{r}')}{3}\boldsymbol{r}'\, dv'. \tag{2.76}$$

Using the definition of the polarization (2.30), the final result for the volume average appears as

$$\boxed{\langle \boldsymbol{e} \rangle = -\frac{\mathfrak{p}}{3\epsilon_0 v} \quad \text{for} \quad \lambda \neq 0 \text{ in } k.} \tag{2.77}$$

The inner electric field. Having the average electric field of spheres with charge density distributions at hand, we are now able to compute the inner electric field $\boldsymbol{e}_p$ of a sphere k including far $\boldsymbol{e}_p^{(fa)}$ and close fields $\boldsymbol{e}_p^{(cl)}$. Due to the superposition principle, the field can be additively decomposed

$$\boldsymbol{e}_p = \boldsymbol{e}_p^{(fa)} + \boldsymbol{e}_p^{(cl)}. \tag{2.78}$$

According to the potential (2.52) for the outer potential, the far-field of all other molecules can be calculated as the integral over the outer volume of this potential

$$\boldsymbol{e}_p^{(fa)} = -\frac{1}{4\pi\epsilon_0}\nabla\int_{v-k}\left(\frac{\overline{\lambda}(\boldsymbol{r}')}{|\boldsymbol{r}-\boldsymbol{r}'|} + \frac{\overline{\boldsymbol{p}}(\boldsymbol{r}')\cdot(\boldsymbol{r}-\boldsymbol{r}')}{|\boldsymbol{r}-\boldsymbol{r}'|^3}\right) dv', \tag{2.79}$$

where $v - k$ is the volume of the insulator outside of the sphere that we defined to be microscopically large and macroscopically small. According to the assumptions made in Section 2.1.3 and the resulting potential (2.52), the electric field is constant in time. Furthermore, we consider the sphere to be macroscopically small. Hence, the field is also constant in space. In contrast, observations on the molecule level are dominated by movements of the molecules, and thus, the close field $\boldsymbol{e}_p^{cl}$ changes in time rapidly. However, for a continuous description, we assume that the average of the fields dominates the macroscopic behavior

$$\langle \boldsymbol{e}_p \rangle = \boldsymbol{e}_p^{(fa)} + \langle \boldsymbol{e}_p^{(cl)} \rangle. \tag{2.80}$$

As mentioned, $\boldsymbol{e}_p^{(fa)}$ is considered to be constant on the microscopic scale of the molecules, which is why we are focusing on the averaging of the close field $\boldsymbol{e}_p^{(cl)}$. Using *Faraday's law* of electrostatics

$$\operatorname{curl} \boldsymbol{e} = \boldsymbol{0} \tag{2.81}$$

and having the Helmholtz decomposition in mind, the close electric field on the molecule level can be written in accordance to Equations (2.9) and (2.10) as the gradient field

$$\boldsymbol{e}_p^{(cl)} = -\frac{1}{4\pi\epsilon_0} \nabla \int_k \frac{\lambda'}{|\boldsymbol{r} - \boldsymbol{r}'|} \, dv'. \tag{2.82}$$

According to Equation (2.44), the time and the space average are identical, see also Figure 2.6. Additionally, time-averaging the time average gives the time average. Thus, the following expression holds

$$\langle \boldsymbol{e}_p^{(cl)} \rangle = \overline{\boldsymbol{e}_p^{cl}} = \overline{\overline{\boldsymbol{e}_p^{cl}}} = \overline{\langle \boldsymbol{e}_p^{(cl)} \rangle}. \tag{2.83}$$

Let us now calculate $\overline{\langle \boldsymbol{e}_p^{(cl)} \rangle}$ through the relation (2.77) $\langle \boldsymbol{e} \rangle = -\mathfrak{p}/(3\epsilon_0 V)$ and by using the polarization (2.30), which gives

$$\overline{\langle \boldsymbol{e}_p^{(cl)} \rangle} = -\frac{1}{3\epsilon_0 V} \int_k \overline{\lambda}(\boldsymbol{r}') \boldsymbol{r}' \, dv'. \tag{2.84}$$

We now consider the contribution of an individual molecule occupying v_m to the integral of the right-hand side. Splitting the integral gives

$$\int_{v_m} \overline{\lambda}'(\boldsymbol{r}' - \boldsymbol{r}_m) \, dv' + \int_{v_m} \overline{\lambda}' \boldsymbol{r}_m \, dv' = \overline{\mathfrak{p}}_m + Q_m \boldsymbol{r}_m. \tag{2.85}$$

In case of no free charges or no ionization of the molecule, the sum of all charges times radius in the sphere vanishes $\sum_m Q_m \boldsymbol{r}_m = \boldsymbol{0}$ due to the symmetry of the sphere. This allows us to write

$$\overline{\langle \boldsymbol{e}_p^{(cl)} \rangle} = -\frac{1}{3\epsilon_0} \frac{\sum_m \overline{\mathfrak{p}}_m}{V} = -\frac{M \overline{\mathfrak{p}}_m}{3\epsilon_0 V} = -\frac{\overline{\boldsymbol{p}}(\boldsymbol{r}_0)}{3\epsilon_0}, \tag{2.86}$$

where we used Equation (2.50) for the polarization density. As the electric field

$$\boldsymbol{e}(\boldsymbol{r}_0) = -\frac{1}{4\pi\epsilon_0} \nabla \int_k \frac{\lambda(\boldsymbol{r}_0)}{|\boldsymbol{r}_0 - \boldsymbol{r}|} \, dv' = \boldsymbol{0} \tag{2.87}$$

vanishes in $\boldsymbol{r}_0$, we can add it to the average electric field (2.86) without changing its value

$$\overline{\langle \boldsymbol{e}_p^{(cl)} \rangle} = -\frac{\overline{\boldsymbol{p}}(\boldsymbol{r}_0)}{3\epsilon_0} - \frac{1}{4\pi\epsilon_0} \nabla \int_k \frac{\overline{\lambda}(\boldsymbol{r}_0)}{|\boldsymbol{r}_0 - \boldsymbol{r}'|} \, dv'. \tag{2.88}$$

Using the identity $\overline{\boldsymbol{p}}(\boldsymbol{r}_0) = \nabla(\overline{\boldsymbol{p}}(\boldsymbol{r}_0)\cdot\boldsymbol{r})$ and the definition of $\boldsymbol{r}$ from Equation (2.75) yields

$$\overline{\boldsymbol{p}}(\boldsymbol{r}_0) = \frac{3}{4\pi}\nabla\int_k \frac{\overline{\boldsymbol{p}}(\boldsymbol{r}_0)\cdot(\boldsymbol{r}-\boldsymbol{r}')}{|\boldsymbol{r}-\boldsymbol{r}'|^3}\,dv',\tag{2.89}$$

which can be further divided by $-\frac{1}{3\epsilon_0}$, giving

$$-\frac{\overline{\boldsymbol{p}}}{3\epsilon_0} = -\frac{1}{4\pi\epsilon_0}\nabla\int_k \frac{\overline{\boldsymbol{p}}(\boldsymbol{r}_0)\cdot(\boldsymbol{r}-\boldsymbol{r}')}{|\boldsymbol{r}-\boldsymbol{r}'|^3}\,dv'.\tag{2.90}$$

As the macroscopic quantities $\overline{\boldsymbol{p}}(\boldsymbol{r}_0)$ and $\overline{\lambda}(\boldsymbol{r}_0)$ are not changing in the microscopic sphere k, we can also write them in terms of the variable $\boldsymbol{r}'$ as $\overline{\boldsymbol{p}}(\boldsymbol{r}')$ and $\overline{\lambda}(\boldsymbol{r}')$. The average electric field (2.88) then appears as

$$\langle\overline{\boldsymbol{e}_p^{(cl)}}\rangle = -\frac{1}{4\pi\epsilon_0}\nabla\int_k \frac{\overline{\lambda}(\boldsymbol{r}')}{|\boldsymbol{r}-\boldsymbol{r}'|} + \frac{\overline{\boldsymbol{p}}(\boldsymbol{r}_0)\cdot(\boldsymbol{r}-\boldsymbol{r}')}{|\boldsymbol{r}-\boldsymbol{r}'|^3}\,dv'.\tag{2.91}$$

where $\boldsymbol{r}_0$ in the nominator of the average was renamed to $\boldsymbol{r}$. We now see that averaging the inner field leads to the same result as the far-field (2.79) in terms of the integrand. Regarding the far-field, the integration region was the volume outside the sphere. For the close field, however, the integration is performed over the volume of the sphere. Consequently, the addition of both terms in (2.78) gives the integration over the whole insulator

$$\langle\overline{\boldsymbol{e}_p^{(cl)}}\rangle = -\frac{1}{4\pi\epsilon_0}\nabla\int_v \frac{\overline{\lambda}(\boldsymbol{r}')}{|\boldsymbol{r}-\boldsymbol{r}'|} + \frac{\overline{\boldsymbol{p}}(\boldsymbol{r}_0)\cdot(\boldsymbol{r}-\boldsymbol{r}')}{|\boldsymbol{r}-\boldsymbol{r}'|^3}\,dv'.\tag{2.92}$$

With the chain rule at hand

$$\frac{\overline{\boldsymbol{p}}'\cdot(\boldsymbol{r}-\boldsymbol{r}')}{|\boldsymbol{r}-\boldsymbol{r}'|^3} = \overline{\boldsymbol{p}}'\cdot\nabla'\frac{1}{|\boldsymbol{r}-\boldsymbol{r}'|} = \mathrm{div}'\frac{\overline{\boldsymbol{p}}'}{|\boldsymbol{r}-\boldsymbol{r}'|} - \frac{\mathrm{div}'\,\overline{\boldsymbol{p}}'}{|\boldsymbol{r}-\boldsymbol{r}'|}\tag{2.93}$$

and application of the divergence theorem, we finally obtain the overall electric field in dielectric matter

$$\boldsymbol{e}_p = -\frac{1}{4\pi\epsilon_0}\nabla\left(\int_v \frac{\lambda'-\mathrm{div}'(\boldsymbol{p}')}{|\boldsymbol{r}-\boldsymbol{r}'|}\,dv' + \int_f \frac{\boldsymbol{p}'}{|\boldsymbol{r}-\boldsymbol{r}'|}\,da'\right),\tag{2.94}$$

where - for convenience - we dropped the overlines indicating the time average.

The electrostatic Maxwell equations in matter. With the previous results at hand, we are now able to formulate Maxwell's equations for dielectrics. Using the decomposition of the electric field

$$\boldsymbol{e} = \boldsymbol{e}_{ext} + \boldsymbol{e}_p,\tag{2.95}$$

we see that the curl of the electric field must vanish

$$\mathrm{curl}\,\boldsymbol{e} = \boldsymbol{0},\tag{2.96}$$

as we know that $\mathrm{curl}\,\boldsymbol{e}_{ext} = \boldsymbol{0}$ from the vacuum equations (2.14) and that $\mathrm{curl}\,\boldsymbol{e}_p = \boldsymbol{0}$, as $\boldsymbol{e}_p$ according to (2.94) is a gradient field. For the second differential equation, we will

use the result for the electric field (2.94) along with the Dirac delta function (2.12) and apply the divergence on both sides

$$
\begin{aligned}
\operatorname{div} \epsilon_0 \boldsymbol{e} &= \lambda_{ext} - \int (\lambda' - \operatorname{div}' \boldsymbol{p}') \frac{1}{4\pi} \Delta \frac{1}{|\boldsymbol{r} - \boldsymbol{r}'|} \, dv' - \int \boldsymbol{p}' \frac{1}{4\pi} \Delta \frac{1}{|\boldsymbol{r} - \boldsymbol{r}'|} \, da' \\
&= \lambda_{ext} - \int (\lambda' - \operatorname{div}' \boldsymbol{p}') \frac{1}{4\pi} \delta(\boldsymbol{r} - \boldsymbol{r}') \, dv' - \int \boldsymbol{p}' \frac{1}{4\pi} \delta(\boldsymbol{r} - \boldsymbol{r}') \, da' \\
&= \lambda_{ext} + \lambda - \operatorname{div} \boldsymbol{p}.
\end{aligned}
\tag{2.97}
$$

As λ_{ext} only exists outside the dielectric matter and λ and $\boldsymbol{p}$ only inside the matter, in vacuum we obtain the known equation $\operatorname{div} \epsilon_0 \boldsymbol{e} = \lambda_{ext}$ In the dielectric matter, we then get

$$
\operatorname{div} \epsilon_0 \boldsymbol{e} = \lambda - \operatorname{div} \boldsymbol{p}.
\tag{2.98}
$$

Introducing the definition of the *electric displacement*

$$
\boldsymbol{d} = \epsilon_0 \boldsymbol{e} + \boldsymbol{p},
\tag{2.99}
$$

we obtain the known set of differential equations for dielectric matter

$$
\boxed{\operatorname{curl} \boldsymbol{e} = \boldsymbol{0} \quad \text{and} \quad \operatorname{div} \boldsymbol{d} = \lambda.}
\tag{2.100}
$$

In order to solve the differential equations, we need a proper description of $\boldsymbol{p}$. As it emerges from the charge density distribution of the matter, we can describe the polarization density through a constitutive law. We now use a linear law

$$
\boxed{\boldsymbol{p} = \epsilon_0 \chi \boldsymbol{e},}
\tag{2.101}
$$

which is a good approximation for some dielectric materials, where the material parameter χ is called the *electric susceptibility*. It is defined by means of the molecular polarization α and the molecular density n as follows

$$
\chi = n\alpha = \frac{M}{v^\Delta} \alpha,
\tag{2.102}
$$

where M is the number of molecules in the volume v^Δ. In analogy to the vacuum equations, the differential equations (2.100) for dielectric matter can be recast into an integral form

$$
\oint_c \boldsymbol{e} \cdot d\boldsymbol{s} = 0 \quad \text{and} \quad \int_a \boldsymbol{d} \cdot d\boldsymbol{A} = \int_g \lambda \, dv = Q.
\tag{2.103}
$$

The field energy in dielectric matter. We now want to know the energy of the electric field in the dielectric matter. In analogy to the vacuum approach, we now assume that there is a given scalar electric potential ϕ that is caused by a given charge density λ and the resulting polarization. Next, we consider an additional charge density $\delta\lambda(\boldsymbol{r})$, that is brought to the location $\boldsymbol{r}$. To do so, the electric field $\boldsymbol{e} = -\nabla\phi$ of the dielectric insulator needs to perform the work $\delta'A$ to move the additional charge computed from the additional charge density as $\delta\lambda(\boldsymbol{r}) \, dv$ from an infinitely far position to the position $\boldsymbol{r}$. The work is computed as

$$
\delta A' = \delta\lambda \, dv \int_\infty^{\boldsymbol{r}} \boldsymbol{e} \cdot d\boldsymbol{r} = -\delta\lambda \, dv \int_{\boldsymbol{r}}^\infty \boldsymbol{e} \cdot d\boldsymbol{r} = \delta\lambda \, dv \int_{\boldsymbol{r}}^\infty \nabla\phi \cdot d\boldsymbol{r} = \delta\lambda \, dv \phi(\boldsymbol{r}).
\tag{2.104}
$$

It is the energy that the electric field needs to perform, thus $\delta A' = -\delta W_e$. Using the relations

$$\lambda = \operatorname{div} \boldsymbol{d} \quad \text{and} \quad \delta\lambda = \operatorname{div} \delta\boldsymbol{d} \tag{2.105}$$

and integration over the whole insulator's volume gives the variation of the field energy

$$\delta W_e = \int \phi \operatorname{div} \delta\boldsymbol{d} \, dv = \int \operatorname{div}(\phi\delta\boldsymbol{d}) \, dv - \int \delta\boldsymbol{d} \cdot \nabla\phi \, dv. \tag{2.106}$$

The first integral can be converted into a surface integral

$$\delta W_e = \int \phi\delta\boldsymbol{d} \cdot \boldsymbol{n} \, da - \int \delta\boldsymbol{d} \cdot \nabla\phi \, dv. \tag{2.107}$$

As we assumed that the additional charges are moved from an infite distance to the location $\boldsymbol{r}$, the surface integral is evaluated at $\boldsymbol{r} \to \infty$. From Equation (2.9), we know that the scalar potential scales with the radius according to $\phi \sim 1/r$ and thus, the surface integral vanishes. Using $\boldsymbol{e} = -\nabla\phi$ then gives

$$\delta W_e = \int \boldsymbol{e} \cdot \delta\boldsymbol{d} \, dv. \tag{2.108}$$

In case of a linear relation between $\boldsymbol{d}$ and $\boldsymbol{e}$ as in Equation (2.101) for dielectric matter

$$\boldsymbol{d} = \epsilon_0\boldsymbol{e} + \boldsymbol{p} = \epsilon_0(1 + \chi)\boldsymbol{e}, \tag{2.109}$$

the dot product between electric field and displacement in (2.108) can be recast

$$\begin{aligned}
\boldsymbol{e} \cdot \delta\boldsymbol{d} &= \epsilon_0(1 + \chi)\boldsymbol{e} \cdot \delta\boldsymbol{e} = \frac{1}{2}\epsilon_0(1 + \chi)(\boldsymbol{e} \cdot \delta\boldsymbol{e} + \delta\boldsymbol{e} \cdot \boldsymbol{e}) \\
&= \frac{1}{2}\delta(\boldsymbol{e} \cdot \epsilon_0(1 + \chi)\boldsymbol{e}) = \frac{1}{2}\delta(\boldsymbol{e} \cdot \boldsymbol{d}).
\end{aligned} \tag{2.110}$$

Insertion of the latter equation into the variation of the dielectric field energy (2.106) allows us to identify the field energy as

$$W_e = \int \frac{1}{2}\boldsymbol{e} \cdot \boldsymbol{d} \, dv = \int \psi_e \, dv. \tag{2.111}$$

Along with the dielectric relation for the electric displacement (2.109), the *energy density function* ψ_e for linear dielectric matter is identified as

$$\boxed{\psi_e = \frac{1}{2}\epsilon_0(1 + \chi)\boldsymbol{e} \cdot \boldsymbol{e}.} \tag{2.112}$$

2.2. Fundamentals of continuum mechanics

In this section, the most important parts of the framework of continuum mechanics at finite deformations that were used in this work are revisited, see also GURTIN ET AL. [67] and MIEHE & TEICHTMEISTER [130] for a deeper discussion on the topic. As a major

concern of the theory of geometrical non-linearity at finite deformation are mappings between a non-deformed reference configuration and the deformed current configuration, we will introduce a deformation map and develop the most important mappings such as tangent, area, and volume map. Furthermore, the stress and strain measures relevant to this work are discussed. In order to provide the above-mentioned mappings and mechanical quantities, we first introduce the notion of scalars and tensors as well as the transformation laws they obey, which is in line with conventions of classical differential geometry [157].

Scalar fields. Scalar fields or scalars ϕ are real functions of coordinates $\boldsymbol{x}'$ and remain constant when performing a change of coordinates to $\boldsymbol{x}$

$$\phi'(\boldsymbol{x}') = \phi'(\boldsymbol{x}'(\boldsymbol{x})) = \phi(\boldsymbol{x}). \tag{2.113}$$

Contravariant vectors. We call a vector contravariant if under a given change in coordinates, it transforms like the differential of the coordinates

$$dx'^a = \frac{\partial x'^a}{\partial x^b} dx^b, \tag{2.114}$$

where we use an upper index to label contravariant vectors.

Covariant vectors. We call a vector covariant if it transforms like the gradient of a scalar field

$$\phi'_{,a} = \frac{\partial \phi'}{\partial x'^a} = \frac{\partial x^b}{\partial x'^a}\frac{\partial \phi}{\partial x^b} = \frac{\partial x^b}{\partial x'^a}\phi_{,b}, \tag{2.115}$$

where we used the chain rule and the definition of a scalar field $\phi'(\boldsymbol{x}') = \phi(\boldsymbol{x})$ according to Equation (2.113). We will label covariant vectors with a lower index.

Tensorial objects. Having the definition of co- and contravariant vectors given above, a tensor field $T^{a_1,a_2,\cdots}_{b_1,b_2,\cdots}$ transforms like the product of the vectors $V_1^{a_1}V_2^{a_2}...V_{b_1}^1V_{b_2}^2...$ as follows

$$T'^{c_1,c_2,\cdots}_{d_1,d_2,\cdots} = \frac{\partial x'^{c_1}}{\partial x^{a_1}}\frac{\partial x'^{c_2}}{\partial x^{a_2}}\cdots\frac{\partial x^{b_1}}{\partial x'^{d_1}}\frac{\partial x^{b_2}}{\partial x'^{d_2}}...T^{a_1,a_2,\cdots}_{b_1,b_2,\cdots}. \tag{2.116}$$

We thus see that if a tensor vanishes in one coordinate system, it must vanish in all coordinate systems [157]. This property is especially useful when formulating physical laws that should be invariant with respect to the choice of coordinate systems.

2.2.1. The material body in space

A material body $\mathcal{B}$ consists of solid matter that we can physically interact with, such as a book that we can touch or a building we can walk in. In order to describe the physical processes that are undergone by this body and its interaction with other bodies, we need to embed the body into a mathematical space where we can define and use fundamental invariants of geometric properties. We, therefore, apply a one-to-one mapping of every point of the material to a certain location $\boldsymbol{X} \in \mathbb{R}^3$ as visualized in Figure 2.7. In our
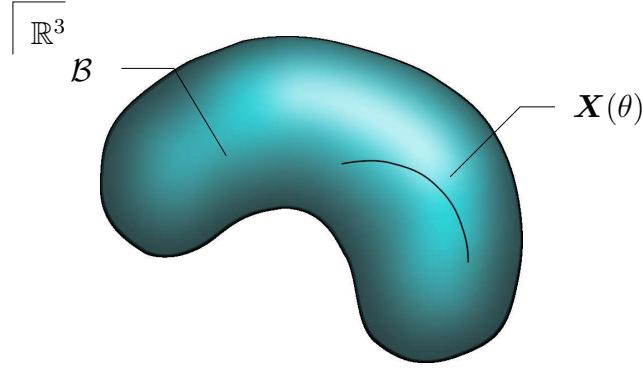
Figure 2.7: A physically experienceable body $\mathcal{B}$ is embedded through a one-to-one map χ_{t_0} into the mathematical Euclidean Space $\mathbb{R}^3$, whose geometry is determined by the Euclidean metric tensor $\boldsymbol{G}$. The metric allows for the invariant computation of lengths of parametrized curves such as $\boldsymbol{X}(\theta)$ and thus the systematic construction of χ_{t_0}.

case, this space is the Euclidean space, and the invariant of the geometry, the Euclidean metric, is in the Pythagorean equation. In Cartesian coordinates, it appears as

$$ds^2 = (dX^1)^2 + (dX^2)^2 + (dX^3)^2, \tag{2.117}$$

where ds^2 is the constant line element of the Euclidean space and dX^A are the differentials of the coordinates. One can also express this invariant in terms of a metric tensor $\boldsymbol{G}$ in index notation as follows

$$ds^2 = G_{AB}dX^A dX^B. \tag{2.118}$$

Comparing the latter equation with Equation (2.117), we see that the entries of the Euclidean metric tensor $\boldsymbol{G}$ in Cartesian coordinates are the ones of the identity. Here, we introduced the up-down index notation, where we state that upper indices can only be contracted with lower indices and the metric serves as a pull-down operation for indices

$$dX_A = G_{AB}dX^B, \tag{2.119}$$

where we denote lower indices as *covariant indices* and upper indices *contravariant indices*. As the Euclidean metric on Cartesian coordinates takes the values of the identity, the components of co- and contravariant vectors such as dX^A and dX_A have the same value, leading again to Equation (2.117).

However, one can also obtain other representations of the Euclidean metric (2.117). Parametrizing $\boldsymbol{X}$ for example in terms of a radius and two angles gives the metric in spherical coordinates, which does not have the identity component values anymore. In such cases, the up-down notation is useful to avoid tensors' contraction without applying the metric appropriately.[1]

With the geometry in terms of the metric at hand, we can now systematically describe the material body in terms of the coordinate system-dependent coordinates $\boldsymbol{X}$ while using invariant quantities such as the scope of a body or some parametrized material lines $\boldsymbol{X}(\Theta)$

---

[1]The theory of differential geometry is a vast field and one could have much deeper discussions on what space and time are, on relativistic metrics, what it means to have matter in space and in general on "what holds the world together at the core" [201]. However, in the continuum mechanics theory applied here, we are concerned with the approximative modeling of material behavior at medium relative velocities, which is why we stick to the Euclidean space.
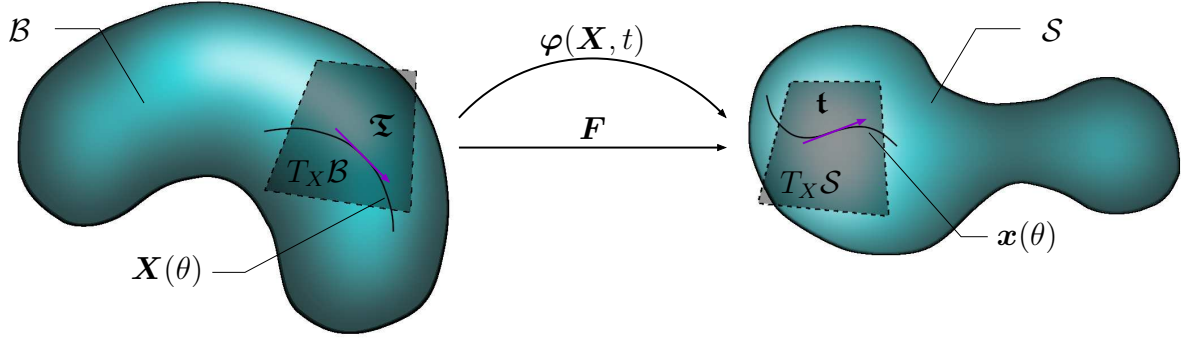
Figure 2.8: The deformation map is a one-to-one map of Lagrangian coordinates $\boldsymbol{X}$ of a manifold $\mathcal{B}$ onto Eulerian coordinates $\boldsymbol{x}$ of the deformed manifold $\mathcal{S}$ at given time t. The deformation gradient $\boldsymbol{F} = \nabla\boldsymbol{\varphi}(\boldsymbol{X},t)$ is a *tensor* and maps Lagrangian tangent vectors $\mathfrak{T}$ of given curves onto their Eulerian representation $\mathbf{t} = \boldsymbol{F}\mathfrak{T}$ at the deformed curve. The tangent vectors are defined within their respective tangent spaces $T_X\mathcal{B}$ in the reference state and $T_X\mathcal{S}$ in the deformed state.

in terms of the free parameter θ. The length of the line, which is obtained through integration of the metric (2.117),

$$ds = \sqrt{\partial_\theta(G_{AB}dX^A(\theta)dX^B(\theta))}\, d\theta, \tag{2.120}$$

should remain constant for a coordinate system change.

2.2.2. Deformation and movement of a material body

Having the embedded body $\mathcal{B}$ in the Euclidean space, we now seek to describe its physical behavior over time in this section, namely its motion and deformation. We, therefore, introduce the *deformation map*

$$\boldsymbol{\varphi}(\boldsymbol{X},t) : \begin{cases} \mathcal{B} \times \mathcal{T} \to \mathcal{S} \subset \mathbb{R}^3, \\ \boldsymbol{X} \mapsto \boldsymbol{x} = \boldsymbol{\varphi}(\boldsymbol{X},t), \end{cases} \tag{2.121}$$

which maps a given mathematical point $\boldsymbol{X} \in \mathcal{B}$ of the *reference* or *Lagrangian configuration* at a given time $t \in \mathcal{T}$ to its *current* or *Eulerian placement* $\boldsymbol{x} \in \mathcal{S}$, see also Figure 2.8. Picking one reference point and evaluating the deformation map over time $\boldsymbol{\varphi}_{\boldsymbol{X}}(t)$ gives the curve of said reference point through space and time. The metric associated with the Eulerian configuration is denoted as $\boldsymbol{g}$. As we are assuming mechnical behavior in the non-relativistic range, the metric is chosen to be the Euclidean metric.

Having the description of the curve of a material point, we can also define the *velocity* and *acceleration* of said point by differentiating the deformation map for time as follows

$$\boldsymbol{V}(\boldsymbol{X},t) = \frac{d}{dt}\boldsymbol{\varphi}_{\boldsymbol{X}}(t) = \frac{\partial}{\partial t}\boldsymbol{\varphi}(\boldsymbol{X},t) \quad \text{and} \quad \boldsymbol{A}(\boldsymbol{X},t) = \frac{d^2}{dt^2}\boldsymbol{\varphi}_{\boldsymbol{X}}(t) = \frac{\partial^2}{\partial t^2}\boldsymbol{\varphi}(\boldsymbol{X},t). \tag{2.122}$$

These definitions of the velocity and acceleration are current quantities parametrized in reference coordinates. The corresponding spatial parametrization can be obtained using the inverse deformation map (2.121) as follows

$$\boldsymbol{v}(\boldsymbol{x},t) = \boldsymbol{V}(\boldsymbol{\varphi}^{-1}(\boldsymbol{x},t),t) \quad \text{and} \quad \boldsymbol{a}(\boldsymbol{x},t) = \dot{\boldsymbol{v}}(\boldsymbol{x},t) = \frac{\partial}{\partial t}\boldsymbol{v}(\boldsymbol{x},t) + \nabla_{\boldsymbol{x}}\boldsymbol{v}(\boldsymbol{x},t) \cdot \boldsymbol{v}. \tag{2.123}$$

In the latter equation, the first term $\frac{\partial}{\partial t}\boldsymbol{v}(\boldsymbol{x},t)$ contributing to the accelration is the *local change of velocity over time*, while the second term $\nabla_{\boldsymbol{x}}\boldsymbol{v}(\boldsymbol{x},t)\cdot\boldsymbol{v}$ accounts for *spatial changes in velocity* as the velocity field may spatially change. This spatial contribution is also known as *convective acceleration*.

2.2.3. The deformation gradient in tangent, area and volume mapping

To formulate accurate physical laws in the Lagrangian and the Eulerian configuration, one needs to know how quantities such as tangential vector, area, and volume transform in between the deformed and the undeformed state. We thus revisit Figure 2.8, where a representative curve in current coordinates is given as $\boldsymbol{x}(\theta)\in\mathcal{S}$. A *referential tangent vector* $\boldsymbol{\mathfrak{T}}\in T_X\mathcal{B}$ of the said curve defined in the *referential tangent space* $T_X\mathcal{B}$ and a *current tangent vector* $\mathbf{t}\in T_X\mathcal{S}$ defined in the *current tangent space* $T_X\mathcal{S}$ can be computed as

$$\boldsymbol{\mathfrak{T}}=\frac{d}{d\theta}\boldsymbol{X}(\theta)\quad\text{and}\quad\mathbf{t}=\frac{d}{d\theta}\boldsymbol{x}(\theta,t). \tag{2.124}$$

As mentioned previously, in this work, the body of interest will always be embedded in the Euclidean space at both configurations, and thus the tangent space at some point will be the Euclidean space itself. Analyzing the current tangent vector and using the deformation map (2.121) gives

$$\mathbf{t}=\frac{d}{d\theta}\boldsymbol{x}(\theta,t)=\frac{d}{d\theta}\boldsymbol{\varphi}(\boldsymbol{X}(\theta),t)=\nabla_{\boldsymbol{X}}\boldsymbol{\varphi}(\boldsymbol{X}(\theta),t)\frac{d}{d\theta}\boldsymbol{X}(\theta)=\boldsymbol{F}\boldsymbol{\mathfrak{T}}, \tag{2.125}$$

where we see that tangential vectors of the referential configuration are mapped to the current configuration by the *deformation gradient*

$$\boldsymbol{F}:\begin{cases}T_X\mathcal{B}\to T_X\mathcal{S},\\ \boldsymbol{\mathfrak{T}}\mapsto\mathbf{t}=\boldsymbol{F}\boldsymbol{\mathfrak{T}}\end{cases}\quad\text{with}\quad\boldsymbol{F}(\boldsymbol{X})=\nabla_{\boldsymbol{X}}\boldsymbol{\varphi}(\boldsymbol{X},t), \tag{2.126}$$

as visualized in Figure 2.8. It is one of the most important tensors for mapping purposes, as we will see in the following. In index notation, the tangent map (2.125) can be written as

$$\mathbf{t}^a=\nabla_{X^B}\boldsymbol{\varphi}(\boldsymbol{X},t)\mathfrak{T}^B=F^a{}_B\,\mathfrak{T}^B. \tag{2.127}$$

Note that even though the deformation map itself maps referential coordinates to current coordinates and is not a tensor as it is not transforming according to Equation (2.116), its gradient is a tensor according to the definitions of the co- and contravariant vectors and the tensorial objects made above. Here, we adopted the notation that small indices are connected to spaces in the Eulerian setting, and capital indices are connected to spaces in the Lagrangian setting. From the latter equation, one immediately sees in line with the definition (2.114) that the deformation gradient maps contravariant tangent tensors $\boldsymbol{\mathfrak{T}}$ of the reference configuration to contravariant tangent tensors $\mathbf{t}$ of the current configuration. One also sees that the deformation gradient tensor itself has one covariant component in the reference configuration and one contravariant component in the current configuration.

Next, consider the reference area of a parallelogram which can be characterized by the cross product of two referential tangent vectors $\boldsymbol{\mathfrak{T}}$ and $\overset{\diamond}{\boldsymbol{\mathfrak{T}}}$ as follows

$$\boldsymbol{A}=\boldsymbol{\mathfrak{T}}\times\overset{\diamond}{\boldsymbol{\mathfrak{T}}}\quad\text{with}\quad A=||\boldsymbol{A}||, \tag{2.128}$$
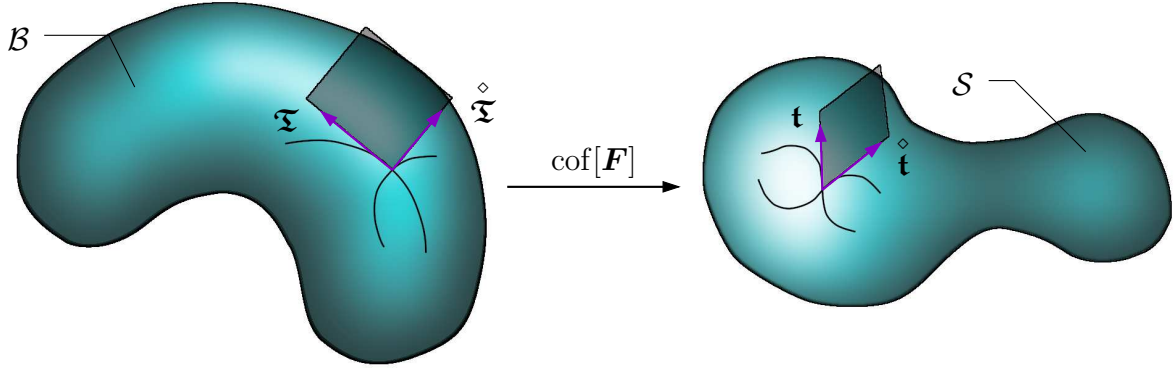
Figure 2.9: A referential area A characterized by the cross product of the referential tangent vectors $\boldsymbol{A} = \mathfrak{T} \times \overset{\diamond}{\mathfrak{T}}$ is transformed into the current area a characterized by the cross product of the current tangent vectors $\boldsymbol{a} = \mathbf{t} \times \overset{\diamond}{\mathbf{t}}$ through the mapping $\mathrm{cof}[\boldsymbol{F}] = \det[\boldsymbol{F}]\boldsymbol{F}^{-T}$.

where $\boldsymbol{A}$ is the surface vector, and A is the area of said surface. What we now want to obtain is a relation between the referential surface vector $\boldsymbol{A}$ and the current surface vector $\boldsymbol{a}$ defined by

$$\boldsymbol{a} = \mathbf{t} \times \overset{\diamond}{\mathbf{t}} \quad \text{with} \quad a = ||\boldsymbol{a}||, \tag{2.129}$$

where a is the area of the deformed surface. Using the tangent map property (2.126) of the deformation gradient, we can write

$$\boldsymbol{a} = \mathbf{t} \times \overset{\diamond}{\mathbf{t}} = (\boldsymbol{F}\mathfrak{T}) \times (\boldsymbol{F}\overset{\diamond}{\mathfrak{T}}) = \boldsymbol{M}_A(\mathfrak{T} \times \overset{\diamond}{\mathfrak{T}}), \tag{2.130}$$

where we now seek to find the area map $\boldsymbol{M}_A$. We start with the relation which is valid for second-order tensors and thus for the deformation gradient. It is given as

$$\boldsymbol{F}\boldsymbol{c}_1 \cdot (\boldsymbol{F}\boldsymbol{c}_2 \times \boldsymbol{F}\boldsymbol{c}_3) = \det[\boldsymbol{F}]\boldsymbol{c}_1 \cdot (\boldsymbol{c}_2 \times \boldsymbol{c}_3), \tag{2.131}$$

in terms of the determinant $\det[\boldsymbol{F}]$ and where $\boldsymbol{c}_i$ are any arbitrary non-zero vectors in Cartesian coordinates. As the latter equation must hold true for all $\boldsymbol{c}_1 \neq \boldsymbol{0}$, we can rearrange as follows

$$\boldsymbol{F}\boldsymbol{c}_2 \times \boldsymbol{F}\boldsymbol{c}_3 = \det[\boldsymbol{F}]\boldsymbol{F}^{-T}(\boldsymbol{c}_2 \times \boldsymbol{c}_3). \tag{2.132}$$

Comparison of the latter equation with relation (2.130) allows us to identify the area map as

$$\boldsymbol{M}_A = \det[\boldsymbol{F}]\boldsymbol{F}^{-T}. \tag{2.133}$$

As the area map is defined through the inverse of the deformation gradient, we can state that it maps *covariant vectors* of the *referential normal space* $T_X^*\mathcal{B}$ onto *covariant vectors* of the *current normal space* $T_X^*\mathcal{S}$ as follows

$$\mathrm{cof}[\boldsymbol{F}] : \begin{cases} T_X^*\mathcal{B} \to T_X^*\mathcal{S}, \\ \boldsymbol{A} \mapsto \boldsymbol{a} = \mathrm{cof}[\boldsymbol{F}]\boldsymbol{A} \end{cases} \quad \text{with} \quad \mathrm{cof}[\boldsymbol{F}] = \det[\boldsymbol{F}]\boldsymbol{F}^{-T}. \tag{2.134}$$

In index notation, this relation can be written as

$$a_a = (\mathrm{cof}[\boldsymbol{F}])_a{}^B A_B = \det[\boldsymbol{F}](F^{-1})^B{}_a A_B. \tag{2.135}$$
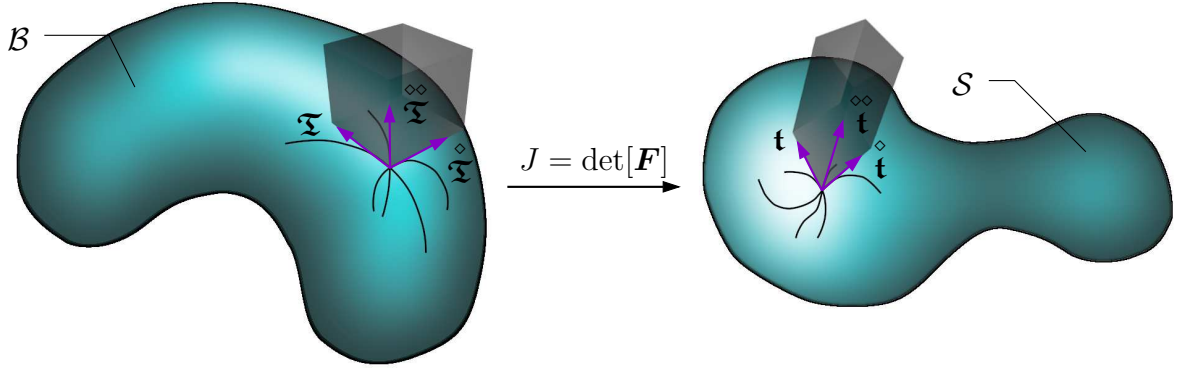
Figure 2.10: A referential volume V characterized by the triple scalar product of the referential tangent vectors $V = \mathfrak{T} \cdot (\overset{\diamond}{\mathfrak{T}} \times \overset{\diamond\diamond}{\mathfrak{T}})$ is transformed into the current volume v characterized by the triple scalar product of the current tangent vectors $v = \mathbf{t} \cdot (\overset{\diamond}{\mathbf{t}} \times \overset{\diamond\diamond}{\mathbf{t}})$ through the mapping $J = \det[\boldsymbol{F}]$.

This mapping property is especially important for numerical methods where the integration of weak forms of differential equations needs to be performed. In line with the previous argumentation, we finally want to motivate the mapping for *referential volume elements* V. Let us therefore consider the scalar triple product between three tangential vectors $\mathfrak{T}$, $\overset{\diamond}{\mathfrak{T}}$, $\overset{\diamond\diamond}{\mathfrak{T}}$ of the referential configuration and the scalar triple product between three tangential vectors $\mathbf{t}$, $\overset{\diamond}{\mathbf{t}}$, $\overset{\diamond\diamond}{\mathbf{t}}$ of the current configuration defined as

$$V = \mathfrak{T} \cdot (\overset{\diamond}{\mathfrak{T}} \times \overset{\diamond\diamond}{\mathfrak{T}}) \quad \text{and} \quad v = \mathbf{t} \cdot (\overset{\diamond}{\mathbf{t}} \times \overset{\diamond\diamond}{\mathbf{t}}), \tag{2.136}$$

where V and v are the volumes of the parallelepiped spanned by the corresponding tangent vectors. We now seek for a mapping between the reference and the current volume of the form

$$v = M_V V. \tag{2.137}$$

Using the definition of the volume v from Equation $(2.136)_2$ along with the mapping of tangential vectors (2.126) and the the determinant's property introduced in (2.131), we obtain

$$\boldsymbol{F}\mathfrak{T} \cdot (\boldsymbol{F}\overset{\diamond}{\mathfrak{T}} \times \boldsymbol{F}\overset{\diamond\diamond}{\mathfrak{T}}) = \det[\boldsymbol{F}]\mathfrak{T} \cdot (\overset{\diamond}{\mathfrak{T}} \times \overset{\diamond\diamond}{\mathfrak{T}}). \tag{2.138}$$

Comparing the latter equation with the general mapping form (2.137), we are able to identify the mapping according to

$$M_V = \det[\boldsymbol{F}]. \tag{2.139}$$

Formally, the volume map is thus defined as

$$J : \begin{cases} \mathbb{R}^+ \to \mathbb{R}^+, \\ V \mapsto v = JV \end{cases} \quad \text{with} \quad J = \det[\boldsymbol{F}]. \tag{2.140}$$

In the latter equation, one important constraint on the deformation gradient $\boldsymbol{F}$ becomes visible, namely that $\det[\boldsymbol{F}] > 0$. This constraint results from the physical argumentation

that volumes should always be positive values $\mathbb{R}^+$, i.e., $V, v > 0$. Otherwise, the conservation of mass and thus of energy would be violated, i.e. the current and reference volume need to be of same sign.

Remark: On the density mapping

We can use the volume map to define a projection of the *reference mass density* ρ_0 onto the *current mass density* ρ. We therefore consider a conservation of mass

$$\int_{\mathcal{B}} \rho_0 \, dV = \int_{\mathcal{S}} \rho \, dv \tag{2.141}$$

and apply the volume map (2.140)

$$\int_{\mathcal{B}} \rho_0 \, dV = \int_{\mathcal{B}} J\rho \, dV. \tag{2.142}$$

We are now able to identify the well-known relation for the mass density mapping

$$\boxed{\rho = \frac{\rho_0}{J}.} \tag{2.143}$$

2.2.4. The right and inverse left Cauchy-Green tensor

Having the definition of the deformation gradient (2.126) as a mapping of tangent vectors at hand, we now want to motivate two additional strain measures that play a central role in continuum mechanics. The deformation of a material can be described by the change in length of some referential contravariant tangent vector $\mathfrak{T}(\boldsymbol{X}) = \mathfrak{T}^a$ as it undergoes deformation. Let us say, the referential tangent vector would be of some *given length*. Its length in the reference frame can be determined using the metric as defined in Equation (2.118) as follows

$$|\mathfrak{T}|_{\boldsymbol{G}} = \sqrt{\mathfrak{T}^A G_{AB} \mathfrak{T}^B}. \tag{2.144}$$

According to the tangent map (2.126) and (2.127), the corresponding Eulerian or current tangent vector is obtained as $\mathbf{t} = \boldsymbol{F} \cdot \mathfrak{T} = F^a{}_B \, \mathfrak{T}^B$. Its norm is obtained using the *current metric* $\boldsymbol{g}$ as follows

$$|\mathbf{t}|_{\boldsymbol{g}} = \sqrt{\mathbf{t}^a g_{ab} \mathbf{t}^b} = \sqrt{F^a{}_B \, \mathfrak{T}^B g_{ab} F^b{}_C \, \mathfrak{T}^C} = \sqrt{\mathfrak{T} \cdot (\boldsymbol{F}^T \boldsymbol{g} \boldsymbol{F}) \mathfrak{T}} = \Lambda |\mathfrak{T}|_{\boldsymbol{G}}, \tag{2.145}$$

where Λ is the *stretch*, i.e. the *change in length* of a vector undergoing a deformation process. Note that we introduced an additional metric $\boldsymbol{g}$ for the current configuration in the latter equation. In all applications considered here, we assume that *both*, the current, and the reference configuration are described accurately enough by an *Euclidean space*. $\boldsymbol{G}$ and $\boldsymbol{g}$ are thus both the Euclidean metric. However, we still distinguish them to have more clarity in the denotation of reference and current configuration. Additionally, we use the notation $\boldsymbol{g}$ or $\boldsymbol{G}$ to denote the metric that is *set* or *chosen*, respectively, while the strain tensors we will derive now follow from the choice of said metric. The *component's values* of the metric chosen might change when changing the coordinate system.

Revisiting the norm of the current tangent vector (2.145), the tensor

$$\boldsymbol{C} = \boldsymbol{F}^T \boldsymbol{g} \boldsymbol{F} \mathrel{\widehat{=}} F^a{}_B \, g_{ab} F^b{}_C = C_{BC} \tag{2.146}$$

a)

b)
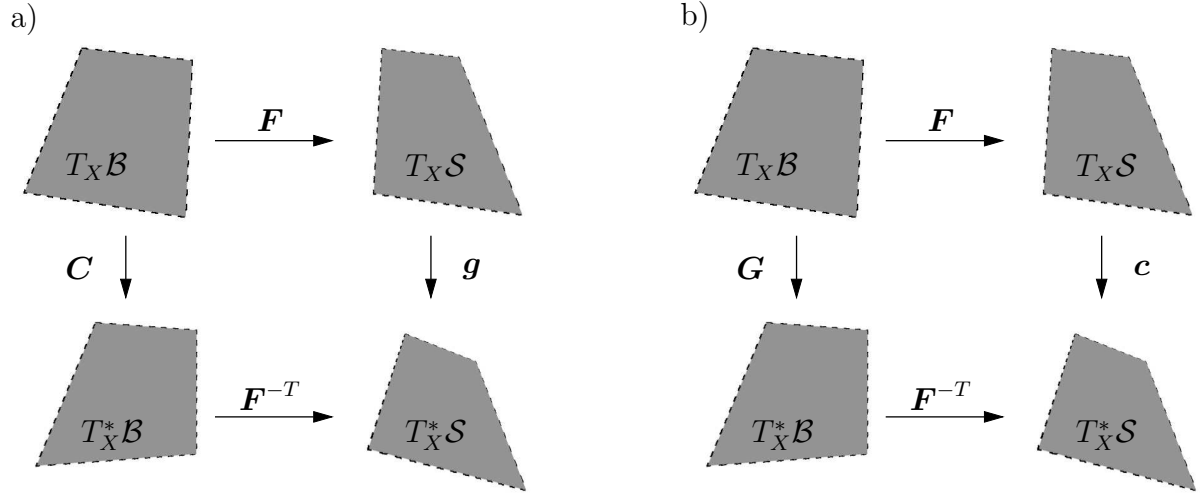
Figure 2.11: a) The right Cauchy-Green tensor $\boldsymbol{C}$ is the referential representation of the current metric $\boldsymbol{g}$. It contracts the referential tangent vector $\mathfrak{T}$ in such a way that it gives the norm of the vectors as obtained *after* deformation in the current configuration $|\mathfrak{T}|_{\boldsymbol{C}} = \sqrt{\mathfrak{T} \cdot \boldsymbol{C}\mathfrak{T}} = \lambda|\mathfrak{T}|_{\boldsymbol{G}}$ where λ is the stretch. b) The inverse left Cauchy-Green tensor $\boldsymbol{c}$ is the current representation of the referential metric $\boldsymbol{G}$. It contracts the current tangent vector $\mathbf{t}$ in such a way, that it gives the norm of the vectors as obtained in the *undeformed state* in the referential configuration $|\mathbf{t}|_{\boldsymbol{c}} = \sqrt{\mathbf{t} \cdot \boldsymbol{c}\mathbf{t}} = \frac{1}{\lambda}|\mathbf{t}|_{\boldsymbol{g}}$.

is called the *right Cauchy-Green tensor*. Comparing it to the norms (2.144) and (2.145), we see that the right Cauchy-Green tensor is the reference representation of the current metric

$$|\mathfrak{T}|_{\boldsymbol{C}} = \sqrt{\mathfrak{T} \cdot \boldsymbol{C}\mathfrak{T}} = \sqrt{\mathfrak{T}^B C_{BC} \mathfrak{T}^C} = \Lambda|\mathfrak{T}|_{\boldsymbol{G}}, \tag{2.147}$$

which relates referential tangential vectors to their *deformed lenght* in the current configuration.

We can also perform this operation backward, assuming that there is some current tangent vector some *given length*

$$|\mathbf{t}|_{\boldsymbol{g}} = \sqrt{\mathbf{t}^a g_{ab} \mathbf{t}^b}. \tag{2.148}$$

Using the *inverse tangent map* in the definition of the length (2.144) gives

$$|\mathfrak{T}|_{\boldsymbol{G}} = \sqrt{\mathfrak{T}^A G_{AB} \mathfrak{T}^B} = \sqrt{(F^{-1})^A{}_b \mathbf{t}^b G_{AB} (F^{-1})^B{}_c \mathbf{t}^c} = \sqrt{\mathbf{t} \cdot (\boldsymbol{F}^{-T} \boldsymbol{G} \boldsymbol{F}^{-1})\mathbf{t}}. \tag{2.149}$$

The tensor

$$\boldsymbol{c} = \boldsymbol{F}^{-T} \boldsymbol{G} \boldsymbol{F}^{-1} \,\widehat{=}\, (F^{-1})^A{}_b G_{AB} (F^{-1})^B{}_c = c_{bc} \tag{2.150}$$

is called the *inverse left Cauchy-Green tensor*. Using the relation (2.145) along with the current norm (2.148), we see that it relates the length of the current tangent vector to the inverse stretch

$$|\mathbf{t}|_{\boldsymbol{c}} = \sqrt{\mathbf{t} \cdot \boldsymbol{c}\mathbf{t}} = \sqrt{\mathbf{t}^b c_{bc} \mathbf{t}^c} = \frac{1}{\Lambda}|\mathbf{t}|_{\boldsymbol{g}}. \tag{2.151}$$

The inverse left Cauchy-Green tensor is thus the current representation of the referential metric. It gives the norm of the current tangential vector as obtained *before* deformation.

2.2.5. Stress measures and stress tensors

Having discussed the essential mapping properties of finite elasticity, we now want to define the most important stress measures. We start with the physically most accessible stress measure, namely the *Cauchy stress tensor* $\boldsymbol{\sigma}$. It is a second-order tensor that relates the unit normal $\boldsymbol{n}$ of the surface in the deformed state to a current traction vector $\boldsymbol{t}$ according to

$$\boldsymbol{t} = \boldsymbol{\sigma}\boldsymbol{n}. \tag{2.152}$$

It thus gives the force related to the deformed area, i.e. the area in the current configuration. From the area mapping relation (2.134), we know that normal vectors $\boldsymbol{n}$ of areas are covariant vectors of the normal space $T_X^*\mathcal{S}$, while $\boldsymbol{t}$ is defined as a contravariant vector in the tangent space $T_X\mathcal{S}$. We thus can formulate Cauchy's theorem as the mapping

$$\boxed{\boldsymbol{\sigma} : \begin{cases} T_X^*\mathcal{S} \to T_X\mathcal{S}, \\ \boldsymbol{n} \mapsto \boldsymbol{t} = \boldsymbol{\sigma}\boldsymbol{n} \end{cases}}. \tag{2.153}$$

In index notation, the latter equation appears as

$$t^a = \sigma^{ab}n_b. \tag{2.154}$$

The second stress tensor we want to discuss is experimentally more accessible than the Cauchy tensor. It is given by *first Piola-Kirchhoff stress tensor* $\widetilde{\boldsymbol{T}}$ and relates a force to an undeformed reference unit area defined by $\boldsymbol{N}$ according to

$$\boldsymbol{t}^0 = \widetilde{\boldsymbol{T}}\boldsymbol{N}. \tag{2.155}$$

Concerning the force, this would give the equality

$$\boldsymbol{t}^0 dA = \boldsymbol{t}da. \tag{2.156}$$

Insertion of the Cauchy theorems (2.152) and (2.155) into the latter equation as well as using the area map (2.134) gives

$$\widetilde{\boldsymbol{T}}d\boldsymbol{A} = \boldsymbol{\sigma}\,\mathrm{cof}[\boldsymbol{F}]d\boldsymbol{A}, \tag{2.157}$$

which allows for the relation of the first Piola Kirchhoff stress tensor and the Cauchy stress to be written down as

$$\widetilde{\boldsymbol{T}} = J\boldsymbol{\sigma}\boldsymbol{F}^{-T}. \tag{2.158}$$

Using the index notation for the cofactor (2.135) and the Cauchy stress (2.154), we obtain the index notation for the first Piola-Kirchhoff stress tensor

$$\widetilde{T}^{aA} = J\sigma^{ab}(F^{-1})^A{}_b, \tag{2.159}$$

where we now see that it has two upper indices and thus maps a unit reference area $\boldsymbol{N}$ of the covariant space onto a current tangent vector $\boldsymbol{t}^0$ of the contravariant space according to

$$\boxed{\widetilde{\boldsymbol{T}} : \begin{cases} T_X^*\mathcal{B} \to T_X\mathcal{S}, \\ \boldsymbol{N} \mapsto \boldsymbol{t}^0 = \widetilde{\boldsymbol{T}}\boldsymbol{N} \end{cases}}. \tag{2.160}$$

In index notation, the latter equation appears as

$$t^{0,a} = \widetilde{T}^{aA}N_A. \tag{2.161}$$
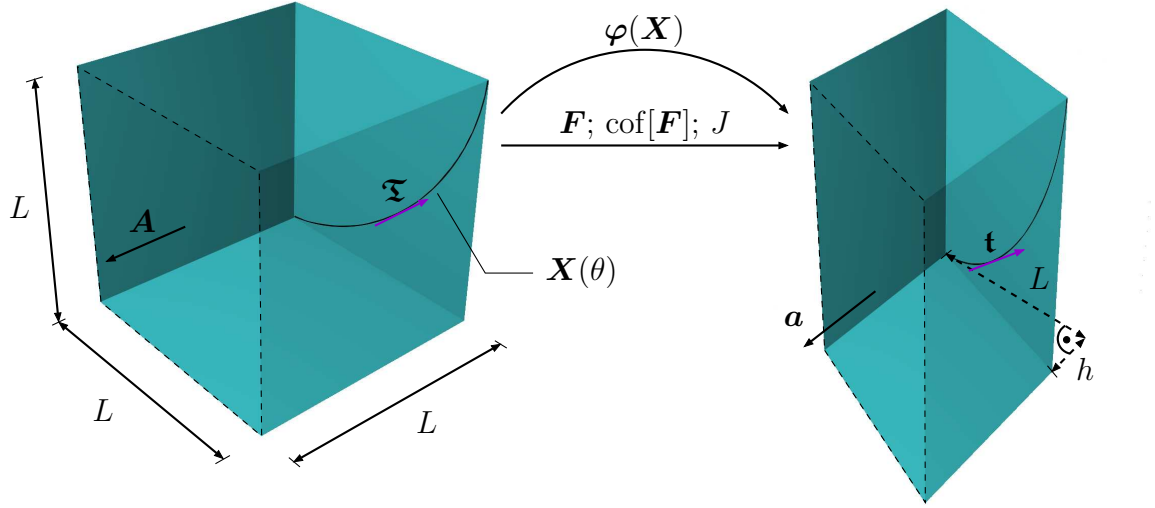
Figure 2.12: A homogeneous shear deformation described by the deformation map $\boldsymbol{\varphi}(\boldsymbol{X})$, where $\boldsymbol{X}$ is given in Cartesian coordinates. The referential tangent vector $\mathfrak{T}$ of the parametrized curve $\boldsymbol{X}(\theta)$ is mapped through the deformation gradient $\boldsymbol{F}$ onto the current tangent vector $\mathbf{t}$. The change in referential area $\boldsymbol{A}$ to the current area $\boldsymbol{a}$ is mapped by the cofactor $\mathrm{cof}[\boldsymbol{F}]$, while the referential volume dV is mapped to the current volume dv by the Jacobian J.

2.2.6. Illustrative Example: Tangent, area and volume map for a homogeneous deformation state

The tangent, area, and volume map properties are now demonstrated based on the example of a homogeneous deformation state. Here, we assume that all coordinates are given in the Eucildean space using a Cartesian coordinate system. Consequently, all quantities in the following equations have Cartesian basis and we assume that the calculation rules for tensor contractions as defined in the Cartesian coordinate system apply. We now consider the following given deformation map and gradient

$$\boldsymbol{\varphi}(\boldsymbol{X}) = \begin{bmatrix} X_1 + \frac{X_2}{L}\,h \\ X_2 + \frac{X_1}{L}\,h \\ X_3 \end{bmatrix} \quad \text{and} \quad \boldsymbol{F} = \nabla\boldsymbol{\varphi} = \begin{bmatrix} 1 & \frac{h}{L} & 0 \\ \frac{h}{L} & 1 & 0 \\ 0 & 0 & 1 \end{bmatrix}, \tag{2.162}$$

where L and h are some given length parameters. As visualized in Figure 2.12, this corresponds to a *homogeneous shear deformation* in the X_1-X_2-plane. Next, consider the following parametrized *referential curve*

$$\boldsymbol{X}(\theta) = \begin{bmatrix} 0 \\ \theta L \\ \theta^2 L \end{bmatrix}, \quad \theta \in [0;1], \tag{2.163}$$

giving the curve visualized in Figure 2.12. The tangent vector $\mathfrak{T}$ of this referential curve evaluated at $\theta = 0.5$ appears as

$$\mathfrak{T}(\theta = 0.5) = \frac{\partial \boldsymbol{X}}{\partial \theta}(\theta = 0.5) = \begin{bmatrix} 0 \\ L \\ L \end{bmatrix}. \tag{2.164}$$

We can now evaluate the tangent vector in the current configuration $\mathbf{t}$ in two ways. For the first approach, we use the deformation map $\boldsymbol{\varphi}(\boldsymbol{X}(\theta))$ to map the curve $\boldsymbol{X}(\theta)$ onto the current configuration and then evaluate the derivative with respect to the parameter θ as follows

$$\mathbf{t} = \frac{\partial \boldsymbol{\varphi}(\boldsymbol{X}(\theta))}{\partial \theta} = \begin{bmatrix} h \\ L \\ 2\theta L \end{bmatrix} \quad \rightarrow \quad \mathbf{t}(\theta = 0.5) = \begin{bmatrix} h \\ L \\ L \end{bmatrix}. \tag{2.165}$$

For the second approach, we can exploit that the deformation gradient $\boldsymbol{F}$ is mapping referential tangent vectors onto current tangent vectors. Applying the multiplication

$$\mathbf{t} = \boldsymbol{F}\mathfrak{T} = \begin{bmatrix} 1 & \frac{h}{L} & 0 \\ \frac{h}{L} & 1 & 0 \\ 0 & 0 & 1 \end{bmatrix} \cdot \begin{bmatrix} 0 \\ L \\ L \end{bmatrix} = \begin{bmatrix} h \\ L \\ L \end{bmatrix} \tag{2.166}$$

gives the identical result as the previous approach. Next, we want to investigate the transformation of a referential area. Note that the deformation state in this example is homogeneous, i.e., the deformation gradient is constant everywhere. Thus, the example can be performed for finite areas and volumes. As for the change of the area $\boldsymbol{A}$ denoted by the dashed line in Figure 2.12, we can calculate the new side length of the edge $\sqrt{L^2 + h^2}$ of the cube by using the dashed triangle. We can see from the deformation map that the height of the cube stays constant and thus, we can multiply the side length by the height of the cube, giving the current area

$$a = L\sqrt{L^2 + h^2}. \tag{2.167}$$

In analogy to the tangent vector transformation, we will now use the cofactor to map the referential area to the current one. We, therefore, need the inverse and the Jacobian of the deformation gradient

$$\boldsymbol{F}^{-1} = \begin{bmatrix} \frac{L^2}{L^2 - h^2} & \frac{hL}{h^2 - L^2} & 0 \\ \frac{hL}{h^2 - L^2} & \frac{L^2}{L^2 - h^2} & 0 \\ 0 & 0 & 1 \end{bmatrix} \quad \text{and} \quad J = \det[\boldsymbol{F}] = 1 - \frac{h^2}{L^2}, \tag{2.168}$$

which allows us to compute the cofactor

$$\text{cof}[\boldsymbol{F}] = \det[\boldsymbol{F}]\boldsymbol{F}^{-T} = \begin{bmatrix} 1 & -\frac{h}{L} & 0 \\ -\frac{h}{L} & 1 & 0 \\ 0 & 0 & 1 \end{bmatrix}. \tag{2.169}$$

Having the area $A = L^2$ in the referential setting, the area vector $\boldsymbol{A}$ appears as

$$\boldsymbol{A} = \begin{bmatrix} 0 \\ L^2 \\ 0 \end{bmatrix} \quad \text{with} \quad A = ||\boldsymbol{A}|| = L^2. \tag{2.170}$$

Applying the cofactor to the area vector $\boldsymbol{A}$ gives

$$\boldsymbol{a} = \text{cof}[\boldsymbol{F}]\boldsymbol{A} = \begin{bmatrix} 1 & -\frac{h}{L} & 0 \\ -\frac{h}{L} & 1 & 0 \\ 0 & 0 & 1 \end{bmatrix} \cdot \begin{bmatrix} 0 \\ L^2 \\ 0 \end{bmatrix} = \begin{bmatrix} -Lh \\ L^2 \\ 0 \end{bmatrix} \quad \text{with} \quad a = ||\boldsymbol{a}|| = L\sqrt{L^2 + h^2}, \tag{2.171}$$

which is in line with the previous result (2.167).

Next, the transform of the referential volume $V = L^3$ is carried out. We first calculate the current volume v of the cube by multiplying the area of the parallelogram formed in the X_1-X_2-plane with the height L of the cube

$$v = L(L^2 - h^2), \tag{2.172}$$

which is also obtained by mapping the referential volume V by the Jacobian (2.168)

$$v = \det[\boldsymbol{F}]V = L(L^2 - h^2). \tag{2.173}$$

We finally want to demonstrate the properties of the right Cauchy-Green tensor $\boldsymbol{C}$. According to Equation (2.146) in our example, it is computed as follows

$$\boldsymbol{C} = \boldsymbol{F}^T \boldsymbol{F} = \begin{bmatrix} 1 & \frac{h}{L} & 0 \\ \frac{h}{L} & 1 & 0 \\ 0 & 0 & 1 \end{bmatrix} \cdot \begin{bmatrix} 1 & \frac{h}{L} & 0 \\ \frac{h}{L} & 1 & 0 \\ 0 & 0 & 1 \end{bmatrix} = \begin{bmatrix} 1 + \frac{h^2}{L^2} & 2\frac{h}{L} & 0 \\ 2\frac{h}{L} & 1 + \frac{h^2}{L^2} & 0 \\ 0 & 0 & 1 \end{bmatrix}. \tag{2.174}$$

If we now want to obtain the deformed lengths of a reference object, we can compute it according to Equations (2.145) and (2.147)

$$|\mathbf{t}|_{\boldsymbol{g}} = h^2 + 2L^2 = |\mathfrak{T}|_{\boldsymbol{C}} = \mathfrak{T} \cdot (\boldsymbol{C}\mathfrak{T}) \begin{bmatrix} 0 \\ L \\ L \end{bmatrix} \cdot \left(\begin{bmatrix} 1 + \frac{h^2}{L^2} & 2\frac{h}{L} & 0 \\ 2\frac{h}{L} & 1 + \frac{h^2}{L^2} & 0 \\ 0 & 0 & 1 \end{bmatrix} \cdot \begin{bmatrix} 0 \\ L \\ L \end{bmatrix} \right) = h^2 + 2L^2, \tag{2.175}$$

where we see that using the Cartesian metric on the current deformed vector $\mathbf{t}$ yields the same result as applying the right Cauchy-Green tensor on the reference vector $\mathfrak{T}$.

Foundations of electro-mechano-statics and variational principles

In this section, the previously considered electrostatic and mechanical considerations are combined into an electro-mechanically coupled framework. Therefore, we first present the electric field's mappings and the electric displacement from the reference undeformed configuration onto the current deformed configuration. We then introduce a coupled variational framework that we will show is identical to the classical differential equilibrium equations for electrostatics (2.100) and the balance of linear momentum for mechanics under given kinematic constraints. We will then prove the variational framework's consistency regarding the second law of thermodynamics by setting up the mechano-electric power expression and evaluating the dissipation postulate. Finally, the concept of dissipation potentials, internal variables, and incremental variational potential for the treatment of rate-dependent problems are discussed.

3.1. The electric field and energy density in a deformable body

As a consequence of Coulomb's law, we saw from Equations (2.8) and (2.9) that the current electric field e is the spatial gradient of the scalar electric potential ϕ. Following definition (2.115), it thus is a covariant vector and its coordinates transform accordingly

$$e_a = -\phi_{,a} = -\frac{\partial \phi}{\partial x^a} = -\frac{\partial \phi}{\partial X^B}\left(\frac{\partial \varphi^a}{\partial X^B}\right)^{-1}, \tag{3.1}$$

where we used that according to Equation (2.113), the scalar ϕ is not changing for any transformation. Recalling the definition of the deformation gradient (2.126) and introducing the *electric field of the reference body*

$$E_B = -\frac{\partial \phi}{\partial X^B}, \tag{3.2}$$

the transform of the current electric field (3.1) can be written in index notation as follows

$$e_a = E_B(F^{-1})^B{}_a \tag{3.3}$$

or in symbolic notation as

$$\boldsymbol{e} = \boldsymbol{E}\boldsymbol{F}^{-1} = \boldsymbol{F}^{-T}\boldsymbol{E}. \tag{3.4}$$

The electric energy (2.111) along with the energy density expression (2.112) is consequently transformed as follows

$$W_e = \int_{\mathcal{S}} \psi_e \, dv = \int_{\mathcal{S}} \frac{1}{2}\epsilon_0(1+\chi)\boldsymbol{e} \cdot \boldsymbol{e} \, dv = \int_{\mathcal{S}} \frac{1}{2}\epsilon_0(1+\chi)(\boldsymbol{F}^{-T}\boldsymbol{E}) \cdot (\boldsymbol{F}^{-T}\boldsymbol{E}) \, dv. \tag{3.5}$$

Note that in line with the considerations done in Section 2.2 concerning the metric as defined in (2.118), we would need to compute the magnitude of the electric field using the metric $|\boldsymbol{e}|_g^2 = \boldsymbol{e} \cdot (\boldsymbol{g}\boldsymbol{e})$. Here, we, however, assume the current metric to be Euclidean in Cartesian coordinates $g_{ab} = \delta_{ab}$, which gives the simplified form above. We now need to integrate over the referential body $\mathcal{B}$ and thus use the volume map (2.140) to obtain

$$W_e = \int_{\mathcal{B}} \frac{1}{2}\epsilon_0(1+\chi)J\boldsymbol{C}^{-1} : (\boldsymbol{E} \otimes \boldsymbol{E}) \, dV, \tag{3.6}$$

where we used the definition of the right Cauchy-Green tensor $\boldsymbol{C} = \boldsymbol{F}^T \cdot \boldsymbol{F}$ according to Equation (2.146). Finally, the definition of the electric susceptibility (2.102) is dependent on the current volume Δv through the molecule density. It is thus convenient to use the volume map (2.140) to give the energy in terms of the *modified susceptibility* χ_0

$$\chi = n\alpha = \frac{M}{\Delta v}\alpha = \frac{M}{J\Delta V}\alpha = \chi_0/J, \tag{3.7}$$

as the number of molecules M, the reference volume ΔV and the molecular polarization α are not changing during the deformation process, and thus χ_0 is assumed to be constant. The electric energy of dielectric matter then appears as

$$\boxed{W_e = \int_{\mathcal{B}} \frac{1}{2}\epsilon_0(1+\frac{\chi_0}{J})J\boldsymbol{C}^{-1} : (\boldsymbol{E} \otimes \boldsymbol{E}) \, dV.} \tag{3.8}$$

3.1.1. Geometrical mapping of the electric displacement

The covariant nature of the electric displacement follows from the integral form of the Maxwell equation (2.103)$_2$. Here, we can exploit that the amount of electric charges is conserved during deformation, and thus we can use (2.103)$_2$ in the reference and current configuration to state

$$\int_{\partial\mathcal{S}} \boldsymbol{d} \cdot d\boldsymbol{a} = Q = \int_{\partial\mathcal{B}} \boldsymbol{D} \cdot d\boldsymbol{A}. \tag{3.9}$$

We now use the area map (2.134) to express the current area in terms of the referential area as follows

$$\int_{\partial\mathcal{B}} \boldsymbol{d} \cdot J\boldsymbol{F}^{-T} d\boldsymbol{A} = \int_{\partial\mathcal{B}} \boldsymbol{D} \cdot d\boldsymbol{A}. \tag{3.10}$$

From the latter equation, one can see that the electric displacement transforms according to the area map, which is a map of covariant vectors of the referential normal space onto covariant vectors of the current normal space

$$\boldsymbol{D} = J\boldsymbol{F}^{-1}\boldsymbol{d}. \tag{3.11}$$
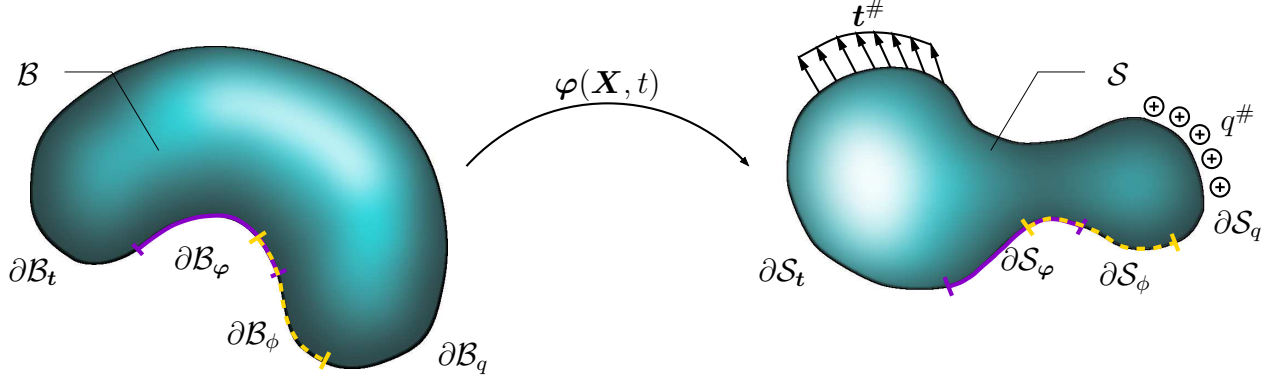
Figure 3.1: A body being exposed to boundary conditions. On Dirichlet boundaries $\partial\mathcal{B}_{\boldsymbol{\varphi}}$ and $\partial\mathcal{B}_{\phi}$, the primary variables $\boldsymbol{\varphi}$ and ϕ are prescribed. On the Neumann boundaries $\partial\mathcal{B}_{\boldsymbol{t}}$ and $\partial\mathcal{B}_{q}$, the tractions and surface charges are prescribed. The same holds for the deformed configuration $\mathcal{S}$. The overall energetic potential is calculated based on these boundary conditions and the internal energy storage behavior of the solid body.

This relation can also nicely be seen in index notation using Equation (2.135)

$$D^B = J(F^{-1})^B{}_a d^a, \tag{3.12}$$

which is a typical pull-pack operation.

3.2. Variational framework for non-dissipative electro-mechanically coupled materials

In Chapter 2.1 regarding the fundamentals of electrostatics, one could see from Equation (2.112) that the energy W_e of an electric field within dielectric matter could be described through the integration of an energy density function ψ_e. We now want to discuss briefly the mathematical framework for electro-mechanically coupled problems within a variational approach, see also [128, 150, 202] for a more detailed discussion. We, therefore, introduce a coupled energy density function

$$\psi = \psi(\boldsymbol{F}, \boldsymbol{E}), \tag{3.13}$$

which is dependent on both the deformation gradient and the electric field. It is not always trivial to formulate such energy densities for complex material behaviors or prove their existence. However, if there exists such an energy density, it can be shown that the results emerging from the resulting variational potential are thermodynamically consistent, as demonstrated in the later Section 3.3. The total stationary energetic potential of a body as presented in Figure 3.1 can then be formulated in terms of said coupled energy density function

$$\Pi(\boldsymbol{\varphi}, \phi) = \int_{\mathcal{B}} \psi(\boldsymbol{F}, \boldsymbol{E})\, dV - \Pi_{ext} \tag{3.14}$$

and the work performed by the external boundary conditions and the external volume contributions as follows

$$\Pi_{ext} = \int_{\mathcal{B}} (\boldsymbol{g}\gamma) \cdot \boldsymbol{\varphi}\, dV + \int_{\partial\mathcal{B}_{\boldsymbol{t}}} (\boldsymbol{g}\boldsymbol{t}^{\#}) \cdot \boldsymbol{\varphi}\, dA - \int_{\mathcal{B}} \lambda\phi\, dV - \int_{\partial\mathcal{B}_q} q^{\#}\phi\, dA, \tag{3.15}$$

where we have one work term due to the displacement of volume forces $\boldsymbol{\gamma}$, one work term due to the displacement of applied tractions $\boldsymbol{t}^{\#}$ on the surface, one work term due to volume charges λ within an electric potential and one work term due to surface charges $q^{\#}$ within an electric potential. In index notation, the global potential appears as

$$\Pi = \int_{\mathcal{B}} \psi \, dV - \int_{\mathcal{B}} g_{ab} \gamma^b \varphi^a \, dV - \int_{\partial \mathcal{B}_t} g_{ab} t^{\#b} \varphi^a \, dA + \int_{\mathcal{B}} \lambda \phi \, dV + \int_{\partial \mathcal{B}_q} q^{\#} \phi \, dA, \quad (3.16)$$

where for the sake of readability, we dropped the notation of dependencies of ψ on $\boldsymbol{F}$ and $\boldsymbol{E}$. From the index notation and comparison with the definition of the traction vector as well as the stress (2.161), it becomes visible why we need the contraction of the metric with the traction and body force for a geometrically consistent setting. From now on, we will, however, assume the Euclidean space and consequently drop the metric in this derivation.

The equilibrium state for a given set of boundary conditions is reached, when the primary variables satisfy the following variational principle

$$\boxed{\{\boldsymbol{\varphi}, \phi\} = \arg \left\{ \inf_{\boldsymbol{\varphi}} \sup_{\phi} \Pi(\boldsymbol{\varphi}, \phi) \right\},} \quad (3.17)$$

i.e., the deformation map $\boldsymbol{\varphi}$ and scalar potential ϕ that minimize the work potential.

3.2.1. Balance of linear momentum

We will now demonstrate that the minimization of the work potential with respect to the primary variables recovers the balance of linear momentum and the Maxwell equation $(2.100)_2$. It can thus be shown that the integral and the differential form are just different representations of the same boundary value problem. The minimization of the work potential can be found performing the variation

$$\delta \Pi = \int_{\mathcal{B}} \frac{\partial \psi}{\partial \boldsymbol{F}} : \delta \boldsymbol{F} + \frac{\partial \psi}{\partial \boldsymbol{E}} \cdot \delta \boldsymbol{E} \, dV - \int_{\mathcal{B}} \boldsymbol{\gamma} \cdot \delta \boldsymbol{\varphi} \, dV - \int_{\partial \mathcal{B}_t} \boldsymbol{t}^{\#} \cdot \delta \boldsymbol{\varphi} \, dA$$
$$+ \int_{\mathcal{B}} \lambda \delta \phi \, dV + \int_{\partial \mathcal{B}_q} q^{\#} \delta \phi \, dA = 0. \quad (3.18)$$

Using the gradient relations for the deformation gradient $\delta \boldsymbol{F} = \delta \nabla \boldsymbol{\varphi}$ and the electric field $\delta \boldsymbol{E} = -\delta \nabla \phi$ along with the expressions

$$\text{Div}(\frac{\partial \psi}{\partial \boldsymbol{F}} \cdot \delta \boldsymbol{\varphi}) = \frac{\partial \psi}{\partial \boldsymbol{F}} : \delta \nabla \boldsymbol{\varphi} + \text{Div}(\frac{\partial \psi}{\partial \boldsymbol{F}}) \cdot \delta \boldsymbol{\varphi} \quad = \frac{\partial \psi}{\partial \boldsymbol{F}} : \delta \boldsymbol{F} + \text{Div}(\frac{\partial \psi}{\partial \boldsymbol{F}}) \cdot \delta \boldsymbol{\varphi},$$
$$\text{Div}(-\frac{\partial \psi}{\partial \boldsymbol{E}} \cdot \delta \phi) = -\frac{\partial \psi}{\partial \boldsymbol{E}} \cdot \delta \nabla \phi + \text{Div}(-\frac{\partial \psi}{\partial \boldsymbol{E}}) \delta \phi \quad = \frac{\partial \psi}{\partial \boldsymbol{E}} \cdot \delta \boldsymbol{E} + \text{Div}(-\frac{\partial \psi}{\partial \boldsymbol{E}}) \delta \phi, \quad (3.19)$$

the variation of the global potential (3.18) can be brought into the following form

$$\delta \Pi = \int_{\mathcal{B}} \text{Div}(\frac{\partial \psi}{\partial \boldsymbol{F}} \cdot \delta \boldsymbol{\varphi}) - \text{Div}(\frac{\partial \psi}{\partial \boldsymbol{F}}) \cdot \delta \boldsymbol{\varphi} \, dV - \int_{\mathcal{B}} \boldsymbol{\gamma} \cdot \delta \boldsymbol{\varphi} \, dV - \int_{\partial \mathcal{B}_t} \boldsymbol{t}^{\#} \cdot \delta \boldsymbol{\varphi} \, dA$$
$$+ \int_{\mathcal{B}} \text{Div}(-\frac{\partial \psi}{\partial \boldsymbol{E}} \delta \phi) - \text{Div}(-\frac{\partial \psi}{\partial \boldsymbol{E}}) \delta \phi \, dV + \int_{\mathcal{B}} \lambda \delta \phi \, dV + \int_{\partial \mathcal{B}_q} q^{\#} \delta \phi \, dA = 0. \quad (3.20)$$

Using the Gauss-theorem to transform volume integrals into surface integrals gives

$$\delta\Pi = \int_{\mathcal{B}}(-\boldsymbol{\gamma} - \text{Div}(\frac{\partial\psi}{\partial\boldsymbol{F}})) \cdot \delta\boldsymbol{\varphi}\, dV + \int_{\mathcal{B}}(\lambda - \text{Div}(-\frac{\partial\psi}{\partial\boldsymbol{E}}))\delta\phi\, dV$$
$$+ \int_{\partial\mathcal{B}_t}(\frac{\partial\psi}{\partial\boldsymbol{F}}\boldsymbol{N} - \boldsymbol{t}^\#) \cdot \delta\boldsymbol{\varphi}\, dA + \int_{\partial\mathcal{B}_q}(-\frac{\partial\psi}{\partial\boldsymbol{E}} \cdot \boldsymbol{N} + q^\#)\delta\phi\, dA = 0. \tag{3.21}$$

According to the fundamental theorem of variational calculus, the variation of the latter potential vanishes if the expression vanishes for *any admissible* variation of the primary fields $\delta\boldsymbol{\varphi}$ and $\delta\phi$. Consequently, the individual terms in the integrals need to, vanish and we see that when equilibrium is reached, then the following *Euler equations* must be fulfilled

$$\boxed{\begin{aligned} \text{Div}(\boldsymbol{T}) + \boldsymbol{\gamma} &= \boldsymbol{0} && \text{in } \mathcal{B} \\ \boldsymbol{T}\boldsymbol{N} &= \boldsymbol{t}^\# && \text{on } \partial\mathcal{B}_t \\ \text{Div}(\boldsymbol{D}) - \lambda &= 0 && \text{in } \mathcal{B} \\ \boldsymbol{D} \cdot \boldsymbol{N} &= -q^\# && \text{on } \partial\mathcal{B}_q. \end{aligned}} \tag{3.22}$$

Here we used the relation $\boldsymbol{T} = \partial\psi/\partial\boldsymbol{F}$ and $\boldsymbol{D} = -\partial\psi/\partial\boldsymbol{E}$, which we will show in the next section to be a thermodynamically consistent approach. In the latter equation, we see that the classical equilibrium equation for electrostatic problems as provided in Chapter 2 as well as the well-known strong form of mechanical equilibrium equations are recovered. We thus are able to conclude that the variational principle governs the same physical laws as the differential form or in other words: If we found the solution for $\boldsymbol{u}$ and ϕ to the optimization principle (3.17) under some given boundary conditions, the solution also satisfies the strong form (3.22).

Remark 1: On the Piola-Kirchhoff stress tensors $\boldsymbol{T}$ and $\widetilde{\boldsymbol{T}}$
Note that strictly speaking, the Piola-Kirchhoff stress tensor $\boldsymbol{T}$ introduced here is not identical to the one $\widetilde{\boldsymbol{T}}$ introduced in the Subsection 2.2.5 in Equation (2.155). One can see this through evaluating the differentiation using index notation

$$\boldsymbol{T} \mathrel{\widehat{=}} \frac{\partial\psi}{\partial F^a{}_B} = T_a{}^B, \tag{3.23}$$

where we see that in contrast to the stress tensor $\widetilde{\boldsymbol{T}}$ from Equation (2.159), $\boldsymbol{T}$ has one contra- and one covariant basis. These co- and contravariant bases are also the reason why the traction vector $\boldsymbol{t}^\#$ appearing in the potential (3.15) must be multiplied with the metric tensor. The stresses can be transformed into each other by use of the metric

$$\boldsymbol{T} = \boldsymbol{g}\widetilde{\boldsymbol{T}} \mathrel{\widehat{=}} g_{ab}\widetilde{T}^{bB} = T_a{}^B. \tag{3.24}$$

As in our simulations, we assume a Euclidean space in a Cartesian system. The entries of both stress tensors are thus identical.

Remark 2: On the electric stress contribution
The Piola-Kirchhoff stress tensor $\boldsymbol{T}$ introduced here is a *total stress*, i.e., it includes mechanical and electrical stress contributions $\boldsymbol{T}_{mech}$ and $\boldsymbol{T}_{elec}$

$$\boldsymbol{T} = \boldsymbol{T}_{mech} + \boldsymbol{T}_{elec}. \tag{3.25}$$

For the case of dielectric matter, the electric stress can be obtained from the energy density in the reference configuration from Equation (3.8)

$$\psi_{elec} = \frac{1}{2}\epsilon_0(1 + \frac{\chi_0}{J})J\boldsymbol{C}^{-1} : (\boldsymbol{E} \otimes \boldsymbol{E}) \tag{3.26}$$

through differentiation

$$\boldsymbol{T}_{elec} = \frac{\partial \psi_{elec}}{\partial \boldsymbol{F}}. \tag{3.27}$$

Physically, one can interpret this stress as the additional contribution due to the attractive force of charges, expressed in terms of the electric field. Insertion of the stress decomposition (3.25) into the balance of linear momentum $(3.22)_1$

$$\text{Div}(\boldsymbol{T}_{mech}) = -\boldsymbol{\gamma} - \text{Div}(\boldsymbol{T}_{elec}) = -\boldsymbol{\gamma} - \boldsymbol{\gamma}_{elec} \tag{3.28}$$

reveals this relation as an additional body-force term [43, 147, 209].

Remark 3: On the volume- and mass-specific energy density
The energy density ψ used here is defined in terms of energy per reference volume. In order to obtain a mass-specific energy density, one would need to divide by the reference density (2.143) accordingly

$$\psi_{mass} = \frac{1}{\rho_0}\psi. \tag{3.29}$$

3.2.2. Balance of angular momentum

The angular momentum is an additional quantity of a material body that is conserved during deformation. The variational formulation thus needs to contain the balance of angular momentum. The balance law postulates a relation between the time differentiation of the *angular momentum* $\mathcal{L}^0 = \int_{\mathcal{B}} \boldsymbol{\varphi} \times \rho_0\dot{\boldsymbol{\varphi}}\,dV$ and the *torque* $\mathcal{T}^0 = \int_{\mathcal{B}} \boldsymbol{\varphi} \times \boldsymbol{\gamma}\,dV + \int_{\partial\mathcal{B}_t} \boldsymbol{\varphi} \times \boldsymbol{t}^\#\,dA$ as follows

$$\frac{d}{dt}\int_{\mathcal{B}} \boldsymbol{\varphi} \times \rho_0\dot{\boldsymbol{\varphi}}\,dV = \mathcal{T}^0 = \int_{\mathcal{B}} \boldsymbol{\varphi} \times \boldsymbol{\gamma}\,dV + \int_{\partial\mathcal{B}_t} \boldsymbol{\varphi} \times \boldsymbol{t}^\#\,dA, \tag{3.30}$$

where the operator $\times$ indicates the cross product of two vectors. Performing the time differentiation and using the relation $(3.22)_2$ between the surface traction and the Piola-Kirchhoff stress tensor as well as the Gauss theorem yields

$$\int_{\mathcal{B}} \dot{\boldsymbol{\varphi}} \times \rho_0\dot{\boldsymbol{\varphi}} + \boldsymbol{\varphi} \times \rho_0\ddot{\boldsymbol{\varphi}}\,dV = \int_{\mathcal{B}} \boldsymbol{\varphi} \times \boldsymbol{\gamma} + \text{Div}(\boldsymbol{\varphi} \times \boldsymbol{T})\,dV, \tag{3.31}$$

where we used that the reference mass density ρ_0 is constant and thus its time differentiation vanishes $\dot{\rho}_0 = 0$. Considering an infinitesimally small domain $dV \to 0$, we obtain the local form

$$\dot{\boldsymbol{\varphi}} \times \rho_0\dot{\boldsymbol{\varphi}} + \boldsymbol{\varphi} \times \rho_0\ddot{\boldsymbol{\varphi}} = \boldsymbol{\varphi} \times \boldsymbol{\gamma} + \text{Div}(\boldsymbol{\varphi} \times \boldsymbol{T}). \tag{3.32}$$

Next, we rewrite the divergence term $\text{Div}(\boldsymbol{\varphi} \times \boldsymbol{T})$ by using the chain rule. In index notation, the term can be written as $(\epsilon^a{}_b{}^c\varphi^b T_c{}^D)_{,D} = \epsilon^a{}_b{}^c\varphi^b{}_{,D}T_c{}^D + \epsilon^a{}_b{}^c\varphi^b T_c{}^D{}_{,D}$, where $\epsilon^a{}_{cd}$ indicates the Levi-Civita symbol. In symbolic notation, the expression appears as

$$\text{Div}(\boldsymbol{\varphi} \times \boldsymbol{T}) = \epsilon : (\boldsymbol{F}\boldsymbol{T}^T) + \boldsymbol{\varphi} \times \text{Div}(\boldsymbol{T}). \tag{3.33}$$

Insertion of the latter expression into the local form of the balance of angular momentum (3.32) yields

$$\dot{\boldsymbol{\varphi}} \times \rho_0 \dot{\boldsymbol{\varphi}} + \boldsymbol{\varphi} \times [\rho_0 \ddot{\boldsymbol{\varphi}} - \boldsymbol{\gamma} - \text{Div}(\boldsymbol{T})] - \boldsymbol{\epsilon} : (\boldsymbol{F}\boldsymbol{T}^T) = \boldsymbol{0}. \tag{3.34}$$

The latter equation can be further simplified. The first term $\dot{\boldsymbol{\varphi}} \times \rho_0 \dot{\boldsymbol{\varphi}}$ vanishes as the cross-product of a vector with itself is zero. Additionally, we assume quasi-static conditions, which allows us to neglect the acceleration $\ddot{\boldsymbol{\varphi}} = \boldsymbol{0}$ and allows us to exploit the static form of the balance of linear momentum $\text{Div}(\boldsymbol{T}) + \boldsymbol{\gamma} = \boldsymbol{0}$ from Equation $(3.22)_1$. We are thus left with

$$\boldsymbol{\epsilon} : (\boldsymbol{F}\boldsymbol{T}^T) = \boldsymbol{0} \tag{3.35}$$

and due to the antisymmetry of $\boldsymbol{\epsilon}$, we arrive at the final result

$$\boxed{\boldsymbol{F}\boldsymbol{T}^T = \boldsymbol{T}\boldsymbol{F}^T,} \tag{3.36}$$

which is the well-known balance of angular momentum [74, 180].

Remark: Material modelling and angular momentum
Using the balance of angular momentum (3.36) and inserting the relation $\boldsymbol{T} = \partial\psi/\partial\boldsymbol{F}$ from Chapter 3.2.1, we obtain

$$\boldsymbol{F}(\frac{\partial\psi}{\partial\boldsymbol{F}})^T = \frac{\partial\psi}{\partial\boldsymbol{F}}\boldsymbol{F}^T. \tag{3.37}$$

As we compute the stress from the energy density function ψ, the balance of angular momentum constrains the way we are allowed to construct the energy density function. It must fulfill the latter equation. Without further proof, this can be done by modelling the energy density function in terms of the right Cauchy-Green tensor $\boldsymbol{C}$. In doing so, the *principle of material objectivity* is also automatically fulfilled. It states that the elastic response must be invariant under any rigid body rotations imposed on the current configuration. As the Cauchy-Green tensor $\boldsymbol{C}$ is apurely referential object, it is not affected by these rotations imposed on the current configuration and ee thus see the equivalence of the modelling approach for fulfilling the balance of angular momentum and the principle of material objectivity. For a more detailed discussion, the interested reader is referred to Miehe & Teichtmeister [130] and Gurtin et al. [67]

3.3. Thermodynamical consistency of the variational formulation

In the previous section, it was shown that the classical equilibrium equations of electro-mechano-statics can be recovered from the variational potential. We now want to demonstrate that a formulation in terms of the energy density $\psi(\boldsymbol{F}, \boldsymbol{E})$ with the relation $\boldsymbol{T} = \partial\psi/\partial\boldsymbol{F}$ and $\boldsymbol{D} = -\partial\psi/\partial\boldsymbol{E}$ also satisfies the second law of thermodynamics, which states that entropy can only grow.

3.3.1. Internal mechanical and electrical power expressions

To look at the work being done within a deforming body with a changing scalar electric potential and to compute the following dissipation of energy, we first develop an expression

for the internal power for said deformation processes, including electric dissipation. We, therefore, start from the spatial velocity $\boldsymbol{v}$ according to (2.123) and the rate of scalar potential $\dot{\phi} = d\phi/dt$ and express the power $\mathcal{P}$ in an integral form

$$\mathcal{P} = \int_{\mathcal{S}} \boldsymbol{\gamma} \cdot (\boldsymbol{g}\boldsymbol{v}) \, dv + \int_{\partial \mathcal{S}_t} \boldsymbol{t}^{\#} \cdot (\boldsymbol{g}\boldsymbol{v}) \, da - \int_{\mathcal{S}} \lambda \dot{\phi} \, dv + \int_{\partial \mathcal{S}_q} q^{\#} \dot{\phi} \, da, \qquad (3.38)$$

where we have a contribution due to the body force, one due to external tractions, one due to the volumetric electric charge, and one due to electric surface charges. These terms are corresponding to the external potential contribution (3.15). From now on, we assume the metric to be the Eucildean metric in Cartesian coordinates and thus drop it in the following derivations as well as the up-down-indices. Using the Cauchy relation for the tractions (2.153) and (2.154), the surface term can be recast into

$$\int_{\partial \mathcal{S}_t} \boldsymbol{t}^{\#} \cdot \boldsymbol{v} \, da = \int_{\partial \mathcal{S}_t} (\boldsymbol{\sigma}\boldsymbol{n}) \cdot \boldsymbol{v} \, da = \int_{\partial \mathcal{S}_t} \sigma_{ab} n_b v_a \, da. \qquad (3.39)$$

Using Gauss theorem, the latter surface integral can be transformed into the following volume integral

$$\int_{\partial \mathcal{S}} \sigma_{ab} n_b v_c \, da = \int_{\mathcal{S}} \sigma_{ab,b} v_a + \sigma_{ab} v_{a,b} \, dv = \int_{\partial \mathcal{S}} \mathrm{div}(\boldsymbol{\sigma}) \cdot \boldsymbol{v} + \boldsymbol{\sigma} : \nabla_{\boldsymbol{x}} \boldsymbol{v} \, dv. \qquad (3.40)$$

We now take a closer look at the *spatial gradient of the spatial velocity* $\nabla_{\boldsymbol{x}} \boldsymbol{v}$ to obtain an explicit expression in terms of the deformation gradient. First, we consider a stretch vector $\boldsymbol{\lambda}$, which is according to the tangent map (2.126) obtained by multiplication of a reference vector $\boldsymbol{M}$ by the deformation gradient as follows

$$\boldsymbol{\lambda} = \boldsymbol{F}\boldsymbol{M}. \qquad (3.41)$$

The reference vector is chosen to be of unit-length. It has no time-dependency, which is why we can take the time-differentiation as follows

$$\dot{\boldsymbol{\lambda}} = \dot{\boldsymbol{F}}\boldsymbol{M}. \qquad (3.42)$$

Setting up the inverse relation for the stretch vector (3.41)

$$\boldsymbol{M} = \boldsymbol{F}^{-1}\boldsymbol{\lambda} \qquad (3.43)$$

allows for the insertion into the time-derivative (3.42)

$$\dot{\boldsymbol{\lambda}} = \dot{\boldsymbol{F}}\boldsymbol{F}^{-1}\boldsymbol{\lambda}, \qquad (3.44)$$

which gives the *rate of the stretch vector* in terms of the deformation gradient. Analyzing the multiplication of the rate of the deformation gradient with the inverse of the deformation gradient allows for the following reformulation

$$\boldsymbol{l} = \dot{\boldsymbol{F}}\boldsymbol{F}^{-1} = (\frac{\partial}{\partial t} \frac{\partial \boldsymbol{\varphi}}{\partial \boldsymbol{X}})(\frac{\partial \boldsymbol{\varphi}}{\partial \boldsymbol{X}})^{-1} = (\frac{\partial}{\partial \boldsymbol{X}} \frac{\partial \boldsymbol{\varphi}}{\partial t})(\frac{\partial \boldsymbol{\varphi}}{\partial \boldsymbol{X}})^{-1} = (\frac{\partial}{\partial \boldsymbol{X}} \boldsymbol{V})(\frac{\partial \boldsymbol{\varphi}}{\partial \boldsymbol{X}})^{-1}, \qquad (3.45)$$

where we used the definition of the material velocity (2.122) and the rule of Schwarz to swap the space and time derivative. Reparametrization according to (2.123) and using the relation of the deformation map $\boldsymbol{x} = \boldsymbol{\varphi}(\boldsymbol{X}, t)$ from (2.121) gives

$$\nabla_{\boldsymbol{x}} \boldsymbol{v} = \boldsymbol{l} = \dot{\boldsymbol{F}}\boldsymbol{F}^{-1}. \qquad (3.46)$$

Insertion of the latter equation into the intermediate result (3.40) and further insertion into the power expression (3.38) allows us to write

$$\mathcal{P} = \int_{\mathcal{S}} (\text{div}(\boldsymbol{\sigma}) + \boldsymbol{\gamma}) \cdot \boldsymbol{v} \, dv + \int_{\mathcal{S}} \boldsymbol{\sigma} : \boldsymbol{l} \, dv - \int_{\mathcal{S}} \lambda \dot{\phi} \, dv + \int_{\partial \mathcal{S}_q} q^{\#} \dot{\phi} \, da. \qquad (3.47)$$

As the first bracket in the first integral term represents the balance of linear momentum in the current configuration, its term vanishes in equilibrium and thus we are left with

$$\mathcal{P} = \int_{\mathcal{S}} \boldsymbol{\sigma} : \boldsymbol{l} \, dv - \int_{\mathcal{S}} \lambda \dot{\phi} \, dv + \int_{\partial \mathcal{S}_q} q^{\#} \dot{\phi} \, da. \qquad (3.48)$$

We now follow a similar procedure for the electric contributions for the power expression. From the integral relations for the Maxwell equation (2.103), one can obtain the material relation $q^{\#} = -\boldsymbol{d} \cdot \boldsymbol{n}$, see also (3.22)$_4$ for the spatial setting from the variation potential. We can thus reformulate the electric surface integral term in (3.38) according to

$$\int_{\partial \mathcal{S}} q^{\#} \dot{\phi} \, da = \int_{\mathcal{S}_q} \boldsymbol{d} \cdot \boldsymbol{n} \dot{\phi} \, da = \int_{\mathcal{S}_q} d_a n_a \dot{\phi} \, da. \qquad (3.49)$$

In analogy with the mechanical approach, we now use the Gauss theorem to transform the surface integral into a volume integral

$$d_a n_a \dot{\phi} \, da = \int_{\mathcal{S}} d_{a,a} \dot{\phi} + d_a \dot{\phi}_{,a} \, dv = \int_{\mathcal{S}} \text{div}(\boldsymbol{d}) \dot{\phi} + \boldsymbol{d} \cdot \nabla_{\boldsymbol{x}} \dot{\phi} \, dv. \qquad (3.50)$$

Insertion into the intermediate result for the power expression yields

$$\mathcal{P} = \int_{\mathcal{S}} \boldsymbol{\sigma} : \boldsymbol{l} \, dv + \int_{\mathcal{S}} (\text{div}(\boldsymbol{d}) - \lambda) \dot{\phi} + \boldsymbol{d} \cdot \nabla_{\boldsymbol{x}} \dot{\phi} \, dv. \qquad (3.51)$$

From Maxwell's equations (2.100) for electrostatic problems we know that the bracket term in the second integral vanishes, and we are thus left with the power expression

$$\mathcal{P} = \int_{\mathcal{S}} \boldsymbol{\sigma} : \boldsymbol{l} \, dv + \int_{\mathcal{S}} \boldsymbol{d} \cdot \nabla_{\boldsymbol{x}} \dot{\phi} \, dv. \qquad (3.52)$$

The spatial gradient of the spatial rate of the scalar potential $\nabla_{\boldsymbol{x}} \dot{\phi}$ appears in analogy to the spatial velocity gradient. We now reformulate said tensor according to

$$\nabla_{\boldsymbol{x}} \dot{\phi} = \left(\frac{\partial}{\partial \boldsymbol{X}} \frac{\partial \phi}{\partial t} \right) \left(\frac{\partial \boldsymbol{\varphi}}{\partial \boldsymbol{X}} \right)^{-1} = \left(\frac{\partial}{\partial t} \frac{\partial \phi}{\partial \boldsymbol{X}} \right) \boldsymbol{F}^{-1} \qquad (3.53)$$

Recalling the definition of the referential electric field (3.2) allows us to write

$$\nabla_{\boldsymbol{x}} \dot{\phi} = -\boldsymbol{F}^{-T} \dot{\boldsymbol{E}}. \qquad (3.54)$$

In order to arrive at an Eulerian description of the internal power, we finally apply the pull-back operation for the electric field (3.4) and arrive at

$$\nabla_{\boldsymbol{x}} \dot{\phi} = -\boldsymbol{F}^{-T} \frac{\partial}{\partial t} (\boldsymbol{F}^T \boldsymbol{e}) = -\boldsymbol{\mathcal{L}_v} \boldsymbol{e}, \qquad (3.55)$$

which is the negative *Lie derivative* of $\boldsymbol{e}$, i.e. a pull-back of $\boldsymbol{e}$ to the reference configuration, differentiation with respect to time followed by a push-forward back to the current configuration. The power expression (3.52) in terms of current quantities then finally appears as

$$\boxed{\mathcal{P} = \int_{\mathcal{S}} \boldsymbol{\sigma} : \boldsymbol{l} \, dv - \int_{\mathcal{S}} \boldsymbol{d} \cdot \boldsymbol{\mathcal{L}_v e} \, dv.} \tag{3.56}$$

We now want to express the latter equation in terms of mechanical two-point tensors and electrical referential tensors within a referential volume integral. We start with the mechanical contribution by using the volume map (2.140) and the definition for $\boldsymbol{l}$ from (3.45)

$$\int_{\mathcal{S}} \boldsymbol{\sigma} : \boldsymbol{l} \, dv = \int_{\mathcal{B}} \boldsymbol{\sigma} : (\dot{\boldsymbol{F}} \boldsymbol{F}^{-1}) J \, dV. \tag{3.57}$$

Further insertion of the relation between the first Piola-Kirchhoff stress tensor $\widetilde{\boldsymbol{T}}$ and the current stress $\boldsymbol{\sigma}$ from (2.158) gives

$$\int_{\mathcal{S}} \boldsymbol{\sigma} : \boldsymbol{l} \, dv = \int_{\mathcal{B}} \frac{1}{J} \boldsymbol{F}^T \widetilde{\boldsymbol{T}} : (\dot{\boldsymbol{F}} \boldsymbol{F}^{-1}) J \, dV = \int_{\mathcal{B}} \widetilde{\boldsymbol{T}} : \dot{\boldsymbol{F}} \, dV = \int_{\mathcal{B}} \boldsymbol{T} : \dot{\boldsymbol{F}} \, dV, \tag{3.58}$$

where we used that $\widetilde{\boldsymbol{T}} = \boldsymbol{T}$ in Cartesian coordinates as computed from Equation (3.24). For the electric contribution, we use the volume map (2.140) along with the pull-back of $\nabla_{\boldsymbol{x}} \dot{\phi}$ defined by (3.54) and (3.55) and the pull-back of the current electric displacement $\boldsymbol{d}$ defined by (3.11) and obtain

$$\int_{\mathcal{S}} \boldsymbol{d} \cdot \boldsymbol{\mathcal{L}_v e} \, dv = \int_{\mathcal{B}} \frac{1}{J} (\boldsymbol{F} \boldsymbol{D}) \cdot (\dot{\boldsymbol{E}} \boldsymbol{F}^{-1}) J \, dV = \int_{\mathcal{B}} \boldsymbol{D} \cdot \dot{\boldsymbol{E}} \, dV. \tag{3.59}$$

Insertion of the mechanical relation (3.58) and the electric relation (3.59) into the power expression (3.56) finally gives the form

$$\boxed{\mathcal{P} = \int_{\mathcal{B}} \boldsymbol{T} : \dot{\boldsymbol{F}} \, dV - \int_{\mathcal{B}} \boldsymbol{D} \cdot \dot{\boldsymbol{E}} \, dV.} \tag{3.60}$$

Remark: Variational approach to power expression. In line with the balance of angular momentum from Chapter 3.2.2, the power expression (3.60) can also be obtained from the variational potential (3.16). We therefore assume a *homogeneity of time* [106], i.e. the potential should be invariant under translations in time. This assumption is reasonable, as experience shows us that the outcome of an experiment under a given setup is not dependent on the explicit point in time the experiment has been carried out. Consequently the variation of the potential in time must vanish

$$\begin{aligned} \delta_t \Pi = \Big[& \int_{\mathcal{B}} \frac{\partial \psi}{\partial \boldsymbol{F}} : \dot{\boldsymbol{F}} + \frac{\partial \psi}{\partial \boldsymbol{E}} : \dot{\boldsymbol{E}} + \frac{\partial \psi}{\partial t} \, dV \\ & - \int_{\mathcal{B}} \boldsymbol{\gamma} \cdot \dot{\boldsymbol{\varphi}} \, dV - \int_{\partial \mathcal{B}_t} \boldsymbol{t}^\# \cdot \dot{\boldsymbol{\varphi}} \, dA + \int_{\mathcal{B}} \lambda \dot{\phi} \, dV - \int_{\partial \mathcal{B}_q} q^\# \dot{\phi} \, dA \Big] \delta t = 0, \end{aligned} \tag{3.61}$$

where we assumed constant surface and volume loads. In line with the assumption of homogeneity of time, the partial derivative of the energy density function in the latter equation must vanish, as the energy density itself should not depend on time explicitly

$$\frac{\partial \psi}{\partial t} = 0, \tag{3.62}$$

which is a reasonable constraint for the construction of energy density functions. As stated above, the energy of a body should not depend on the specific point in time itself but only on the *state of variables* $\{\boldsymbol{F}, \boldsymbol{E}\}$. We are thus left with

$$\delta_t \Pi = \Big[\int_{\mathcal{B}} \frac{\partial \psi}{\partial \boldsymbol{F}} : \dot{\boldsymbol{F}} + \frac{\partial \psi}{\partial \boldsymbol{E}} : \dot{\boldsymbol{E}} \, dV$$
$$- \int_{\mathcal{B}} \boldsymbol{\gamma} \cdot \dot{\boldsymbol{\varphi}} \, dV - \int_{\partial \mathcal{B}_t} \boldsymbol{t}^{\#} \cdot \dot{\boldsymbol{\varphi}} \, dA + \int_{\mathcal{B}} \lambda \dot{\phi} \, dV - \int_{\partial \mathcal{B}_q} q^{\#} \dot{\phi} \, dA \Big] \delta t = 0. \tag{3.63}$$

Using the definition of the stress $\boldsymbol{T} = \partial \psi / \partial \boldsymbol{F}$ and the electric displacement $\boldsymbol{D} = -\partial \psi / \partial \boldsymbol{E}$, the internal power appears in accordance to (3.60)

$$\mathcal{P} = \int_{\mathcal{B}} \boldsymbol{T} : \dot{\boldsymbol{F}} \, dV - \int_{\mathcal{B}} \boldsymbol{D} \cdot \dot{\boldsymbol{E}} \, dV \tag{3.64}$$

and is equilibrated with the external power

$$\mathcal{P}^{ext} = - \int_{\mathcal{B}} \boldsymbol{\gamma} \cdot \dot{\boldsymbol{\varphi}} \, dV - \int_{\partial \mathcal{B}_t} \boldsymbol{t}^{\#} \cdot \dot{\boldsymbol{\varphi}} \, dA + \int_{\mathcal{B}} \lambda \dot{\phi} \, dV - \int_{\partial \mathcal{B}_q} q^{\#} \dot{\phi} \, dA. \tag{3.65}$$

Additionally, we can pull the partial differentiation and the time variation out of the integral and obtain

$$\frac{\partial}{\partial t} \Big[\int_{\mathcal{B}} \boldsymbol{T} : \boldsymbol{F} \, dV - \int_{\mathcal{B}} \boldsymbol{D} \cdot \boldsymbol{E} \, dV$$
$$- \int_{\mathcal{B}} \boldsymbol{\gamma} \cdot \boldsymbol{\varphi} \, dV - \int_{\partial \mathcal{B}_t} \boldsymbol{t}^{\#} \cdot \boldsymbol{\varphi} \, dA + \int_{\mathcal{B}} \lambda \phi \, dV - \int_{\partial \mathcal{B}_q} q^{\#} \phi \, dA \Big] \delta t = 0. \tag{3.66}$$

In the latter equation, we see that the time derivative of sum of the integrals must vanish and thus the sum of integrals must stay constant in time. We identify this as the *conservation of energy* and the integral as the energy

$$\mathcal{E} = \int_{\mathcal{B}} \boldsymbol{T} : \boldsymbol{F} \, dV - \int_{\mathcal{B}} \boldsymbol{D} \cdot \boldsymbol{E} \, dV$$
$$- \int_{\mathcal{B}} \boldsymbol{\gamma} \cdot \boldsymbol{\varphi} \, dV - \int_{\partial \mathcal{B}_t} \boldsymbol{t}^{\#} \cdot \boldsymbol{\varphi} \, dA + \int_{\mathcal{B}} \lambda \phi \, dV - \int_{\partial \mathcal{B}_q} q^{\#} \phi \, dA = \text{constant}, \tag{3.67}$$

which is in line with Noether's theorem [97, 141].

3.3.2. Dissipation postulate for electro-mechano-statics

In the previous section, the overall internal stress power $\mathcal{P}$ of a body being subject to mechanical and electrical loads was derived. In order to obtain the dissipative contribution of the power, we need to substract its elastic contribution. This elastic contribution can

be expressed in terms of *change* in non-dissipative energy storage through deformation and within the electric field

$$\mathcal{P}^e = \int_{\mathcal{B}} \frac{d}{dt} \psi(\boldsymbol{F}, \boldsymbol{E}) \, dV. \tag{3.68}$$

The second law of thermodynamics states that the dissipation rate, which is the overall internal power substracted by the elastic contribution, must always be positive

$$\mathcal{D}_{\mathcal{P}} = \mathcal{P} - \mathcal{P}^e = \int_{\mathcal{B}} \boldsymbol{T} : \dot{\boldsymbol{F}} - \boldsymbol{D} \cdot \dot{\boldsymbol{E}} - \frac{d}{dt} \psi \, dV \geq 0, \tag{3.69}$$

which corresponds to the statement that entropy can only stay the same or grow in a closed system[1]. Applying the chain rule in the latter equation and considering a purely elastic case with $\mathcal{D}_{\mathcal{P}} = 0$, we obtain

$$\boxed{\int_{\mathcal{B}} (\boldsymbol{T} - \frac{\partial \psi}{\partial \boldsymbol{F}}) : \dot{\boldsymbol{F}} - (\boldsymbol{D} + \frac{\partial \psi}{\partial \boldsymbol{E}}) \cdot \dot{\boldsymbol{E}} \, dV = 0} \tag{3.70}$$

We now see that the latter equation indeed is always fulfilled for the relation

$$\boldsymbol{T} = \frac{\partial \psi}{\partial \boldsymbol{F}} \quad \text{and} \quad \boldsymbol{D} = -\frac{\partial \psi}{\partial \boldsymbol{E}}, \tag{3.71}$$

which proves the thermodynamical consistency of the relations used in Section 3.2.

3.3.3. Concept of dissipation potentials and internal variables

A large set of material models exhibits dissipative material behavior due to internal friction. Such effects include for example viscoelasticity. To consistently model such behavior, we now consider rate-dependent problems and further introduce the concept of *internal variables*. Internal variables $\boldsymbol{q}$ might be viscous or plastic strains. In an experiment, they cannot be prescribed directly via boundary conditions, but rather *evolve* due to boundary conditions applied for the primary variables such as displacement and scalar electric potential. In such a scenario, where the energy density function $\psi(\boldsymbol{F}, \boldsymbol{E}, \boldsymbol{q})$ is dependent on internal variables, the dissipation postulate (3.69) can be brought in the form

$$\mathcal{D}_{\mathcal{P}} = \int_{\mathcal{B}} (\boldsymbol{T} - \frac{\partial \psi}{\partial \boldsymbol{F}}) : \dot{\boldsymbol{F}} + (-\boldsymbol{D} - \frac{\partial \psi}{\partial \boldsymbol{E}}) \cdot \dot{\boldsymbol{E}} - \partial_{\boldsymbol{q}} \psi \cdot \dot{\boldsymbol{q}} \, dV \geq 0. \tag{3.72}$$

We now decompose the stress and electric displacement into an elastic and a dissipative contribution

$$\boldsymbol{T} = \boldsymbol{T}^e + \boldsymbol{T}^d \quad \text{and} \quad \boldsymbol{D} = \boldsymbol{D}^e + \boldsymbol{D}^d, \tag{3.73}$$

and introduce the definition

$$\begin{aligned} \boldsymbol{T}^e &= \partial_{\boldsymbol{F}} \psi(\boldsymbol{F}, \boldsymbol{E}, \boldsymbol{q}) \\ \boldsymbol{D}^e &= -\partial_{\boldsymbol{E}} \psi(\boldsymbol{F}, \boldsymbol{E}, \boldsymbol{q}) \\ \mathfrak{h} &= -\partial_{\boldsymbol{q}} \psi(\boldsymbol{F}, \boldsymbol{E}, \boldsymbol{q}). \end{aligned} \tag{3.74}$$

---

[1]This is an extremely condensed description of the second law of thermodynamics and entropy in continua. At this point, we make do with the statement that the second law is motivated by the observation that there cannot be a Perpetuum mobile of the second kind, i.e., a periodic machine that extracts heat from a reservoir and transforms it into work without leaving other changes in the environment. For further considerations, the interested reader is referred to GURTIN ET AL. [67]

Insertion of the latter equation into the dissipation postulate (3.72) gives the reduced form

$$\mathcal{D}_{\mathcal{P}} = \boldsymbol{T}^d : \dot{\boldsymbol{F}} - \boldsymbol{D}^d \cdot \dot{\boldsymbol{E}} + \mathfrak{h} \cdot \dot{\boldsymbol{q}}, \tag{3.75}$$

which can also be written in the general form

$$\mathcal{D}_{\mathcal{P}} = \begin{bmatrix} \boldsymbol{T}^d \\ -\boldsymbol{D}^d \\ \mathfrak{h} \end{bmatrix} \diamond \begin{bmatrix} \dot{\boldsymbol{F}} \\ \dot{\boldsymbol{E}} \\ \dot{\boldsymbol{q}} \end{bmatrix} = \mathfrak{F} \diamond \dot{\mathfrak{Q}} \geq 0. \tag{3.76}$$

Here, we introduce the generalized fluxes $\dot{\mathfrak{Q}}$ and the generalized driving force $\mathfrak{F}$. Additionally, the diamond operator $\diamond$ represents a generic contraction operator that contracts the tensors corresponding to their order, i.e. single or double contraction in the context of the upper equation. To obtain an evolution for the fluxes, we need to constitutively model the driving force under the restrictions of thermodynamical consistency as prescribed by the latter equation. We, therefore, introduce a dissipation potential $\mathfrak{d}$ from which the driving force can be obtained through differentiation

$$\mathfrak{F} = \partial_{\dot{\mathfrak{Q}}} \mathfrak{d}(\mathfrak{Q}, \dot{\mathfrak{Q}}). \tag{3.77}$$

Insertion of the latter equation into the dissipation postulate (3.76) yields the form

$$\mathcal{D}_{\mathcal{P}} = \partial_{\dot{\mathfrak{Q}}} \mathfrak{d}(\mathfrak{Q}, \dot{\mathfrak{Q}}) \diamond \dot{\mathfrak{Q}} \geq 0. \tag{3.78}$$

Usually, one chooses the dissipation potential to be convex in $\dot{\mathfrak{Q}}$ [130], in order to always fulfill the dissipation inequality independent of the deformation or electrical state. However, strictly speaking, it is not a necessary constraint: As long as the latter equation is fulfilled, the second law of thermodynamics is fulfilled, no matter the form of the dissipation potential. However, it is convenient to model it so that it always fulfills (3.78) to rule out any unphysical processes without further checking during computations.

Comparison of the dissipation postulate (3.76) with the definition of the driving force (3.77) allows us to identify the dissipative stress and electric displacement

$$\boldsymbol{T}^d = \partial_{\dot{\boldsymbol{F}}} \mathfrak{d}(\mathfrak{Q}, \dot{\mathfrak{Q}}) \quad \text{and} \quad \boldsymbol{D}^d = -\partial_{\dot{\boldsymbol{E}}} \mathfrak{d}(\mathfrak{Q}, \dot{\mathfrak{Q}}). \tag{3.79}$$

Further using the definition of the elastic stress and electric displacement (3.74) gives the absolute stress and electric displacement (3.73)

$$\boxed{\boldsymbol{T} = \partial_{\boldsymbol{F}} \psi(\mathfrak{Q}) + \partial_{\dot{\boldsymbol{F}}} \mathfrak{d}(\mathfrak{Q}, \dot{\mathfrak{Q}}) \quad \text{and} \quad \boldsymbol{D} = -\partial_{\boldsymbol{E}} \psi(\mathfrak{Q}) - \partial_{\dot{\boldsymbol{E}}} \mathfrak{d}(\mathfrak{Q}, \dot{\mathfrak{Q}})} \tag{3.80}$$

as computed from the constitutive energy density and dissipation potential. The evolution equation for the internal variables can be obtained from the comparison of the definition of the driving force (3.77) with the definition (3.74) as follows

$$\boxed{-\partial_{\boldsymbol{q}} \psi(\mathfrak{Q}) = \partial_{\dot{\boldsymbol{q}}} \mathfrak{d}(\mathfrak{Q}, \dot{\mathfrak{Q}}),} \tag{3.81}$$

which is called *Biot's equation* [10].

3.3.4. Time-discrete incremental variational potentials for rate-dependent problems

In order to describe rate-dependent problems that are time-dependent, we introduce the concept of a *rate-type variational potential*. At a given state, say $\{\boldsymbol{\varphi}, \phi\}$ as an example for the electromechanical case, it is given in terms of the *rates* of the primary variables

$$\Pi(\dot{\boldsymbol{\varphi}}, \dot{\phi}) = \int_{\mathcal{B}} \frac{d}{dt}\psi(\boldsymbol{\mathfrak{Q}}) + \mathfrak{d}(\boldsymbol{\mathfrak{Q}}, \dot{\boldsymbol{\mathfrak{Q}}}) \, dV - \Pi_{ext}(\dot{\boldsymbol{\varphi}}, \dot{\phi}), \tag{3.82}$$

where the dissipation potential, as introduced in the last section, is used to constitutively model the rate-dependent material behavior at hand. In analogy to the static potential introduced in Equations (3.14) and (3.15), we now have an external rate potential due to the boundary conditions and volume forces

$$\Pi_{ext}(\dot{\boldsymbol{\varphi}}, \dot{\phi}) = \int_{\mathcal{B}} (\boldsymbol{g}\boldsymbol{\gamma}) \cdot \dot{\boldsymbol{\varphi}} \, dV + \int_{\partial \mathcal{B}_t} (\boldsymbol{g}\boldsymbol{t}^{\#}) \cdot \dot{\boldsymbol{\varphi}} \, dA - \int_{\mathcal{B}} \lambda \dot{\phi} \, dV + \int_{\partial \mathcal{B}_q} q^{\#} \dot{\phi} \, dA. \tag{3.83}$$

In order to numerically solve the rate-type potential, we now consider a discrete finite time interval

$$\Delta t = t - t_n > 0 \tag{3.84}$$

in between a *previous time t_n* and the *current time t*. We then obtain the *time-discrete incremental potential* by means of a discrete time-integration algorithm

$$\Pi^{\Delta t} = \mathrm{ALGO}\left\{ \int_{t_n}^{t} \Pi \, dt \right\}. \tag{3.85}$$

This time-integration can be performed, for example, with a right Riemann sum, where the functional is evaluated at the current and last time step and multiplied with the time-increment Δt as follows

$$\Pi^{\Delta t} = \int_{\mathcal{B}} \left[\frac{\psi(\boldsymbol{\mathfrak{Q}}) - \psi(\boldsymbol{\mathfrak{Q}}_n)}{\Delta t} + \mathfrak{d}(\boldsymbol{\mathfrak{Q}}, \frac{\boldsymbol{\mathfrak{Q}} - \boldsymbol{\mathfrak{Q}}_n}{\Delta t}) \right] dV \Delta t + \Pi_{ext}^{\Delta t}, \tag{3.86}$$

where we used a finite difference approximation, i.e. a backward Euler scheme, for the time derivatives appearing in the potential. Consequently, the external contribution using the Riemann sum and the backward Euler scheme takes the explicit form

$$\begin{aligned}\Pi_{ext}^{\Delta t} = \Big[&\int_{\mathcal{B}} (\boldsymbol{g}\boldsymbol{\gamma}) \cdot \frac{\boldsymbol{\varphi} - \boldsymbol{\varphi}_n}{\Delta t} \, dV + \int_{\partial \mathcal{B}_t} (\boldsymbol{g}\boldsymbol{t}^{\#}) \cdot \frac{\boldsymbol{\varphi} - \boldsymbol{\varphi}_n}{\Delta t} \, dA \\ &- \int_{\mathcal{B}} \lambda \frac{\phi - \phi_n}{\Delta t} \, dV + \int_{\partial \mathcal{B}_q} q^{\#} \frac{\phi - \phi_n}{\Delta t} \, dA \Big] \Delta t.\end{aligned} \tag{3.87}$$

In line with the variational approach for the rate-independent case (3.17), physical equilibrium is achieved for the primary variable fields $\{\boldsymbol{\varphi}, \phi\}$ that optimize the incremental potential

$$\boxed{\{\boldsymbol{\varphi}, \phi\} = \arg\left\{ \inf_{\boldsymbol{\varphi}} \sup_{\phi} \Pi^{\Delta t}(\boldsymbol{\varphi}, \phi) \right\}.} \tag{3.88}$$

The solution to such a problem can again be found using a variation

$$\delta \Pi^{\Delta t} = 0, \tag{3.89}$$

which needs to vanish for all admissible $\{\delta\boldsymbol{\varphi}, \delta\phi\}$.

<div align="right">

Chapter 4

</div>

The Concept of micro-to-macro transition
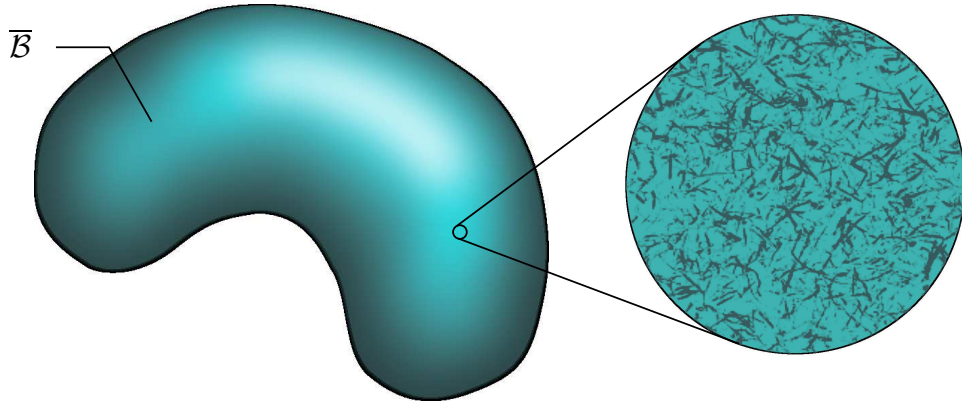
Figure 4.1: A macroscopically homogeneous appearing body $\overline{\mathcal{B}}$ reveals a heterogeneous microstructure at a much lower length scale. Voids, cracks, or grains may influence the macroscopically observed properties, such as stiffness or viscosity.

Many materials for industrial applications have a distinct microstructure: when zooming into small length scales, one can observe voids, cracks, or grains, as shown in Figure 4.1. Properties of the macroscopic component may be largely influenced by effects appearing on the microstructure and lead to a large deviation of the properties of the pure homogeneous material's theoretical values. However, as the length scales of the macroscopic component and the microscale can differ by several magnitudes, a computer-based computation of the component at the full resolution of the microstructure is uneconomical. Instead, we will theoretically separate the length scales and condense the microstructure to a point problem on the macroscale. However, this reduction leads to a loss of the boundary information on the microscale, as a point possesses no information on boundary values. In order to close this gap, we have to formulate physically reasonable assumptions. One is the equivalence of macroscopic and averaged microscopic energy density

$$\overline{\psi}(\overline{\boldsymbol{F}}, \overline{\boldsymbol{E}}) = \frac{1}{|\mathcal{B}|} \inf_{\boldsymbol{u} \in \mathcal{W}_{\boldsymbol{u}}(\overline{\boldsymbol{F}})} \sup_{\phi \in \mathcal{W}_{\phi}(\overline{\boldsymbol{E}})} \int_{\mathcal{B}} \psi(\boldsymbol{F}, \boldsymbol{E}) \, dV. \tag{4.1}$$

It states that the macroscopic energy density $\overline{\psi}$ in terms of the macroscopic deformation gradient $\overline{F}$ and the electric field $\overline{E}$ is the average of the *equilibrated microscopic energy density* ψ in terms of the microscopic deformation gradient F and electric field E under some *given* macroscopic deformation gradient $\overline{F}$ and electric field $\overline{E}$. The optimization for the microscopic displacement u and electric potential ϕ is carried out in the admissible space of given constant macroscopic deformation gradient and electric field $\mathcal{W}_u(\overline{F})$ and $\mathcal{W}_\phi(\overline{E})$.

The second assumption is the assumption of *scale separation*. We, therefore, consider problems in which the fields on the microscopic scale can be decomposed into two contributions, namely the *microscopically constant* macroscopic fields $\{\overline{F}, \overline{E}\}$ and the *microscopically fluctuating* microscopic fields $\{\widetilde{F}, \widetilde{E}\}$. In order to meet such scale separation assumption, the fields on the microscale need to have wave-lengths much smaller than the macroscopic fields. As a consequence, the RVE needs to be chosen large enough to reflect those modes. In general, it might not be possible to find a suitable RVE. We will, however, always assume the existence of such an RVE in this work. The latter assumption resorts to a *first-order homogenization*. These two postulates, namely the Hill-Mandel averaging rule (4.1) and the scale-separation assumption allow us to derive *variationally consistent microscopic boundary conditions* which themselves induce relations between the macroscopic primary fields $\{\overline{F}, \overline{E}\}$ and the microscopic fields $\{F, E\}$.

4.1. Microscopic equilibrium equations

To derive the restrictions of the microscopic boundary value problem, we will first present the equations that need to be fulfilled in microscopic equilibrium. We, therefore, start with the microscopic global energy potential, which we recall from Equation (3.14) to be

$$\Pi(\varphi, \phi) = \int_{\mathcal{B}} \psi(F, E)\, dV - \Pi_{ext}, \tag{4.2}$$

with the external coupled potential contribution (3.15)

$$\Pi_{ext} = \int_{\mathcal{B}} (g\gamma) \cdot \varphi\, dV + \int_{\partial \mathcal{B}_t} (g t^{\#}) \cdot \varphi\, dA - \int_{\mathcal{B}} \lambda \phi\, dV + \int_{\partial \mathcal{B}_q} q^{\#} \phi\, dA. \tag{4.3}$$

We further recall the gradient relations for the electric field (2.10) and the deformation gradient (2.126)

$$F = \nabla_X \varphi \quad \text{and} \quad E = -\nabla_X \phi. \tag{4.4}$$

In line with the assumption of scale separation, we assume the macroscopic driving contribution to be constant and perform an additive split of the primary fields into some constant contribution $\{\overline{\mathfrak{C}}_{\overline{F}}, \overline{\mathfrak{C}}_{\overline{E}}\}$ and a non-constant fluctuating part $\{\widetilde{F}, \widetilde{E}\}$

$$F = \overline{\mathfrak{C}}_{\overline{F}} + \widetilde{F}(X) \quad \text{and} \quad E = \overline{\mathfrak{C}}_{\overline{E}} + \widetilde{E}(X). \tag{4.5}$$

Using the gradient relation (4.4), the deformation map and scalar potential then appear as

$$\varphi = \overline{\mathfrak{C}}_{\overline{F}} X + \widetilde{\varphi}(X) \quad \text{and} \quad \phi = -\overline{\mathfrak{C}}(\overline{E}) \cdot X + \widetilde{\phi}(X). \tag{4.6}$$

Later, we will connect the constants $\{\overline{\mathfrak{C}}_{\overline{F}}, \overline{\mathfrak{C}}_{\overline{E}}\}$ to the physical macroscopic fields $\{\overline{F}, \overline{E}\}$, but as for now, we treat them as any arbitrary constants that drive the microscopic

fields $\{\boldsymbol{F}, \boldsymbol{E}\}$. Having the equation of the primary variables (4.6), the variation of the potential (4.2) can be recalled from Equation (3.21) to be

$$
\begin{aligned}
\delta\Pi = &\int_{\mathcal{B}}(-\boldsymbol{\gamma} - \text{Div}(\frac{\partial\psi}{\partial\boldsymbol{F}})) \cdot \delta\boldsymbol{\varphi}\, dV + \int_{\mathcal{B}}(\lambda - \text{Div}(-\frac{\partial\psi}{\partial\boldsymbol{E}}))\delta\phi\, dV \\
&+ \int_{\partial\mathcal{B}_t}(\frac{\partial\psi}{\partial\boldsymbol{F}}\boldsymbol{N} - \boldsymbol{t}^{\#}) \cdot \delta\boldsymbol{\varphi}\, dA + \int_{\partial\mathcal{B}_q}(-\frac{\partial\psi}{\partial\boldsymbol{E}} \cdot \boldsymbol{N} - q^{\#})\delta\phi\, dA = 0,
\end{aligned}
\tag{4.7}
$$

where we can extract the following individual *volume and surface integral relations* that need to hold for all variations of the primary fields

$$
\int_{\mathcal{B}} \text{div}[\partial_{\boldsymbol{F}}\psi] \cdot \delta\widetilde{\boldsymbol{\varphi}}\, dV = -\int_{\mathcal{B}} \boldsymbol{\gamma} \cdot \delta\widetilde{\boldsymbol{\varphi}}\, dV
\tag{4.8a}
$$

$$
\int_{\partial\mathcal{B}_t} (\partial_{\boldsymbol{F}}\psi\,\boldsymbol{N}) \cdot \delta\widetilde{\boldsymbol{\varphi}}\, dA = \int_{\partial\mathcal{B}_t} \boldsymbol{t}^{\#} \cdot \delta\widetilde{\boldsymbol{\varphi}}\, dA
\tag{4.8b}
$$

$$
\int_{\mathcal{B}} \text{div}[\partial_{\boldsymbol{E}}\psi]\delta\widetilde{\phi}\, dV = \int_{\mathcal{B}} \lambda\delta\widetilde{\phi}\, dV
\tag{4.8c}
$$

$$
\int_{\partial\mathcal{B}_q} \partial_{\boldsymbol{E}}\psi \cdot \boldsymbol{N}\delta\widetilde{\phi}\, dA = \int_{\partial\mathcal{B}_q} q^{\#}\delta\widetilde{\phi}\, dA,
\tag{4.8d}
$$

where we used the decomposition (4.6) to write $\{\delta\boldsymbol{\varphi}, \delta\phi\} = \{\delta\widetilde{\boldsymbol{\varphi}}, \delta\widetilde{\phi}\}$. From the latter equation we see, that we need to fulfill integral equations to reach equilibrium or vice versa, *the integral relations (4.8) are fulfilled when we have reached equilibrium*. This will be an important insight for the following derivations of consistent boundary conditions. We will therefore denote electric fields and deformation gradients that fulfill the equations (4.8), i.e. the ones obtained in microscopic equilibrium, with a hash $\{\boldsymbol{F}^{\#}, \boldsymbol{E}^{\#}\}$.

4.2. The Hill-Mandel macrohomogeneity conditions

Now that we know the equations that need to be fulfilled in equilibrium (4.8), we take a closer look at the energy density assumption (4.1) between the micro- and the macroscale. We now assume that the macroscopic boundary value problem can also be governed by a variational form in analogy to the microscopic potential (4.2) as follows

$$
\overline{\Pi}(\overline{\boldsymbol{\varphi}}, \overline{\phi}) = \int_{\overline{\mathcal{B}}} \overline{\psi}(\overline{\boldsymbol{F}}, \overline{\boldsymbol{E}})\, dV - \overline{\Pi}_{ext},
\tag{4.9}
$$

where the external load contribution appears in analogy

$$
\overline{\Pi}_{ext} = \int_{\overline{\mathcal{B}}} (\overline{\boldsymbol{g}}\,\overline{\boldsymbol{\gamma}}) \cdot \overline{\boldsymbol{\varphi}}\, dV + \int_{\partial\overline{\mathcal{B}}_{\overline{t}}} (\overline{\boldsymbol{g}}\overline{\boldsymbol{t}}^{\#}) \cdot \overline{\boldsymbol{\varphi}}\, dA - \int_{\overline{\mathcal{B}}} \overline{\lambda}\,\overline{\phi}\, dV + \int_{\partial\overline{\mathcal{B}}_{\overline{q}}} \overline{q}^{\#}\overline{\phi}\, dA.
\tag{4.10}
$$

To find *macroscopic equilibrium*, we perform the variation of the macroscopic potential (4.9)

$$
\delta\overline{\Pi}(\overline{\boldsymbol{\varphi}}, \overline{\phi}) = \int_{\overline{\mathcal{B}}} \delta\overline{\psi}(\overline{\boldsymbol{F}}, \overline{\boldsymbol{E}})\, dV - \delta\overline{\Pi}_{ext},
\tag{4.11}
$$

where the variation of the macroscopic energy density $\delta\overline{\psi}$ is now connected to a microscopic boundary value problem through the Hill-Mandel-condition (4.1). Using said

postulate, we perform the variation on both sides of the equation and use the splits (4.5)

$$
\begin{aligned}
\delta\overline{\psi} = \partial_{\overline{\boldsymbol{F}}}\overline{\psi} : \delta\overline{\boldsymbol{F}} + \partial_{\overline{\boldsymbol{E}}}\overline{\psi} \cdot \delta\overline{\boldsymbol{E}} = {} & \frac{1}{|\mathcal{B}|} \int_{\mathcal{B}} \partial_{\boldsymbol{F}}\psi(\boldsymbol{F}^{\#}, \boldsymbol{E}^{\#}) : (\partial_{\overline{\boldsymbol{F}}}\overline{\mathfrak{C}}_{\overline{\boldsymbol{F}}} : \delta\overline{\boldsymbol{F}})\, dV \\
& + \frac{1}{|\mathcal{B}|} \int_{\mathcal{B}} \partial_{\boldsymbol{F}}\psi(\boldsymbol{F}^{\#}, \boldsymbol{E}^{\#}) : \delta\widetilde{\boldsymbol{F}}\, dV \\
& + \frac{1}{|\mathcal{B}|} \int_{\mathcal{B}} \partial_{\boldsymbol{E}}\psi(\boldsymbol{F}^{\#}, \boldsymbol{E}^{\#}) \cdot (\partial_{\overline{\boldsymbol{E}}}\overline{\mathfrak{C}}_{\overline{\boldsymbol{E}}}\, \delta\overline{\boldsymbol{E}})\, dV \\
& + \frac{1}{|\mathcal{B}|} \int_{\mathcal{B}} \partial_{\boldsymbol{E}}\psi(\boldsymbol{F}^{\#}, \boldsymbol{E}^{\#}) \cdot \delta\widetilde{\boldsymbol{E}}\, dV.
\end{aligned}
\tag{4.12}
$$

In line with the Hill-Mandel equation (4.1) and as mentioned previously, we use the hash $\{\boldsymbol{F}^{\#}, \boldsymbol{E}^{\#}\}$ to denote that the primary fields are obtained from a microscopic equilibrium. When varying the macroscopic fields $\{\overline{\boldsymbol{F}}, \overline{\boldsymbol{E}}\}$, we need to vary both macroscopic fields and microscopic fluctuations $\{\widetilde{\boldsymbol{F}}, \widetilde{\boldsymbol{E}}\}$ on the microscale, as a difference in the macroscopic fields can induce differences in the fluctuations. Additionally, the microscopically constant quantities $\{\overline{\mathfrak{C}}_{\overline{\boldsymbol{F}}}, \overline{\mathfrak{C}}_{\overline{\boldsymbol{E}}}\}$ might be dependent on the macroscopic primary fields as we will see later. Using the same variational procedure that led to the microvariation (4.7) and the fact that $\{\overline{\mathfrak{C}}_{\overline{\boldsymbol{F}}}, \overline{\mathfrak{C}}_{\overline{\boldsymbol{E}}}\}$ as well as $\{\overline{\boldsymbol{F}}, \overline{\boldsymbol{E}}\}$ are not dependent on $\boldsymbol{X}$, we can reformulate the latter equation into

$$
\begin{aligned}
\partial_{\overline{\boldsymbol{F}}}\overline{\psi} : \delta\overline{\boldsymbol{F}} + \partial_{\overline{\boldsymbol{E}}}\overline{\psi} \cdot \delta\overline{\boldsymbol{E}} = {} & \frac{1}{|\mathcal{B}|} \int_{\mathcal{B}} \partial_{\boldsymbol{F}}\psi(\boldsymbol{F}^{\#}, \boldsymbol{E}^{\#})\, dV : \partial_{\overline{\boldsymbol{F}}}\overline{\mathfrak{C}}_{\overline{\boldsymbol{F}}} : \delta\overline{\boldsymbol{F}} \\
& + \frac{1}{|\mathcal{B}|} \underbrace{\int_{\mathcal{B}} \mathrm{div}[\partial_{\boldsymbol{F}}\psi(\boldsymbol{F}^{\#}, \boldsymbol{E}^{\#})] \cdot \delta\widetilde{\boldsymbol{\varphi}}\, dV}_{(A)} + \frac{1}{|\mathcal{B}|} \underbrace{\int_{\partial\mathcal{B}_{t}} (\partial_{\boldsymbol{F}}\psi(\boldsymbol{F}^{\#}, \boldsymbol{E}^{\#})\boldsymbol{N}) \cdot \delta\widetilde{\boldsymbol{\varphi}}\, dA}_{(B)} \\
& + \frac{1}{|\mathcal{B}|} \int_{\mathcal{B}} \partial_{\boldsymbol{E}}\psi(\boldsymbol{F}^{\#}, \boldsymbol{E}^{\#})\, dV \cdot \partial_{\overline{\boldsymbol{E}}}\overline{\mathfrak{C}}_{\overline{\boldsymbol{E}}}\, \delta\overline{\boldsymbol{E}} \\
& + \frac{1}{|\mathcal{B}|} \underbrace{\int_{\mathcal{B}} \mathrm{div}[\partial_{\boldsymbol{E}}\psi(\boldsymbol{F}^{\#}, \boldsymbol{E}^{\#})]\delta\widetilde{\phi}\, dV}_{(C)} + \frac{1}{|\mathcal{B}|} \underbrace{\int_{\partial\mathcal{B}_{\sigma}} \partial_{\boldsymbol{E}}\psi(\boldsymbol{F}^{\#}, \boldsymbol{E}^{\#}) \cdot \boldsymbol{N}\, \delta\widetilde{\phi}\, dA}_{(D)},
\end{aligned}
\tag{4.13}
$$

which are the *Hill-Mandel macrohomogeneity conditions*. Comparing coefficients on the left and on the right side, we see that the volume average rules

$$
\partial_{\overline{\boldsymbol{F}}}\overline{\psi} = \frac{1}{|\mathcal{B}|} \int_{\mathcal{B}} \partial_{\boldsymbol{F}}\psi(\boldsymbol{F}^{\#}, \boldsymbol{E}^{\#})\, dV : \partial_{\overline{\boldsymbol{F}}}\overline{\mathfrak{C}}_{\overline{\boldsymbol{F}}} \quad \text{and} \quad \partial_{\overline{\boldsymbol{E}}}\overline{\psi} = \frac{1}{|\mathcal{B}|} \int_{\mathcal{B}} \partial_{\boldsymbol{E}}\psi(\boldsymbol{F}^{\#}, \boldsymbol{E}^{\#})\, dV \cdot \partial_{\overline{\boldsymbol{E}}}\overline{\mathfrak{C}}_{\overline{\boldsymbol{E}}}
\tag{4.14}
$$

only hold for vanishing terms (A), (B), (C) and (D) in Equation (4.13). Comparing term (A) with (4.8a), term (B) with (4.8b), term (C) with (4.8c) and term (D) with (4.8d), i.e.
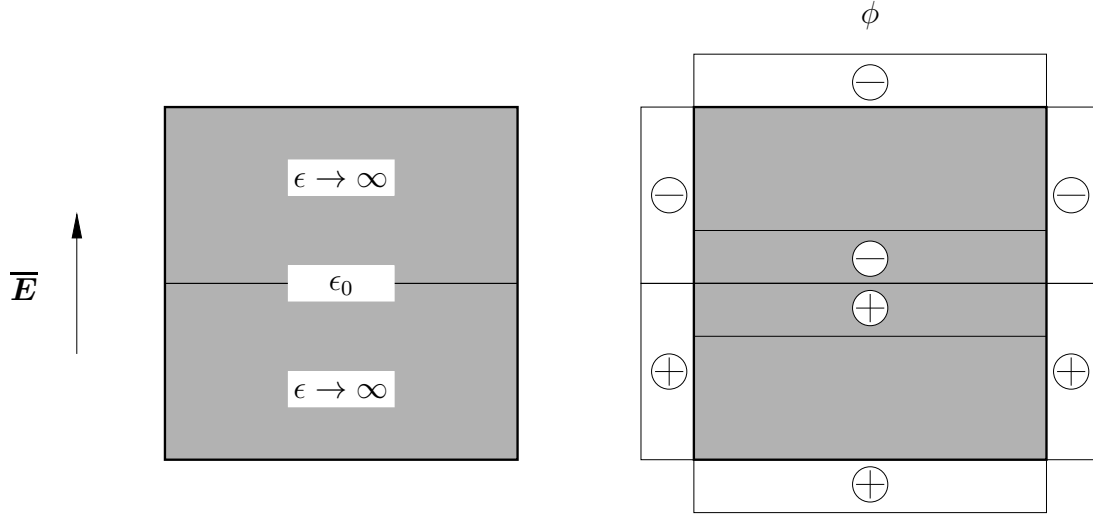
Figure 4.2: A metal RVE with a line defect. The permittivity ϵ in the metal tends to infinity, while the permittivity in the line defect is some finite value (of air, for example). This leads to a localization of the whole electric field inside the defect, as shown on the left side.

the integral equilibrium conditions, it follows that this is a priori always fulfilled for

$$-\int_{\mathcal{B}} \boldsymbol{\gamma} \cdot \delta \widetilde{\boldsymbol{\varphi}} \, dV = 0 \tag{4.15a}$$

$$\int_{\partial \mathcal{B}_t} \boldsymbol{t}^{\#} \cdot \delta \widetilde{\boldsymbol{\varphi}} \, dA = 0 \tag{4.15b}$$

$$\int_{\mathcal{B}} \lambda \delta \widetilde{\phi} \, dV = 0 \tag{4.15c}$$

$$\int_{\partial \mathcal{B}_q} q^{\#} \delta \widetilde{\phi} \, dA = 0. \tag{4.15d}$$

For fulfilling the Equations (4.15a) and (4.15c), we usually simply assume that there is no volume body force and charge on the microscale $\boldsymbol{\gamma} = \boldsymbol{0}$ and $\lambda = 0$. Regarding the surface integrals, there are several techniques for making sure that they vanish. One is to consider representative volume elements that have no prescribed surface tractions or charge boundaries, i.e., prescribing $\{\widetilde{\boldsymbol{\varphi}}, \widetilde{\phi}\}$ on the boundary which makes the variations vanish on the boundary $\{\delta \widetilde{\boldsymbol{\varphi}}, \delta \widetilde{\phi}\} = \{\boldsymbol{0}, 0\}$. The Hill-Mandel conditions give *restrictions* on the boundary conditions, but they do not grant a *unique solution* for effective properties. There are many ways of prescribing boundary conditions that satisfy the Hill-Mandel condition, and they lead to different values for the macroscopic quantities $\{\partial_{\overline{\boldsymbol{F}}} \overline{\psi}, \partial_{\overline{\boldsymbol{E}}} \overline{\psi}\}$ on the macroscale. We want to now take a closer look at the definition of the macroscopic fields $\{\overline{\boldsymbol{F}}, \overline{\boldsymbol{E}}\}$, and two associated ways of imposing it on the microscale.

4.3. Macroscopic averaging and boundary conditions

Now that we know the restrictions on the boundary conditions, we know how we are allowed to prescribe the primary variables $\{\boldsymbol{\varphi}, \phi\}$ on the boundary in terms of an *energy consideration*. However, we still have not answered yet how some given macroscopic deformation gradient and electric field is imposed and measured on the microscale. One

could think of defining the macroscopic deformation gradient and electric field $\{\overline{\boldsymbol{F}}, \overline{\boldsymbol{E}}\}$ as the volume average of the microscopic deformation gradient and electric field. However, this is not always the best choice as shown for the example shown in Figure 4.2: A macroscopic electric field is imposed on an RVE of high permittivity $\epsilon \to \infty$. The RVE has a *line defect*, a crack, for example, in which the permittivity is some finite number ϵ_0. This line defect leads to a scalar potential, as shown on the left of Figure 4.2. The electric field fully localizes in the line defect while the electric field right above and below the defect is zero. Measuring the macroscopic electric field's volume average would now give zero, which is not in line with the imposed macroscopic electric field. This is due to the line having no physical extent in the vertical direction. Analogous mechanical considerations for the displacement field for a cracked body lead to analogous consequences for the macroscopic deformation gradient definition. A more accurate definition which captures the described effects can be found by integrating the primary variables over the surface

$$\overline{\boldsymbol{F}} = \frac{1}{|\mathcal{B}|} \int_{\partial \mathcal{B}} \boldsymbol{\varphi} \otimes \boldsymbol{N} \, dA \quad \text{and} \quad \overline{\boldsymbol{E}} = -\frac{1}{|\mathcal{B}|} \int_{\partial \mathcal{B}} \phi \boldsymbol{N} \, dA. \tag{4.16}$$

We will now have a look at two different types of boundary value problems, namely zero fluctuation Dirichlet and periodic Dirichlet boundary conditions, and show that they fulfill the Hill-Mandel restriction (4.15). For an elegant proof including zero traction boundaries, the reader is referred to MAUGIN [119]. We then further investigate the implication of the definition of the macroscopic fields (4.16) on the general constants $\{\overline{\mathfrak{C}}_{\overline{F}}, \overline{\mathfrak{C}}_{\overline{E}}\}$ introduced in the additive split of the microscopic fields (4.5).

4.3.1. Zero fluctuation Dirichlet boundary conditions

In this case, we prescribe zero body force $\boldsymbol{\gamma} = \boldsymbol{0}$ and volume charge $\lambda = 0$ inside the RVE in order to fulfill (4.15a) and (4.15c) and zero fluctuations $\{\widetilde{\boldsymbol{\varphi}} = \boldsymbol{0}, \widetilde{\phi} = 0\}$ on the whole boundary $\partial \mathcal{B}$ of the RVE in order to automatically fulfill (4.15b) and (4.15d). According to the definition of the deformation map and scalar electric field (4.6), we have the simple form on the boundary

$$\boldsymbol{\varphi} = \overline{\mathfrak{C}}_{\overline{F}} \boldsymbol{X} \quad \text{and} \quad \phi = -\overline{\mathfrak{C}}_{\overline{E}} \cdot \boldsymbol{X} \qquad \text{on} \qquad \partial \mathcal{B}. \tag{4.17}$$

Insertion of the latter relation into the definition of the macroscopic fields (4.16) then yields the form

$$\overline{\boldsymbol{F}} = \overline{\mathfrak{C}}_{\overline{F}} \frac{1}{|\mathcal{B}|} \int_{\partial \mathcal{B}} \boldsymbol{X} \otimes \boldsymbol{N} \, dA \quad \text{and} \quad \overline{\boldsymbol{E}} = \overline{\mathfrak{C}}_{\overline{E}} \frac{1}{|\mathcal{B}|} \int_{\partial \mathcal{B}} \boldsymbol{X} \otimes \boldsymbol{N} \, dA, \tag{4.18}$$

where we pulled the constants out of the integral. Assuming there are *no jumps* in the location vector $\boldsymbol{X}$, we can use the divergence theorem to transform the surface integral into a volume integral

$$\overline{\boldsymbol{F}} = \overline{\mathfrak{C}}_{\overline{F}} \frac{1}{|\mathcal{B}|} \int_{\mathcal{B}} \nabla_{\boldsymbol{X}} \boldsymbol{X} \, dV = \overline{\mathfrak{C}}_{\overline{F}} \frac{1}{|\mathcal{B}|} \int_{\mathcal{B}} \boldsymbol{1} \, dV = \overline{\mathfrak{C}}_{\overline{F}} \quad \text{and} \quad \overline{\boldsymbol{E}} = \overline{\mathfrak{C}}_{\overline{E}} \frac{1}{|\mathcal{B}|} \int_{\mathcal{B}} \nabla_{\boldsymbol{X}} \boldsymbol{X} \, dV = \overline{\mathfrak{C}}_{\overline{E}},$$
$$\tag{4.19}$$

where we see that for these particular boundary conditions, the constants themselves are the macroscopic imposed fields. One further interpretation can be found when we assume that there are *no jumps* of the deformation map and the scalar electric field $\{\boldsymbol{\varphi}, \phi\}$ in

$\mathcal{B}$. We then can reformulate the definition of the macroscopic fields (4.16) using the divergence theorem in terms of a volume integral

$$\overline{\boldsymbol{F}} = \frac{1}{|\mathcal{B}|} \int_{\mathcal{B}} \nabla_{\boldsymbol{X}} \boldsymbol{\varphi} \, dV = \frac{1}{|\mathcal{B}|} \int_{\mathcal{B}} \boldsymbol{F} \, dV \quad \text{and} \quad \overline{\boldsymbol{E}} = \frac{1}{|\mathcal{B}|} \int_{\mathcal{B}} -\nabla_{\boldsymbol{X}} \phi \, dV = \frac{1}{|\mathcal{B}|} \int_{\mathcal{B}} \boldsymbol{E} \, dV. \tag{4.20}$$

We thus can alternatively compute the macroscopic electric field in terms of the volume average in this case. Comparing the latter result with the result obtained for the constants $\{\overline{\mathfrak{C}_{\boldsymbol{F}}}, \overline{\mathfrak{C}_{\boldsymbol{E}}}\}$ from Equation (4.19), we identify the constants $\{\overline{\mathfrak{C}_{\boldsymbol{F}}}, \overline{\mathfrak{C}_{\boldsymbol{E}}}\}$ as the volume average of the microscopic fields

$$\overline{\mathfrak{C}_{\boldsymbol{F}}} = \overline{\boldsymbol{F}} = \frac{1}{|\mathcal{B}|} \int_{\mathcal{B}} \boldsymbol{F} \, dV \quad \text{and} \quad \overline{\mathfrak{C}_{\boldsymbol{E}}} = \overline{\boldsymbol{E}} = \frac{1}{|\mathcal{B}|} \int_{\mathcal{B}} \boldsymbol{E} \, dV. \tag{4.21}$$

The calculation of the macroscopic derivatives $\{\partial_{\overline{\boldsymbol{F}}} \overline{\psi}, \partial_{\overline{\boldsymbol{E}}} \overline{\psi}\}$ from Equation (4.14) then simply becomes

$$\partial_{\overline{\boldsymbol{F}}} \overline{\psi} = \frac{1}{|\mathcal{B}|} \int_{\mathcal{B}} \partial_{\boldsymbol{F}} \psi(\boldsymbol{F}^{\#}) \, dV \quad \text{and} \quad \partial_{\overline{\boldsymbol{E}}} \overline{\psi} = \frac{1}{|\mathcal{B}|} \int_{\mathcal{B}} \partial_{\boldsymbol{E}} \psi(\boldsymbol{E}^{\#}) \, dV, \tag{4.22}$$

or in terms of the mechanical stress and electric displacement according to (3.71)

$$\overline{\boldsymbol{T}} = \frac{1}{|\mathcal{B}|} \int_{\mathcal{B}} \boldsymbol{T}(\boldsymbol{F}^{\#}) \, dV \quad \text{and} \quad \overline{\boldsymbol{D}} = \frac{1}{|\mathcal{B}|} \int_{\mathcal{B}} \boldsymbol{D}(\boldsymbol{E}^{\#}) \, dV. \tag{4.23}$$

4.3.2. Periodic fluctuation Dirichlet boundary conditions

For this type of boundary value problem, we also prescribe zero body force $\boldsymbol{\gamma} = \boldsymbol{0}$ and volume charge $\lambda = 0$ inside the RVE fulfilling (4.15a) and (4.15c). We are not applying free surface charges which again fulfills (4.15b) and (4.15d). However, in this case we restrict the fluctuative contribution of the deformation map and the scalar potential to be periodic on the boundaries

$$\widetilde{\boldsymbol{\varphi}}(\boldsymbol{X}^{+}) = \widetilde{\boldsymbol{\varphi}}(\boldsymbol{X}^{-}) \quad \text{and} \quad \widetilde{\phi}(\boldsymbol{X}^{+}) = \widetilde{\phi}(\boldsymbol{X}^{-}) \qquad \text{on} \qquad \partial\mathcal{B}, \tag{4.24}$$

where $\boldsymbol{X}^{+}$ and $\boldsymbol{X}^{-}$ are points on opposite faces of the periodic RVE. Having this special type of boundary condition, we can further evaluate the boundary terms of the equilibrium equation (4.8b) and (4.8d), however on the whole boundary without surface tractions and charges but with the periodic restriction in $\{\delta\widetilde{\boldsymbol{\varphi}}, \delta\widetilde{\phi}\}$ as

$$\int_{\partial\mathcal{B}} (\partial_{\boldsymbol{F}} \psi \boldsymbol{N}) \cdot \delta\widetilde{\boldsymbol{\varphi}} \, dA = \int_{\partial\mathcal{B}} \partial_{\boldsymbol{F}} \psi^{+} \boldsymbol{N}(\boldsymbol{X}^{+}) \cdot \delta\widetilde{\boldsymbol{\varphi}}(\boldsymbol{X}^{+}) + \partial_{\boldsymbol{F}} \psi^{-} \boldsymbol{N}(\boldsymbol{X}^{-}) \cdot \delta\widetilde{\boldsymbol{\varphi}}(\boldsymbol{X}^{-}) \, dA$$

$$= \int_{\partial\mathcal{B}} [\partial_{\boldsymbol{F}} \psi^{+} \boldsymbol{N}(\boldsymbol{X}^{+}) + \partial_{\boldsymbol{F}} \psi^{-} \boldsymbol{N}(\boldsymbol{X}^{-})] \cdot \delta\widetilde{\boldsymbol{\varphi}} \, dA = 0$$

$$\int_{\partial\mathcal{B}} \partial_{\boldsymbol{E}} \psi \cdot \boldsymbol{N} \delta\widetilde{\phi} \, dA = \int_{\partial\mathcal{B}} \partial_{\boldsymbol{E}} \psi^{+} \cdot \boldsymbol{N}(\boldsymbol{X}^{+}) \delta\widetilde{\phi}(\boldsymbol{X}^{+}) + \partial_{\boldsymbol{E}} \psi^{-} \cdot \boldsymbol{N}(\boldsymbol{X}^{-}) \delta\widetilde{\phi}(\boldsymbol{X}^{-}) \, dA$$

$$= \int_{\partial\mathcal{B}} [\partial_{\boldsymbol{E}} \psi^{+} \cdot \boldsymbol{N}(\boldsymbol{X}^{+}) + \partial_{\boldsymbol{E}} \psi^{-} \cdot \boldsymbol{N}(\boldsymbol{X}^{-})] \delta\widetilde{\phi} \, dA = 0. \tag{4.25}$$

In order for the latter equation to hold true for all periodic $\{\delta\widetilde{\boldsymbol{\varphi}} \neq \boldsymbol{0}, \delta\widetilde{\phi} \neq 0\}$, the well-known antiperiodic boundaries for the tractions and surface charges

$$\partial_{\boldsymbol{F}}\psi^+\boldsymbol{N}(\boldsymbol{X}^+) = -\partial_{\boldsymbol{F}}\psi^-\boldsymbol{N}(\boldsymbol{X}^-) \quad \text{and} \quad \partial_{\boldsymbol{E}}\psi^+ \cdot \boldsymbol{N}(\boldsymbol{X}^+) = -\partial_{\boldsymbol{E}}\psi^- \cdot \boldsymbol{N}(\boldsymbol{X}^-) \quad (4.26)$$

are recovered. As a last step, we now want to again identify the constants $\{\overline{\mathfrak{C}}_{\overline{\boldsymbol{F}}}, \overline{\mathfrak{C}}_{\overline{\boldsymbol{E}}}\}$. Inserting the split of the deformation map and the scalar potential (4.6) into the definition of the macroscopic deformation gradient and electric field (4.16) yields

$$\overline{\boldsymbol{F}} = \frac{1}{|\mathcal{B}|} \int_{\partial\mathcal{B}} (\overline{\mathfrak{C}}_{\overline{\boldsymbol{F}}}\boldsymbol{X} + \widetilde{\boldsymbol{\varphi}}) \otimes \boldsymbol{N} \, dA$$

$$= \frac{1}{|\mathcal{B}|} \int_{\partial\mathcal{B}} (\overline{\mathfrak{C}}_{\overline{\boldsymbol{F}}}\boldsymbol{X}) \otimes \boldsymbol{N} \, dA + \frac{1}{|\mathcal{B}|} \int_{\partial\mathcal{B}} \widetilde{\boldsymbol{\varphi}}(\boldsymbol{X}^+) \otimes \boldsymbol{N}(\boldsymbol{X}^+) + \widetilde{\boldsymbol{\varphi}}(\boldsymbol{X}^-) \otimes \boldsymbol{N}(\boldsymbol{X}^-) \, dA$$

$$\overline{\boldsymbol{E}} = -\frac{1}{|\mathcal{B}|} \int_{\partial\mathcal{B}} (-\overline{\mathfrak{C}}_{\overline{\boldsymbol{E}}} \cdot \boldsymbol{X} + \widetilde{\phi})\boldsymbol{N} \, dA$$

$$= \frac{1}{|\mathcal{B}|} \int_{\partial\mathcal{B}} (\overline{\mathfrak{C}}_{\overline{\boldsymbol{E}}} \cdot \boldsymbol{X})\boldsymbol{N} \, dA - \frac{1}{|\mathcal{B}|} \int_{\partial\mathcal{B}} \widetilde{\phi}(\boldsymbol{X}^+)\boldsymbol{N}(\boldsymbol{X}^+) + \widetilde{\phi}(\boldsymbol{X}^-)\boldsymbol{N}(\boldsymbol{X}^-) \, dA.$$

$$(4.27)$$

Using the periodicity of $\{\widetilde{\boldsymbol{\varphi}}, \widetilde{\phi}\}$ on the boundary and further assuming a shape of the RVE such that $\boldsymbol{N}(X^+) = -\boldsymbol{N}(X^-)$ such as a *cube*, a *sphere* or any periodic structure, the last integral vanishes. Further, in analogy to the zero fluctuation boundary conditions. we use the divergence theorem in absence of jump discontinuities and end up with

$$\overline{\mathfrak{C}}_{\overline{\boldsymbol{F}}} = \overline{\boldsymbol{F}} = \frac{1}{|\mathcal{B}|} \int_{\mathcal{B}} \boldsymbol{F} \, dV \quad \text{and} \quad \overline{\mathfrak{C}}_{\overline{\boldsymbol{E}}} = \overline{\boldsymbol{E}} = \frac{1}{|\mathcal{B}|} \int_{\mathcal{B}} \boldsymbol{E} \, dV. \quad (4.28)$$

We thus conclude that the macroscopic constants in both, the zero fluctuation and the periodic fluctuation boundary value problem are the volume averages of the macroscopically applied fields $\{\boldsymbol{F}, \boldsymbol{E}\}$. In analogy to the zero fluctuation boundaries, the calculation of the macroscopic derivative $\{\partial_{\overline{\boldsymbol{F}}}\overline{\psi}, \partial_{\overline{\boldsymbol{E}}}\overline{\psi}\}$ from Equation (4.14) becomes

$$\boxed{\partial_{\overline{\boldsymbol{F}}}\overline{\psi} = \frac{1}{|\mathcal{B}|} \int_{\mathcal{B}} \partial_{\boldsymbol{F}}\psi(\boldsymbol{F}^{\#}) \, dV \quad \text{and} \quad \partial_{\overline{\boldsymbol{E}}}\overline{\psi} = \frac{1}{|\mathcal{B}|} \int_{\mathcal{B}} \partial_{\boldsymbol{E}}\psi(\boldsymbol{E}^{\#}) \, dV,} \quad (4.29)$$

or in terms of the mechanical stress and electric displacement according to (3.71)

$$\boxed{\overline{\boldsymbol{T}} = \frac{1}{|\mathcal{B}|} \int_{\mathcal{B}} \boldsymbol{T}(\boldsymbol{F}^{\#}) \, dV \quad \text{and} \quad \overline{\boldsymbol{D}} = \frac{1}{|\mathcal{B}|} \int_{\mathcal{B}} \boldsymbol{D}(\boldsymbol{E}^{\#}) \, dV.} \quad (4.30)$$

4.3.3. Averaging of the macroscopic tangent operator

We have shown that in both cases, the zero and periodic fluctuation boundary conditions, the averaging, i.e., the scale transition, of the microscopic quantities $\{\partial_{\boldsymbol{F}}\psi(\boldsymbol{F}^{\#}), \partial_{\boldsymbol{E}}\psi(\boldsymbol{E}^{\#})\}$ is performed through the same volume averaging procedure (4.22) and (4.29). To solve material and geometrical nonlinear problems, we usually need a linearized form of these macroscopic quantities

$$\text{Lin}\,\partial_{\boldsymbol{F}}\overline{\psi} = \partial_{\overline{\boldsymbol{F}}}\,\overline{\psi}\big|_{\overline{\boldsymbol{F}}_i, \overline{\boldsymbol{E}}_i} + \partial_{\overline{\boldsymbol{F}}}^2\,\overline{\psi}\big|_{\overline{\boldsymbol{F}}_i, \overline{\boldsymbol{E}}_i} : \Delta\overline{\boldsymbol{F}} + \partial_{\overline{\boldsymbol{F}}}\partial_{\overline{\boldsymbol{E}}}\,\overline{\psi}\big|_{\overline{\boldsymbol{F}}_i, \overline{\boldsymbol{E}}_i} \cdot \Delta\overline{\boldsymbol{E}}$$
$$\text{Lin}\,\partial_{\boldsymbol{E}}\overline{\psi} = \partial_{\overline{\boldsymbol{E}}}\,\overline{\psi}\big|_{\overline{\boldsymbol{F}}_i, \overline{\boldsymbol{E}}_i} + \partial_{\overline{\boldsymbol{E}}}\partial_{\overline{\boldsymbol{F}}}\,\overline{\psi}\big|_{\overline{\boldsymbol{F}}_i, \overline{\boldsymbol{E}}_i} : \Delta\overline{\boldsymbol{F}} + \partial_{\overline{\boldsymbol{E}}}^2\,\overline{\psi}\big|_{\overline{\boldsymbol{F}}_i, \overline{\boldsymbol{E}}_i} \cdot \Delta\overline{\boldsymbol{E}},$$

$$(4.31)$$

where $\{\overline{\boldsymbol{F}}_i, \overline{\boldsymbol{E}}_i\}$ are the macroscopic deformation gradient and electric field at the linearization point. To arrive at a more compact notation, in line with the thermodynamic considerations done in Section 3.3.2 in Equation (3.71) we now introduce the *generalized strains* $\overline{\mathbb{G}}$ *and stresses* $\overline{\mathbb{S}}$ as follows

$$\overline{\mathbb{G}} = \begin{bmatrix} \overline{\boldsymbol{F}} \\ \overline{\boldsymbol{E}} \end{bmatrix} \quad \text{and} \quad \overline{\mathbb{S}}_i = \begin{bmatrix} \overline{\boldsymbol{T}}_i \\ -\overline{\boldsymbol{D}}_i \end{bmatrix} = \begin{bmatrix} \partial_{\overline{\boldsymbol{F}}} \, \overline{\psi}|_{\overline{\boldsymbol{F}}_i, \overline{\boldsymbol{E}}_i} \\ \partial_{\overline{\boldsymbol{E}}} \, \overline{\psi}|_{\overline{\boldsymbol{F}}_i, \overline{\boldsymbol{E}}_i} \end{bmatrix} = \begin{bmatrix} \partial_{\overline{\boldsymbol{F}}} \, \overline{\psi}|_{\overline{\mathbb{G}}_i} \\ \partial_{\overline{\boldsymbol{E}}} \, \overline{\psi}|_{\overline{\mathbb{G}}_i} \end{bmatrix}. \tag{4.32}$$

as well as the generalized increment between the linearization point and the next iterative generalized strain state $\{\Delta\overline{\boldsymbol{F}}, \Delta\overline{\boldsymbol{E}}\}$ as follows

$$\Delta\overline{\mathbb{G}} = \begin{bmatrix} \Delta\overline{\boldsymbol{F}} \\ \Delta\overline{\boldsymbol{E}} \end{bmatrix} = \begin{bmatrix} \overline{\boldsymbol{F}} - \overline{\boldsymbol{F}}_i \\ \overline{\boldsymbol{E}} - \overline{\boldsymbol{E}}_i \end{bmatrix}. \tag{4.33}$$

Further introducing the *material moduli*

$$\overline{\mathbb{A}}_i = \partial_{\overline{\boldsymbol{F}}} \, \overline{\boldsymbol{T}}|_{\overline{\boldsymbol{F}}_i, \overline{\boldsymbol{E}}_i}, \quad \overline{\boldsymbol{q}}_i = \partial_{\overline{\boldsymbol{E}}} \, \overline{\boldsymbol{T}}|_{\overline{\boldsymbol{F}}_i, \overline{\boldsymbol{E}}_i} = - \left[\partial_{\overline{\boldsymbol{F}}} \overline{\boldsymbol{D}}|_{\overline{\boldsymbol{F}}_i, \overline{\boldsymbol{E}}_i} \right]^T \quad \text{and} \quad \overline{\mathbb{K}}_i = - \, \partial_{\overline{\boldsymbol{E}}} \overline{\boldsymbol{D}}|_{\overline{\boldsymbol{F}}_i, \overline{\boldsymbol{E}}_i}. \tag{4.34}$$

we can set up the *macroscopic generalized tangent operator*

$$\overline{\mathbb{C}}^{algo} = \partial_{\overline{\mathbb{G}}} \, \overline{\mathbb{S}}|_{\overline{\mathbb{G}}_i} = \begin{bmatrix} \overline{\mathbb{A}}_i & \overline{\boldsymbol{q}}_i \\ \overline{\boldsymbol{q}}_i^T & \overline{\mathbb{K}}_i \end{bmatrix}, \tag{4.35}$$

which allows us to write the linearized macroscopic form (4.31) as follows

$$\text{Lin} \, \overline{\mathbb{S}} = \overline{\mathbb{S}}_i + \overline{\mathbb{C}}^{algo} \diamond \Delta\overline{\mathbb{G}}. \tag{4.36}$$

Again, we use the generic operator $\diamond$ denoting the appropriate contractions according to Equation (4.31). We now want to derive an explicit expression for the macroscopic moduli appearing in Equations (4.34) and (4.35). From the two previous subsections, we know from Equations (4.30) and (4.30) that in a homogenization context, the generalized macroscopic stresses are themselves dependent on the generalized microscopic stresses in the sense of a volume average. We thus need to apply the chain rule when evaluating the derivatives in (4.35)

$$\overline{\mathbb{C}}^{algo} = \partial_{\overline{\mathbb{G}}} \frac{1}{|\mathcal{B}|} \int_{\mathcal{B}} \mathbb{S} \, dV = \frac{1}{|\mathcal{B}|} \int_{\mathcal{B}} \partial_{\mathbb{G}} \mathbb{S} \diamond \partial_{\overline{\mathbb{G}}} \mathbb{G} \, dV = \frac{1}{|\mathcal{B}|} \int_{\mathcal{B}} \mathbb{C} \diamond \partial_{\overline{\mathbb{G}}} \mathbb{G} \, dV, \tag{4.37}$$

where in analogy to the macro-quantities (4.33), we introduced the *microscopic generalized stress and strain*

$$\mathbb{S} = \begin{bmatrix} \boldsymbol{T}_i \\ -\boldsymbol{D}_i \end{bmatrix} = \begin{bmatrix} \partial_{\boldsymbol{F}} \, \psi|_{\overline{\boldsymbol{F}}_i, \overline{\boldsymbol{E}}_i} \\ \partial_{\boldsymbol{E}} \, \psi|_{\overline{\boldsymbol{F}}_i, \overline{\boldsymbol{E}}_i} \end{bmatrix}, \quad \mathbb{G} = \begin{bmatrix} \boldsymbol{F} \\ \boldsymbol{E} \end{bmatrix} \quad \text{and} \quad \mathbb{C} = \partial_{\mathbb{G}} \, \mathbb{S}|_{\overline{\mathbb{G}}_i} = \begin{bmatrix} \mathbb{A}_i & \boldsymbol{q}_i \\ \boldsymbol{q}_i^T & \mathbb{K}_i \end{bmatrix}. \tag{4.38}$$

We now take a closer look at the partial derivative of the microscopic generalized strains with respect to the macroscopic generalized strains $\partial_{\overline{\mathbb{G}}}\mathbb{G}$. We utilize the strain decomposition (4.6) and the relation (4.28) to obtain

$$\overline{\mathbb{C}}^{algo} = \frac{1}{|\mathcal{B}|} \int_{\mathcal{B}} \mathbb{C} \diamond (\partial_{\overline{\mathbb{G}}}\overline{\mathbb{G}} + \partial_{\overline{\mathbb{G}}}\widetilde{\mathbb{G}}) \, dV, \tag{4.39}$$

which gives the explicit expression for the macroscopic tangent operator

$$\overline{\mathbb{C}}^{algo} = \frac{1}{|\mathcal{B}|} \int_{\mathcal{B}} \mathbb{C} + \mathbb{C} \diamond \partial_{\overline{\mathbb{G}}} \widetilde{\mathbb{G}} \, dV \qquad (4.40)$$

in terms of the fluctuation derivatives $\partial_{\overline{\mathbb{G}}} \widetilde{\mathbb{G}}$. We thus see that in contrast to the averaging of the macroscopic stresses (4.30), the averaging of the macroscopic tangent operator is not just the volume average of the microscopic moduli, but an additional term in dependence of said fluctuation derivatives $\partial_{\overline{\mathbb{G}}} \widetilde{\mathbb{G}}$ must be taken into account. This additional term is often referred to as a softening term. The determination of these derivatives will be subject of Chapter 6.

— Part II —

Trigonometric Approximation and Fourier Transform-Based Solution Schemes

Approximation of field variables and their gradients through trigonometric functions

The Fourier transform is the representation of a function in terms of an infinite harmonic series. With this, a function is represented or approximated by trigonometric base functions, namely the sine and cosine function. The truncation of the integral or infinite sum of Fourier transform leads to the discrete Fourier transform. It can be applied to given discrete data points to obtain a trigonometric approximation of the underlying function and thus the possibility to evaluate derivatives and gradients. According to HEIDEMAN ET AL. [73], the first reported discrete cosine transform goes back to CLAIRAUT [28] in 1754, the first sine transform to LAGRANGE [104] in 1762. In 1822, FOURIER [49] published his seminal work on the representation of functions through harmonic series. The nowadays most popular and efficient implementation for such a transformation is called the fast Fourier transform. Interestingly, GAUSS already proposed such an algorithm at the beginning of the 18th century [73]. Nowadays, the Cooley-Tukey implementation [29] of the said algorithm is well established in various computational fields. This chapter will briefly discuss the most important quantities of the discrete Fourier transform in our context with a special focus on approximating derivatives and solving differential equations. Some small numerical examples are included for better understanding.

5.1. The discrete Fourier transform

The discrete Fourier transform results from a truncation of the continuous Fourier transform in terms of the wave numbers k [193, 206]. Having a complex vector $y_j \in \mathbb{C}^N; j = 0, ..., N - 1$ of one-dimensional values belonging to the gridpoints $x_j = j/N$, the forward discrete Fourier transform (DFT) appears as

$$\widehat{y}_k = \sum_{j=0}^{N-1} e^{-2\pi \mathrm{i} k x_j} y_j \quad \text{for} \quad k = \frac{-N+1}{2}, ..., \frac{N-1}{2}, \tag{5.1}$$
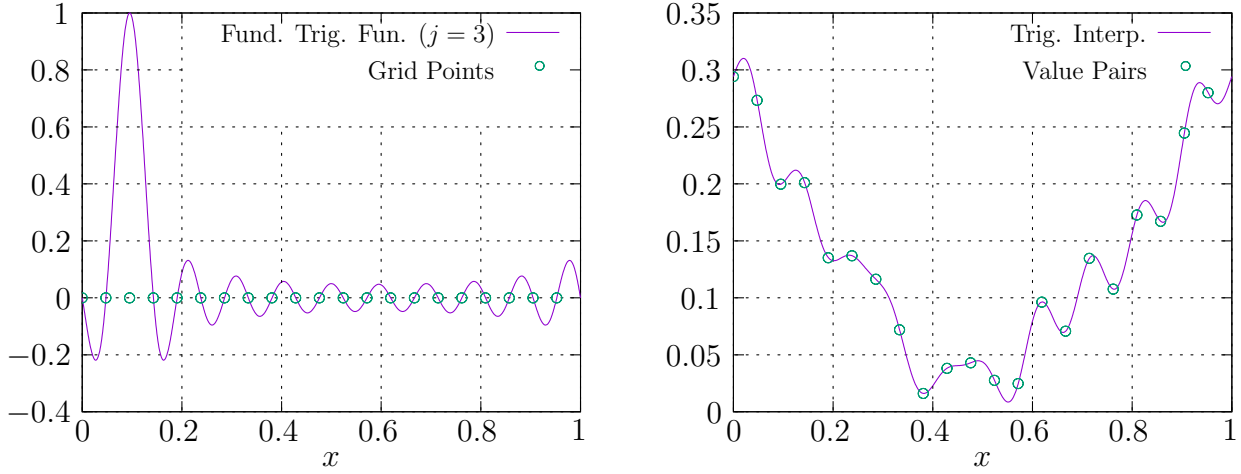
Figure 5.1: To the left, a plot of the fundamental trigonometric function for the grid point $j = 3$ is shown. One can see that the approximation satisfies the partition-of-unity. To the right, the complete trigonometric approximation of the $N = 21$ given value pairs using 21 wave numbers is depicted.

where $\mathrm{i} = \sqrt{-1}$ is the complex root and $\widehat{y}$ are the so-called discrete Fourier coefficients. The inverse discrete Fourier transform is then performed according to

$$y_j = \frac{1}{N} \sum_{k=0}^{N-1} e^{2\pi \mathrm{i} k x_j} \widehat{y}_k \quad \text{for} \quad j = 0, ..., N - 1. \tag{5.2}$$

For the special case that the input vector only consists of real numbers $y_j \in \mathbb{R}^N; j = 0, ..., N - 1$, the Fourier coefficients satisfy the symmetry

$$\widehat{y}_{N-k} = \overline{\widehat{y}_k} \quad \text{for} \quad k \neq 0, \tag{5.3}$$

where the overline in this context denotes the complex conjugate of the complex number.[1] A more convenient way of writing the discrete Fourier transform can be obtained by defining the transformation matrices

$$\omega_{kj} = e^{-2\pi \mathrm{i} k x_j} \quad \text{and} \quad \omega_{jk}^{-1} = e^{2\pi \mathrm{i} k x_j} \tag{5.4}$$

and rewriting the sums in the transforms (5.1) and (5.2) as matrix-vector multiplications

$$\widehat{y}_k = \omega_{kj} y_j \quad \text{and} \quad y_j = \frac{1}{N} \omega_{jk}^{-1} \widehat{y}_k. \tag{5.5}$$

One sees that performing the DFT and then the inverse discrete Fourier transform (IDFT) gives back the original input vector. In Fourier space, the approximation has local support as $\widehat{y}_k = 0$ for all wave numbers $k \neq (-N + 1)/2, ..., (N - 1)/2$. In real space, the interpolation is not locally supported [210]. One can see the interpolation behavior better when evaluating the IDFT (5.2) on a finer grid, i.e. $j' = 0, ..., N' - 1$ with $N' > N$. Figure 5.1 shows an example for a Fourier approximation using $N = 21$ value pairs

---

[1]Note that the arrangement of the wave numbers k might change from implementation to implementation, and thus the details in the indexing of k change.
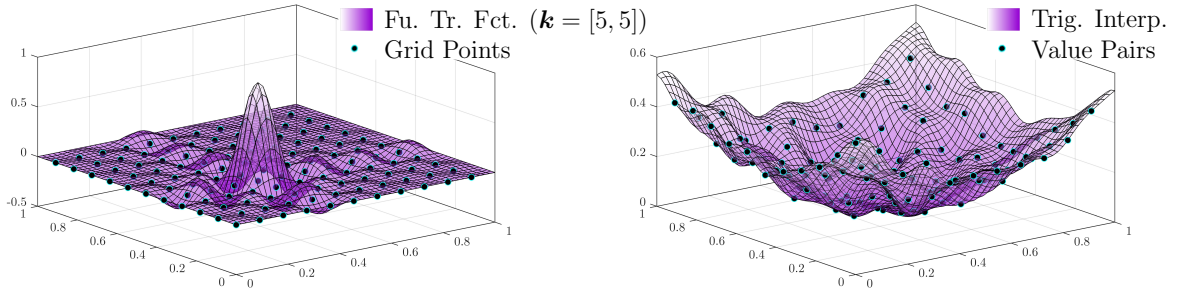
Figure 5.2: To the left, a plot of the two-dimensional fundamental trigonometric function for the grid point $\boldsymbol{k} = [5, 5]$ is shown. One can see that the approximation satisfies the partition-of-unity. To the right, the complete trigonometric approximation of the $N = 11$ given value pairs using 11 wave numbers is depicted.

(x_N, y_N) and 21 wave numbers. The approximation is evaluated at $N' = 1001$ grid points, which can be written down compactly according to Equation (5.5) as

$$y_{j'} = \frac{1}{N} \omega_{j'k}^{-1} \omega_{kj} y_j. \tag{5.6}$$

The approximation satisfies the partition-of-unity as

$$\frac{1}{N} \omega_{j'k}^{-1} \omega_{kj} = \delta_{j'j}, \tag{5.7}$$

which is shown for $j = 3$ on the left-hand side of Figure 5.1. One can see the fundamental trigonometric function for the third value pair at $j = 3$, i.e. the contribution $\omega_{j'k}^{-1} \omega_{k3}$ becomes 1 at $j = j'$ and is zero at the other grid points of the original value pairs. The right-hand side of Figure 5.1 shows the full approximation (5.6). One can see that the interpolation function approximates the original value pairs exactly.

Furthermore, the DFT can easily be extended to a higher dimension. In two dimensions, for example, it takes the form

$$\widehat{y}_{kl} = \sum_{h=0}^{M-1} \sum_{j=0}^{N-1} e^{-2\pi i k x_{1,h}} e^{-2\pi i l x_{2,j}} y_{hj} \quad \text{for} \quad k = \frac{-M+1}{2}, ..., \frac{M-1}{2}; \;\; l = \frac{-N+1}{2}, ..., \frac{N-1}{2}, \tag{5.8}$$

for a given complex vector $y_{hj} \in \mathbb{C}^{M \times N}$ on a grid $\boldsymbol{x} = [x_1, x_2] = [h/M, j/N]$ with wave number $\boldsymbol{k} = [k, l]$. The IDFT in two dimensions then appears as

$$y_{hj} = \frac{1}{MN} \sum_{k=0}^{M-1} \sum_{l=0}^{N-1} e^{2\pi i k x_{1,h}} e^{2\pi i l x_{2,j}} \widehat{y}_{kl} \quad \text{for} \quad h = 0, ..., M-1; \;\; j = 0, ..., N-1. \tag{5.9}$$

Figure 5.2 shows the corresponding fundamental trigonometric function and the function interpolation on the grid $[M, N] = [11, 11]$, see also [210] for more details.

5.2. Derivative approximation through the discrete Fourier transform

In order to solve differential equations by means of Fourier-based methods, it is necessary to evaluate the derivatives of the trigonometric interpolation function at the grid
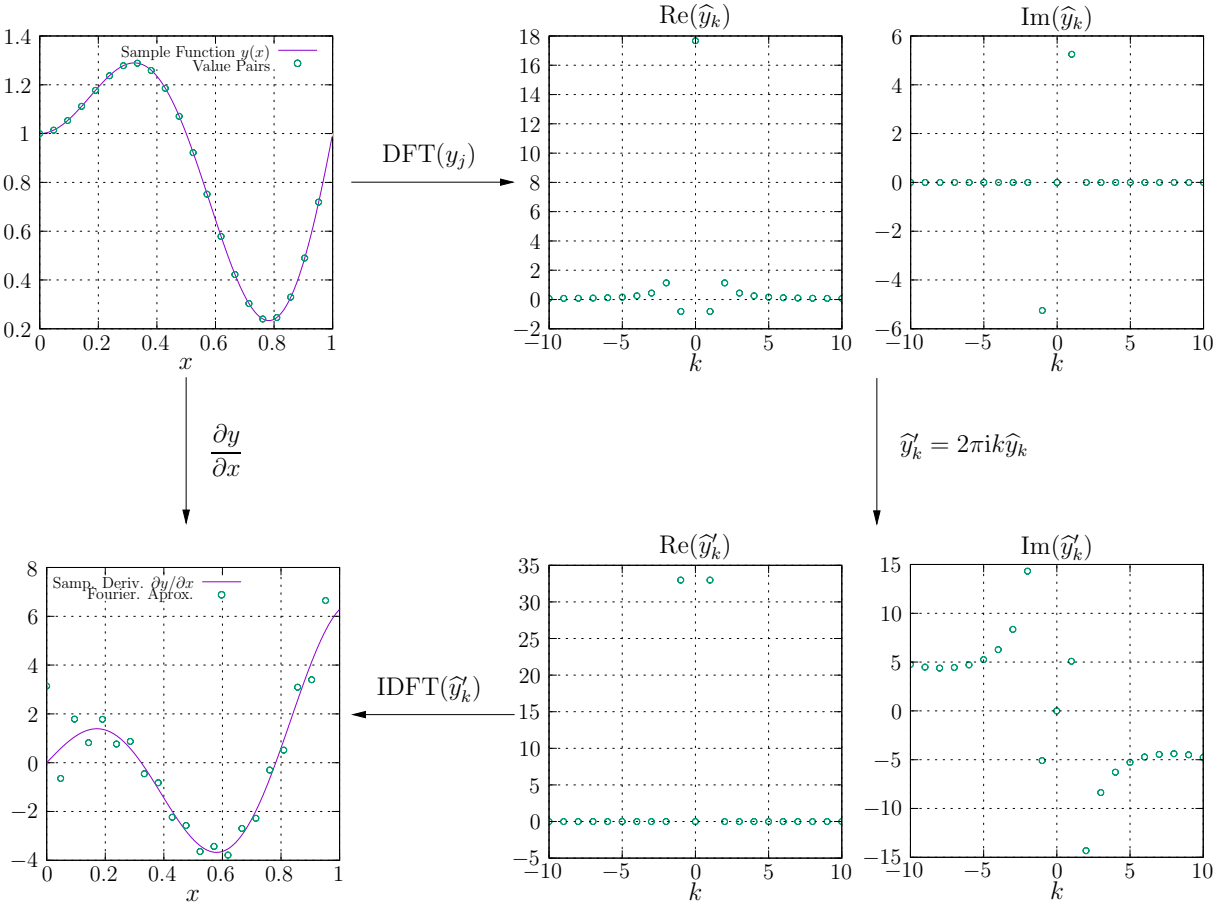
Figure 5.3: Fourier approximation of the derivatives of some given data points. $N = 21$ data points as indicated by the circles are drawn from the sample function $y(x) = 1 + x \sin(2\pi x)$. A DFT is used to obtain the Fourier coefficients of the data points. In the case of unit length of the periodic cell, the coefficients are then multiplied with $2\pi \mathrm{i} k$. The IDFT then gives the approximation of the data points as indicated on the bottom left graph.

points x_j. Having a look at the inverse discrete Fourier transform (5.2), we see that only the exponential term depends on x_j, as we summed over all x_j when calculating the Fourier coefficients $\widehat{y}_k$ in the forward discrete Fourier transform (5.1). Consequently, the approximated derivative at point x_j for a one-dimensional problem appears as

$$\frac{\partial y}{\partial x}(x_j) \approx \frac{1}{N} \sum_{k=0}^{N-1} e^{2\pi \mathrm{i} k x_j} 2\pi \mathrm{i} k \widehat{y}_k \quad \text{for} \quad j = 0, ..., N - 1. \tag{5.10}$$

Comparing the latter equation with Equation (5.2), we see that it is in fact again an inverse DFT using modified Fourier coefficients $\widehat{y}'_k = 2\pi \mathrm{i} k \widehat{y}_k$. Figure 5.3 gives an example on the approximation of the derivatives computed from given value pairs (x_j, y_j). In our specific example, we draw $N = 21$ value pairs from the sample function $y(x) = 1 + x \sin(2\pi x)$, where the distance between the two neighboring value pairs x_j and x_{j-1} is equidistant. The function is periodic on $x \in [0, 1]$, its derivative however is not. In a first step, we apply the DFT using 21 wave numbers to the value pairs and obtain the complex Fourier coefficients $\widehat{y}_k$. Here, one can see an additional feature of the DFT. As the value pairs are all real numbers, the Fourier coefficients are of a certain symmetry: The Fourier coefficient at wave number k_i is the complex conjugate of the Fourier coefficient at k_{-i}, see Equation 5.3. Numerical algorithms exploit this in order to gain a speedup. The next
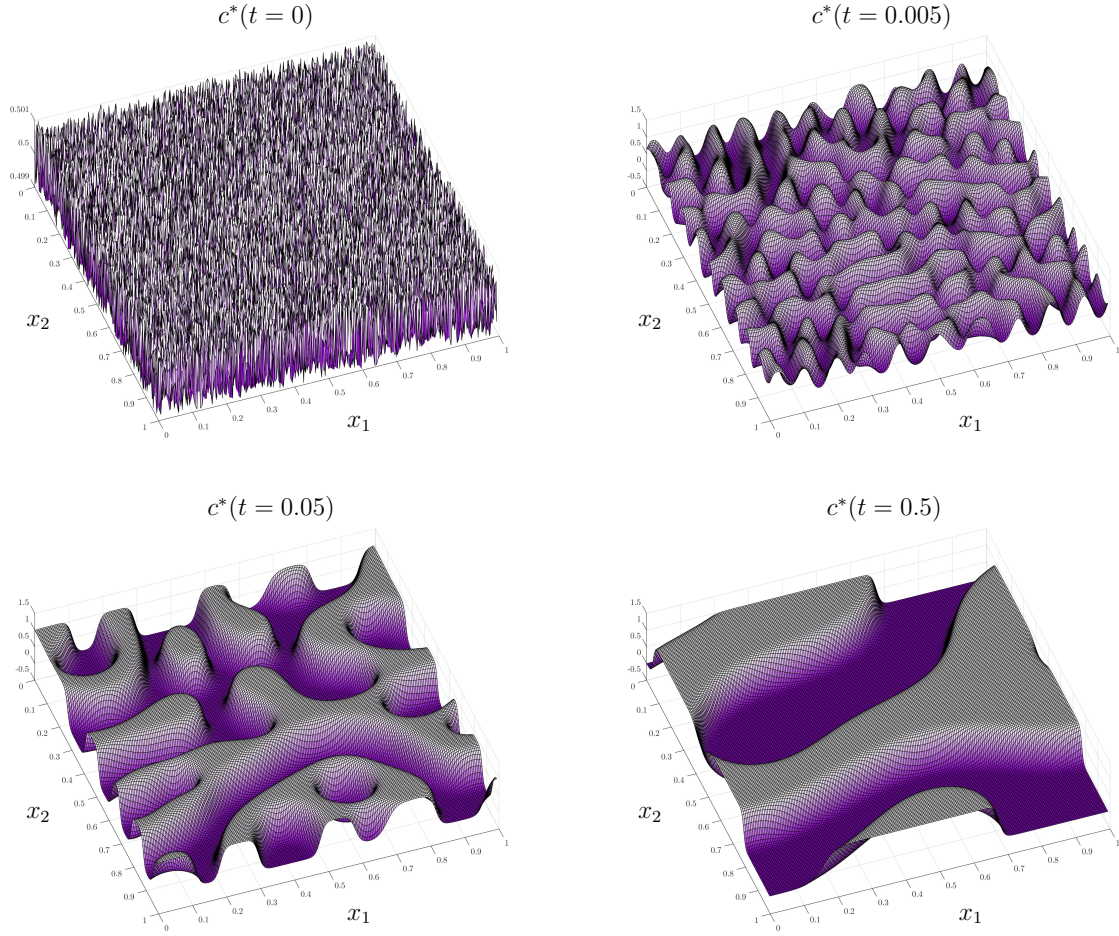
Figure 5.4: A solution of the Cahn-Hilliard equation for a binary fluid mixture starting from a random initial contribution at $t = 0$ where the average of c is approximately 0.5. One can see phase segregation, as the fluids try to minimize their surface. The domains merge and grow.

step is to multiply the Fourier coefficients according to Equation (5.10) with the factor $2\pi\mathrm{i}k$. Finally, the IDFT is applied to the modified Fourier coefficients, and we obtain the trigonometric approximation of the value pairs' derivative.

The results directly carry over to higher dimensions. For convenience, we then define the modified wave-vector $\boldsymbol{k}^* = 2\pi\boldsymbol{k}$ of dimension n and write the gradient or the Laplacian of the approximated function as

$$\nabla y \approx \mathrm{IDFT}(\mathrm{i}\boldsymbol{k}^*\widehat{y}) \quad \text{and} \quad \nabla^2 y \approx \mathrm{IDFT}(-|\boldsymbol{k}^*|^2\widehat{y}), \tag{5.11}$$

where the IDFT is carried out in analogy to Equation (5.10). The latter equation must be interpreted as a multiplication *per grid point*, i.e. at each grid point the corresponding wave vector $\boldsymbol{k}^* = [2\pi k, 2\pi l]$ or its magnitude $|\boldsymbol{k}^*|^2 = (2\pi k)^2 + (2\pi l)^2$ is multiplied with the scalar $\widehat{y}_{kl}$ and the whole array is then inversely transformed to obtain the gradient or the Laplacian. This convention will be used in the following chapters as well.

5.3. Numerical example: Solving the Cahn-Hilliard equation

Having the trigonometric approximation at hand along with the computation of the gradients (5.11), we now want to demonstrate its validity by solving the Cahn-Hilliard equation

$$\frac{\partial c}{\partial t} = D\nabla^2(\partial_c f(c) - \gamma\nabla^2 c). \tag{5.12}$$

It describes the process of phase separation of a mixture of two fluids in terms of the concentration c, e.g., $c = 0.6$ would correspond to 60% of fluid one, and 40% of fluid two. The parameter D is a diffusion coefficient and γ is a length scale parameter accounting for the transition between the two phases. Finally, the function $f(c)$ is modeled to represent a double-well potential with respect to the concentration c. In this example, we closely follow [46], where the double-well potential takes the form

$$f(c) = c^2(c-1)^2. \tag{5.13}$$

The Cahn-Hilliard equation in (5.12) in discrete Fourier space then appears as

$$\frac{\partial \widehat{c}}{\partial t} = -D|\boldsymbol{k}^*|^2(\widehat{\partial_c f}(c) + \gamma|\boldsymbol{k}^*|^2\,\widehat{c}), \tag{5.14}$$

where the wide hat denotes the Fourier transformed quantities. Following [46], we now use a semi-implicit time discretization

$$\frac{\widehat{c}_{n+1} - \widehat{c}_n}{\Delta t} = -D|\boldsymbol{k}^*|^2(\widehat{\partial_c f}(c_n) + \gamma|\boldsymbol{k}^*|^2\,\widehat{c}_{n+1}). \tag{5.15}$$

Rearranging then gives the semi-implicit update rule

$$\widehat{c}_{n+1} = \frac{\widehat{c}_n - D|\boldsymbol{k}^*|^2\widehat{\partial_c f}(c_n)\Delta t}{1 + \gamma|\boldsymbol{k}^*|^4 D\Delta t}. \tag{5.16}$$

For our unitless numerical example, the time step size is set to $\Delta t = 5 \cdot 10^{-6}$. The square domain is of unit length $L_1 = L_2 = 1$ and is discretized by 201×201 equidistant grid points. The diffusion coefficient is set to $D = 1$. As length scale parameter, we choose $\gamma = 0.0001$. The MATLAB [118] code that generated this example is attached. Figure 5.4 shows the results for the concentration c at the initial step, at 10^3 iterations, 10^4 iterations and 10^5 iterations. At time $t = 0$, the concentration is initialized as $c_0 = 0.5 + \mathcal{U}(-1, 1)$ at every grid point, where $\mathcal{U}(-1, 1)$ denotes a uniform random distribution between -1 and 1. As a consequence, the average concentration is approximately 0.5. At $t = 0.005$, one can see that the phases already start to separate. At $t = 0.05$ one can see the formation of larger domains of fluid one where $c \approx 1$ and fluid two where $c \approx 0$. At $t = 0.5$, the domains merge further.

Listing 5.1: Cahn-Hilliard Matlab implementation

```matlab
close all
clear all

% Material Parameters and time step
gamma = 0.0001;
```

```matlab
 6  D = 1.0;
 7  dt = 0.000005;
 8
 9  % Build grid in real space and wave numbers
10  N = 201;
11  x = 0:1/N:1-(1/N);
12  k = (-N+1)/2:1:(N-1)/2;
13
14  [k1,k2] = meshgrid(k,k);
15  [x1,x2] = meshgrid(x,x);
16
17  % Randomly initialize the concentration
18  c0 = 0.5 + (1.0-2.0*rand(size(x1)))*10^(-3);
19  cc_n = c0;
20
21  % Calculate magnitude of wave numbers on grid (including (2*pi)
        ^2)
22  kabs = 4.0*pi^(2)*(k1.^(2) + k2.^(2));
23
24
25  for t = 1:100000
26      % Fourier transform of concentration and shift of
            frequencies
27      ccF_n = fft2(cc_n);
28      ccF_n = fftshift(ccF_n);
29
30      % Compute derivative of double-well potential of last time
            step
31      % (semi-implicit scheme)
32      g = 4.0*cc_n.^3.0 - 6.0*cc_n.^2.0 + 2.0*cc_n;
33
34      % Fourier transform of double-well derivative and shift
35      gF = fft2(g);
36      gF = fftshift(gF);
37
38      % Second Laplacian in Fourier space using magnitude of k
39      ccF = (ccF_n - D*kabs.*gF*dt).*(1.0+gamma*D*dt*kabs.*kabs)
            .^(-1.0);
40
41      % Inverse Fourier transform of second Laplacian
42      ccF = ifftshift(ccF);
43      cc = ifft2(ccF);
44
45      % Update history variable
46      cc_n = cc;
47  end
```

5.4. Numerical example: Solving a one-dimensional Ginzburg-Landau type equation

We now want to show that the solution of a differential equation under periodic boundary conditions can be solved by setting up the system matrix and right-hand side explicitly and inversion of the system matrix. We, therefore, consider a one-dimensional Ginzburg-Landau type differential equation defined as

$$d - l^2 \Delta d - 2(1 - d)\mathcal{H}(x)\frac{l}{g_c} = 0, \tag{5.17}$$

where d is now our phase-field variable at hand (analogously to c in the previous example), $\mathcal{H}(x)$ is an arbitrary real-valued field, l is a length scale parameter accounting for the diffuse interface between two phases and g_c is some material parameter. Using the gradient relations in Fourier space (5.10) and $(5.11)_2$ in combination with the matrix representation of the inverse Fourier transform (5.4), we can define the Laplacian transformation matrices

$$\overline{\omega}_{jk}^{-1} = -(4\pi^2 k^2)e^{2\pi \mathrm{i}k x_j}. \tag{5.18}$$

With this definition at hand, the Ginzburg-Landau type differential equation can be discretized on a grid with N grid points where all indices run from 0 to $N - 1$ as follows

$$(\delta_{ij} - \frac{l^2}{N}\overline{\omega}_{ix}^{-1}\omega_{xj} + \frac{2l}{g_c}\delta_{ij}\mathcal{H}_j)d_j = \frac{2l}{g_c}\mathcal{H}_i. \tag{5.19}$$

The latter equation is a system of linear equations in d_j from which we can directly identify the stiffness matrix K and right-hand side b as

$$\mathrm{K}_{ij} = \delta_{ij} - \frac{l^2}{N}\overline{\omega}_{ix}^{-1}\omega_{xj} + \frac{2l}{g_c}\delta_{ij}\mathcal{H}_j \quad \text{and} \quad \mathrm{b}_i = \frac{2l}{g_c}\mathcal{H}_i. \tag{5.20}$$

The solution vector d_j^* is then obtained by inversion of the stiffness matrix

$$d_j^* = \mathrm{K}_{ji}^{-1}\mathrm{b}_i. \tag{5.21}$$

As a one-dimensional, unit-less example, we choose a domain $x \in [0, 1]$ which is discretized by 201 equidistant grid points. The material parameters are set to $l = 0.05$ and $g_c = 0.0027$. The applied $\mathcal{H}$-field as shown on the left side of Figure 5.5 is governed by the function

$$\mathcal{H} = \frac{1}{a\sqrt{\pi}}\mathrm{e}^{\frac{-(x-0.5)^2}{a^2}}, \tag{5.22}$$

which is an approximation to the Dirac delta function. The MATLAB [118] code that generated this example can be found in the following subsection. Figure 5.5 shows the result d of the phase field for the discretized problem. One can see that the gradient of the phase field is regularized. A property of the differential equation that can be tuned by the parameter l. One can also see that the solution field is always $d \leq 1$. As by construction of the Ginzburg-Landau type equation (5.17), d degrades the driving $\mathcal{H}$-field.
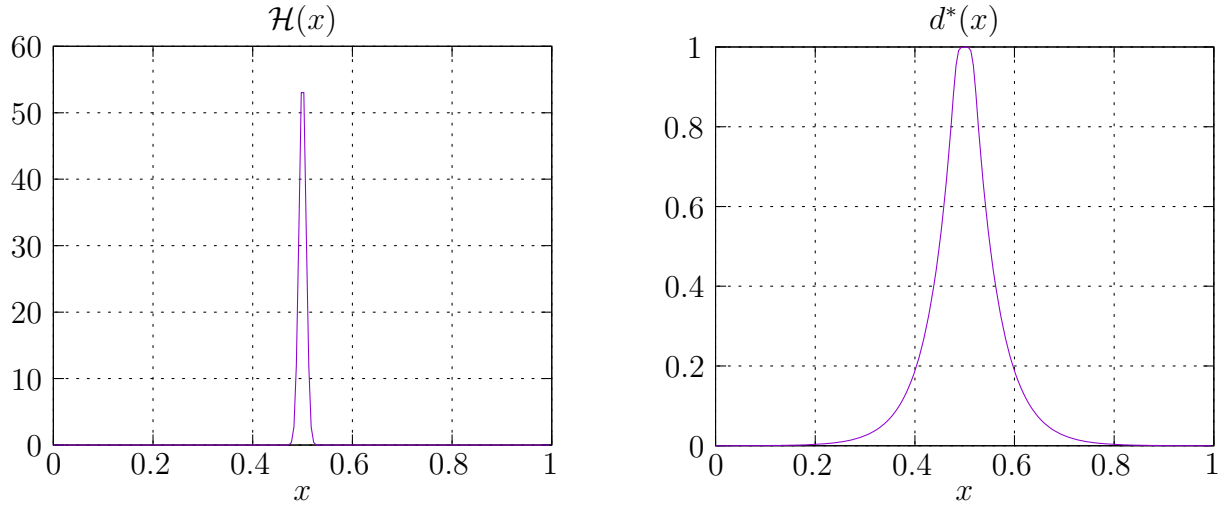
Figure 5.5: To the left, the applied $\mathcal{H}$-field governed by the function $1/(a\sqrt{\pi})\exp(-(x-0.5)^2/a^2)$ is shown. To the left, the solution d^* of the phase-field obtained from the Fourier discretized boundary value problem using $N = 201$ grid points and material parameters $l = 0.05$, $g_c = 0.0027$ is shown.

Listing 5.2: Ginzburg-Landau Matlab Implementation

```matlab
close all
clear all

% Build grid in real space and wave numbers
N = 201;
x = 0:1/N:1-(1/N);
k = (-N+1)/2:1:(N-1)/2;

% Applied driving force approximated by the delta distribution
a = 0.01;
H = 1/(sqrt(pi)*a)*exp(-(x-0.5).^2/a^2);

% Material parameters of the differential equation
l = 0.05;
gc = 0.0027;

% Initialize DFT matrices
W = zeros(N,N);
Winv = zeros(N,N);
ddWinv = zeros(N,N);

% Build DFT matrices
for i = 1:N
    for j = 1:N
        % Forward Fourier transform matrix
        W(i,j) = exp(-2*pi*1i*k(i)*x(j));
        % Inverse Fourier transform matrix
        Winv(i,j) = exp(2*pi*1i*k(j)*x(i));
```

```matlab
29            % Laplacian  inverse  Fourier  transform  matrix
30            ddWinv(i,j) = (2*pi*1i*k(j))^(2)*exp(2*pi*1i*k(j)*x(i));
31        end
32  end
33
34  % System Matrix of Fourier discretized boundary value problem
35  Stiffness = real(eye(N,N) - (l^(2)/N)*(ddWinv*W)  ...
36      + (2*l/gc)*diag(H));
37  % Right hand side of Fourier discretized boundary value problem
38  RightHandSide = real((2*l/(gc))*H');
39
40  % Solution of phase field: d = b\A
41  d = Stiffness\RightHandSide;
```

<div align="right">

Chapter **6**

</div>

Fast Fourier transform-based computational homogenization of composites

We now want to use the previously presented Fourier methods to efficiently solve homogenization problems. One could now think of setting up a global stiffness matrix for the equilibrium equations (3.22), see also Equation (4.8) for the variational microscopic form, employing the trigonometric Fourier transform matrices (5.4) as presented in Section 5.1. However, the explicit calculation of stiffness matrices demands much memory for larger problems. We therefore focus now on an approach presented by MOULINEC & SU-QUET [136]. It relies on the construction of a periodic Green operator Γ^0 in Fourier space and allows for an efficient iterative solution of the physical problem, see also MOULINEC & SUQUET [137]. The procedure finally results in the solution of a *Lippmann-Schwinger equation* [113] known from quantum scattering theory

$$\boxed{f = \overline{f} + \Gamma^0 * \tau(f),} \tag{6.1}$$

which states that the solution f of some associated suitable differential equation can be decomposed into a constant contribution $\overline{f}$ and a contribution obtained by the convolution of a Green operator Γ^0 with a perturbation field $\tau(f)$ over the solution domain $\mathcal{B}$ as follows

$$(\Gamma^0 * \tau(f))(X) = \int_{\mathcal{B}} \Gamma^0(X - Y) \cdot \tau(f, Y) dY, \tag{6.2}$$

see also DUFFY [40] for a more detailed discussion on Green operators. An early variant of this equation where there is no fixed-point iteration involved was already used by MAX BORN [12] on the field of quantum scattering, also known as Born approximation. In this chapter, it is shown how to obtain the Lippmann-Schwinger equation for mechanical boundary value problems and the explicit periodic Green operators in Fourier space will be derived. As a second objective, the computation of the macroscopic tangent operators as defined in Equation (4.40) is dealt with. It is shown that the Lippmann-Schwinger equation can be exploited to directly compute the fluctuation sensitivities through a set of linear equations. Regarding the electro-mechanically coupled boundary value problems, a special focus lies on the incorporation of reference moduli within the Green operator as well as on coupled and decoupled computations of the macroscopic tangent operators.

<div align="center">

77

</div>

6.1. Lippmann-Schwinger equation of mechanical boundary value problems

We now want to transform the previously defined mechanical boundary value problem $(3.22)_1$ and $(3.22)_2$

$$\operatorname{Div} \boldsymbol{T} = \boldsymbol{0} \ \text{ in } \ \mathcal{B} \ \text{ and } \ [\![\boldsymbol{T}]\!]\boldsymbol{N} = \boldsymbol{0} \ \text{ on } \ \partial\mathcal{B}, \tag{6.3}$$

into a form that resembles the Lippmann-Schwinger equation (6.1). In the latter equation, $[\![(\bullet)]\!]$ denotes the jump of some quantity $(\bullet)$ across the surface of two adjacent RVEs. As for the first Piola-Kirchoff stress $\boldsymbol{T}$, it is defined as

$$(\boldsymbol{T}^+ - \boldsymbol{T}^-)\boldsymbol{N} = \boldsymbol{0} \ \text{ on } \ \partial\mathcal{B}^0, \tag{6.4}$$

where $\boldsymbol{T}^+ = \boldsymbol{T}(\boldsymbol{X}^+)$ and $\boldsymbol{T}^- = \boldsymbol{T}(\boldsymbol{X}^-)$ are the stresses evaluated at opposing points of on the RVE's boundary. As demonstrated in HASHIN & SHTRIKMAN [70],WILLIS [204] and MOULINEC & SUQUET [136, 137], we perform a zero-addition to the stress $\boldsymbol{T}$ by a constant reference material $\mathbb{A}^0$ contracted with the strain field $\boldsymbol{F}$

$$\boldsymbol{T} = \boldsymbol{T} + \mathbb{A}^0 : \boldsymbol{F} - \mathbb{A}^0 : \boldsymbol{F}. \tag{6.5}$$

Here, $\mathbb{A}^0$ can be any fourth-order tensor and will later act as a preconditioner. By defining a perturbation field

$$\boldsymbol{\tau}^m = \boldsymbol{T} - \mathbb{A}^0 : \boldsymbol{F}, \tag{6.6}$$

the first Piola-Kirchhoff stress can be written in the form

$$\boldsymbol{T} = \mathbb{A}^0 : \boldsymbol{F} + \boldsymbol{\tau}^m(\boldsymbol{F}). \tag{6.7}$$

Insertion of the latter definition into the equilibrium equation (6.3) yields the representation

$$\operatorname{Div}[\mathbb{A}^0 : \boldsymbol{F}] = -\operatorname{Div}[\boldsymbol{\tau}^m(\boldsymbol{F})]. \tag{6.8}$$

Interpreting the right-hand side as some general driving term, the solution of the differential equation can be written down in terms of a fourth-order Green operator $\boldsymbol{\Gamma}^0$ as follows

$$\boldsymbol{F} = \overline{\boldsymbol{F}} + \boldsymbol{\Gamma}^0 * \boldsymbol{\tau}^m(\boldsymbol{F}), \tag{6.9}$$

where we recall from Equations (4.5) and (4.28) that for the special case of periodic homogenization, $\overline{\boldsymbol{F}}$ denotes the macroscopic constant deformation and $\boldsymbol{\Gamma}^0$ is calculated based on boundary conditions compatible with the Hill-Mandel conditions (4.1). In the latter equation, we use the symbol $*$ to denote the convolution defined by

$$\boldsymbol{\Gamma}^0 * \boldsymbol{\tau}(\boldsymbol{F}) = (\boldsymbol{\Gamma}^0 * \boldsymbol{\tau}(\boldsymbol{F}))(\boldsymbol{X}) = \int_{\mathcal{B}} \boldsymbol{\Gamma}^0(\boldsymbol{X}) : \boldsymbol{\tau}(\boldsymbol{F}(\boldsymbol{X} - \boldsymbol{Y})) \, dV(\boldsymbol{Y}), \tag{6.10}$$

with $\boldsymbol{X}$ being the spatial variable and $\boldsymbol{Y}$ being the spatial integration variable. The illustrative example 6.6 on page 94 shows how to derive and use a Green function for a simple one-dimensional boundary value problem. For higher-dimensional problems and more complex geometries, a Green operator's construction in real space might be a challenging task. However, due to the way derivatives can be evaluated in Fourier space as described in Section 5.2, it is possible to construct explicit expressions for the Green operator under

periodic boundary conditions in Fourier space [16, 136, 173, 182, 205].

In order to use advanced solvers such as the conjugate gradient and Newton-Raphson methods, we need a linearized form of the Lippmann-Schwinger equation (6.9). Following GÉLÉBART & MONDON-CANCEL [54] and KABEL ET AL. [86] and using the incremental update $\boldsymbol{F}^{i+1} = \boldsymbol{F}^i + \Delta \boldsymbol{F}$, consistent linearization yields

$$\boldsymbol{F}^i - \overline{\boldsymbol{F}} - \boldsymbol{\Gamma}^0 * \left[\boldsymbol{T}^i - \mathbb{A}^0 : \boldsymbol{F}^i \right] + \mathbb{I} : \Delta \boldsymbol{F} - \boldsymbol{\Gamma}^0 * \left[(\mathbb{A}^i - \mathbb{A}^0) : \Delta \boldsymbol{F} \right] = \boldsymbol{0}. \qquad (6.11)$$

The latter *linear* equation can now be solved for $\Delta \boldsymbol{F}$ employing some iterative solver such as conjugate gradient or GMRES. Note that not only the choice of the solver influences the convergence speed of the iterative process, but also the choice of reference medium as discussed in SCHNEIDER [171].

6.2. Lippmann-Schwinger-based analytic macroscopic tangent operator

We now want to demonstrate an explicit procedure for computing the macroscopic tangent operator as presented in GÖKÜZÜM & KEIP [62]. Revisiting the expression (4.40) for the purely mechanical macroscopic tangent operator

$$\overline{\mathbb{A}} = \frac{1}{|\mathcal{B}|} \left[\int_{\mathcal{B}} \mathbb{A} \, dV + \int_{\mathcal{B}} \mathbb{A} : \frac{\partial \widetilde{\boldsymbol{F}}}{\partial \overline{\boldsymbol{F}}} \, dV \right], \qquad (6.12)$$

we see that in equilibrium, the microscopic moduli $\mathbb{A}$ can be obtained from the material law, whereas we need to still find a way to compute the fluctuation sensitivities $\partial \widetilde{\boldsymbol{F}} / \partial \overline{\boldsymbol{F}}$. Comparison of the Lippmann-Schwinger equation (6.9) with the micro-macro decomposition of the deformation gradient (4.5) and (4.28) reveals the explicit expression of the fluctuative deformation gradient in terms of the Green operator

$$\widetilde{\boldsymbol{F}} = \boldsymbol{\Gamma}^0 * \boldsymbol{\tau}^m(\boldsymbol{F}) = \boldsymbol{\Gamma}^0 * \left[\boldsymbol{T} - \mathbb{A}^0 : \boldsymbol{F} \right], \qquad (6.13)$$

where we used the definition of the perturbation field (6.6). With this expression at hand, differentiation with respect to the macroscopic deformation gradient $\overline{\boldsymbol{F}}$ is performed

$$\frac{\partial \widetilde{\boldsymbol{F}}}{\partial \overline{\boldsymbol{F}}} = \boldsymbol{\Gamma}^0 * \left[\frac{\partial \boldsymbol{T}}{\partial \boldsymbol{F}} : \frac{\partial \boldsymbol{F}}{\partial \overline{\boldsymbol{F}}} - \mathbb{A}^0 : \frac{\partial \boldsymbol{F}}{\partial \overline{\boldsymbol{F}}} \right], \qquad (6.14)$$

where we used the chain rule. Insertion of the decomposition of the deformation gradient (4.5) and (4.28) yields

$$\frac{\partial \widetilde{\boldsymbol{F}}}{\partial \overline{\boldsymbol{F}}} = \boldsymbol{\Gamma}^0 * \left[\frac{\partial \boldsymbol{T}}{\partial \boldsymbol{F}} : \frac{\partial (\overline{\boldsymbol{F}} + \widetilde{\boldsymbol{F}})}{\partial \overline{\boldsymbol{F}}} - \mathbb{A}^0 : \frac{\partial (\overline{\boldsymbol{F}} + \widetilde{\boldsymbol{F}})}{\partial \overline{\boldsymbol{F}}} \right]. \qquad (6.15)$$

Evaluating the derivatives finally gives a linear equation in terms of the fluctuation sensitivities

$$-\boldsymbol{\Gamma}^0 * \left[\mathbb{A} - \mathbb{A}^0 \right] = \boldsymbol{\Gamma}^0 * \left[(\mathbb{A} - \mathbb{A}^0) : \frac{\partial \widetilde{\boldsymbol{F}}}{\partial \overline{\boldsymbol{F}}} \right] - \frac{\partial \widetilde{\boldsymbol{F}}}{\partial \overline{\boldsymbol{F}}}, \qquad (6.16)$$

where we used the abbreviation $\mathbb{A} = \partial \boldsymbol{T} / \partial \boldsymbol{F}$. When using periodic boundary conditions, according to the procedure in Section 4.3.2, the volume integral of the periodic fluctuative deformation gradient $\widetilde{\boldsymbol{F}}$ vanishes. Consequently, the latter equation is solved under the constraint

$$\frac{1}{|\mathcal{B}|} \int_{\mathcal{B}} \frac{\partial \widetilde{\boldsymbol{F}}}{\partial \overline{\boldsymbol{F}}} \, dV = \boldsymbol{0}. \tag{6.17}$$

Equation (6.16) is an equation which needs to be solved for the $n_{dim} \times n_{dim} \times n_{dim} \times n_{dim}$ unknowns of the fourth-order tensor $\partial \widetilde{\boldsymbol{F}} / \partial \overline{\boldsymbol{F}}$, with n_{dim} being the spatial dimension. As the moduli $\mathbb{A}$ are the ones obtained at equilibrium, it can be easily computed in a post-processing step after the solution of the Lippmann-Schwinger equation (6.9) is found. Solving for the fluctuation derivatives is usually done utilizing a fixed-point or conjugate gradient method.

Memory efficient implementation. As demonstrated in [62], the problem (6.16) can be reduced to $n_{dim} \times n_{dim}$ problems of size $n_{dim} \times n_{dim}$, allowing to reuse the solver routines that were used for the equilibrium problem, see also MA & TRUSTER [116]. We therefore multiply Equation (6.16) with independent tensors $\boldsymbol{I}$ of size $n_{dim} \times n_{dim}$. For the two-dimensional case, these tensors appear as

$$\boldsymbol{I}_1 = \begin{bmatrix} 1 & 0 \\ 0 & 0 \end{bmatrix}, \quad \boldsymbol{I}_2 = \begin{bmatrix} 0 & 1 \\ 0 & 0 \end{bmatrix}, \quad \boldsymbol{I}_3 = \begin{bmatrix} 0 & 0 \\ 1 & 0 \end{bmatrix} \quad \text{and} \quad \boldsymbol{I}_4 = \begin{bmatrix} 0 & 0 \\ 0 & 1 \end{bmatrix}. \tag{6.18}$$

Multiplication of these independent tensors with Equation (6.16) yields four modified equations of the form

$$\boxed{\boldsymbol{\Xi}_i - \boldsymbol{\Gamma}^0 * [(\mathbb{A} - \mathbb{A}^0) : \boldsymbol{\Xi}_i] = -\boldsymbol{\Gamma}^0 * [(\mathbb{A} - \mathbb{A}^0) : \boldsymbol{I}_i] \quad \text{with} \quad i = 1, ..., n_{dim}} \tag{6.19}$$

which can be solved individually for the $n_{dim} \times n_{dim}$ entries of $\boldsymbol{\Xi}_i$. The components of the fourth-order fluctuation sensitivities can then be obtained from the relation

$$\boldsymbol{\Xi}_i = \frac{\partial \widetilde{\boldsymbol{F}}}{\partial \overline{\boldsymbol{F}}} : \boldsymbol{I}_i. \tag{6.20}$$

Lippmann-Schwinger-type implementation. The linear Equation (6.16) can be brought in a more familiar Lippmann-Schwinger-type form, allowing for a basic scheme in the sense of a fixed-point iteration. We therefore define a *sensitivity polarization tensor* as follows

$$\mathbb{T} = (\mathbb{A} - \mathbb{A}^0) : \frac{\partial \widetilde{\boldsymbol{F}}}{\partial \overline{\boldsymbol{F}}}. \tag{6.21}$$

Insertion of the latter equation into Equation (6.16) and rearrangement gives the Lippmann-Schwinger-type equation.

$$\boxed{\frac{\partial \widetilde{\boldsymbol{F}}}{\partial \overline{\boldsymbol{F}}} = \boldsymbol{\Gamma}^0 * [(\mathbb{A} - \mathbb{A}^0) + \mathbb{T}].} \tag{6.22}$$

6.3. Fourier discretization and solution approach

In the previous sections, we derived a theoretical framework for the solution of the deformation $\boldsymbol{F}$ in equilibrium equation through the linearized Lippmann-Schwinger equation (6.11) and the solution to the fluctuation sensitivities $\partial\widetilde{\boldsymbol{F}}/\partial\overline{\boldsymbol{F}}$ through the linear Lippmann-Schwinger-type equation (6.16). We now want to numerically find the solution to these fields employing the Fourier discretization introduced in Chapter 5. Accordingly, in the two-dimensional case, we discretize the *real reference space* by means of the discrete spatial coordinates

$$\boldsymbol{X}_{\alpha\beta} = \big\{(\alpha-1)\frac{L_1}{N_1}, (\beta-1)\frac{L_2}{N_2}\big\} \quad \text{with} \quad \alpha,\beta = 1, ..., N_{1,2}, \tag{6.23}$$

where α is the grid point index of a total of N_1 grid points in X_1-direction. Analogously, β is the grid point index of a total of N_2 grid points in X_2-direction. L_1 and L_2 are the spatial physical lengths in X_1- and X_2-direction of the problem domain. The corresponding quantity in Fourier space to the spatial coordinates are the truncated discrete *referential Fourier wave numbers* or *referential frequencies*

$$\boldsymbol{K}_{\alpha\beta} = \big\{(N_1-\alpha)\frac{1}{L_1}, (N_2-\beta)\frac{1}{L_2}\big\} \quad \text{with} \quad \alpha,\beta = 1, ..., N_{1,2}. \tag{6.24}$$

This is a further modification of the wave vector introduced in Chapter 5 and applies for domains that do not have unit lengths. Depending on the implementation of the fast Fourier transform, one has to additionally multiply the wave vector with 2π, as described in Chapter 5.

6.3.1. Construction of the discrete Green operator

With the Fourier discretization at hand, we now want to construct the discrete Green operator introduced in (6.9) in Fourier space, see also MOULINEC & SUQUET [136]. Let us, therefore, revisit the intermediate result (6.8) in index notation

$$[\mathbb{A}^0{}_a{}^B{}_c{}^D F^c{}_D]_{,B} = -\tau^m(\boldsymbol{F})_a{}^B{}_{,B}, \tag{6.25}$$

where the up-down indices follow the logic introduced in Chapter 2.2. Here, we assume to be at one specific grid point $\alpha,\beta = \alpha',\beta'$ for the evaluation of the divergence, which is why we dropped the grid indices α,β here and remained with the *spatial dimensional indices* a, B, c, D. Using the global Fourier approximation of Chapter 5, we can compute the derivatives according to Section 5.2 as follows

$$\begin{aligned}\mathbb{A}^0{}_a{}^B{}_c{}^D \widehat{F}^c{}_D \mathrm{i}K_B &= -\widehat{\tau}^m(\boldsymbol{F})_a{}^B \mathrm{i}K_B \quad &\text{for} \quad \boldsymbol{K} \neq \boldsymbol{0} \\ \widehat{F}^c{}_D &= \overline{F}^c{}_D \quad &\text{for} \quad \boldsymbol{K} = \boldsymbol{0}.\end{aligned} \tag{6.26}$$

As in Fourier space, the Fourier coefficient of the zeroth frequency is associated with the average. We can see from the decomposition (4.5) and (4.28) that all other Fourier coefficients are associated with the fluctuative contribution. We thus can state that the relation in real space

$$F^c{}_D = \widetilde{\varphi}(\boldsymbol{X})^c{}_{,D} \tag{6.27}$$

can be transformed into the Fourier representation

$$\widehat{F}^c{}_D = \widehat{\varphi}(\boldsymbol{X})^c{}_{,D} = \widehat{\varphi}(\boldsymbol{X})^c \, \mathrm{i} K_D \quad \text{for} \quad \boldsymbol{K} \neq \boldsymbol{0}. \tag{6.28}$$

Insertion of the latter equation into the equilibrium equation $(6.26)_1$ and relabeling summation indices allows for the representation

$$\widehat{\varphi}(\boldsymbol{X})^c = (\widehat{A}^{-1})^{ca} \mathrm{i} K_B \, \widehat{\tau}^m(\boldsymbol{F})_a{}^B \quad \text{with} \quad \widehat{A}_{ca} = \mathbb{A}^0{}_c{}^X{}_a{}^Y K_X K_Y, \tag{6.29}$$

Where $\widehat{\boldsymbol{A}}$ is often called the *acoustic tensor*. Finally, we can reinsert the latter equation into the deformation gradient in Fourier space (6.28), which along with $(6.26)_2$ gives the set of equations

$$\boxed{\begin{aligned} \widehat{F}^c{}_D = \widehat{\varphi}(\boldsymbol{X})^c{}_{,D} = -(\widehat{A}^{-1})^{ca} K_B K_D \, \widehat{\tau}^m(\boldsymbol{F})_a{}^B \quad &\text{for} \quad \boldsymbol{K} \neq \boldsymbol{0} \\ \widehat{F}^c{}_D = \overline{F}^c{}_D \qquad\qquad\qquad\qquad\qquad &\text{for} \quad \boldsymbol{K} = \boldsymbol{0}. \end{aligned}} \tag{6.30}$$

According to the convolution theorem, convolutions in real space become contractions in Fourier space. We thus see that the latter equation is the discrete Fourier counterpart to the Lippmann-Schwinger equation in real space (6.9). The Green operator in Fourier space can then be identified as

$$\begin{aligned} \widehat{\Gamma}^{0ca}{}_{BD} = -(\widehat{A}^{-1})^{ca} K_B K_D \quad &\text{for} \quad \boldsymbol{K} \neq \boldsymbol{0} \\ \widehat{\boldsymbol{\Gamma}}^0 = \boldsymbol{0} \qquad\qquad\qquad &\text{for} \quad \boldsymbol{K} = \boldsymbol{0}. \end{aligned} \tag{6.31}$$

The same Green operator can then be used in the solution of the linearized form (6.11) when using conjugate gradient solvers, for example. However, the constraint is then $\Delta\widehat{\boldsymbol{F}} = \boldsymbol{0}$ for $\boldsymbol{K} = \boldsymbol{0}$, as strictly speaking, we are solving for the incremental fluctuations $\Delta\widetilde{\boldsymbol{F}}$, which are zero on average according to the periodic boundary conditions and considerations made in Section 4.3.2.

6.3.2. Discrete solution scheme for primary variabels and fluctuation sensitivities

Having the Fourier discretization and the Green operator at hand, we want to solve the deformation gradient at equilibrium. We, therefore, assemble all deformation gradients at the grid points in a global matrix

$$\underline{\boldsymbol{F}} = \overset{N_{\alpha,\beta}}{\underset{\alpha,\beta=1}{\mathbf{A}}} \boldsymbol{F}_{\alpha\beta}, \tag{6.32}$$

which in two dimensions gives a global matrix of size $N_1 \times N_2 \times 4$. In analogy to the deformation, we assemble all quantities occurring in the fixed point scheme (6.9), i.e.

$$\underline{\boldsymbol{T}} = \overset{N_{\alpha,\beta}}{\underset{\alpha,\beta=1}{\mathbf{A}}} \boldsymbol{T}_{\alpha\beta}, \quad \underline{\mathbb{A}}^0 = \overset{N_{\alpha,\beta}}{\underset{\alpha,\beta=1}{\mathbf{A}}} \mathbb{A}^0_{\alpha\beta} \quad \text{and} \quad \underline{\widehat{\boldsymbol{\Gamma}}}^0 = \overset{N_{\alpha,\beta}}{\underset{\alpha,\beta=1}{\mathbf{A}}} \widehat{\Gamma}^0_{\alpha\beta}. \tag{6.33}$$

As the Fourier method presented here is a collocation method with no difference between nodal and integration points, the assembly procedure is different from the assembly performed within a finite element method. Here, the assembly simply denotes the gathering

of the individual nodal real and Fourier space quantities within one global array. With those assemblations at hand, updating the deformation gradient in terms of the fixed point iteration can be carried out in Fourier space according to

$$
\begin{aligned}
\underline{\widehat{\boldsymbol{F}}}_{i+1} &= \widehat{\boldsymbol{\Gamma}}^0 : \widehat{\boldsymbol{\tau}}(\underline{\widehat{\boldsymbol{F}}}) && \text{for} \quad \boldsymbol{K} \neq \boldsymbol{0} \\
\underline{\widehat{\boldsymbol{F}}}_{i+1} &= \overline{\underline{\boldsymbol{F}}}_{i+1} && \text{for} \quad \boldsymbol{K} = \boldsymbol{0},
\end{aligned}
\tag{6.34}
$$

where for the evaluation of $\boldsymbol{\tau}$ according to (6.6), an inverse Fourier transform on $\underline{\widehat{\boldsymbol{F}}}_{i+1}$ has to be performed for each iteration.

When using conjugate gradient-based solvers, one further has to assemble the additional quantities occurring in the linearized Lippmann-Schwinger form (6.11)

$$
\Delta \underline{\boldsymbol{F}} = \overset{N_{\alpha,\beta}}{\underset{\alpha,\,\beta\,=\,1}{\mathbf{A}}} \Delta \boldsymbol{F}_{\alpha\beta} \quad \text{and} \quad \underline{\mathbb{A}} = \overset{N_{\alpha,\beta}}{\underset{\alpha,\,\beta\,=\,1}{\mathbf{A}}} \mathbb{A}_{\alpha\beta}.
\tag{6.35}
$$

Having the assembled quantities, one can then apply a conjugate gradient method along with the constraint

$$
\begin{aligned}
\Delta \underline{\boldsymbol{F}}_{i+1} &= \text{cg}\{\underline{\mathbf{A}} \cdot \underline{\mathbf{x}}, \underline{\mathbf{b}}\} \\
\Delta \underline{\widehat{\boldsymbol{F}}}_{i+1} &= \boldsymbol{0} && \text{for} \quad \boldsymbol{K} = \boldsymbol{0},
\end{aligned}
\tag{6.36}
$$

where the matrix-vector multiplication $\underline{\mathbf{A}} \cdot \underline{\mathbf{x}}$ and the right-hand side $\underline{\mathbf{b}}$ are obtained from the Lippmann-Schwinger form (6.11) as

$$
\begin{aligned}
\underline{\mathbf{A}} \cdot \underline{\mathbf{x}} &= \mathbb{I} : \Delta \boldsymbol{F} + \text{fft}^{-1}\{-\widehat{\boldsymbol{\Gamma}}^0 : \text{fft}\{(\mathbb{A}^i - \mathbb{A}^0) : \Delta \boldsymbol{F}\}\} \\
\underline{\mathbf{b}} &= -\text{fft}^{-1}\{\boldsymbol{F}^i - \overline{\boldsymbol{F}} - \widehat{\boldsymbol{\Gamma}}^0 : \text{fft}\{\boldsymbol{T}^i - \mathbb{A}^0 : \boldsymbol{F}^i\}\}.
\end{aligned}
\tag{6.37}
$$

Note that it is sufficient to initializize $\Delta \underline{\widehat{\boldsymbol{F}}} = \boldsymbol{0}$ at $\boldsymbol{K} = \boldsymbol{0}$ once at the beginning of the solution scheme. The constraint $\Delta \underline{\widehat{\boldsymbol{F}}}_{i+1} = \boldsymbol{0}$ at $\boldsymbol{K} = \boldsymbol{0}$ is then automatically satisfied through the definition of the Green operator $\widehat{\boldsymbol{\Gamma}}^0 = \boldsymbol{0}$ at zeroth frequency at $\boldsymbol{K} = \boldsymbol{0}$, see Equation $(6.31)_2$. Thus, the zeroth-frequency entry of the incremental deformation gradient $\Delta \underline{\widehat{\boldsymbol{F}}}_{i+1}$ is not updated at all.

Having converged to an equilibrium state, one can proceed to use the solution of $\boldsymbol{F}$ to compute the fluctuation sensitivities, which we will pool at each grid point α, β in the tensor $\mathbb{F}_{\alpha\beta}$ as follows

$$
\mathbb{F}_{\alpha\beta} = \frac{\partial \widetilde{\boldsymbol{F}}_{\alpha\beta}}{\partial \overline{\boldsymbol{F}}_{\alpha\beta}}.
\tag{6.38}
$$

In two dimensions, the tensor has $2 \times 2 \times 2 \times 2$ independent entries, which can be written in Voigt notation as follows

$$
\underline{\mathbb{F}}_{\alpha\beta} = \begin{bmatrix}
\mathbb{F}_{\alpha\beta}{}^1_{11}{}^1 & \mathbb{F}_{\alpha\beta}{}^1_{12}{}^2 & \mathbb{F}_{\alpha\beta}{}^1_{11}{}^2 & \mathbb{F}_{\alpha\beta}{}^1_{12}{}^1 \\
\mathbb{F}_{\alpha\beta}{}^2_{21}{}^1 & \mathbb{F}_{\alpha\beta}{}^2_{22}{}^2 & \mathbb{F}_{\alpha\beta}{}^2_{21}{}^2 & \mathbb{F}_{\alpha\beta}{}^2_{22}{}^1 \\
\mathbb{F}_{\alpha\beta}{}^1_{21}{}^1 & \mathbb{F}_{\alpha\beta}{}^1_{22}{}^2 & \mathbb{F}_{\alpha\beta}{}^1_{21}{}^2 & \mathbb{F}_{\alpha\beta}{}^1_{22}{}^1 \\
\mathbb{F}_{\alpha\beta}{}^2_{11}{}^1 & \mathbb{F}_{\alpha\beta}{}^2_{12}{}^2 & \mathbb{F}_{\alpha\beta}{}^2_{11}{}^2 & \mathbb{F}_{\alpha\beta}{}^2_{12}{}^1
\end{bmatrix}.
\tag{6.39}
$$

In analogy to the previous assembling for the fields used in the solution of the equilibrium, we assemble a global $\underline{\mathbb{F}}$ from the individual grid points

$$
\underline{\mathbb{F}} = \overset{N_{\alpha,\beta}}{\underset{\alpha,\,\beta\,=\,1}{\mathbf{A}}} \mathbb{F}_{\alpha\beta}.
\tag{6.40}
$$

Having the assembled quantities *at equlibrium* at hand, we now can solve for the fluctuation sensitivities $\underline{\mathbb{F}}$ using the Lippmann-Schwinger-type fixed point form (6.22) as follows

$$
\begin{aligned}
\widehat{\underline{\mathbb{F}}}_{i+1} &= \widehat{\boldsymbol{\Gamma}}^0 : \mathrm{fft}\{(\underline{\mathbb{A}} - \underline{\mathbb{A}}^0) + \underline{\mathbb{T}}(\mathbb{F})\} &&\text{for}\quad \boldsymbol{K} \neq \boldsymbol{0} \\
\widehat{\underline{\mathbb{F}}}_{i+1} &= \boldsymbol{0} &&\text{for}\quad \boldsymbol{K} = \boldsymbol{0}.
\end{aligned}
\tag{6.41}
$$

After each iterative update, an inverse Fourier transform has to be carried out in order to evaluate $\underline{\mathbb{T}}(\mathbb{F})$ in real space.

In line with the solution scheme for the equilibrium equation, conjugate gradient methods might give a speedup in solving for the fluctuation sensitivities

$$
\mathbb{F}_{i+1} = \mathrm{cg}\{\underline{\mathbf{A}}' \cdot \underline{\mathbf{x}}', \underline{\mathbf{b}}'\}.
\tag{6.42}
$$

In contrast to the equilibrium equation, no linearization is needed and we are able to directly identify the matrix-vector multiplication $\underline{\mathbf{A}}' \cdot \underline{\mathbf{x}}'$ and the right hand side $\underline{\mathbf{b}}'$ from Equation (6.16) as follows

$$
\underline{\mathbf{A}}' \cdot \underline{\mathbf{x}}' = \mathrm{fft}^{-1}\{\hat{\underline{\boldsymbol{\Gamma}}}^0 \cdot \mathrm{fft}\{[\underline{\mathbb{A}} - \underline{\mathbb{A}}^0] \cdot \underline{\mathbb{F}}\}\} \quad\text{and}\quad \underline{\mathbf{b}}' = \mathrm{fft}^{-1}\{\hat{\underline{\boldsymbol{\Gamma}}}^0 \cdot \mathrm{fft}\{[\underline{\mathbb{A}} - \underline{\mathbb{A}}^0]\}\}.
\tag{6.43}
$$

It is again sufficient, to initialize $\widehat{\underline{\mathbb{F}}}_{i+1} = \boldsymbol{0}$ for $\boldsymbol{K} = \boldsymbol{0}$ once at the beginning of the solution scheme due to the way $\hat{\boldsymbol{\Gamma}}^0$ was defined in Equation $(6.31)_2$.

Having obtained the solution for $\underline{\mathbb{F}}$ by one of the methods described above, we can finally compute the *consistent macroscopic tangent operator* or *effective stiffness* according to

$$
\boxed{\overline{\mathbb{A}}^{algo} = \frac{1}{V}\left[\int_{\mathcal{B}} \mathbb{A}\, dV + \int_{\mathcal{B}} \mathbb{A} \cdot \mathbb{F}\, dV\right] = \frac{1}{V}\int_{\mathcal{B}} \mathbb{A} \cdot (\mathbb{I} + \mathbb{F})\, dV.}
\tag{6.44}
$$

In the following numerical examples, we will test the validity and robustness of the proposed method through various material models and multiscale simulations. We further compare the algorithmically consistent tangent and a tangent computed based on a finite difference approximation. For the latter, the macroscopic deformation gradient occurring in the non-linear Lippmann-Schwinger equation is perturbed by four independent tensors $\epsilon \boldsymbol{I}_i$. We then solve the Lippmann-Schwinger equation for the perturbed deformation gradient $\boldsymbol{F}'_i$ according to

$$
\boldsymbol{F}'_i - \boldsymbol{\Gamma}^0 * [\boldsymbol{T}(\boldsymbol{F}'_i) - \mathbb{A}^0 : \boldsymbol{F}'_i] = \overline{\boldsymbol{F}} + \epsilon\,\boldsymbol{I}_i,
\tag{6.45}
$$

where $\boldsymbol{I}_i$ can be taken from Equation (6.18) and ϵ is the perturbation magnitude, usually chosen to be in between 10^{-6} and 10^{-8}. The individual entries of the finite difference-based macroscopic stiffness matrix $\overline{\mathbb{A}}^{fd}$ can then be computed from the difference to the perturbed macroscopic stress according to the following equation

$$
\Delta\overline{\boldsymbol{T}}_i = \frac{1}{V}\int_{\mathcal{B}} [\boldsymbol{T}(\boldsymbol{F}'_i) - \boldsymbol{T}(\boldsymbol{F})]dV = \overline{\mathbb{A}}^{fd} : \epsilon\,\boldsymbol{I}_i.
\tag{6.46}
$$

Here, $\boldsymbol{F}$ is the deformation gradient field of the non-perturbed equilibrium state and thus $\boldsymbol{T}(\boldsymbol{F})$ remains constant for all perturbations.

The major differences of using Equation (6.16) compared to finite difference-based approaches are as follows:

1. The consistent analytic approach always leads to a set of linear equations. This is of great advantage, especially for material or geometrical non-linear models, where a finite difference-based approach demands the solution of a perturbed non-linear state.

2. As the consistent analytic approach from Equation (6.16) is linear, it can be solved up to machine accuracy, whereas a finite difference-based approach for non-linear models contains an additional error due to the derivative approximation.

3. When storing the fluctuation sensitivities of the last load step, one can use them in the next load step as initial values for the computation of the current fluctuation sensitivities. In specific load cases where there is no change in the tangent, this approach saves time, as the finite difference approximation is always associated with a certain amount of computational effort.

4. Compared with a finite difference-based approach, the values for the moduli need to be stored, resulting in a higher memory storage demand.

6.4. FE-FFT driver for macroscopically homogeneous point problems

In a classical multiscale simulation, one usually considers an FE-discretized boundary value problem on the macroscale and an FE- or Fourier-discretized periodic boundary value problem on the microscale. The macroscopic boundary value problem's convergence is guaranteed through the variationally consistent computation of macroscopically effective properties on the microscale, as outlined in Chapter 4. However, it is sufficient to consider one homogeneous macroscopic point for testing such convergence properties, where prescribed macroscopic stresses and strains drive the microscopic problem at said point. In this chapter, we outline the construction of a driver routine which allows for the convergence analysis of such problems as described in ZÄH [209].
The framework presented in this work so far covers the prescription of macroscopic strains. If we want to prescribe macroscopic stresses however, we need to either apply mixed boundary conditions as presented in MOULINEC & SUQUET [137], see also KABEL ET AL. [87], or use a macroscopic Newton iteration. For the latter case, we imagine that we would like to prescribe the macroscopic stretches $\overline{F}^1{}_1$ and $\overline{F}^2{}_1$ and the macroscopic equilibrated stress components $\overline{T}^{\#}{}_1{}^2$ and $\overline{T}^{\#}{}_2{}^2$. Then, the macroscopic vector of unknowns at a homogenized macroscopic point for a two-dimensional problem would appear as

$$\overline{U} = [\overline{T}_1{}^1 \overline{F}^2{}_2 \overline{F}^1{}_2 \overline{T}_2{}^1]^T, \tag{6.47}$$

i.e., if we prescribe a macroscopic strain component, the unknown quantity is the macroscopic stress component and vice versa. Let us now denote the macroscopic stress at equilibrium as

$$\overline{T}^{\#} = [\overline{T}^{\#}{}_1{}^1 \overline{T}^{\#}{}_2{}^2 \overline{T}^{\#}{}_1{}^2 \overline{T}^{\#}{}_2{}^1]. \tag{6.48}$$

If we now want to drive macroscopic stresses, which should, in general, be equilibrated, then the difference between the equilibrated stress $\overline{T}^{\#}$ we want to prescribe and the actual

homogenized stress at some applied macroscopic deformation state $\overline{\boldsymbol{F}}(\overline{\boldsymbol{U}})$ is given as

$$\overline{\boldsymbol{R}}(\overline{\boldsymbol{U}}) = \overline{\boldsymbol{T}}(\overline{\boldsymbol{F}}(\overline{\boldsymbol{U}})) - \overline{\boldsymbol{T}}^{\#}(\overline{\boldsymbol{U}}) = \boldsymbol{0} \tag{6.49}$$

and should vanish when we reach a macroscopic deformation state that generates our desired equilibrium stress (6.48). The latter expression thus serves as our macroscopic homogenized residuum. To use a Newton-Raphson scheme for the solution of the macroscopic deformation state, we linearize said residuum according to

$$\text{Lin}\,\overline{\boldsymbol{R}} = \overline{\boldsymbol{R}}_i + \left.\frac{d\overline{\boldsymbol{R}}}{d\overline{\boldsymbol{U}}}\right|_i \Delta\overline{\boldsymbol{U}}_{i+1} = \boldsymbol{0}, \tag{6.50}$$

where the differentiation of the residuum with respect to the vector of unknowns is denoted as driver's macroscopic tangent and can be expressed as follows

$$\overline{\mathbb{A}}^{driver} = \frac{d\overline{\boldsymbol{R}}}{d\overline{\boldsymbol{U}}} = \frac{d}{d\overline{\boldsymbol{U}}}\left[\overline{\boldsymbol{T}}(\overline{\boldsymbol{F}}(\overline{\boldsymbol{U}})) - \overline{\boldsymbol{T}}^{\#}(\overline{\boldsymbol{U}})\right] = \partial_{\overline{\boldsymbol{F}}}\overline{\boldsymbol{T}}\,\partial_{\overline{\boldsymbol{U}}}\overline{\boldsymbol{F}} - \partial_{\overline{\boldsymbol{U}}}\overline{\boldsymbol{T}}^{\#}. \tag{6.51}$$

Here we identfiy the macroscopic effective stiffness $\overline{\mathbb{A}}^{algo} = \partial_{\overline{\boldsymbol{F}}}\overline{\boldsymbol{T}}$ as defined in Equations (4.35) and (4.40), which allows for the more compact notation of the driver's macroscopic tangent

$$\overline{\mathbb{A}}^{driver} = \overline{\mathbb{A}}^{algo}\,\partial_{\overline{\boldsymbol{U}}}\overline{\boldsymbol{F}} - \partial_{\overline{\boldsymbol{U}}}\overline{\boldsymbol{T}}^{\#}. \tag{6.52}$$

The partial derivatives remaining in the latter equation would form diagonal matrices

$$\partial_{\overline{\boldsymbol{U}}}\overline{\boldsymbol{F}} = \text{diag}[\alpha_1, \alpha_2, ..., \alpha_n] \quad \text{and} \quad \partial_{\overline{\boldsymbol{U}}}\overline{\boldsymbol{T}}^{\#} = \text{diag}[\beta_1, \beta_2, ..., \beta_n] \tag{6.53}$$

where there are zeros or ones on the diagonal entries depending on whether $\overline{\boldsymbol{F}}$ or $\overline{\boldsymbol{T}}^{\#}$ is prescribed. In our example with the vector of unknowns according to (6.47), these diagonal matrices would have the following entries

$$\partial_{\overline{\boldsymbol{U}}}\overline{\boldsymbol{F}} = \text{diag}[0, 1, 1, 0] \quad \text{and} \quad \partial_{\overline{\boldsymbol{U}}}\overline{\boldsymbol{T}}^{\#} = \text{diag}[1, 0, 0, 1]. \tag{6.54}$$

Insertion of the latter equation into the driver's macroscopic tangent (6.52) gives the explicit expression in Voigt notation

$$\overline{\mathbb{A}}^{driver} = \begin{bmatrix} -1 & \overline{\mathbb{A}}^{algo\ 1\ 2}_{\quad 1\ 2} & \overline{\mathbb{A}}^{algo\ 1\ 2}_{\quad 1\ 1} & 0 \\ 0 & \overline{\mathbb{A}}^{algo\ 2\ 2}_{\quad 2\ 2} & \overline{\mathbb{A}}^{algo\ 2\ 2}_{\quad 2\ 1} & 0 \\ 0 & \overline{\mathbb{A}}^{algo\ 2\ 2}_{\quad 1\ 2} & \overline{\mathbb{A}}^{algo\ 2\ 2}_{\quad 1\ 1} & 0 \\ 0 & \overline{\mathbb{A}}^{algo\ 1\ 2}_{\quad 2\ 2} & \overline{\mathbb{A}}^{algo\ 1\ 2}_{\quad 2\ 1} & -1 \end{bmatrix} \tag{6.55}$$

in terms of the components of the homogenized macroscopic tangent operator $\mathbb{A}$. The update of the vector of unknowns can then be updated according to

$$\boxed{\Delta\overline{\boldsymbol{U}}_{i+1} = -(\overline{\mathbb{A}}^{driver})_i^{-1}\overline{\boldsymbol{R}}_i,} \tag{6.56}$$

where the final macroscopic strains for the prescribed stresses are obtained, when the residual norm reaches an appropriate tolerance. From the structure of the driver's macroscopic tangent (6.55), we see that the stretches which are actively prescribed are not

updated, such as $\overline{F}^1{}_1$ and $\overline{F}^2{}_1$ in our example, whereas the stretches $\overline{F}^1{}_2$ and $\overline{F}^2{}_2$ which are prescribed for finding the desired macroscopic equilibrium stresses $\overline{T}^{\#}{}_1{}^2$ and $\overline{T}^{\#}{}_2{}^2$ are updated until convergence. The norm of the residuum can be taken as an indicator for macroscopic convergence and thus for the validity of the homogenized macroscopic tangent operator $\overline{\mathbb{A}}^{algo}$ used for computing $\overline{\mathbb{A}}^{driver}$, as done in the following Numerical Examples 6.5.

6.5. Numerical examples

In the following, we will investigate the performance of the presented method for computing the macroscopic tangent operator. This is done for different material models and multiscale simulations, where the macroscopic problem is either a plate with a hole or a macroscopic point problem with prescribed stretches or stresses as computed through the driver routine as described in chapter 6.4, see also ZÄH [209] and VALLICOTTI [194]. The microscopic boundary value problem is modeled through a periodic RVE. The material models used are a small-strain viscoelastic model and a geometrically non-linear Neo-Hookean hyperelastic model. Note that in this section, we always compute results based on a Cartesian coordinate system in Euclidean space and thus the up-down indexing is dropped in this section.

6.5.1. Homogenization approach for small-strain viscoelastic material behavior

In this example, we demonstrate the method's validity based on the non-linear material behavior of small-strain viscoelasticity. We, therefore, consider the viscoelastic energy-density function

$$\psi(\boldsymbol{\varepsilon}, \boldsymbol{\alpha}) = \frac{1}{2}\kappa(\operatorname{tr}\boldsymbol{\varepsilon})^2 + \mu \operatorname{tr}[(\boldsymbol{\varepsilon}' - \boldsymbol{\alpha})^2] + \mu_0 \operatorname{tr}[(\boldsymbol{\varepsilon}')^2], \tag{6.57}$$

where κ is the bulk modulus, μ the shear modulus and μ_0 the ground shear modulus. Here, $\boldsymbol{\varepsilon}' = \operatorname{dev}\boldsymbol{\varepsilon}$ is the deviatoric part of the symmetric elastic strain tensor $\boldsymbol{\varepsilon} = \nabla^s \boldsymbol{u}$ and the internal variable α is the viscous strain. The dissipation potential governs the time dependence of the material response

$$\mathfrak{d} = \frac{1}{2}\hat{\eta}\,||\dot{\boldsymbol{\alpha}}||^2, \tag{6.58}$$

where $\hat{\eta}$ is a viscosity parameter. The stresses can then be computed as according to (3.71)

$$\boldsymbol{\sigma} = \partial_{\boldsymbol{\varepsilon}}\psi = \kappa \operatorname{tr}\boldsymbol{\varepsilon}\,\mathbf{1} + 2\mu(\boldsymbol{\varepsilon}' - \boldsymbol{\alpha}) + 2\mu_0\boldsymbol{\varepsilon}', \tag{6.59}$$

In line with Biot's equation (3.81), the evolution equation for the viscous strain can be computed from the energy density and the dissipation potential in the following form

$$\dot{\boldsymbol{\alpha}} = \frac{2\mu}{\hat{\eta}}(\boldsymbol{\varepsilon}' - \boldsymbol{\alpha}). \tag{6.60}$$

For the evaluation of the derivatives, we use a time-discrete implicit backward Euler scheme

$$\boldsymbol{\alpha}_{n+1} = \boldsymbol{\alpha}_n + \Delta t\,\dot{\boldsymbol{\alpha}}_{n+1}. \tag{6.61}$$
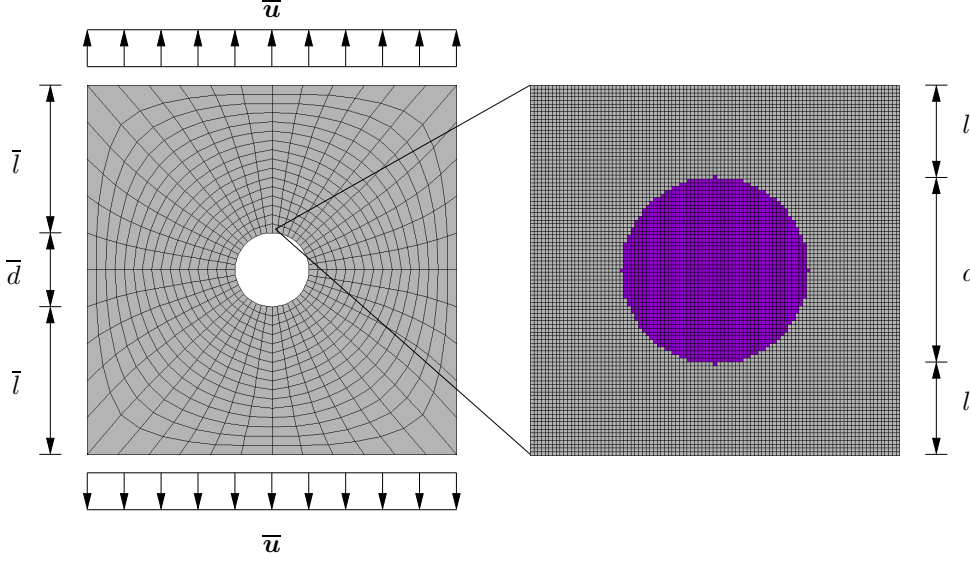
Figure 6.1: Boundary problem at macro- and microscale. To the left, the macroscopic boundary is a square plate of side length 1m with a hole of diameter $\overline{d}$ =0.2m. It is vertically stretched by $\overline{u}_2$ =0.05m and then held constant to see the material's relaxation behavior. To the left, the microstructure is modeled through a square RVE of side length 1mm. It consists of soft matrix material and a stiff circular inclusion of diameter d =0.5mm.

Insertion of the evolution equation (6.60) into the latter time discrete form gives

$$\boldsymbol{\alpha}_{n+1} = \frac{\alpha_n + \Delta t/\tau \boldsymbol{\varepsilon}'_{n+1}}{1 + \Delta t/\tau}, \tag{6.62}$$

where we used the abbreviation $\tau = \eta/2\mu$. Plugging the latter equation into the expression for the viscous stresses (6.59) yields the discrete form

$$\boldsymbol{\sigma}_{n+1} = \kappa \operatorname{tr} \boldsymbol{\varepsilon}_{n+1} \, \mathbf{1} + 2\mu(\boldsymbol{\varepsilon}'_{n+1} - \frac{\alpha_n + \Delta t/\tau \boldsymbol{\varepsilon}'_{n+1}}{1 + \Delta t/\tau}) + 2\mu_0 \boldsymbol{\varepsilon}'_{n+1}. \tag{6.63}$$

Finally, we need an expression for the viscous moduli in order to solve Equation (6.16) for the fluctuation derivatives. Differentiating the latter equation with respect to the current strains $\boldsymbol{\varepsilon}_{n+1}$, we obtain the explicit expression for the moduli

$$\mathbb{A}_{n+1} = \frac{\partial \boldsymbol{\sigma}_{n+1}}{\partial \boldsymbol{\varepsilon}_{n+1}} = \kappa \mathbf{1} \otimes \mathbf{1} + \left[\frac{2\mu}{1 + \Delta t/\tau} + 2\mu_0 \right] \mathbb{P}, \tag{6.64}$$

which gives us everything at hand to perform our numerical computations.

Two-scale FE-FFT simulation for small-strain viscoelastic material behavior.
We now consider a multiscale boundary value problem as depicted in Figure 6.1. On the macroscopic scale, a square plate of overall length 1m with a hole of diameter $\overline{d}$ =0.2m is stretched by $\overline{u}_2$ =0.05m into the vertical direction. The plate can move freely in the horizontal direction and is only fixed at one point in the vertical direction to avoid rotations. Due to the symmetry of the problem, only one quarter of the plate is discretized by 176 quadrilateral finite elements with four Gauss points each. At each Gauss point, the material response is computed using the RVE shown to the right of Figure 6.1. The RVE of side length 1mm consists of soft matrix material and a stiff circular inclusion of
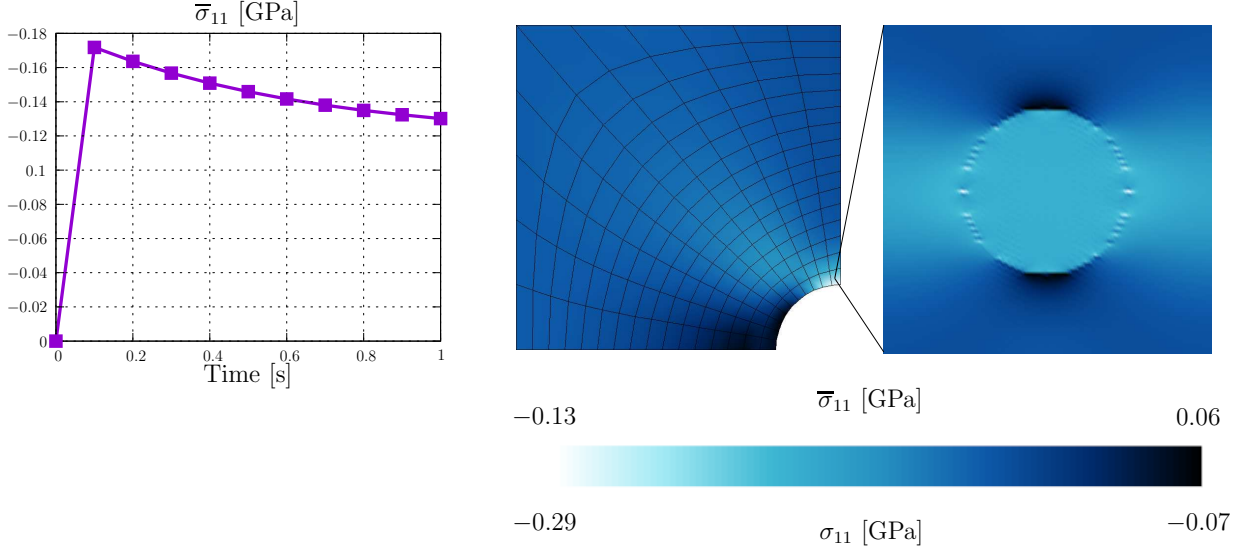
Figure 6.2: To the left, the increase and relaxation of the macroscopic stress component $\overline{\sigma}_{11}$ at the Gauss point during the loading process is depicted. To the right, one can see one quarter of the macroscopic plate with a hole and the macroscopic stress distribution $\overline{\sigma}_{11}$. The microscopic RVE has stress concentrations $\overline{\sigma}_{11}$ at the interfaces, where the absolute of the maximum compressing stress in the RVE is more than two times higher than the macroscopically observable stress.

diameter $d =$ 0.5mm. The microstructure is discretized by 101×101 grid points and will be solved by means of an FFT method.

The material parameters in the constitutive model (6.59) are chosen as $\lambda^{matr} = 2$GPa, $\lambda^{incl} = 10$GPa, $\mu^{matr} = 1$GPa, $\mu^{incl} = 5$GPa, $\widehat{\eta}^{matr} = 1$GPas and $\widehat{\eta}^{incl} = 0.5$GPas. It thus follows that $\kappa^{matr} = \lambda^{matr} + \frac{2}{3}\mu^{matr} = 2.66$GPa and $\kappa^{incl} = \lambda^{incl} + \frac{2}{3}\mu^{incl} = 13.33$GPa. The macroscopic displacement $\overline{u}_2 = 0.05$m is applied in one load step over 0.1 seconds and held constant. Figure 6.2 shows the loading and relaxation of one Gauss point at the macroscale as computed from the microscopic homogenization procedure. One can see that the stresses are decreasing asymptotically over time as the material is viscously deforming. To the right, the macroscopic stress $\overline{\sigma}_{11}$ in GPa for a quarter of the plate is shown, and for one Gauss point, the microscopic stress σ_{11}. Stronger compressing stresses are occurring at the Gauss point due to the boundary value problem's macroscopic geometry. Averaging over the full-field solution of the microscopic stresses in the RVE gives the macroscopic stresses. However, note how the magnitude of the maximum compressive stress in the RVE is more than two times higher than the macroscopically observable stress due to the microstructure's geometry. This is often observed in multiscale simulations and needs to be considered, especially if it comes to the choice between small- and large-strain formulations.

Algorithmic tangent computation in comparison to finite difference-based approach. We now want to compare the performance of the algorithmic tangent computation (6.16) compared with a finite difference-based approach (7.46). We will compare the computational time as well as the error

$$\zeta = \frac{||\overline{\mathbb{A}}^{fd} - \overline{\mathbb{A}}^{algo}||}{||\overline{\mathbb{A}}^{algo}||}, \tag{6.65}$$
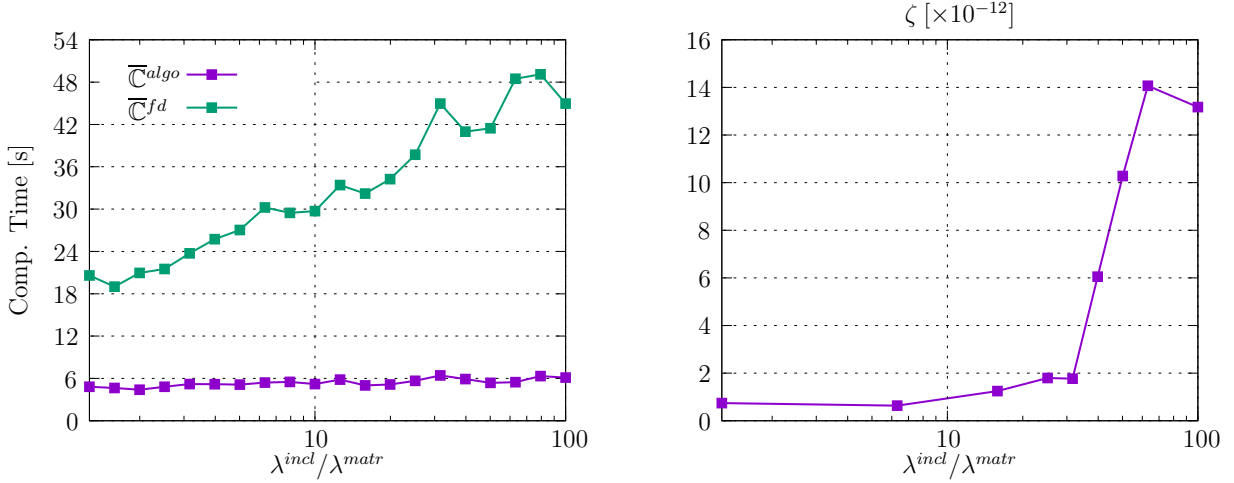
Figure 6.3: To the left, one can see a runtime comparison between the finite difference-based and the algorithmic tangent computation. One can see that the algorithmic tangent is much faster, especially for high phase contrasts in this model. To the right, the error ζ between the two tangent computations is shown. One can see that the error is of low order 10^{-11}, and thus, both tangents provide accurate macroscopic convergence.

and we will shortly discuss memory storage demands. In the RVE, we consider the same microstructure as depicted in the right of Figure 6.1 whereas we only take one point on the macroscale to drive stresses and strains. The RVE is discretized by 101×101 grid points. For both, the linearized equilibrium equation (6.11) and the Lippmann-Schwinger type equation for the fluctuation derivatives (6.16), we use a conjugate gradient solver with a tolerance of $\text{tol}^{cg} = 10^{-12}$. For the Newton-Raphson method, we follow GÉLÉBART & MONDON-CANCEL [54], KABEL ET AL. [86] and EISENLOHR ET AL. [41] and set $\text{tol}^{nr} = 10^{-7}$. In order to investigate micro-macro convergence, we use the FE-FFT driver as described in Section 6.4, see also [209]. Here, we prescribe macroscopic shear stresses $\overline{\sigma}_{12}$ and $\overline{\sigma}_{21}$ which are increased to 0.1GPa within one load step. The normal stresses are kept zero $\overline{\sigma}_{11} = \overline{\sigma}_{22} = 0$. The stresses are then held constant and the RVE relaxes within $t = 3$ seconds, where we used the time increment $\Delta t = 0.1$ seconds for our computation. The material parameters appearing in the viscoelastic material model (6.59) are chosen as $\lambda^{matr} = 1\text{GPa}$, $\lambda^{incl} = 1\text{GPa}$, $\mu^{matr} = 1\text{GPa}$, $\mu^{incl} = 0.5\text{GPa}$, $\widehat{\eta}^{matr} = 1\text{GPas}$ and $\widehat{\eta}^{incl} = 0.5\text{GPas}$. The phase contrast is then gradually increased by increasing the values for λ^{incl} up to 100GPa.

Figure 6.3 shows the comparison of computational time for the algorithmic computation and the finite difference-based approach for the whole loading procedure as well as the difference of the two tangents as defined by (6.65). Here, the error ζ is computed as the average of the errors of tangents at each of the 30 time steps. One can see that the computational speed of the algorithmic approach is superior to the finite difference-based approach. One possible reason for the large difference between the two methods might be, that the viscous strains are asymptotically approaching zero during the relaxation process, and thus the macroscopic tangent is hardly changing at the end of the loading process. As we load the fluctuation sensitivities of the last load step as initial values for solving the equilibrium of the next load step, the initial guess is already close to the solution and thus little iterations are needed. In contrast, the finite difference-based approach always demands a minimum amount of computational effort according to the perturbation magnitude. Additionally, for the finite difference-based approach, a *nonlin-*

ear viscoelastic perturbed state needs to be solved in order to find the correct tangent, whereas the algorithmic approach only needs the solution of a linear equation. In contrast to a finite difference-based approach, the memory demand of the algorithmic computation is increased as the moduli at equilibrium must be stored for the solution of (6.16). Analyzing the difference between the finite difference-based and the algorithmic tangent on the right of Figure 6.3, we see that the maximum error is of the order 10^{-11}. The convergence at the macroscale is thus for both methods assured.

6.5.2. Homogenization approach at finite strains

As shown in Numerical Example 6.5.1, strains occurring on the microscale might be much larger compared with strains applied on the macroscale. The framework is therefore tested for geometrical non-linearity. We will consider a large strain elastic energy density, namely the Neo-Hookean material model

$$\psi(\boldsymbol{F}) = \frac{\mu}{2}[\text{tr}(\boldsymbol{F}^T \cdot \boldsymbol{F}) - 3] + \frac{\mu}{\beta}[(\det \boldsymbol{F})^{-\beta} - 1], \qquad (6.66)$$

in terms of the deformation gradient and where the material parameter β can be computed from Poisson's ratio ν as follows

$$\beta = \frac{2\nu}{1 - 2\nu}. \qquad (6.67)$$

For the FE method as well as for the FFT-based solution scheme, the stress can be derived from the energy density function according to

$$\boldsymbol{T} = \partial_{\boldsymbol{F}}\psi = \mu\boldsymbol{F} - \mu(\det \boldsymbol{F})^{-\beta}\boldsymbol{F}^{-T}, \qquad (6.68)$$

while the mechanical stiffness in index notation is obtained from the second differentiation

$$\mathbb{A}_{ijkl} = \partial^2_{\boldsymbol{F}_{ij}\boldsymbol{F}_{kl}}\psi = \mu\delta_{ik}\delta_{jl} + \mu\beta(\det \boldsymbol{F})^{-\beta}F^{-1}_{lk}F^{-1}_{ji} + \mu(\det \boldsymbol{F})^{-\beta}F^{-1}_{jk}F^{-1}_{li}. \qquad (6.69)$$

As we assume a Euclidean space and Cartesian coordinates, the up-down index notation is dropped.

Two-dimensional multiscale simulation at finite strains. The boundary value problem for the large strain simulation at hand is identical to the previous one shown in Figure 6.1. However, the plate is now stretched vertically in both directions by $\overline{u} = 0.5m$ within 10 load steps and the material parameters for the Neo-Hookean (6.66) material model are chosen as $\mu^{matr} = 2\text{GPa}$, $\beta^{matr} = 1$, $\mu^{incl} = 4\text{GPa}$ and $\beta^{incl} = 2$.

Figure 6.4 shows the results for the macroscopic first Piola-Kirchhoff stress component $\overline{T}_{11}$ in the plate with hole and the results for the macroscopic first Piola-Kirchhoff stress component T_{11} in the RVE. One can see a large deformation of the plate with hole. Peaks in compressive and tensile stresses are occurring at the boundaries of the hole. The microscopic RVE is deforming according to the macroscale. However, we again see stresses on the microscale exceeding the macroscopic stresses by far. There are oscillations on the microscale at the interface of the stiff inclusion. This might be caused by the circular inclusion's voxel discretization, which leads to many edges along the interface.

To validate the consistency of the macroscopic tangent computation, we further analyze the convergence properties of the macroscopic Newton-Raphson scheme. Figure 6.5
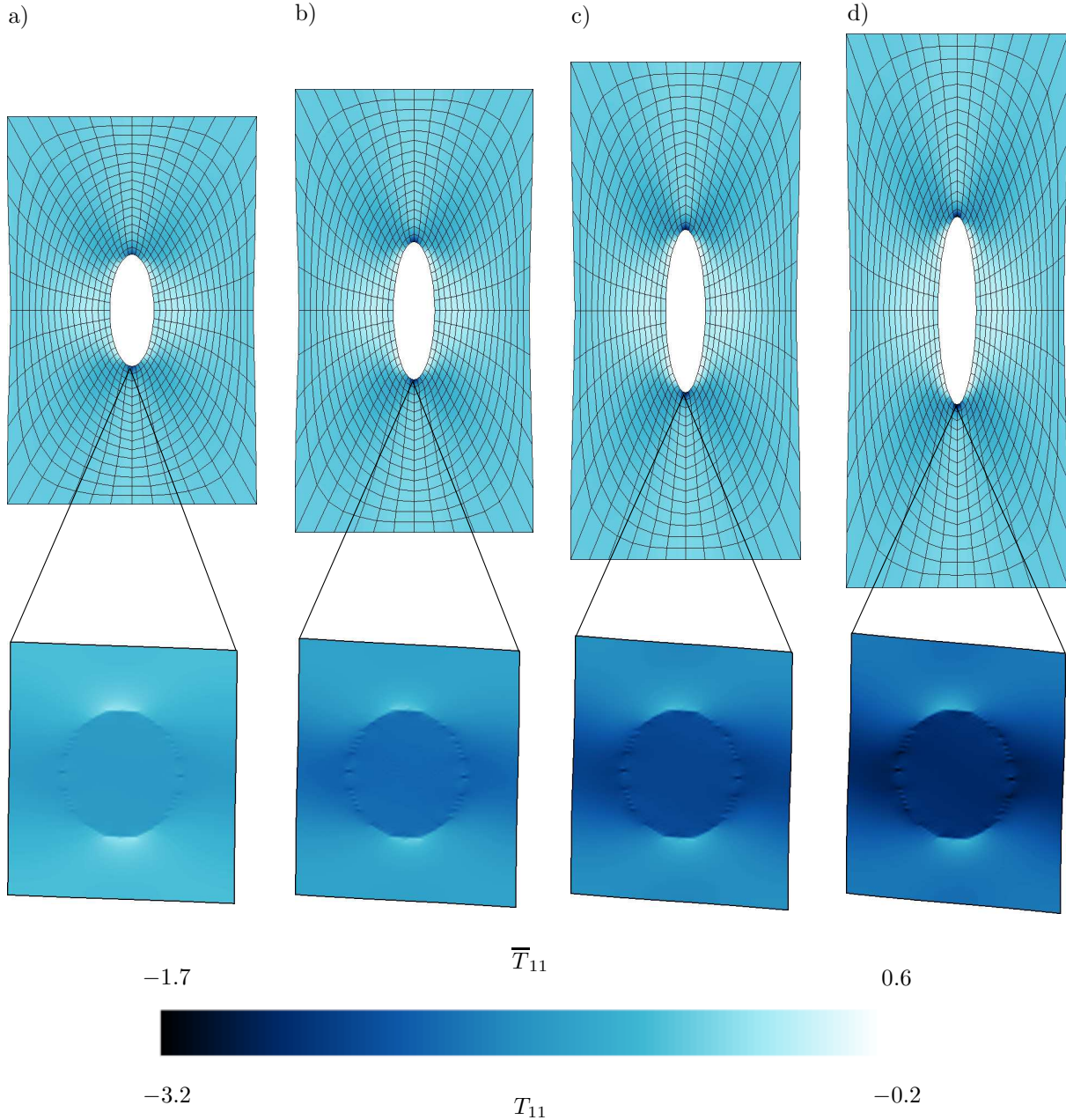
Figure 6.4: A macroscopic disk with a hole at applied load of a) 0.2m, b) 0.3m, c) 0.4m, and d) 0.5m. The macroscopic stress component $\overline{T}_{11}$ has its peaks at the boundary of the circular hole. On the bottom, the microscopic RVE of one Gauss point at the corresponding loads are visualized. Again, we see that the microscopic stresses T_{11} are much larger than the macroscopic ones.

shows the macroscopic residuals of the Newton-Raphson method as computed by the finite element program *FEAP* [188]. In the vicinity of the solution, the macroscopic Newton-Raphson scheme exhibits quadratic convergence even at large loads. We thus see that the algorithmic tangent complies with the macroscopic variational principle and thus can be used for geometrical and material nonlinearities.

Three-dimensional microstructure with random spheres. We now want to demonstrate that the framework can be easily carried over to three-dimensional problems. We,
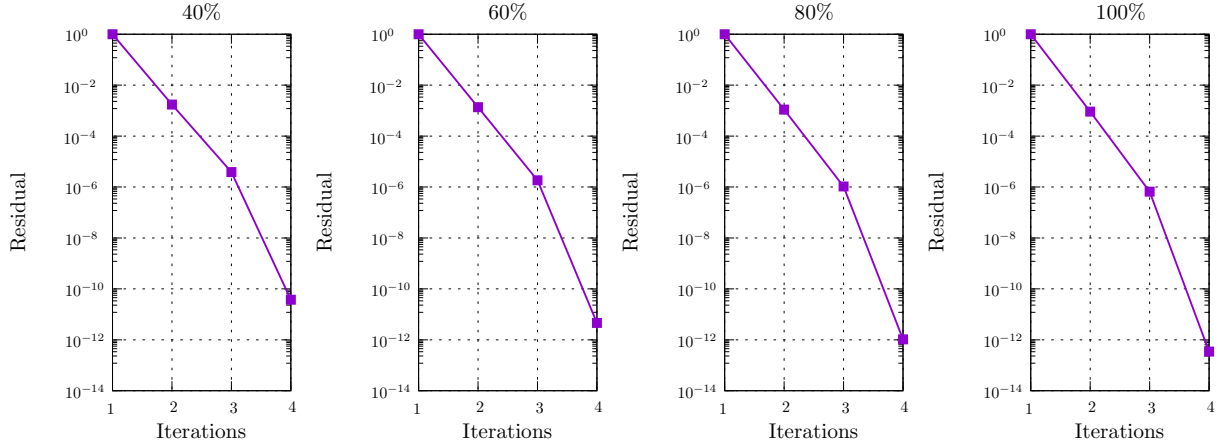
Figure 6.5: Macroscopic relative residual at 40%, 60%, 80%, and 100% load as calculated by the finite element program *FEAP* [188]. One sees that in the vicinity of the solution, the macroscopic solver shows quadratic convergence, validating the correctness of the algorithmic tangent approach even at large strains.
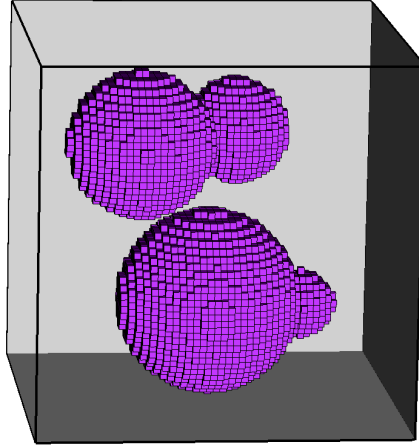

Figure 6.6: An RVE of side length $l = 1mm$ is considered. It consists of soft matrix material and randomly distributed stiff spherical inclusions of different sizes.

therefore, consider a microstructure consisting of soft matrix material and randomly distributed stiff spherical inclusions of different size as depicted in Figure 6.6. The RVE is discretized by $51{\times}51{\times}51$ equidistant grid points. The tolerance for the conjugate gradient solver for the linearized problem is $\text{tol}^{cg}=10^{-12}$ while the tolerance for the Newton-Raphson solver is $\text{tol}^{nr}=10^{-8}$. We now compute the equilibrium state for a strain driven shear deformation of the RVE. We, therefore, increase all shear stretches F_{ij} with $i \neq j$ up to 20% within 10 load steps while the normal strains are kept zero. The material parameters of the Neo-Hookean material models for the matrix are chosen as $\mu^{matr}{=}2$ GPa and $\beta^{matr}{=}2$ and for the inclusion as $\mu^{matr}{=}60$ GPa and $\beta^{matr}{=}3$.

Figure 6.7 shows the shear deformation of the RVE and the contour plots of the first Piola-Kirchhoff stress component T_{12}. The top contour plots show the stresses at the periodic boundary surfaces of the RVE at 12%, 16%, and 20% load. The bottom plots show a cut into the RVE where stress concentrations at the phase interfaces become visible. Finally, we want to compare the consistent tangent computation's runtimes against a finite difference-based approach for the three-dimensional case. We therefore equally
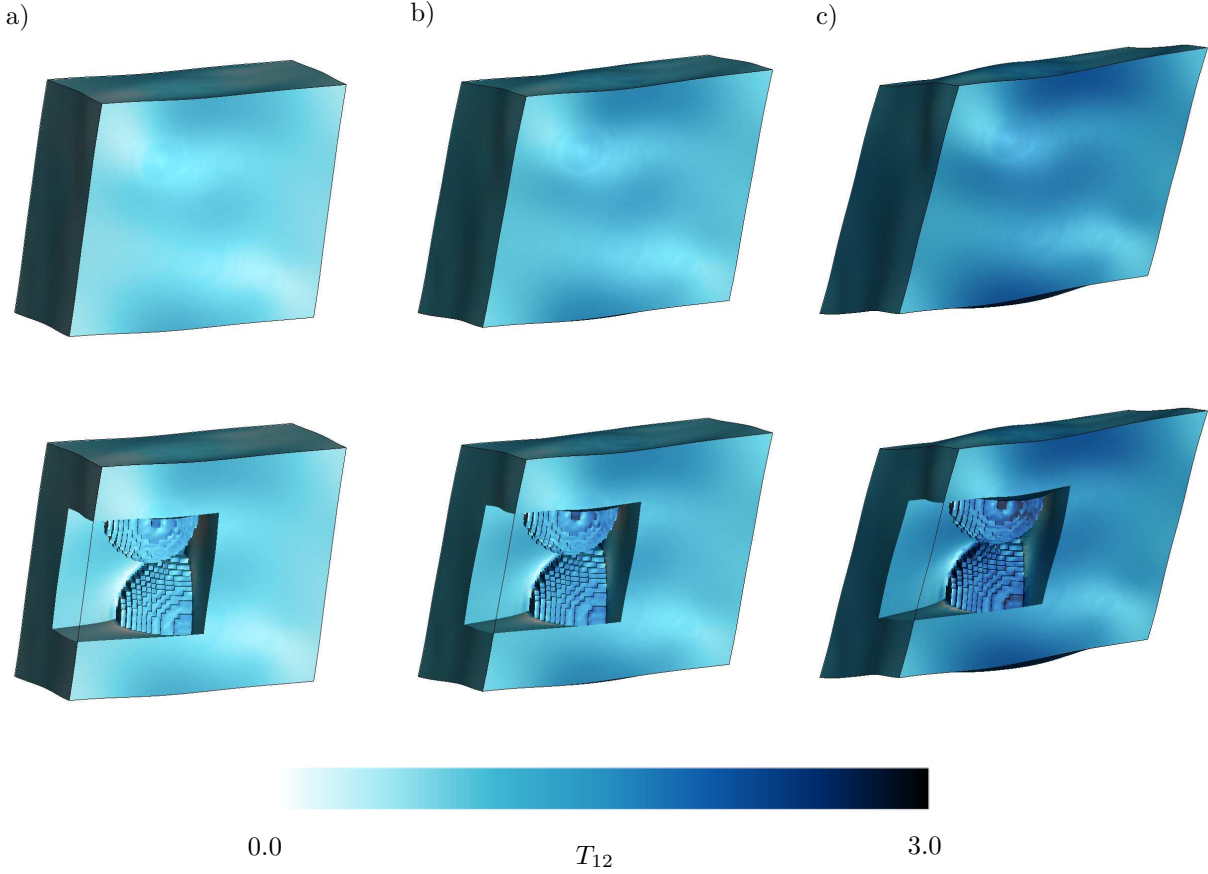
a)   b)   c)

Figure 6.7: Contour plot for first Piola-Kirchhoff stress component T_{12} at a) 12%, b) 16%, and c) 20% load. A cut into the RVE, as shown on the bottom line, reveals stress concentrations at the phase interfaces.

set the material parameter $\beta^{incl} = \beta^{matr}$ in both the matrix and inclusion. The phase contrast μ^{incl}/μ^{matr} is then increased in a stepwise manner. For each phase contrast, a macroscopic load of $\overline{F}_{12} = \overline{F}_{12} = 0.2$ is applied over the course of 10 load steps while the other components are kept unchaged.

Figure 6.8 is showing the proportion t^{fd}/t^{algo} between the computational time needed for the finite difference-based scheme compared to the algorithmically consistent approach. The consistent approach used here needs more memory than a finite difference-based approach, as the fluctuation sensitivities $\partial\widetilde{F}/\partial\overline{F}$ of the last load step are stored as initial values for the next load step computation. However, one can see that the consistent approach gives speed-ups up to 85%.

6.6. Illustrative example: Green operator for a one-dimensional ordinary differential equation

This example as presented in the lecture notes of PEACOCK [148] serves to illustrate the mathematical functionality of the Green operator Γ^0. Having the ordinary differential equation

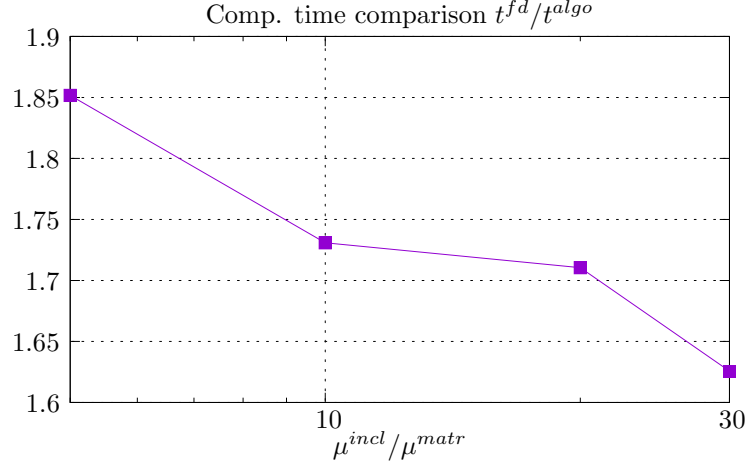$$\frac{\partial^2 u}{\partial x^2} + u = x \tag{6.70}$$

Figure 6.8: Runtime comparison between a finite difference-based approach and the algorithmically consistent-based computation for different phase contrasts μ^{incl}/μ^{matr} and constant β. One can see speed-ups up to 85% for the algorithmically consistent approach.

we set the boundary conditions to $u(0) = 0$ and $u(\frac{\pi}{2}) = 0$. The Green operator can then be found using those boundary conditions and solving the modified differential equation (6.70) as follows

$$\frac{\partial^2 \Gamma^0}{\partial x^2} + \Gamma^0 = \delta(x - z) \tag{6.71}$$

where we exchanged u by the Green operator Γ^0 and the right-hand side x by the Dirac delta function $\delta(x - z)$. Here, z can take any value in between the solution domain 0 and $\frac{\pi}{2}$. The solution of the Green operator must fulfill the same boundary conditions as u. As the Dirac delta function is zero for $z < x$ and for $x > z$, we can split our solution domain in two parts. We then have to solve the differential equation

$$\frac{\partial^2 \Gamma^0}{\partial x^2} + \Gamma^0 = 0 \tag{6.72}$$

on both sub-domains using transition conditions to find the solution. The fundamental solution to the latter equation in both sub-domains appears as

$$\Gamma^0 = \begin{cases} A(z)\sin(x) + B(z)\cos(x) & x < z \\ \\ C(z)\sin(x) + D(z)\cos(x) & x > z \end{cases}, \tag{6.73}$$

where the constants A, B, C and D with respect to x can be found using boundary conditions. The first two boundary conditions are the ones assumed in the beginning $u(0) = 0$ and $u(\frac{\pi}{2}) = 0$, which gives $B(z) = 0$ and $C(z) = 0$. We further assume continuity of Γ^0 which implies

$$A(z)\sin(z) = D(z)\cos(z). \tag{6.74}$$

We need one last boundary or transition condition in order to solve for all constants. As described in [148], see also [161], we therefore integrate the differential equation (6.71) in an infinitesimal region around z from $z - \epsilon$ and $z + \epsilon$ as follows

$$\int_{z-\epsilon}^{z+\epsilon} \frac{\partial^2 \Gamma^0}{\partial x^2} dx + \int_{z-\epsilon}^{z+\epsilon} \Gamma^0 dx = \int_{z-\epsilon}^{z+\epsilon} \delta(x - z) dx, \tag{6.75}$$

where we let $\epsilon \to 0$. In doing so, the right side becomes 1 due to the properties of the Dirac delta function. The second term on the left side vanishes due to the finite nature of Γ^0, leaving the terms

$$\left.\frac{\partial \Gamma^0}{\partial x}\right|_{z+\epsilon} - \left.\frac{\partial \Gamma^0}{\partial x}\right|_{z-\epsilon} = 1; \tag{6.76}$$

which for $\epsilon \to 0$ implies a discontinuity of der derivative of the Green operator $\partial \Gamma^0 / \partial x$ by 1. Carrying out the differentiation $\partial \Gamma^0 / \partial x$ using the expression for Γ^0 (6.73), we thus obtain the equation

$$- D(z)\sin(z) - A(z)\cos(z) = 1. \tag{6.77}$$

The latter equation, along with Equation (6.74), allows us to solve for the 2 remaining constants, yielding $A(z) = -\cos(z)$ and $D(z) = -\sin(z)$. The result for the Green operator then finally appears as

$$\Gamma^0 = \begin{cases} -\cos(z)\sin(x) & x < z \\ -\sin(z)\cos(x) & x > z \end{cases}. \tag{6.78}$$

Having the right-hand side x in (6.70), we obtain the integral form of the solution

$$u(x) = -\cos(x) \int_0^x z\sin(z)dz - \sin(x) \int_x^{\pi/2} z\cos(z)dz. \tag{6.79}$$

Evaluating the integrals at the boundaries using integration by parts yields the final result

$$u(x) = x - \frac{\pi}{2}\sin(x). \tag{6.80}$$

FFT-based computational homogenization of electroactive polymers

In analogy to Chapter 6, we now want to use Fourier-based methods to solve differential equations that govern the mechanical as well as the electric response of materials. That the two fields will interact and influence each other can be seen from the following example: Imagine two deformable electrodes glued onto a soft polymer. When applying some voltage to the electrodes, they will attract each other and thus deform the polymer. However, as the electrodes are attached to the polymer, they will deform accordingly which influences the electric field. In our case, such electro-mechanically coupled behavior will be modeled through coupled constitutive laws. As a consequence, the Lippmann-Schwinger equation will be coupled as well. In this chapter, we will focus on the derivation of the coupled Lippmann-Schwinger equation and the incidental coupled fluctuation sensitivities needed in the computation of the coupled macroscopic tangent. Numerical studies will be conducted on the impact of the coupled reference moduli in the Lippmann-Schwinger equation as well as on the influence of the coupled sensitivity terms on the macroscopic convergence behavior and speed. The framework's robustness is tested for different two- and three-dimensional microstructures as well as for multiscale simulations.

7.1. Lippmann-Schwinger approach to electro-mechano-statics

In order to arrive at a Lippmann-Schwinger set of equations as defined in Chapter 6 in Equation (6.1), we first reconsider the mechanical and electrical boundary value problems 3.22

$$
\begin{aligned}
\mathrm{Div}[\boldsymbol{T}] &= \boldsymbol{0} \ \ \text{in} \ \ \mathcal{B}^0 \ \ \text{and} \ \ \boldsymbol{T} \cdot \boldsymbol{N}(\boldsymbol{X}^+) = -\boldsymbol{T} \cdot \boldsymbol{N}(\boldsymbol{X}^-) \qquad \text{on} \ \ \partial\mathcal{B}^0, \\
\mathrm{Curl}[\boldsymbol{E}] &= \boldsymbol{0} \ \ \text{in} \ \ \mathcal{B}^0 \ \ \text{and} \ \ \boldsymbol{E} \times \boldsymbol{N}(\boldsymbol{X}^+) = -\boldsymbol{E} \times \boldsymbol{N}(\boldsymbol{X}^-) \ \ \ \text{on} \ \ \partial\mathcal{B}^0.
\end{aligned}
\tag{7.1}
$$

However, here we choose a vector potential-based approach where we solve Faraday's law $(2.100)_1$ and satisfy Gauss' law $(2.100)_2$ automatically by describing the electric displacement as the curl of a vector potential $\boldsymbol{a}$ as follows

$$
\boldsymbol{D} = \mathrm{Curl}(\boldsymbol{a}).
\tag{7.2}
$$

Having said relation, the equilibrium equations (7.1) in terms of the electric field can also be cast into a variational form, where the energy density is obtained from a Legendre-transformation. In line with the previous Chapter 6, we again follow the ideas formulated in HASHIN & SHTRIKMAN [70], see also WILLIS [204] MOULINEC & SUQUET [136, 137], and augment the differential equations by a *linear comparison material*. We now, however, have the choice between augmenting the purely mechanical stiffness $\mathbb{A}$ and electric permittivity $\mathbb{K}^0$ or additionally augmenting the *coupled stiffnesses* $\boldsymbol{q}^0$ and $\boldsymbol{g}^0$. Here, we choose the latter approach as follows

$$
\begin{aligned}
\boldsymbol{T} &= \mathbb{A}^0 : \boldsymbol{F} + \boldsymbol{q}^0 \cdot \boldsymbol{D} + \boldsymbol{T} - \mathbb{A}^0 : \boldsymbol{F} - \boldsymbol{q}^0 \cdot \boldsymbol{D}, \\
\boldsymbol{E} &= \boldsymbol{g}^0 : \boldsymbol{F} + \mathbb{K}^0 \cdot \boldsymbol{D} + \boldsymbol{E} - \boldsymbol{g}^0 : \boldsymbol{F} - \mathbb{K}^0 \cdot \boldsymbol{D},
\end{aligned}
\tag{7.3}
$$

and will later qualitatively analyze the impact of the coupled medium. We will now call the mechanical and electric perturbation fields

$$
\begin{aligned}
\boldsymbol{\tau}^m &= \boldsymbol{T} - \mathbb{A}^0 : \boldsymbol{F} - \boldsymbol{q}^0 \cdot \boldsymbol{D} \\
\boldsymbol{\tau}^e &= \boldsymbol{E} - \boldsymbol{g}^0 : \boldsymbol{F} - \mathbb{K}^0 \cdot \boldsymbol{D},
\end{aligned}
\tag{7.4}
$$

which allows us to rewrite the augmented stress and electric field (7.3) according to

$$
\begin{aligned}
\boldsymbol{T} &= \mathbb{A}^0 : \boldsymbol{F} + \boldsymbol{q}^0 \cdot \boldsymbol{D} + \boldsymbol{\tau}^m(\boldsymbol{F}, \boldsymbol{D}) \\
\boldsymbol{E} &= \boldsymbol{g}^0 : \boldsymbol{F} + \mathbb{K}^0 \cdot \boldsymbol{D} + \boldsymbol{\tau}^e(\boldsymbol{F}, \boldsymbol{D}).
\end{aligned}
\tag{7.5}
$$

Insertion of the latter stress and electric field into the differential equations and rearranging gives the following form

$$
\begin{aligned}
\mathrm{Div}[\mathbb{A}^0 : \boldsymbol{F} + \boldsymbol{q}^0 \cdot \boldsymbol{D}] &= -\mathrm{Div}[\boldsymbol{\tau}^m(\boldsymbol{F}, \boldsymbol{D})] \\
\mathrm{Curl}[\boldsymbol{g}^0 : \boldsymbol{F} + \mathbb{K}^0 \cdot \boldsymbol{D}] &= -\mathrm{Curl}[\boldsymbol{\tau}^e(\boldsymbol{F}, \boldsymbol{D})].
\end{aligned}
\tag{7.6}
$$

The latter equation can now be solved in terms of a *coupled Lippmann-Schwinger equation*

$$
\boxed{
\begin{bmatrix} \boldsymbol{F} \\ \boldsymbol{D} \end{bmatrix} = \begin{bmatrix} \overline{\boldsymbol{F}} \\ \overline{\boldsymbol{D}} \end{bmatrix} + \begin{bmatrix} \boldsymbol{\Gamma}^m & \boldsymbol{\Gamma}^{m,e} \\ \boldsymbol{\Gamma}^{e,m} & \boldsymbol{\Gamma}^e \end{bmatrix} * \begin{bmatrix} \boldsymbol{\tau}^m \\ \boldsymbol{\tau}^e \end{bmatrix},
}
\tag{7.7}
$$

where the off-diagonal terms $\boldsymbol{\Gamma}^{m,e}$ and $\boldsymbol{\Gamma}^{e,m}$ in the summarized Green operator occur due to the coupled preconditioning. Choosing the coupled stiffnesses $\boldsymbol{q}^0 = \boldsymbol{g}^0 = \boldsymbol{0}$ to be zero gives a Green operator with off-diagonals being zero

$$
\begin{bmatrix} \boldsymbol{F} \\ \boldsymbol{D} \end{bmatrix} = \begin{bmatrix} \overline{\boldsymbol{F}} \\ \overline{\boldsymbol{D}} \end{bmatrix} + \begin{bmatrix} \boldsymbol{\Gamma}^m & \boldsymbol{0} \\ \boldsymbol{0} & \boldsymbol{\Gamma}^e \end{bmatrix} * \begin{bmatrix} \boldsymbol{\tau}^m \\ \boldsymbol{\tau}^e \end{bmatrix}.
\tag{7.8}
$$

As the Lippmann-Schwinger equation is usually solved utilizing iterative solvers, one can imagine that the Green operator's structure determines the rate of convergence. The explicit form for the Green operators is given in the Appendix 7.5.2.

7.2. Lippmann-Schwinger-based coupled macroscopic tangent computation

For non-linear material behavior, the effective macroscopic properties are state-dependent. Having found the equilibrated state for an electromechanically coupled material by solving

the coupled Lippmann-Schwinger equation (7.7), we now provide the computation of these effective properties by means of the macroscopic coupled effective tangent operator. In analogy to Section 6.2 for the purely mechanical problem, we now extend the framework for coupled materials as outlined in GÖKÜZÜM ET AL. [64], see also [47, 129, 181] for finite element-based implementations. The extension is done for a vector potential-based implementation of the electric problem but can be recast to the scalar potential-based formulation. We start from the linearization of the increment of macroscopic stress and electric field

$$
\left[\begin{array}{c} \Delta \overline{T} \\ \Delta \overline{E} \end{array} \right] = \left[\begin{array}{cc} \dfrac{\partial \overline{T}}{\partial \overline{F}} & \dfrac{\partial \overline{T}}{\partial \overline{D}} \\[2mm] \dfrac{\partial \overline{E}}{\partial \overline{F}} & \dfrac{\partial \overline{E}}{\partial \overline{D}} \end{array} \right] \cdot \left[\begin{array}{c} \Delta \overline{F} \\ \Delta \overline{D} \end{array} \right],
\tag{7.9}
$$

where we need to take into account that the mechanical stresses can be dependent on the electric displacement and the electric field on the deformation gradient. To simplify the equations to come, we will express the partial derivatives of the stress and electric field in terms of the following symbols

$$
\frac{\partial \overline{T}}{\partial \overline{F}} =: \overline{\mathbb{A}}, \quad \frac{\partial \overline{T}}{\partial \overline{D}} = \left[\frac{\partial \overline{E}}{\partial \overline{F}} \right]^{T} =: \overline{q} \quad \text{and} \quad \frac{\partial \overline{E}}{\partial \overline{D}} =: \overline{\mathbb{K}}.
\tag{7.10}
$$

We further condense the stress and electric field, their dual variables as well as the moduli into generalized tensors

$$
\overline{\mathbb{S}} = \left[\begin{array}{c} \overline{T} \\ \hline \overline{E} \end{array} \right], \quad \overline{\mathbb{G}} = \left[\begin{array}{c} \overline{F} \\ \hline \overline{D} \end{array} \right] \quad \text{and} \quad \overline{\mathbb{C}}^{algo} = \left[\begin{array}{cc} \overline{\mathbb{A}} & \overline{q} \\ \hline \overline{q}^{T} & \overline{\mathbb{K}} \end{array} \right],
\tag{7.11}
$$

where we call $\overline{\mathbb{S}}$ the generalized stress, $\overline{\mathbb{G}}$ generalized strain and $\overline{\mathbb{C}}^{algo}$ the generalized moduli. With such notation at hand, the linearized macroscopic increments (7.9) can be written down in the short form

$$
\Delta \overline{\mathbb{S}} = \overline{\mathbb{C}}^{algo} \diamond \Delta \overline{\mathbb{G}},
\tag{7.12}
$$

where the $\diamond$ is a generic operator denoting the appropriate contractions of the moduli with their corresponding generalized strains. In analogy to (7.11), we introduce the generalized notation for the microscopic generalized stress, strain, and moduli

$$
\mathbb{S} = \left[\begin{array}{c} T \\ \hline E \end{array} \right], \quad \mathbb{G} = \left[\begin{array}{c} F \\ \hline D \end{array} \right] \quad \text{and} \quad \mathbb{C} = \left[\begin{array}{cc} \mathbb{A} & q \\ \hline q^{T} & \mathbb{K} \end{array} \right].
\tag{7.13}
$$

Here, the moduli appearing are the partial derivatives of the microscopic stress and electric field with respect to the microscopic strain and electric displacement

$$
\mathbb{A} = \frac{\partial T}{\partial F}, \quad q = \frac{\partial T}{\partial D} = \left[\frac{\partial E}{\partial F} \right]^{T} \quad \text{and} \quad \mathbb{K} = \frac{\partial E}{\partial D}.
\tag{7.14}
$$

As outlined in Chapter 4, the macroscopic tangent operator can now be obtained using the integral relation (4.30). When differentiating the macroscopic generalized stresses $\overline{\mathbb{S}}$

with respect to the macroscopic generalized strains $\overline{\mathbb{G}}$, we can use the decomposition of $\mathbb{G}$ and the chain rule to arrive at

$$\Delta\overline{\mathbb{S}} = \frac{1}{V}\int_{\mathcal{B}^0}\left(\mathbb{C} + \mathbb{C}\diamond\frac{\partial\widetilde{\mathbb{G}}}{\partial\overline{\mathbb{G}}}\right)dV\diamond\Delta\overline{\mathbb{G}}. \tag{7.15}$$

Comparison of the latter equation with the general form (7.12) allows identifying the variationally consistent macroscopic tangent operator as

$$\overline{\mathbb{C}}^{algo} = \frac{1}{V}\int_{\mathcal{B}^0}\left(\mathbb{C} + \mathbb{C}\diamond\frac{\partial\widetilde{\mathbb{G}}}{\partial\overline{\mathbb{G}}}\right)dV, \tag{7.16}$$

which is the coupled counterpart of (6.12). We now need to determine the fluctuation sensitivities $\partial\widetilde{\mathbb{G}}/\partial\overline{\mathbb{G}}$, where for the case of electro-mechanically coupled materials, we obtain the form

$$\frac{\partial\widetilde{\mathbb{G}}}{\partial\overline{\mathbb{G}}} = \left[\begin{array}{cc}\dfrac{\partial\widetilde{\boldsymbol{F}}}{\partial\overline{\boldsymbol{F}}} & \dfrac{\partial\widetilde{\boldsymbol{F}}}{\partial\overline{\boldsymbol{D}}}\\[2mm]\dfrac{\partial\widetilde{\boldsymbol{D}}}{\partial\overline{\boldsymbol{F}}} & \dfrac{\partial\widetilde{\boldsymbol{D}}}{\partial\overline{\boldsymbol{D}}}\end{array}\right], \tag{7.17}$$

including coupled sensitivities between the fluctuative deformation gradient and the macroscopically applied electric displacement and vice versa between the fluctuative displacement and the macroscopically applied deformation gradient. A more detailed expression for the effective coupled tangent is given in Appendix 7.5.1.

Having the Lippmann-Schwinger equation solution at hand, it is possible to formulate an explicit expression for the coupled sensitivities. Comparison of the Lippmann-Schwinger equation (7.7) with the decomposition of the generalized strains (4.5) and (4.28), we can identify the fluctuative fields in terms of the Green operator and the perturbation fields as follows

$$\widetilde{\mathbb{G}} = \left[\begin{array}{c}\widetilde{\boldsymbol{F}}\\[1mm]\widetilde{\boldsymbol{D}}\end{array}\right] = \left[\begin{array}{cc}\boldsymbol{\Gamma}^m & \boldsymbol{\Gamma}^{m,e}\\[1mm]\boldsymbol{\Gamma}^{e,m} & \boldsymbol{\Gamma}^e\end{array}\right]*\left[\begin{array}{c}\boldsymbol{\tau}^m\\[1mm]\boldsymbol{\tau}^e\end{array}\right]. \tag{7.18}$$

With the explicit expression for the fluctuative fields at hand, we can now perform the differentiation with respect to the macroscopic fields

$$\frac{\partial\widetilde{\mathbb{G}}}{\partial\overline{\mathbb{G}}} = \left[\begin{array}{cc}\boldsymbol{\Gamma}^m & \boldsymbol{\Gamma}^{m,e}\\[1mm]\boldsymbol{\Gamma}^{e,m} & \boldsymbol{\Gamma}^e\end{array}\right]*\left[\begin{array}{cc}\dfrac{\partial\boldsymbol{\tau}^m}{\partial\overline{\boldsymbol{F}}} & \dfrac{\partial\boldsymbol{\tau}^m}{\partial\overline{\boldsymbol{D}}}\\[2mm]\dfrac{\partial\boldsymbol{\tau}^e}{\partial\overline{\boldsymbol{F}}} & \dfrac{\partial\boldsymbol{\tau}^e}{\partial\overline{\boldsymbol{D}}}\end{array}\right], \tag{7.19}$$

where the perturbation fields in equilibrium are dependent on the macroscopic fields. Using the definition of the perturbation fields (7.4) along with the abbreviation

$$\mathbb{C}^\Delta = \mathbb{C} - \mathbb{C}^0 = \left[\begin{array}{cc}\mathbb{A} - \mathbb{A}^0 & \boldsymbol{q} - \boldsymbol{q}_0\\[1mm]\boldsymbol{q}^T - \boldsymbol{q}_0^T & \mathbb{K} - \mathbb{K}^0\end{array}\right] \quad\text{and}\quad \boldsymbol{\Gamma} = \left[\begin{array}{cc}\boldsymbol{\Gamma}^m & \boldsymbol{\Gamma}^{m,e}\\[1mm]\boldsymbol{\Gamma}^{e,m} & \boldsymbol{\Gamma}^e\end{array}\right], \tag{7.20}$$

we can apply the chain rule $\partial(\bullet)/\partial\overline{\mathbb{G}} = \partial(\bullet)/\partial\mathbb{G}\diamond\partial\mathbb{G}/\partial\overline{\mathbb{G}}$ to the differentiation in Equation (7.19) and use the decompostion (4.5) and (4.28) to arrive at the linear *Lippmann-Schwinger-type* equation for the fluctuation sensitivities

$$\boxed{-\boldsymbol{\Gamma}*\mathbb{C}^\Delta = \boldsymbol{\Gamma}*\left(\mathbb{C}^\Delta\diamond\frac{\partial\widetilde{\mathbb{G}}}{\partial\overline{\mathbb{G}}}\right) - \frac{\partial\widetilde{\mathbb{G}}}{\partial\overline{\mathbb{G}}}}, \tag{7.21}$$

which needs to be solved with zero-average constraint for the fluctuation sensitivities

$$\int_{\mathcal{B}^0} \frac{\partial \widetilde{\mathbb{G}}}{\partial \overline{\mathbb{G}}} \, dV = \boldsymbol{0}. \tag{7.22}$$

For a more detailed derivation of the fluctuation sensitivities, the reader is referred to Appendix 7.5.3. We now want to further reformulate the Lippmann-Schwinger-type (7.21). Following the arguments outlined in MOULINEC & SUQUET [137], there exists the relation

$$\mathbb{G} = \boldsymbol{\Gamma} * \left(\mathbb{C}^0 \diamond \mathbb{G} \right) \tag{7.23}$$

in terms of the convolution of the Green operator with the microscopic fields. Differentiation of the latter equation with respect to the macroscopic fields yields the relation in terms of the fluctuation sensitivities

$$\frac{\partial \mathbb{G}}{\partial \overline{\mathbb{G}}} = \frac{\partial \widetilde{\mathbb{G}}}{\partial \overline{\mathbb{G}}} + \mathbb{I} = \boldsymbol{\Gamma} * \left(\mathbb{C}^0 \diamond \frac{\partial \widetilde{\mathbb{G}}}{\partial \overline{\mathbb{G}}} + \mathbb{C}^0 \right), \tag{7.24}$$

with $\mathbb{I}$ being the fourth-order identity. Rearranging the latter equation for convolution between the Green operator and the contraction of the linear reference material and the fluctuation sensitivities gives

$$\boldsymbol{\Gamma} * \left(\mathbb{C}^0 \diamond \frac{\partial \widetilde{\mathbb{G}}}{\partial \overline{\mathbb{G}}} \right) = \frac{\partial \widetilde{\mathbb{G}}}{\partial \overline{\mathbb{G}}} + \mathbb{I} - \boldsymbol{\Gamma} * \mathbb{C}^0. \tag{7.25}$$

Insertion of the latter equation into the linear equation for the fluctuation sensitivities (7.21) leads to the intermediate form

$$- \boldsymbol{\Gamma} * \mathbb{C}^\Delta = \boldsymbol{\Gamma} * \left(\mathbb{C} \diamond \frac{\partial \widetilde{\mathbb{G}}}{\partial \overline{\mathbb{G}}} \right) + \mathbb{I} - \boldsymbol{\Gamma} * \mathbb{C}^0. \tag{7.26}$$

Finally, we state that the constant contributions such as $\mathbb{I}$ and $\boldsymbol{\Gamma} * \mathbb{C}^0$ in the latter equation do not influence the solution, as we prescribe a zero average of the fluctuation sensitivities according to (7.22). In Fourier space, when constructing the Green operator, this property becomes more evident, as described in the next section. The neglection of the constant contributions allows for the simplification of Equation (7.26) according to

$$\boxed{- \boldsymbol{\Gamma} * \mathbb{C} = \boldsymbol{\Gamma} * \left(\mathbb{C} \diamond \frac{\partial \widetilde{\mathbb{G}}}{\partial \overline{\mathbb{G}}} \right).} \tag{7.27}$$

We can now perform one last reformulation of Equation (7.21) to arrive at a form that resembles the original Lippmann-Schwinger equation. Following the concept of perturbation fields outlined in Equation (7.4), we now introduce the perturbation field of the fluctuation sensitivities with respect to the linear reference material as follows

$$\mathbb{T} = \mathbb{C}^\Delta \diamond \frac{\partial \widetilde{\mathbb{G}}}{\partial \overline{\mathbb{G}}}. \tag{7.28}$$

Using the upper definition, Equation (7.21) can be recast into

$$\boxed{\frac{\partial \widetilde{\mathbb{G}}}{\partial \overline{\mathbb{G}}} = \mathbf{\Gamma} * [\mathbb{C}^{\Delta} + \mathbb{T}].} \tag{7.29}$$

The latter equation allows for the classical fixed-point iteration which was initially used by MOULINEC & SUQUET [136] for the equilibrium equation and is nowadays called the basic scheme.

7.3. Discrete solution scheme for coupled multiscale problems

In analogy to the purely mechanical approach from Chapter 6.3, we now introduce the nodal field variables and their dual variables. The spatial discretization in real and Fourier space follows equations (6.23) and (6.24). Here, we assemble the mechanical and electrical fields to generalized nodal tensors

$$\mathbb{G}_{\alpha\beta} = [\boldsymbol{F}_{\alpha\beta}, \boldsymbol{D}_{\alpha\beta}] \quad \text{and} \quad \mathbb{S}_{\alpha\beta} = [\boldsymbol{T}_{\alpha\beta}, \boldsymbol{E}_{\alpha\beta}]. \tag{7.30}$$

For the further computation of the coupled macroscopic tangent operator, we again need the fluctuation sensitivities, i.e., the differentiation of the fluctuations with respect to the macroscopic quantities

$$\mathbb{F}_{\alpha\beta} = \left(\frac{\widetilde{\mathbb{G}}}{\overline{\mathbb{G}}}\right)_{\alpha\beta} = \left[\left(\frac{\partial \widetilde{\boldsymbol{F}}}{\partial \overline{\boldsymbol{F}}}\right)_{\alpha\beta}, \left(\frac{\partial \widetilde{\boldsymbol{D}}}{\partial \overline{\boldsymbol{D}}}\right)_{\alpha\beta}, \left(\frac{\partial \widetilde{\boldsymbol{F}}}{\partial \overline{\boldsymbol{D}}}\right)_{\alpha\beta}, \left(\frac{\partial \widetilde{\boldsymbol{D}}}{\partial \overline{\boldsymbol{F}}}\right)_{\alpha\beta}\right]. \tag{7.31}$$

As mentioned previously, for a consistent numerical framework and quadratic convergence, it is important to account for the coupled sensitivities as well, because a macroscopic deformation gradient $\overline{\boldsymbol{F}}$ might affect fluctuative electric displacements $\widetilde{\boldsymbol{D}}$ and vice versa. In line with the treatment in the previous Chapter 6.3, we assemble the nodal quantities in global discretized tensors

$$\underline{\mathbb{G}} = \overset{N_{\alpha,\beta}}{\underset{\alpha,\beta=1}{\mathbf{A}}} \mathbb{G}_{\alpha\beta}, \quad \underline{\mathbb{S}} = \overset{N_{\alpha,\beta}}{\underset{\alpha,\beta=1}{\mathbf{A}}} \mathbb{S}_{\alpha\beta} \quad \text{and} \quad \underline{\mathbb{F}} = \overset{N_{\alpha,\beta}}{\underset{\alpha,\beta=1}{\mathbf{A}}} \mathbb{F}_{\alpha\beta}. \tag{7.32}$$

We apply the same assembly procedure to the difference of generalized stiffness and linear reference material $\underline{\mathbb{C}}^{\Delta}$ and the Green operator in Fourier space $\widehat{\underline{\mathbf{\Gamma}}}_{\alpha\beta}$ as follows

$$\underline{\mathbb{C}}^{\Delta} = \overset{N_{\alpha,\beta}}{\underset{\alpha,\beta=1}{\mathbf{A}}} \underline{\mathbb{C}}^{\Delta}_{\alpha\beta}, \quad \text{and} \quad \widehat{\underline{\mathbf{\Gamma}}} = \overset{N_{\alpha,\beta}}{\underset{\alpha,\beta=1}{\mathbf{A}}} \widehat{\underline{\mathbf{\Gamma}}}_{\alpha\beta}. \tag{7.33}$$

The Green operator $\widehat{\underline{\mathbf{\Gamma}}}_{\alpha\beta}$ can again be given in an explicit form in Fourier space. Due to the coupled nature of our problem, the expressions appearing in the Green operator, however, become a little lengthy, which is why said expressions can be found in Appendix 7.5.2.

Having all discretized quantities at hand, we are now able to formulate a solution scheme for the equilibrium equation. Using the generalized perturbation field

$$\underline{\boldsymbol{\tau}} = \underline{\mathbb{S}} - \underline{\mathbb{C}}^{\Delta} \diamond \underline{\mathbb{G}}, \tag{7.34}$$

the coupled Lippmann-Schwinger equation in real space appears as

$$\underline{\mathbb{G}}_{i+1} = \overline{\underline{\mathbb{G}}} + \underline{\boldsymbol{\Gamma}} * \underline{\boldsymbol{\tau}}_n. \tag{7.35}$$

In Fourier space, the Lippmann-Schwinger equation appears as the volume constrained update rule

$$\begin{aligned} \widehat{\underline{\mathbb{G}}}_{i+1} &= \widehat{\underline{\boldsymbol{\Gamma}}} \diamond \widehat{\underline{\boldsymbol{\tau}}}_n \quad \text{for} \quad \boldsymbol{K} \neq \boldsymbol{0}, \\ \widehat{\underline{\mathbb{G}}}_{i+1} &= \overline{\underline{\mathbb{G}}}_{i+1} \quad \text{for} \quad \boldsymbol{K} = \boldsymbol{0}, \end{aligned} \tag{7.36}$$

where the convolution turns into a simple contraction of the Fourier coefficients. After having found the equilibrium using a suitable tolerance, the macroscopic generalized stress can be found according to the volume average (4.30). What is left to compute for a multiscale update is the macroscopic tangent operator at equilibrium (7.16). From Equation (7.29), we can see that this can be done as well by means of a fixed-point iteration when setting

$$\underline{\mathbb{F}}_{i+1} = \underline{\boldsymbol{\Gamma}} * [\underline{\mathbb{C}}^{\Delta} + \underline{\mathbb{T}}_n], \tag{7.37}$$

where Equation (7.28) defines $\underline{\mathbb{T}}_n$ to be a function of $\underline{\mathbb{F}}_n$. In analogy to the equilibrium equation, we write the update in Fourier space as follows

$$\begin{aligned} \widehat{\underline{\mathbb{F}}}_{i+1} &= \widehat{\underline{\boldsymbol{\Gamma}}} \diamond [\widehat{\underline{\mathbb{C}}}^{\Delta} + \widehat{\underline{\mathbb{T}}}_n] \quad \text{for} \quad \boldsymbol{K} \neq \boldsymbol{0}, \\ \widehat{\underline{\mathbb{F}}}_{i+1} &= \boldsymbol{0} \quad \text{for} \quad \boldsymbol{K} = \boldsymbol{0}. \end{aligned} \tag{7.38}$$

Again, the convolutions are turning to simple tensor contractions and the zero-average constraint known from Equation (7.22) is satisfied through constraining the Fourier coefficient at zeroth frequency.

Recalling the discussion after Equation (7.26) in the previous Section 7.2, it becomes now clearer why the contribution $\underline{\boldsymbol{\Gamma}} * \underline{\mathbb{C}}^0$ is not influencing the solution. As $\underline{\mathbb{C}}^0$ is a constant field, its Fourier transform $\widehat{\underline{\mathbb{C}}}^0$ has only one non-zero Fourier coefficient at its zeroth frequency $\boldsymbol{K} = \boldsymbol{0}$, namely the volume average $\mathbb{C}^0$ itself. The contribution of the term $\widehat{\underline{\boldsymbol{\Gamma}}} \diamond \widehat{\underline{\mathbb{C}}}^0$ is thus only acting on the volume average of the solution. However, as we are constraining the volume average of the fluctuation sensitivities, this contribution is omitted, and we are allowed to neglect the term in the upper equation. Additionally, using Equation (7.23), the fixed-point scheme can be recast into the following form

$$\begin{aligned} \widehat{\underline{\mathbb{F}}}_{i+1} &= \widehat{\underline{\mathbb{F}}}_n + \widehat{\underline{\boldsymbol{\Gamma}}} \diamond [\widehat{\underline{\mathbb{C}}} + \widehat{\underline{\mathbb{T}}}_n^*] \quad \text{for} \quad \boldsymbol{K} \neq \boldsymbol{0}, \\ \widehat{\underline{\mathbb{F}}}_{i+1} &= \boldsymbol{0} \quad \text{for} \quad \boldsymbol{K} = \boldsymbol{0}, \end{aligned} \tag{7.39}$$

where we introduced the modified perturbation tensor

$$\underline{\mathbb{T}}^* = \underline{\mathbb{C}} \diamond \underline{\mathbb{F}}. \tag{7.40}$$

Equation (7.39) resembles a fixed-point scheme for the equilibrium equation introduced in MOULINEC & SUQUET [136].

As in purely mechanical problems, speedups in solving the Lippmann-Schwinger equation can be obtained by using advanced iterative solvers such as the conjugate gradient method

$$\underline{\mathbb{F}}_{i+1} = \text{cg}\{\underline{\mathbf{A}} \cdot \underline{\mathbf{x}}, \underline{\mathbf{b}}\}. \tag{7.41}$$

The standard conjugate gradient method demands for a linearized problem, where we need to provide the solver with the system matrix multiplied with the vectors of unknowns $\underline{\mathbf{A}} \cdot \underline{\mathbf{x}}$

and the right-hand side $\underline{\mathbf{b}}$. It is convenient to solve Equation (7.21) by means of the conjugate gradient method as it is a linear equation by nature. We therefore can identify the terms as from Equation (7.21) as follows

$$\underline{\mathbf{A}} \cdot \underline{\mathbf{x}} = \mathrm{fft}^{-1}\{\widehat{\underline{\mathbf{\Gamma}}} \diamond \mathrm{fft}\{\underline{\mathbb{C}}^{\Delta} \diamond \underline{\mathbb{F}}\}\} - \underline{\mathbb{F}} \quad \text{and} \quad \underline{\mathbf{b}} = \mathrm{fft}^{-1}\{-\widehat{\underline{\mathbf{\Gamma}}} \diamond \mathrm{fft}\{\underline{\mathbb{C}}^{\Delta}\}\}. \tag{7.42}$$

Following the same arguments given for the fixed-point iteration, the expression for the matrix-vector multiplication and the right-hand side can be further simplified to

$$\underline{\mathbf{A}}^{*} \cdot \underline{\mathbf{x}} = \mathrm{fft}^{-1}\{\widehat{\underline{\mathbf{\Gamma}}} \diamond \mathrm{fft}\{\underline{\mathbb{C}} \diamond \underline{\mathbb{F}}\}\} \quad \text{and} \quad \underline{\mathbf{b}}^{*} = \mathrm{fft}^{-1}\{-\widehat{\underline{\mathbf{\Gamma}}} \diamond \mathrm{fft}\{\underline{\mathbb{C}}\}\}. \tag{7.43}$$

In total, for the two-dimensional case, the number of unknowns to solve for is $N_1 \times N_2 \times n_{dof}^4$. Here, the degrees of freedom are related to the primary field variables and thus, in the two-dimensional case, we have $n_{dof} = 6$ as there are 4 independent strain components and 2 independent electric displacement components.

With the converged fluctuation sensitivities at hand, we are able to compute the macroscopic tangent operator from Equation (7.15) as follows

$$\boxed{\overline{\mathbb{C}}^{algo} = \frac{1}{V} \left[\int_{\mathcal{B}^0} \mathbb{C} \, dV + \int_{\mathcal{B}^0} \mathbb{C} \diamond \underline{\mathbb{F}} \, dV \right] = \frac{1}{V} \int_{\mathcal{B}^0} \mathbb{C} \diamond (\mathbb{I} + \underline{\mathbb{F}}) \, dV.} \tag{7.44}$$

The overall algorithmic scheme for the multiscale simulation presented in this section can be found in Box 7.1 taken from GÖKÜZÜM ET AL. [64]. In the following section, the framework is numerically validated for one-, two-, and three-dimensional RVEs with different microstructures. Furthermore, the performance is compared with a conventional finite difference-based approach, where the tangent is obtained through applying small perturbations $\epsilon \boldsymbol{I}_i$ to the equilibrated fields $\mathbb{G}_i^{pert} = \mathbb{G} + \epsilon \boldsymbol{I}_i$ where $\boldsymbol{I}_i$ are n_{dof}^2 independent tensors of size n_{dof}^2. Next, the new perturbed equilibrium is computed from the perturbed Lippmann-Schwinger equation

$$\mathbb{G}_i^{pert} - \boldsymbol{\Gamma} * [\mathbb{S}(\mathbb{G}_i^{pert}) - \mathbb{C}^0 : \mathbb{G}_i^{pert}] = \overline{\mathbb{G}} + \epsilon \boldsymbol{I}_i \tag{7.45}$$

and the individual entries of the macroscopic tangent operator can be obtained from the finite difference approximation

$$\Delta \overline{\mathbb{S}}_i = \frac{1}{V} \int_{\mathcal{B}^0} [\mathbb{S}(\mathbb{G}_i') - \mathbb{S}(\mathbb{G})] \, dV = \overline{\mathbb{C}}^{fd} \diamond [\epsilon \boldsymbol{I}_i]. \tag{7.46}$$

7.4. Numerical examples

We now want to test the presented electro-mechanically coupled multiscale framework for different numerical examples. First, we consider analytical one- and two-dimensional homogenization problems to validate our model's accuracy and correctness. Finally, an electro-active gripper is computed on two scales.

> **Box 7.1:** Algorithm for the computation of material response and consistent macroscopic tangent using the fast Fourier transform for electro-mechanically coupled problems [64].

---

1. **Equilibrium:** Solve Lippmann-Schwinger equation for the equilibrium state

$$\underline{\mathbb{G}}_{i+1} = \overline{\underline{\mathbb{G}}} + \underline{\boldsymbol{\Gamma}} * \underline{\boldsymbol{\tau}}_n,$$

   while choosing an appropriate reference medium $\mathbb{C}^0$ for better convergence.

2. **Fluctuation sensitivities:** Apply conjugate-gradient method for linear integral system of equations

$$\mathbb{F}_{i+1} = \mathrm{cg}\{\underline{\mathbf{A}} \cdot \underline{\mathbf{x}}, \underline{\mathbf{b}}\},$$

   where $\underline{\mathbf{A}} \cdot \underline{\mathbf{x}}$ and $\underline{\mathbf{b}}$ are obtained from (7.21) via

$$\underline{\mathbf{A}} \cdot \underline{\mathbf{x}} = \mathrm{fft}^{-1}\{\widehat{\underline{\boldsymbol{\Gamma}}} \diamond \mathrm{fft}\{\mathbb{C}^\Delta \diamond \mathbb{F}\}\} - \mathbb{F} \quad \text{and} \quad \underline{\mathbf{b}} = \mathrm{fft}^{-1}\{-\widehat{\underline{\boldsymbol{\Gamma}}} \diamond \mathrm{fft}\{\mathbb{C}^\Delta\}\},$$

   or from the simplified equation (7.26) via

$$\underline{\mathbf{A}}^* \cdot \underline{\mathbf{x}} = \mathrm{fft}^{-1}\{\widehat{\underline{\boldsymbol{\Gamma}}} \diamond \mathrm{fft}\{\mathbb{C} \diamond \mathbb{F}\}\} \quad \text{and} \quad \underline{\mathbf{b}}^* = \mathrm{fft}^{-1}\{-\widehat{\underline{\boldsymbol{\Gamma}}} \diamond \mathrm{fft}\{\mathbb{C}\}\}.$$

3. **Integration:** The consistent macroscopic tangent is computed as

$$\overline{\mathbb{C}}^{algo} = \frac{1}{N_1 N_2} \sum_{\alpha=1}^{N_1} \sum_{\beta=1}^{N_2} \left[\mathbb{C}_{\alpha\beta} + \underline{\mathbb{C}}_{\alpha\beta} \diamond \mathbb{F}_{\alpha\beta} \right].$$

7.4.1. Constitutive material model

We are describing electro-mechanically coupled material behavior by a coupled constitutive energy density function

$$\psi(\boldsymbol{F}, \boldsymbol{E}) = \psi_{mech}(\boldsymbol{F}) + \psi_{elec}(\boldsymbol{F}, \boldsymbol{E}), \tag{7.47}$$

that takes into account mechanical effects through the contribution ψ_{mech} as well as electrical ones through ψ_{elec}. In our model, the purely mechanical contribution is modeled through the Neo-Hookean energy density (6.66) for hyperelasticity

$$\psi_{mech}(\boldsymbol{F}) = \frac{\mu}{2}(\mathrm{tr}\, \boldsymbol{C} - 3) + \frac{\mu}{\beta}(J^{-\beta} - 1). \tag{7.48}$$

For the dielectric contribution, we use the energy density from Equation (3.8) given in Section 3.1, see also MCMEEKING & LANDIS [123] and MIEHE ET AL. [131],

$$\psi_{elec}(\boldsymbol{F}, \boldsymbol{E}) = -\frac{\epsilon_0}{2}\left(1 + \frac{\chi_0}{J}\right) J\boldsymbol{C}^{-1} : (\boldsymbol{E} \otimes \boldsymbol{E}). \tag{7.49}$$

where the vacuum permittivity $\epsilon_0 \approx 8.854 \cdot 10^{-12}$ Fm^{-1} as defined in Coulomb's law (2.1) is appearing. The susceptibility χ_0 is a material parameter emerging from the constitutive

law for dielectric polarization (2.101) in Section 2.1. As the units of the elastic parameters and the units for the vacuum permittivity differ in the order of several magnitudes, one usually normalizes said parameters to obtain stable numerical simulations. We thus divide the energy density function (7.49) by some μ_n and give the energy with respect to the normalized electric field $\boldsymbol{E}' = \sqrt{\mu_n/\epsilon_0}^{-1} \boldsymbol{E}$ including the vacuum permittivity

$$\psi'(\boldsymbol{F}, \boldsymbol{E}') = \frac{\mu'}{2}(\operatorname{tr} \boldsymbol{C} - 3) + \frac{\mu'}{\beta}(J^{-\beta} - 1) - \frac{1}{2}(1 + \frac{\chi_0}{J}) J\boldsymbol{C}^{-1} : (\boldsymbol{E}' \otimes \boldsymbol{E}'). \qquad (7.50)$$

Here $\mu' = \mu/\mu_n$ denotes the normalized shear modulus. Differentiation of the latter equation with respect to $\boldsymbol{E}'$ would yield the normalized electric displacement $\boldsymbol{D}' = \sqrt{\mu_n\epsilon_0}^{-1}\boldsymbol{D}$. The formulation of the energy density in terms of $\boldsymbol{F}$ and $\boldsymbol{E}$ yields a saddle-point problem for the stationarity of the global potential. In terms of iterative solvers, it might lead to increased stability and convergence rates to use a minimization formulation in terms of $\boldsymbol{F}$ and $\boldsymbol{D}$ as follows

$$\psi^*(\boldsymbol{F}, \boldsymbol{D}) = \psi_{mech}(\boldsymbol{F}) + \psi^*_{elec}(\boldsymbol{F}, \boldsymbol{D}). \qquad (7.51)$$

The electric energy density with respect to the electric displacement can be obtained employing a Legendre transformation of Equation (7.49) [123]. The transformed energy density then appears as

$$\psi^*_{elec}(\boldsymbol{F}, \boldsymbol{D}) = \frac{1}{2\epsilon_0(J + \chi_0)} \boldsymbol{C} : (\boldsymbol{D} \otimes \boldsymbol{D}). \qquad (7.52)$$

Normalization and summation with the elastic contribution finally yields

$$\psi^{*\prime}(\boldsymbol{F}, \boldsymbol{D}') = \frac{\mu'}{2}(\operatorname{tr} \boldsymbol{C} - 3) + \frac{\mu'}{\beta}(J^{-\beta} - 1) + \frac{1}{2(J + \chi_0)} \boldsymbol{C} : (\boldsymbol{D}' \otimes \boldsymbol{D}'). \qquad (7.53)$$

7.4.2. Coupled one-dimensional examples

This section explores the features of the presented coupled homogenization scheme for a set of one-dimensional problems. First, a one-dimensional multiscale problem that allows for a comparison to an analytic solution is considered. In a second example, the impact of the reference medium on the convergence rate and stability of the basic scheme is numerically tested, where special interest lies on the coupled nature of the problem.
In the one-dimensional setting, we will use the scalar potential-based formulation of the physical problem, where we need to solve for the the electric field and deformation gradient. Their one-dimensional reductions with respect to the scalar potential and the displacement follow from Equations (2.10) and (2.126) as

$$F = \frac{\partial\varphi(X)}{\partial X} = 1 + \frac{\partial u(x)}{\partial X} \quad \text{and} \quad E = -\frac{\partial\phi}{\partial X}, \qquad (7.54)$$

The one-dimensional reduction of the coupled energy density function (7.50) appears as

$$\psi(F, E') = \frac{\mu'}{2}(F^2 - 1) + \frac{\mu'}{\beta}(F^{-\beta} - 1) - \frac{1}{2}(1 + \frac{\chi_0}{F})\frac{(E')^2}{F}, \qquad (7.55)$$

where the shear modulus for normalization is set to $\mu_n = 1$ GPa. The dual fields can then be computed from the energy density through differentiation

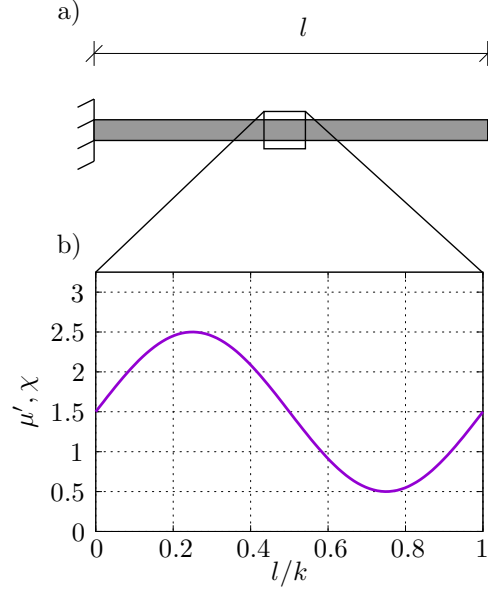$$T = \frac{\partial\psi}{\partial F} \quad \text{and} \quad D = -\frac{\partial\psi}{\partial E}. \qquad (7.56)$$

Figure 7.1: a) A one-dimensional bar is exposed to axial electrical and mechanical volume load according to Equation (7.58). b) The material properties follow the periodic function in space $\mu' = \chi = 3/2 + \sin(2\pi k X)$ with $k \in \mathbb{N}\backslash\{0\}$ [64].

Second differentiation with respect to the electric field and the deformation gradient yield the moduli

$$\mathbb{A} = \frac{\partial^2 \psi}{\partial F^2}, \quad q = -\frac{\partial^2 \psi}{\partial E \partial F} \quad \text{and} \quad \mathbb{K} = -\frac{\partial^2 \psi}{\partial E^2}. \tag{7.57}$$

Analytical Example. We now consider a one-dimensional problem that admits an analytic solution. This somewhat academic problem serves as an example of how the homogenized response corresponds to a full-field solution with decreasing RVE size. As visualized in Figure 7.1, the macroscopic problem is a bar that is exposed to a linear volumetric electrical and mechanical load according to the differential equations

$$\frac{\partial T}{\partial X} + X = 0 \quad \text{and} \quad \frac{\partial D}{\partial X} + X = 0, \tag{7.58}$$

where we have Dirichlet boundary conditions $u = \phi = 0$ to the left and traction-free Neumann boundary conditions $T = D = 0$ to the right. For our computation, the material parameters μ' and χ_0 are varying periodically in

$$\mu' = \chi_0 = \frac{3}{2} + \sin(2\pi k X), \tag{7.59}$$

whereas we set the parameter $\beta = 1$ in the energy density (7.55). According to Figure 7.1b), the free parameter k in Equation (7.59) determines the periodically repeating material domain size as $1/k$. Consequently, l/k gives the ratio between the overall length of the macroscopic problem and the size of a potential RVE. For example, when setting the dimensionless length $l = 1$ and the parameter $k = 2$, the bar would consist of two RVEs. The question then arises how the macroscopic response behaves in dependence of the RVE's size and if at some point, one can assume a scale separation.

Figure 7.2 shows the analytic solution of the boundary value problem defined above. One can see the solutions for the dimensionless displacement u' and scalar potential ϕ' for two
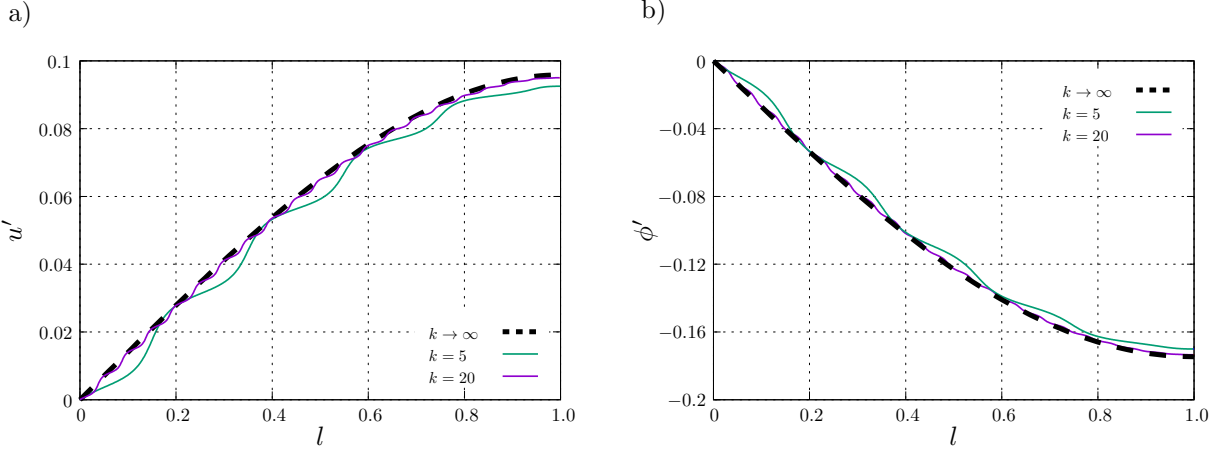
a)

b)

Figure 7.2: Analytic full-field solution to the boundary value problem presented in Figure 7.1 for different RVE sizes for a) the displacement u' and b) the scalar electric potential ϕ'. The dashed-dotted lines for $k \to \infty$ indicate the homogenized solution when scale separation is completely accomplished. One sees that the full-field solution for finite-sized RVEs converges to the homogenized solution for decreasing RVE size.

different RVE sizes with $k = 5$ and $k = 10$ as well as the solution for a homogenized approach using $k \to \infty$. For the homogenized approach, the microstructure is condensed to a point problem at the macroscale, and only the homogenized generalized stress and stiffness obtained from one single RVE is used in the solution of the boundary value problem. This approach corresponds to the previously mentioned scale separation assumption. In Figure 7.2, one can see that for a larger RVE size $k = 5$, the deviation of the full-field solution in comparison to the homogenized approach in dotted black lines is still distinct. Decreasing the RVE size by setting $k = 20$ gives a full-field solution much closer to the homogenized solution. As k is continuously increased, the difference between the full-field and the homogenized approach becomes small enough to justify the assumption of scale separation[1].

In this example, we see that the basic scheme successfully solves saddle point problems as well. The choice of linear reference medium is crucial for the convergence of the solver, which in this analysis was chosen to be

$$\mathbb{C}_0 = \max \mathbb{C}, \quad \mathbb{K}_0 = \min \mathbb{K} \quad \text{over } \mathcal{B}. \tag{7.60}$$

Numerical stability analysis of the fixed-point scheme. In this example, the reference medium's impact on the stability of the fixed-point scheme (7.37) is numerically investigated. The generalized form of the fixed-point scheme appears as

$$\mathbb{F}_{n+1} = \mathbf{K} \diamond \mathbb{F}_n + \mathbf{B}, \tag{7.61}$$

with the discretized system matrix $\mathbf{K}$ and the discrete constant vector $\mathbf{B}$. The stability of the fixed-point scheme is determined by the spectral radius ρ, which is the maximum absolute eigenvalue λ_{max} of the system matrix

$$\rho = \lambda_{max} = \max_i |\lambda_i(\mathbf{K})|. \tag{7.62}$$

---

[1]This example only serves as intuitive access to the concept of scale separation. The choice of RVE size can be a challenging task and is the topic of recent research [58, 169, 208].

For the case of non-linear problems such as solving the mechanical and electrical equilibrium equations for non-linear material models, the system matrix is dependent on the variables, and thus the eigenvalues are constantly changing while iterating. This makes it difficult to make statements on the convergence stability. Independent of the material models used, the computation of the fluctuation sensitivities is, however, always a linear equation, which leads to a constant system matrix $\mathbf{K}$, see Equation (7.21). For such scenarios, one can state that the fixed-point iteration converges to the solution of the boundary value problem if the spectral radius of $\mathbf{K}$ is lower than one

$$\rho < 1. \tag{7.63}$$

One can additionally find relations between the spectral radius and the fixed-point scheme's convergence rate, see, for example, ESTEP [44]. A low spectral radius corresponds to high convergence rates, while a spectral radius close to one leads to a strong decrease in convergence rate. The system matrix of the fixed-point scheme (7.61) can be identified from Equations (7.38) and (7.28) as follows

$$\mathbf{K} = \omega^{-1}(\widehat{\underline{\Gamma}}\,(\omega\,\underline{\mathbb{C}}^{\Delta})), \tag{7.64}$$

where ω and ω^{-1} denote the discrete forward and inverse Fourier transform matrices as defined for the one-dimensional case in Equation (5.4).

In the multiscale framework outlined previously, one would usually first solve the non-linear equilibrium equation and then use the converged moduli to solve the linear equation for the fluctuation sensitivities. As this example focuses on the convergence of the linear solver, however, we will immediately prescribe the moduli with some given phase contrast and skip the equilibrium equation. As we are now considering a one-dimensional laminate with two layers of the same thickness, the stiffness within one layer must be constant.

In this example, the stiffness in phase one is $\mathbb{A}^{*(1)} = 1$, $\mathbb{K}^{*(1)} = -1$ and $q^{*(1)} = 1$. We consider a phase contrast of five and set the stiffness in the second layer to $\mathbb{A}^{*(2)} = 5$, $\mathbb{K}^{*(2)} = -5$ and $q^{*(2)} = 5$. The RVE is coarsely discretized by 2^4 grid points. However, this is sufficient as in the one-dimensional case, the stiffness is constant and thus the maximum eigenvalue of $\mathbf{K}$ in dependence of the reference medium and the phase contrast is independent of the mesh resolution. Using a coarse grid then saves time as the computation of the eigenvalues of the system matrix is a computationally costly operation.

With the mechanical boundary value problem at hand, we now investigate the impact of the reference medium $\mathbb{A}^0$, $\mathbb{K}^0$ and q^0 on the convergence rate through the spectral radius. Figure 7.3 shows the boundary of stability with respect to the reference medium, which is the isosurface of the spectral radius $\rho = 1$. For a spectral radius lower than one, convergence is assured. For a spectral radius larger than one, physical solutions can be obtained, but there is no guarantee for convergence. One can see that one does not necessarily need to use a coupled preconditioning for stable convergence, i.e., $q^0 = 0$. However, the range of reference medium for $\mathbb{A}^0$ and $\mathbb{K}^0$ then narrows down. Having a look at the value for the spectral radius ρ in the first contour plot of Figure 7.3 for the uncoupled preconditioning, we also see that the lowest spectral radius is larger compared to the cases where there is coupled preconditioning in B) and C). Using coupled preconditioning thus enables higher convergence rates. It should be mentioned that the coupled preconditioning also needs a higher amount of computations as the Green operator then has coupled blocks as well. However, a coupled preconditioning grants more flexibility when choosing the reference medium.
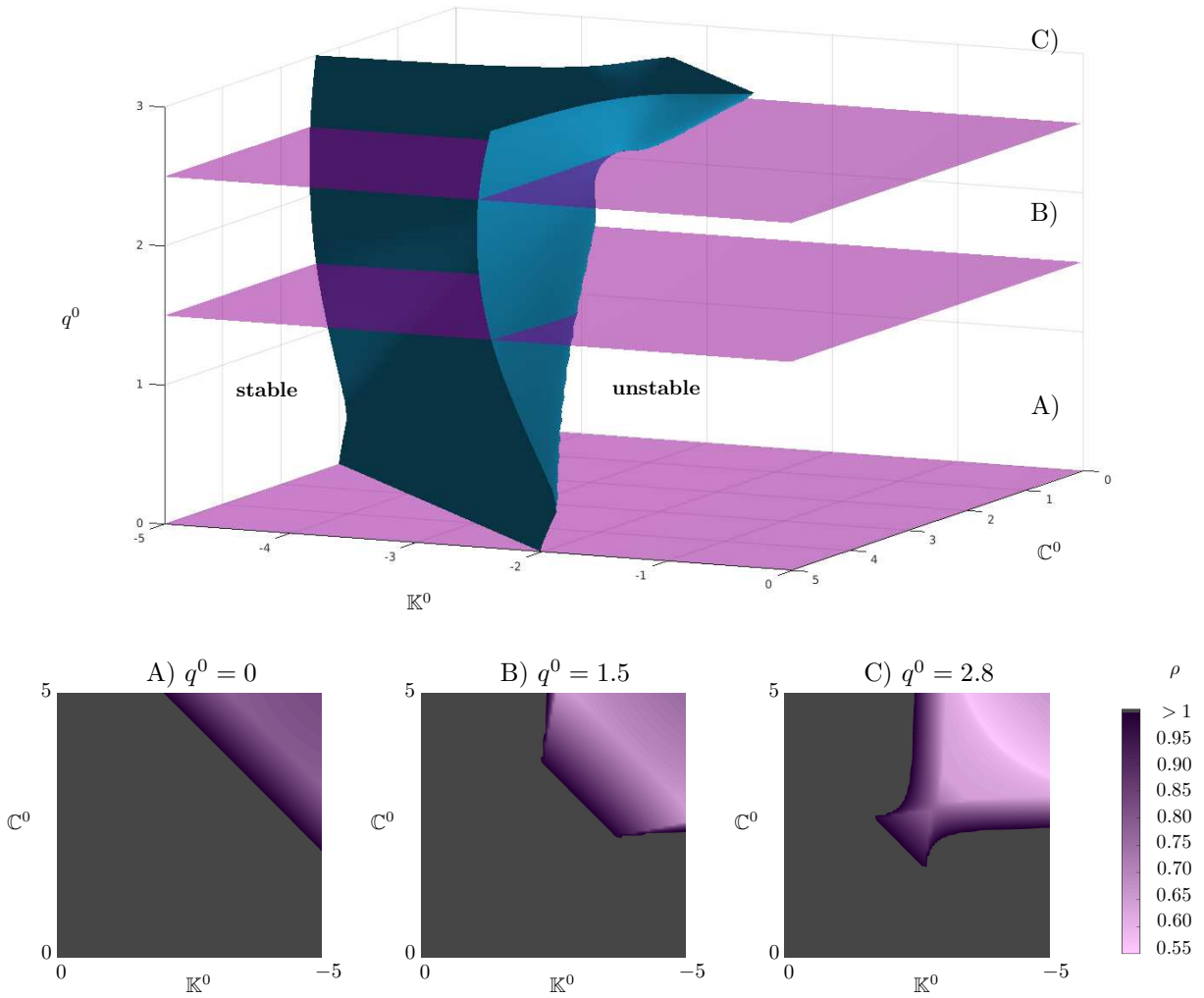
Figure 7.3: On top, the isosurface for $\rho = 1$ in dependence of the linear reference medium is depicted. Left of the isosurface is the stable region where $\rho < 1$. One can see that the stable region widens up, applying a coupled preconditioning q^0. On the bottom, one can see contour plots for the value of ρ at different coupled reference medium A) $q^0 = 0$, B) $q^0 = 1.5$ and C) $q^0 = 2.8$ as indicated by the surfaces in the upper graph. Here, the grey region indicates the instability of the solver due to $\rho > 1$. The contour plots show that using coupled preconditioning allows for a larger stability region and potentially gives lower spectral radii.

7.4.3. Coupled two-dimensional examples

In this section, the framework is extended to two-dimensional problems. First, a simple two-dimensional laminate problem that allows for an analytic solution is considered for testing the code's validity and convergence properties. Next, simulations using a more complex random microstructure are carried out, where the focus lies on the convergence of the homogenized macro-solver. Lastly, a full multiscale simulation is carried out for an electroactive gripper.

Analytic and numeric homogenization for a two-dimensional laminate. As a first two-dimensional example, we consider a simple two-dimensional laminate structure as visualized in Figure 7.4. It consists of two phases where the volume fraction of material
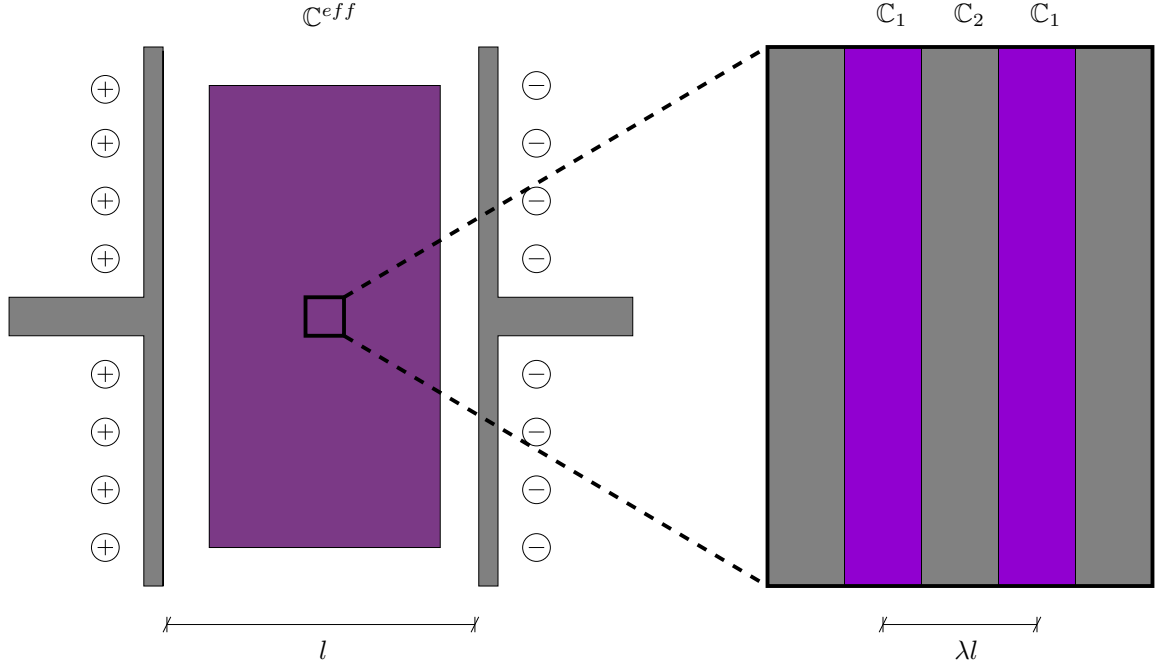
Figure 7.4: A macroscopically homogeneously appearing body reveals a laminar microstructure on a lower scale, where $\lambda \ll 1$. As the microstructure is periodically repeating, we choose an RVE of size λl where the volume fraction of the material one and two is 50%. In this example, we do not consider a fully discretized macroscopic problem, but use a homogenized macro-solver according to Section 6.4.

one and material two is 50%. In line with the Hill-Mandel condition, we assume periodic boundary conditions for the primary variables. For such a boundary value problem with laminate microstructure, it is possible to derive analytic solutions for some given macroscopic load. In the following, we will derive said analytic solution to compare our simulations to and to prove the validity of the underlying code. We, therefore, start with the two-dimensional reduction of the differential equilibrium equations (2.100) and (3.22)$_1$ in the absence of volume charges and body forces

$$
\begin{aligned}
T_{11,1} + T_{12,2} = 0, \qquad F_{12,1} - F_{11,2} = 0, \\
T_{21,1} + T_{22,2} = 0, \qquad F_{22,1} - F_{21,2} = 0, \\
E_{2,1} - E_{1,2} = 0, \qquad D_{1,1} + D_{2,2} = 0,
\end{aligned}
\tag{7.65}
$$

where we use index notation to indicate the differentiation with respect to X_1 and X_2. Next, we take into account that the laminate microstructure is only changing when going along the X_1-direction. In such a case and for periodic boundary conditions, any point within the laminate cannot be distinguished by any other point, which is shifted in the X_2-direction. The solution thus can be only dependent on the X_1 coordinate. Consequently, all derivatives with respect to X_2 in the equilibrium equations (7.65) can be neglected, and we obtain the reduced set

$$
\begin{aligned}
T_{11,1} = 0, \qquad F_{12,1} = 0, \\
T_{21,1} = 0, \qquad F_{22,1} = 0, \\
E_{2,1} = 0, \qquad D_{1,1} = 0.
\end{aligned}
\tag{7.66}
$$

Looking at the latter equation, we see that these components of the stress, strain, electric displacement and the electric field are not dependent on X_1. As they are also not dependent on X_2 as previously mentioned, they must be constant within the whole solution

domain

$$T_{11} = \text{constant}, \qquad F_{12} = \text{constant},$$
$$T_{21} = \text{constant}, \qquad F_{22} = \text{constant}, \qquad\qquad (7.67)$$
$$E_2 = \text{constant}, \qquad D_1 = \text{constant}.$$

Additionally, as the stress and the electric displacement are constant within one phase and are described through the material law with respect to the strain and electric field, the strain and electric field must also be *constant within one phase*. In the following, we will therefore use the notation $(\bullet)^{(1)}$ for quantities associated with phase one and $(\bullet)^{(2)}$ for quantities associated with phase two.

Additional equations for the solution of the strain and electric displacement emerge from the average relation between the macroscopic applied load $\overline{F}_{ij}$ and $\overline{D}_i$ and the microscopic fields $F_{ij}^{(1)}$, $F_{ij}^{(2)}$, $D_i^{(1)}$ and $D_i^{(2)}$. For a laminate with 50% volume fraction, said average can be obtained as

$$\frac{1}{2}(F_{ij}^{(1)} + F_{ij}^{(2)}) = \overline{F}_{ij} \quad \text{and} \quad \frac{1}{2}(D_i^{(1)} + D_i^{(2)}) = \overline{D}_i. \qquad (7.68)$$

Equations (7.67) and (7.68) give twelve equations for twelve unknowns. These equations are summarized below

$$
\boxed{
\begin{aligned}
&F_{22}^{(1)} = F_{22}^{(2)} = \overline{F}_{22}, && \frac{1}{2}(F_{11}^{(1)} + F_{11}^{(2)}) = \overline{F}_{11}, && \frac{\partial \psi^{*\prime(1)}}{\partial F_{22}} = \frac{\partial \psi^{*\prime(2)}}{\partial F_{22}}, \\[2mm]
&F_{12}^{(1)} = F_{12}^{(2)} = \overline{F}_{12}, && \frac{1}{2}(F_{21}^{(1)} + F_{21}^{(2)}) = \overline{F}_{21}, && \frac{\partial \psi^{*\prime(1)}}{\partial F_{21}} = \frac{\partial \psi^{*\prime(2)}}{\partial F_{21}}, \\[2mm]
&D_1^{(1)} = D_1^{(2)} = \overline{D}_1, && \frac{1}{2}(D_2^{(1)} + D_2^{(2)}) = \overline{D}_2, && \frac{\partial \psi^{*\prime(1)}}{\partial D_2} = \frac{\partial \psi^{*\prime(2)}}{\partial D_2},
\end{aligned}
}
\qquad (7.69)
$$

where we use the constitutive relation that $\boldsymbol{T} = \dfrac{\partial \psi}{\partial \boldsymbol{F}}$ and $\boldsymbol{E} = -\dfrac{\partial \psi}{\partial \boldsymbol{D}}$ in the last column of the boxed equations. Depending on the energy density function's complexity, the last column gives non-linear equations with respect to $\boldsymbol{F}$ and $\boldsymbol{D}$. This non-linearity is the case for the energy density (7.53) we are using. We thus use a numerical solver with high accuracy to obtain the solution to the set of equations (7.69). Having the solution, the macroscopic tangent can then be determined by a finite difference approximation of the analytic solution, where we use the perturbation magnitude $\epsilon = 10^{-6}$.

We now want to investigate the mesh convergence of an FFT-based solution scheme against the analytic solution. We therefore apply a macroscopic load of $\overline{F}_{11} = 1.0$, $\overline{F}_{12} = 0.5$, $\overline{F}_{21} = 0.0$, $\overline{F}_{22} = 1.5$, $\overline{D}_1' = 0.45$ and $\overline{D}_2' = 0.05$. The material parameters used in the simulation for the two phases can be found in Table 7.1. The simulation is then carried out for an increasing mesh resolution in X_1-direction, while the number of grid points in X_2-direction is kept constant with 5 grid points. The error between the analytic and the numerically computed tangent using Equation (7.21) is measured through the following error norm

$$\text{Error} = ||\mathbb{C}^{algo} - \mathbb{C}^{anal}||. \qquad (7.70)$$

The results for the mesh convergence study are visualized in Figure 7.5. Figure 7.5a) shows the fluctuative deformation of the laminate and Figure 7.5b) shows the error norm (7.70) against the grid resolution in a double logarithmic plot. As expected, one sees that the error is decreasing for an increasing mesh resolution and that the convergence rate is approximately 1.

Table 7.1: Material parameters used for laminate simulation.

no.	par.	name	unit	value
1.	$\mu^{(1)}$	shear modulus phase 1	GPa	1.0
2.	$\mu^{(2)}$	shear modulus phase 2	GPa	2.0
3.	$\beta^{(1)}$	compressibility parameter phase 1	–	10
4.	$\beta^{(2)}$	compressibility parameter phase 2	–	10
5.	$\chi^{(1)}$	electric susceptibility phase 1	–	10
6.	$\chi^{(2)}$	electric susceptibility phase 2	–	20

a)

b)
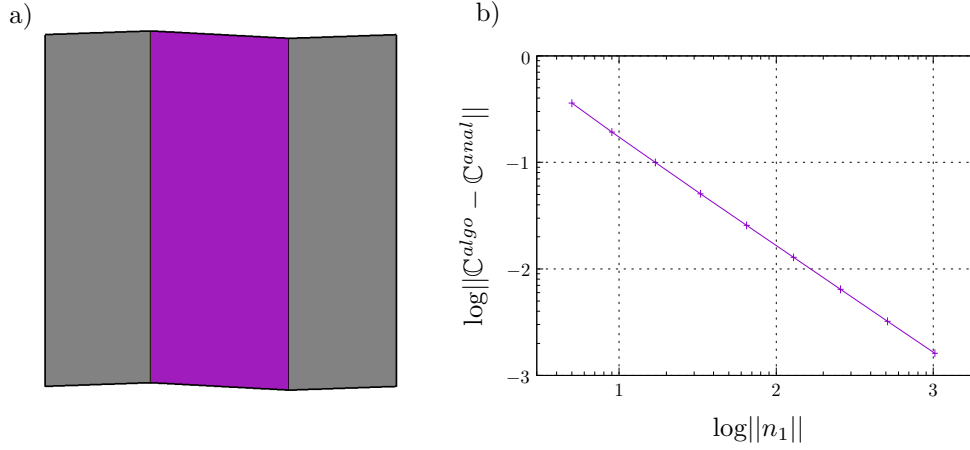
Figure 7.5: a) The laminate RVE is deformed due to the macroscopic load $\overline{F}_{11} = 1.0$, $\overline{F}_{12} = 0.5$, $\overline{F}_{21} = 0.0$, $\overline{F}_{22} = 1.5$, $\overline{D}'_1 = 0.45$ and $\overline{D}'_2 = 0.05$. Only the fluctuative contribution of the displacements are visualized. b) Increasing the mesh resolution decreases the error between analytic and algorithmically consistent tangent, where a convergence rate of approximately 1 is observed.
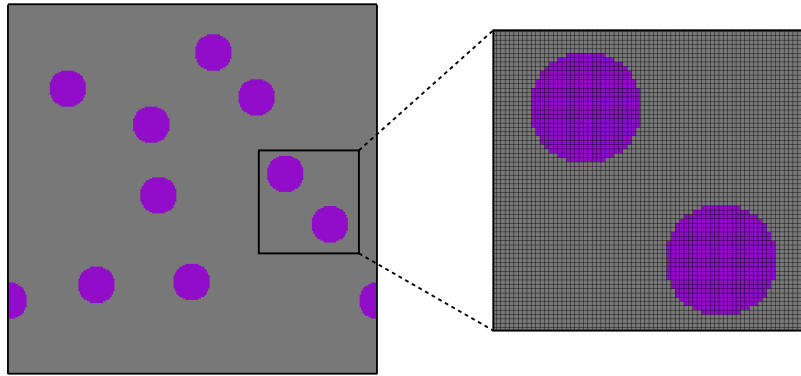
Figure 7.6: To the left, one can see the RVE with its periodic microstructure. The microstructure consists of two phases: A soft matrix material and ten randomly distributed spherical stiff inclusions of radius $r = 0.05$. The volume fraction of the inclusions is approximately 8%. To the right, one can see a zoom in on the voxel discretization of two spherical inclusions.

Homogenization for electro-mechanically coupled random microstructure. In the previous section, we used a simple microstructure example to show that the computational framework satisfies mesh convergence and converges against the analytic solution. Now, we want to demonstrate that the framework is stable and can be extended to the more complex microstructure presented in Figure 7.6. The RVE at hand consists of a soft

Table 7.2: Normalized material parameters used for laminate simulation.

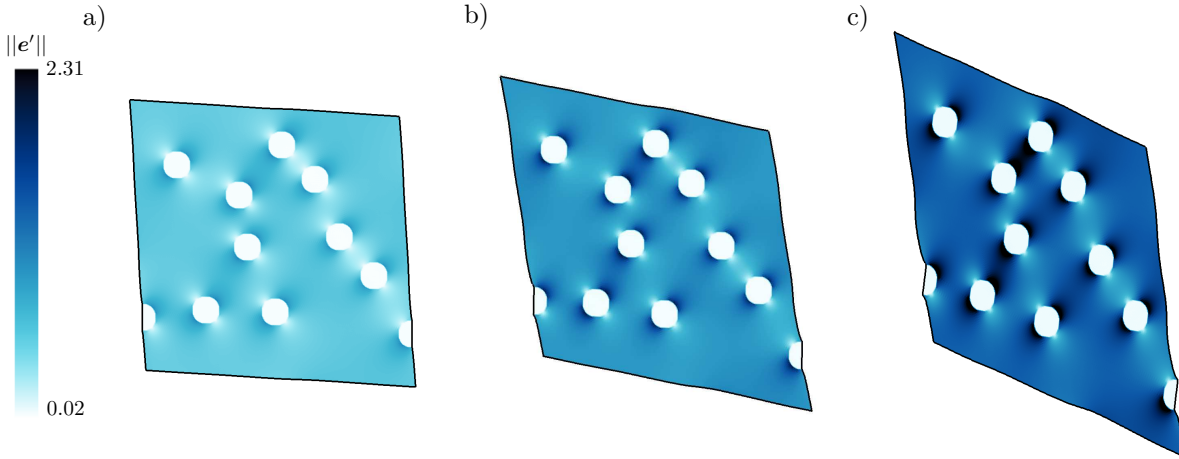| no.	par.	name	unit	value
1.	$\mu'^{,matr}$	shear modulus matrix	–	1.0
2.	$\mu'^{,incl}$	shear modulus inclusions	–	100.0
3.	$\beta'^{,matr}$	compressibility parameter matrix	–	10
4.	$\beta'^{,incl}$	compressibility parameter inclusions	–	1
5.	χ^{matr}	electric susceptibility matrix	–	1
6.	χ^{incl}	electric susceptibility inclusions	–	100

Figure 7.7: An RVE consisting of a soft polymer matrix and stiff, quasi-conducting particles deforms under a macroscopically applied electric displacement $\overline{\boldsymbol{D}}$. The inclusions have a radius of $0.05l$ and a volume fraction of 8%. The deformed RVE is visualized at load step a) $\overline{D}'_1 = \overline{D}'_2 = 0.6$, b) $\overline{D}'_1 = \overline{D}'_2 = 1.2$ and c) $\overline{D}'_1 = \overline{D}'_2 = 1.8$. The contour shows the magnitude of the normalized electric field $||\boldsymbol{e}'||$ in the current space.

polymer matrix and ten randomly distributed stiff spheres of high electric susceptibility. The inclusions have a radius of $r = 0.05l$ where l is the side length of the squared RVE. The volume fraction of the spherical inclusions with respect to the RVE's volume is approximately 8%. Here, we use 257×257 equidistant grid points for the discretization of the boundary value problem.

We now apply a macroscopic homogenized electric displacement of $\overline{D}'_1 = \overline{D}'_2 = 1.8$ within 18 loadsteps. The loading process is performed under zero shear stress $\overline{T}'_{12} = \overline{T}'_{21} = 0$, which is assured by using a homogenized driver as described in Section 6.4. Additionally, the macroscopic normal strain components $\overline{F}'_{11} = \overline{F}'_{22} = 0$ are kept zero to avoid rotations of the RVE, which would lead to instabilities in the solution scheme. The material parameters for the matrix material and the inclusions can be found in Table 7.2. The choice of parameters is supposed to reflect a soft but rather incompressible polymer matrix that envelopes stiff, quasi-conducting particles. Figure 7.8 shows the contour plot for the magnitude of the current electric field $||\boldsymbol{e}'||$ as obtained through the push-forward defined in Equation (3.4). One can see characteristic peaks in the magnitude at the interface of matrix and inclusion as well as regions of high electric fields in between particles which are close to each other. These concentrations in the electric field might lead to material instabilities and, consequently, to a loss of the iterative solver's convergence. For a quantitative investigation of such instabilities, the reader is referred to MIEHE ET AL. [131]. Additionally, as we are using a non-linear model, the phase contrast is load-dependent,
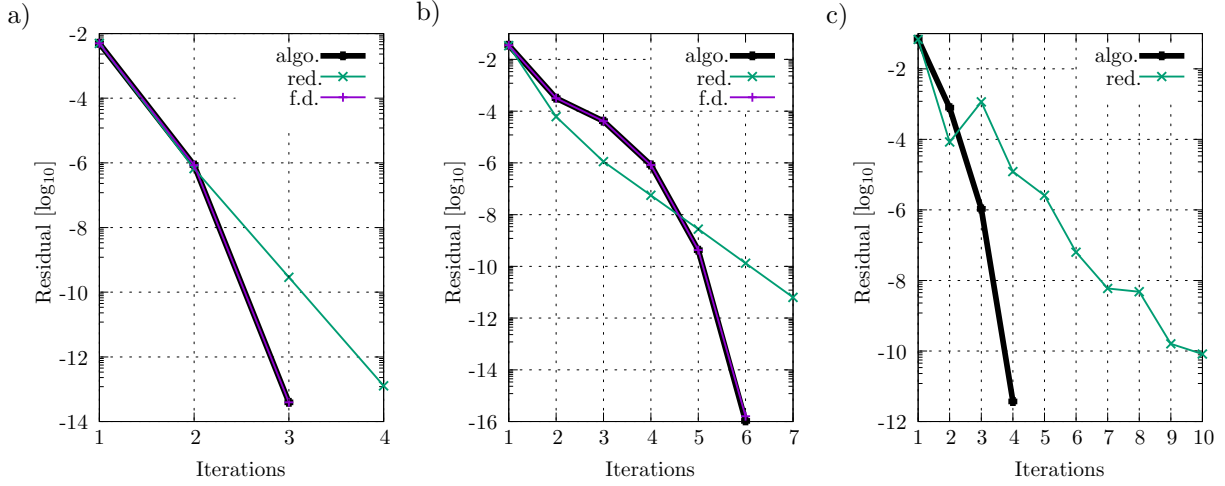
a)   b)   c)

Figure 7.8: Macroscopic convergence at loads a) $\overline{D}'_1 = \overline{D}'_2 = 0.6$, b) $\overline{D}'_1 = \overline{D}'_2 = 1.2$ and c) $\overline{D}'_1 = \overline{D}'_2 = 1.8$. The driver's residual over the Netwon iterations is displayed for the algorithmic tangent computation, the reduced algorithmic tangent computation with $\frac{\partial \overline{F}}{\partial \overline{D}} = \frac{\partial \overline{D}}{\partial \overline{F}} = \boldsymbol{0}$ and a finite difference-based approach. One can see that the algorithmic and the finite difference-based approach gives almost identical results, but the finite difference-based approach fails to give any results in the last load step. The higher the load, the more macroscopic iterations are needed for the reduced approach, as the error in the reduced tangent due to the neglected coupling becomes larger.

and thus the convergence rate deteriorates for large loads.

We now want to take a closer look at the macroscopic convergence of the homogenized driver, where we use the algorithmic tangent to update the macroscopic strains until we reach the prescribed macroscopic stress, which are in our case $\overline{T}'_{12} = \overline{T}'_{21} = 0$. For our study, we have a look at the residual (6.49) of the Newton update for three different macroscopic tangent computations:

(i) a tangent computation based on Equation (7.21) taking full coupling into account,

(ii) a tangent computation based on Equation (7.21) but neglecting coupling terms $\frac{\partial \overline{F}}{\partial \overline{D}} = \frac{\partial \overline{D}}{\partial \overline{F}} = \boldsymbol{0}$ and

(iii) a finite difference-based approach according to Equation (7.46).

In Figure 7.8, the residual of the homogenized driver at each Netwon iteration is displayed at loads a) $\overline{D}'_1 = \overline{D}'_2 = 0.6$, b) $\overline{D}'_1 = \overline{D}'_2 = 1.2$ and c) $\overline{D}'_1 = \overline{D}'_2 = 1.8$. The macroscopic driver stops at a given load state when the residual takes a value below $\overline{\boldsymbol{R}} < 10^{-10}$. As expected, the algorithmic solution and the finite difference-based approach give almost identical convergence rates for load step one and two, as both take full coupling into account. Both show quadratic convergence in the vicinity of the solution. However, in our example, the finite difference-based approach failed to converge in the last load step. The reduced approach without coupling terms shows rather a linear convergence rate, where the convergence is faster for low loading. This is due to increasing coupling effects with larger loads. The reduced tangent needs less computational effort compared to the other two approaches. It thus might be viable to use the reduced approach when loading is still low to moderate.

Figure 7.9 compares the computational time of the algorithmic tangent and the finite difference-based approach with respect to the reduced approach. One can see that the finite difference-based computation is the slowest of the three approaches. Its compu-
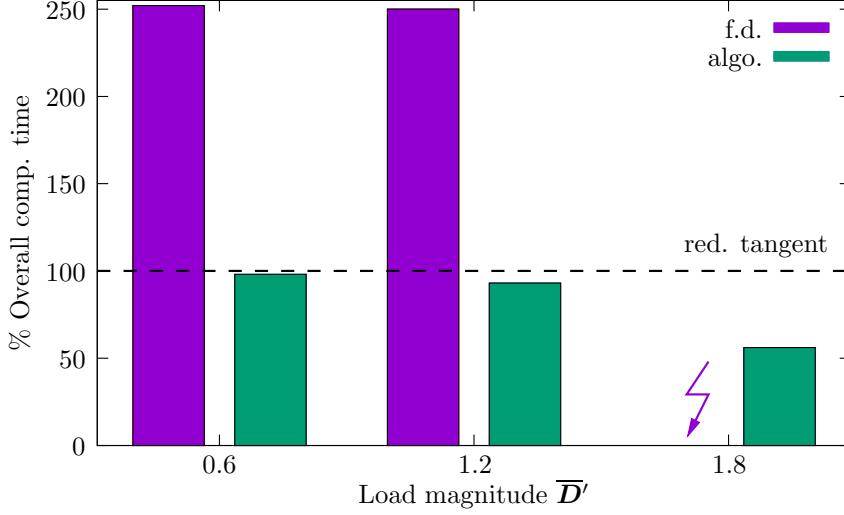
Figure 7.9: Time comparison between finite difference-based, algorithmic and reduced tangent at loads $\overline{D}'_1 = \overline{D}'_2 = 0.6$, $\overline{D}'_1 = \overline{D}'_2 = 1.2$ and $\overline{D}'_1 = \overline{D}'_2 = 1.8$. One can see that the reduced and the algorithmic tangent both need less computational time. At the higher loads, the full algorithmic tangent's overall computation time is the lowest, indicating that the coupling terms become relatively important for the overall macroscopic convergence.

tational times is increased by a factor of approximately 2.5 compared to the reduced approach. At load $\overline{D}' = 0.6$, the computational time of the algorithmic approach and the reduced one is almost equal, which indicates that in this examples this is the load state where the advantage of the computational reduction in the tangent and its lower accuracy within the Netwon iteration equal out compared to the fully coupled approach. At load $\overline{D}' = 1.2$, the fully coupled one is then faster than the other two. The advantage in computational time becomes more distinct at the highest load $\overline{D}' = 1.8$.

Multiscale simulation of electroactive gripper. Finally, we want to test the framework for a full FE-FFT multiscale example, as shown in Figure 7.10. It is inspired by experimental research on similar electroactive grippers [2, 5]. The macroscopic gripper consists of two arms, which are clamped to the left and right. A vector potential of up to $\overline{A}' = \pm 7.2$ is applied left and right, which corresponds to an applied electric field in the vertical direction. These electric boundary conditions are supposed to mimic electrodes that are attached to the solid on top and on bottom of each arm. Note that it might be difficult for more complicated geometries to apply physically reasonable boundary conditions through a vector potential. In such cases, mixed formulations might be a viable option. On the microscale, these problems are not arising as we assume periodicity in the electric potential, and the boundary geometry of the RVE is relatively simple. The microstructure in our example consists of a soft polymer matrix and a stiff quasi-conducting spherical inclusion of unit-less diameter $d = 0.5$. The material parameters are the same as in the previous example and can be found in Table 7.2. The macroscale is discretized by 80 rectangular bilinear finite elements, where we use 4 Gauss quadrature points for the integration. The software FEAP [188] is used for the FEM-simulation of the macroscale. The microscale is discretized by 51×51 equidistant grid points, where we use a self-written FFT-based solver for the periodic microscale simulation.
Figure 7.11 shows the solution for the multiscale simulation at load a) $\overline{A}' = \pm 0.6$,
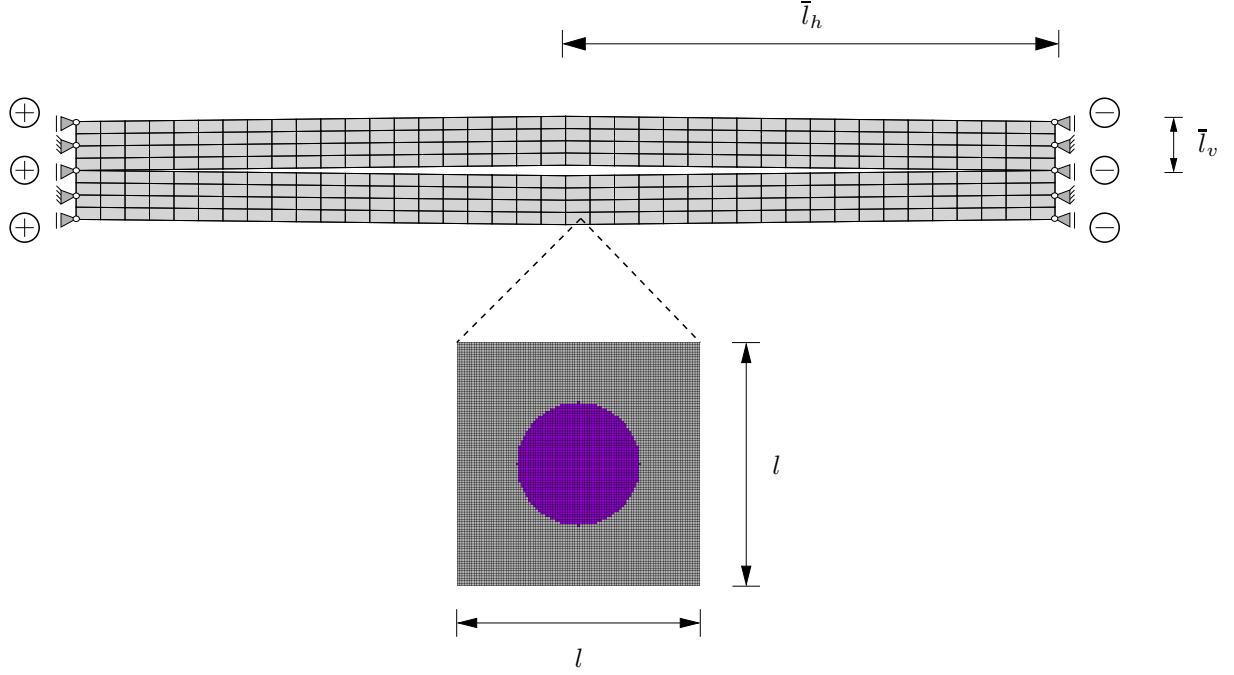
Figure 7.10: Boundary value problem for an electro-active gripper. The two arms are clamped on the left and right, restricting any horizontal movement. The unit-less lengths of the gripper are $\bar{l}_h = 10$ and $\bar{l}_h = 1$. A vector potential of up to $\overline{A}' = \pm 7.2$ is applied at the left and right, which corresponds to a vertical gradient in scalar potential, i.e., a vertically applied electric field. On the microscale, the RVE of side-length $l = 1/1000$ consists of a soft polymer matrix and a stiff quasi-conducting spherical inclusion of unit-less diameter $d = 0.5l$.
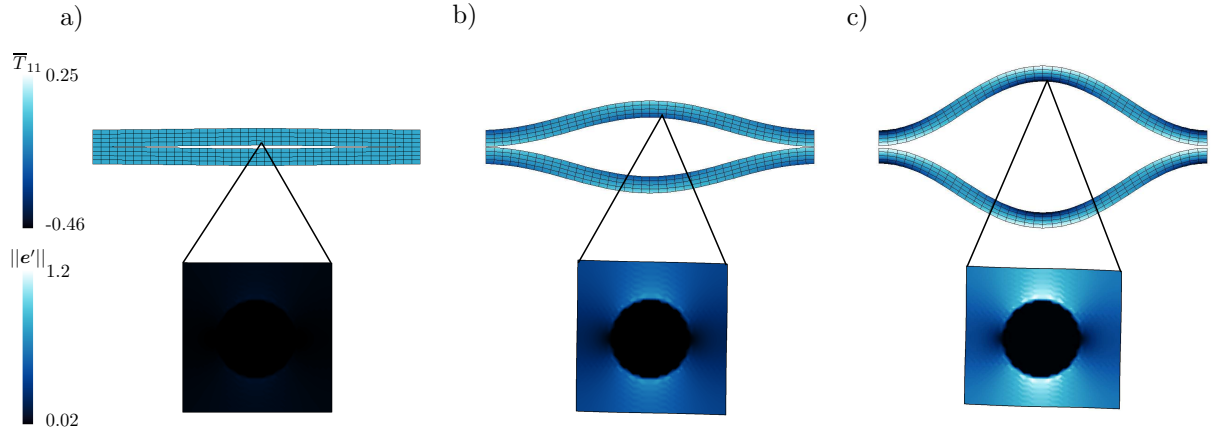

Figure 7.11: Solution for the multiscale gripper simulation at load a) $\overline{A}' = \pm 0.6$, b) $\overline{A}' = \pm 3.6$ and c) $\overline{A}' = \pm 7.2$. On the macroscale, one sees that the gripper is buckling. On the outer sides of the arms, one observes tension, while the inner sides are compressed. This behavior can also be observed on a microscale. Here, we see low electric fields in the quasi-conducting stiff inclusion.

b) $\overline{A}' = \pm 3.6$ and c) $\overline{A}' = \pm 7.2$. One can see that the gripper opens up as the electric load is increased. The macroscopic effect can be explained by the attraction of the electrodes on the top and the bottom of each arm. As the electric field strength is increased, which corresponds to the increase of vector potential as depicted in Figure 7.10, the electrodes attract each other and compress the material in between them. Due to the high Poisson ratio of the material, it tries to elongate in perpendicular direction of the compression, i.e., to the sides. However, its movement in this direction is restricted

by the walls to the left and right, which leads to buckling. On the microscale, we see that the RVE is compressed as well, where the electric field is low in the quasi-conducting inclusion. Theoretically, such a set-up would work without any underlying microstructure. However, the inclusion of quasi-conducting particles into a soft polymer matrix might favorably influence the contraction behavior and lowers the electric field required for opening the gripper, see VALLICOTTI ET AL. [195], for example.

7.5. Appendices

7.5.1. Macroscopic tangent computation

We now want to outline the explicit expression of the coupled softening term appearing in the computation of the algorithmic tangent (4.40), see also (7.16). We, therefore, start with the linearized increment of the macroscopic stresses (7.9) in terms of the macroscopic tangent

$$
\begin{bmatrix} \Delta\overline{\boldsymbol{T}} \\ \Delta\overline{\boldsymbol{E}} \end{bmatrix} = \overline{\mathbb{C}}^{algo} \diamond \begin{bmatrix} \Delta\overline{\boldsymbol{F}} \\ \Delta\overline{\boldsymbol{D}} \end{bmatrix} = \begin{bmatrix} \dfrac{\partial\overline{\boldsymbol{T}}}{\partial\overline{\boldsymbol{F}}} & \dfrac{\partial\overline{\boldsymbol{T}}}{\partial\overline{\boldsymbol{D}}} \\ \dfrac{\partial\overline{\boldsymbol{E}}}{\partial\overline{\boldsymbol{F}}} & \dfrac{\partial\overline{\boldsymbol{E}}}{\partial\overline{\boldsymbol{D}}} \end{bmatrix} \diamond \begin{bmatrix} \Delta\overline{\boldsymbol{F}} \\ \Delta\overline{\boldsymbol{D}} \end{bmatrix}. \tag{7.71}
$$

As outlined in Chapter 4, the macroscopic stresses are volume averages of the microscopic stresses. As a consequence, the macroscopic dual variables $\mathbb{S}$ are dependent on the microscopic primary fields $\mathbb{G}$, which themselves are dependent on the macroscopic load states $\overline{\mathbb{G}}$. We thus need to apply the chain rule, which gives

$$
\begin{bmatrix} \Delta\overline{\boldsymbol{T}} \\ \Delta\overline{\boldsymbol{E}} \end{bmatrix} = \begin{bmatrix} \dfrac{1}{V}\displaystyle\int_{\mathcal{B}^0}\left(\dfrac{\partial\boldsymbol{T}}{\partial\boldsymbol{F}}:\dfrac{\partial\boldsymbol{F}}{\partial\overline{\boldsymbol{F}}}+\dfrac{\partial\boldsymbol{T}}{\partial\boldsymbol{D}}\cdot\dfrac{\partial\boldsymbol{D}}{\partial\overline{\boldsymbol{F}}}\right)dV & \dfrac{1}{V}\displaystyle\int_{\mathcal{B}^0}\left(\dfrac{\partial\boldsymbol{T}}{\partial\boldsymbol{D}}\cdot\dfrac{\partial\boldsymbol{D}}{\partial\overline{\boldsymbol{D}}}+\dfrac{\partial\boldsymbol{T}}{\partial\boldsymbol{F}}:\dfrac{\partial\boldsymbol{F}}{\partial\overline{\boldsymbol{D}}}\right)dV \\ \dfrac{1}{V}\displaystyle\int_{\mathcal{B}^0}\left(\dfrac{\partial\boldsymbol{E}}{\partial\boldsymbol{F}}:\dfrac{\partial\boldsymbol{F}}{\partial\overline{\boldsymbol{F}}}+\dfrac{\partial\boldsymbol{E}}{\partial\boldsymbol{D}}\cdot\dfrac{\partial\boldsymbol{D}}{\partial\overline{\boldsymbol{F}}}\right)dV & \dfrac{1}{V}\displaystyle\int_{\mathcal{B}^0}\left(\dfrac{\partial\boldsymbol{E}}{\partial\boldsymbol{D}}\cdot\dfrac{\partial\boldsymbol{D}}{\partial\overline{\boldsymbol{D}}}+\dfrac{\partial\boldsymbol{E}}{\partial\boldsymbol{F}}:\dfrac{\partial\boldsymbol{F}}{\partial\overline{\boldsymbol{D}}}\right)dV \end{bmatrix} \diamond \begin{bmatrix} \Delta\overline{\boldsymbol{F}} \\ \Delta\overline{\boldsymbol{D}} \end{bmatrix}. \tag{7.72}
$$

Insertion of the decomposition of the primary variables (4.5) and (4.28) then yields

$$
\begin{bmatrix} \Delta\overline{\boldsymbol{T}} \\ \Delta\overline{\boldsymbol{E}} \end{bmatrix} = \begin{bmatrix} \dfrac{1}{V}\displaystyle\int_{\mathcal{B}^0}\mathbb{A}+\mathbb{A}:\dfrac{\partial\widetilde{\boldsymbol{F}}}{\partial\overline{\boldsymbol{F}}}+\boldsymbol{q}\cdot\dfrac{\partial\widetilde{\boldsymbol{D}}}{\partial\overline{\boldsymbol{F}}}\,dV & \dfrac{1}{V}\displaystyle\int_{\mathcal{B}^0}\boldsymbol{q}+\boldsymbol{q}\cdot\dfrac{\partial\widetilde{\boldsymbol{D}}}{\partial\overline{\boldsymbol{D}}}+\mathbb{A}:\dfrac{\partial\widetilde{\boldsymbol{F}}}{\partial\overline{\boldsymbol{D}}}\,dV \\ \dfrac{1}{V}\displaystyle\int_{\mathcal{B}^0}\boldsymbol{q}^T+\boldsymbol{q}^T:\dfrac{\partial\widetilde{\boldsymbol{F}}}{\partial\overline{\boldsymbol{F}}}+\mathbb{K}\cdot\dfrac{\partial\widetilde{\boldsymbol{D}}}{\partial\overline{\boldsymbol{F}}}\,dV & \dfrac{1}{V}\displaystyle\int_{\mathcal{B}^0}\mathbb{K}+\mathbb{K}\cdot\dfrac{\partial\widetilde{\boldsymbol{D}}}{\partial\overline{\boldsymbol{D}}}+\boldsymbol{q}^T:\dfrac{\partial\widetilde{\boldsymbol{F}}}{\partial\overline{\boldsymbol{D}}}\,dV \end{bmatrix} \cdot \begin{bmatrix} \Delta\overline{\boldsymbol{F}} \\ \Delta\overline{\boldsymbol{D}} \end{bmatrix}, \tag{7.73}
$$

where we used the abbreviations introduced in Equation (7.14). Comparing the latter equation with the stress increment (7.15) and the general form (7.16) allows us to identify the softening contribution

$$
\mathbb{C} \diamond \dfrac{\partial\widetilde{\mathbb{G}}}{\partial\overline{\mathbb{G}}} = \begin{bmatrix} \mathbb{A}:\dfrac{\partial\widetilde{\boldsymbol{F}}}{\partial\overline{\boldsymbol{F}}}+\boldsymbol{q}\cdot\dfrac{\partial\widetilde{\boldsymbol{D}}}{\partial\overline{\boldsymbol{F}}} & \boldsymbol{q}\cdot\dfrac{\partial\widetilde{\boldsymbol{D}}}{\partial\overline{\boldsymbol{D}}}+\mathbb{A}:\dfrac{\partial\widetilde{\boldsymbol{F}}}{\partial\overline{\boldsymbol{D}}} \\ \boldsymbol{q}^T:\dfrac{\partial\widetilde{\boldsymbol{F}}}{\partial\overline{\boldsymbol{F}}}+\mathbb{K}\cdot\dfrac{\partial\widetilde{\boldsymbol{D}}}{\partial\overline{\boldsymbol{F}}} & \mathbb{K}\cdot\dfrac{\partial\widetilde{\boldsymbol{D}}}{\partial\overline{\boldsymbol{D}}}+\boldsymbol{q}^T:\dfrac{\partial\widetilde{\boldsymbol{F}}}{\partial\overline{\boldsymbol{D}}} \end{bmatrix}, \tag{7.74}
$$

in terms of the fluctuation sensitivities.

7.5.2. Electro-mechanically coupled Green operator

We now want to demonstrate the computation of the coupled Green operator as needed in the Lippmann-Schwinger and Lippmann-Schwinger-type equations (7.7) and (7.27). We will now use index notation for the following computation, where we assume that the metric is described by the Euclidean metric in Cartesian coordinates. Consequently, there is no difference in the co- and contravariant space entries. No up-down-indication is needed. Therefore, all indices are lowered. The governing differential equations (7.6) then appear in index notation as follows

$$
\begin{aligned}
(\mathbb{A}^0_{ijkl} F_{kl} + q^0_{ijk} D_k)_{,j} &= -\tau^m_{ij,j}, \\
\epsilon_{ijk}(g^0_{klm} F_{lm} + \mathbb{K}^0_{kl} D_l)_{,j} &= -\epsilon_{ijk}\tau^e_{k,j},
\end{aligned}
\tag{7.75}
$$

where ϵ_{ijk} indicates the Levi-Civita symbol. Key idea is to evaluate the derivatives appearing in the latter equations by means of Fourier transforms. The explicit expression for derivatives in the discrete Fourier space (5.11) can be written in a generic index-form at *each node*

$$
(\bullet)_{,j} = \text{fft}^{-1}\{\text{fft}(\bullet)\, \mathrm{i} K_j\} \quad \text{with} \quad \mathrm{i}^2 = -1,
\tag{7.76}
$$

where K_j, $j = 1, ..., n_{dim}$ is now the wave vector at some given node of spatial dimension n_{dim} and is obtained at each node from the global wave vector $\boldsymbol{K}$. Applying said derivatives, the explicit form of the Lippmann-Schwinger equation given in (7.7) can be recovered in Fourier space, where the Green operators appear as

$$
\begin{aligned}
\widehat{\Gamma}^m_{ijkl} &= -K_j K_l(\kappa^{-1}_{ik} - \kappa^{-1}_{ir}\varrho_{rn}\omega_{np}\varsigma_{ps}\kappa^{-1}_{sk}), & \widehat{\Gamma}^{m,e}_{ijk} &= -K_j K_r\kappa^{-1}_{is}\varrho_{sn}\omega_{np}\epsilon_{prk}, \\
\widehat{\Gamma}^{e,m}_{ijk} &= -K_k K_l\epsilon_{iln}\omega^{-1}_{nm}\varsigma_{mr}\kappa^{-1}_{rj}, & \widehat{\Gamma}^e_{ij} &= K_l K_r\epsilon_{iln}\epsilon_{mrj}\omega^{-1}_{nm},
\end{aligned}
\tag{7.77}
$$

and where the following abbreviations were used

$$
\begin{aligned}
\kappa_{ik} &= \mathbb{A}^0_{ijkl}K_l K_j, & \varrho_{in} &= q^0_{ijk}\epsilon_{kmn}K_m K_j, \\
\varsigma_{ik} &= \epsilon_{ijl}g^0_{lkm}K_m K_j, & \eta_{in} &= \epsilon_{ijk}\epsilon_{lmn}\mathbb{K}^0_{kl}K_m K_j, \\
\omega_{in} &= \varsigma_{ik}\kappa^{-1}_{kr}\varrho_{rn} - \eta_{in}.
\end{aligned}
\tag{7.78}
$$

Note that in the three-dimensional case, there is no uniqueness of the solution vector potential due to the identity $\boldsymbol{D} = \text{Curl}(\boldsymbol{A} + \nabla\theta) = \text{Curl}(\boldsymbol{A})$. One can thus add arbitrary gradient fields to the solution vector $\boldsymbol{A}$, which causes problems when solving the equilibrium equations. One therefore usually applies a gauge restriction on the divergence of the vector potential employing a penalty parameter Λ. Forcing the divergence of $\boldsymbol{A}$ to be zero, this gauge restriction appears in the differential equation (7.75) as follows

$$
\begin{aligned}
(\mathbb{A}^0_{ijkl} F_{kl} + q^0_{ijk} D_k)_{,j} &= -\tau^m_{ij,j}, \\
\epsilon_{ijk}(g^0_{klm} F_{lm} + \mathbb{K}^0_{kl} D_l)_{,j} &= -\epsilon_{ijk}\tau^e_{k,j} - \Lambda A_{k,ki}.
\end{aligned}
\tag{7.79}
$$

The modified Green operator can be found in the same fashion as presented before, where only one term in (7.78) changes due to the gauge restriction

$$
\eta^{gauge}_{in} = \epsilon_{ijk}\epsilon_{lmn}\mathbb{K}^0_{kl}K_m K_j - \Lambda K_i K_n,
\tag{7.80}
$$

while all other terms remain the same. The Green operators can then again be computed according to (7.77).

7.5.3. Fluctuation sensitivities

We now want to provide an explicit expression for the fluctuation sensitivities occurring in the Lippmann-Schwinger-type equation (7.21). We, therefore, recall the explicit expression for the fluctuations (7.18)

$$
\begin{aligned}
\widetilde{\boldsymbol{F}} &= \boldsymbol{\Gamma}^m * \boldsymbol{\tau}^m + \boldsymbol{\Gamma}^{m,e} * \boldsymbol{\tau}^e, \\
\widetilde{\boldsymbol{D}} &= \boldsymbol{\Gamma}^{e,m} * \boldsymbol{\tau}^m + \boldsymbol{\Gamma}^e * \boldsymbol{\tau}^e.
\end{aligned}
\tag{7.81}
$$

The fluctuation sensitivities can now be obtained by differentiation with respect to the macroscopic deformation gradient $\overline{\boldsymbol{F}}$ and electric displacement $\overline{\boldsymbol{D}}$. The coupled perturbations $\boldsymbol{\tau}^m$ and $\boldsymbol{\tau}^e$ (7.4) are linked to the generalized stresses, which are computed based on the microscopic deformation gradient and electric field. The microscopic deformation gradient and electric field are themselves linked to their respective macroscopic quantities by means of the decomposition (4.5) and (4.28), which allows us to perform the differentiation according to

$$
\begin{aligned}
\frac{\partial \widetilde{\boldsymbol{F}}}{\partial \overline{\boldsymbol{F}}} &= \boldsymbol{\Gamma}^m \quad * \left[\frac{\partial \boldsymbol{\tau}^m}{\partial \boldsymbol{F}} : \frac{\partial \boldsymbol{F}}{\partial \overline{\boldsymbol{F}}} + \frac{\partial \boldsymbol{\tau}^m}{\partial \boldsymbol{D}} \cdot \frac{\partial \boldsymbol{D}}{\partial \overline{\boldsymbol{F}}} \right] \quad + \quad \boldsymbol{\Gamma}^{m,e} * \left[\frac{\partial \boldsymbol{\tau}^e}{\partial \boldsymbol{F}} : \frac{\partial \boldsymbol{F}}{\partial \overline{\boldsymbol{F}}} + \frac{\partial \boldsymbol{\tau}^e}{\partial \boldsymbol{D}} \cdot \frac{\partial \boldsymbol{D}}{\partial \overline{\boldsymbol{F}}} \right], \\
\frac{\partial \widetilde{\boldsymbol{F}}}{\partial \overline{\boldsymbol{D}}} &= \boldsymbol{\Gamma}^m \quad * \left[\frac{\partial \boldsymbol{\tau}^m}{\partial \boldsymbol{F}} : \frac{\partial \boldsymbol{F}}{\partial \overline{\boldsymbol{D}}} + \frac{\partial \boldsymbol{\tau}^m}{\partial \boldsymbol{D}} \cdot \frac{\partial \boldsymbol{D}}{\partial \overline{\boldsymbol{D}}} \right] \quad + \quad \boldsymbol{\Gamma}^{m,e} * \left[\frac{\partial \boldsymbol{\tau}^e}{\partial \boldsymbol{F}} : \frac{\partial \boldsymbol{F}}{\partial \overline{\boldsymbol{D}}} + \frac{\partial \boldsymbol{\tau}^e}{\partial \boldsymbol{D}} \cdot \frac{\partial \boldsymbol{D}}{\partial \overline{\boldsymbol{D}}} \right], \\
\frac{\partial \widetilde{\boldsymbol{D}}}{\partial \overline{\boldsymbol{D}}} &= \boldsymbol{\Gamma}^{e,m} * \left[\frac{\partial \boldsymbol{\tau}^m}{\partial \boldsymbol{F}} : \frac{\partial \boldsymbol{F}}{\partial \overline{\boldsymbol{D}}} + \frac{\partial \boldsymbol{\tau}^m}{\partial \boldsymbol{D}} \cdot \frac{\partial \boldsymbol{D}}{\partial \overline{\boldsymbol{D}}} \right] \quad + \quad \boldsymbol{\Gamma}^e \quad * \left[\frac{\partial \boldsymbol{\tau}^e}{\partial \boldsymbol{F}} : \frac{\partial \boldsymbol{F}}{\partial \overline{\boldsymbol{D}}} + \frac{\partial \boldsymbol{\tau}^e}{\partial \boldsymbol{D}} \cdot \frac{\partial \boldsymbol{D}}{\partial \overline{\boldsymbol{D}}} \right], \\
\frac{\partial \widetilde{\boldsymbol{D}}}{\partial \overline{\boldsymbol{F}}} &= \boldsymbol{\Gamma}^{e,m} * \left[\frac{\partial \boldsymbol{\tau}^m}{\partial \boldsymbol{F}} : \frac{\partial \boldsymbol{F}}{\partial \overline{\boldsymbol{F}}} + \frac{\partial \boldsymbol{\tau}^m}{\partial \boldsymbol{D}} \cdot \frac{\partial \boldsymbol{D}}{\partial \overline{\boldsymbol{F}}} \right] \quad + \quad \boldsymbol{\Gamma}^e \quad * \left[\frac{\partial \boldsymbol{\tau}^e}{\partial \boldsymbol{F}} : \frac{\partial \boldsymbol{F}}{\partial \overline{\boldsymbol{F}}} + \frac{\partial \boldsymbol{\tau}^e}{\partial \boldsymbol{D}} \cdot \frac{\partial \boldsymbol{D}}{\partial \overline{\boldsymbol{F}}} \right].
\end{aligned}
\tag{7.82}
$$

Insertion of the aforementioned decomposition $\boldsymbol{F} = \overline{\boldsymbol{F}} + \widetilde{\boldsymbol{F}}$ and $\boldsymbol{D} = \overline{\boldsymbol{D}} + \widetilde{\boldsymbol{D}}$ finally gives

$$
\begin{aligned}
\frac{\partial \widetilde{\boldsymbol{F}}}{\partial \overline{\boldsymbol{F}}} &= \boldsymbol{\Gamma}^m \quad * \left[\mathbb{A}^\Delta + \mathbb{A}^\Delta : \frac{\partial \widetilde{\boldsymbol{F}}}{\partial \overline{\boldsymbol{F}}} + \boldsymbol{q}^\Delta \cdot \frac{\partial \widetilde{\boldsymbol{D}}}{\partial \overline{\boldsymbol{F}}} \right] + \boldsymbol{\Gamma}^{m,e} * \left[(\boldsymbol{q}^\Delta)^T + (\boldsymbol{q}^\Delta)^T : \frac{\partial \widetilde{\boldsymbol{F}}}{\partial \overline{\boldsymbol{F}}} + \mathbb{K}^\Delta \cdot \frac{\partial \widetilde{\boldsymbol{D}}}{\partial \overline{\boldsymbol{F}}} \right], \\
\frac{\partial \widetilde{\boldsymbol{F}}}{\partial \overline{\boldsymbol{D}}} &= \boldsymbol{\Gamma}^m \quad * \left[\boldsymbol{q}^\Delta + \boldsymbol{q}^\Delta \cdot \frac{\partial \widetilde{\boldsymbol{D}}}{\partial \overline{\boldsymbol{D}}} + \mathbb{A}^\Delta : \frac{\partial \widetilde{\boldsymbol{F}}}{\partial \overline{\boldsymbol{D}}} \right] + \boldsymbol{\Gamma}^{m,e} * \left[\mathbb{K}^\Delta + \mathbb{K}^\Delta \cdot \frac{\partial \widetilde{\boldsymbol{D}}}{\partial \overline{\boldsymbol{D}}} + (\boldsymbol{q}^\Delta)^T : \frac{\partial \widetilde{\boldsymbol{F}}}{\partial \overline{\boldsymbol{D}}} \right], \\
\frac{\partial \widetilde{\boldsymbol{D}}}{\partial \overline{\boldsymbol{D}}} &= \boldsymbol{\Gamma}^{e,m} * \left[\boldsymbol{q}^\Delta + \boldsymbol{q}^\Delta \cdot \frac{\partial \widetilde{\boldsymbol{D}}}{\partial \overline{\boldsymbol{D}}} + \mathbb{A}^\Delta : \frac{\partial \widetilde{\boldsymbol{F}}}{\partial \overline{\boldsymbol{D}}} \right] + \boldsymbol{\Gamma}^e \quad * \left[\mathbb{K}^\Delta + \mathbb{K}^\Delta \cdot \frac{\partial \widetilde{\boldsymbol{D}}}{\partial \overline{\boldsymbol{D}}} + (\boldsymbol{q}^\Delta)^T : \frac{\partial \widetilde{\boldsymbol{F}}}{\partial \overline{\boldsymbol{D}}} \right], \\
\frac{\partial \widetilde{\boldsymbol{D}}}{\partial \overline{\boldsymbol{F}}} &= \boldsymbol{\Gamma}^{e,m} * \left[\mathbb{A}^\Delta + \mathbb{A}^\Delta : \frac{\partial \widetilde{\boldsymbol{F}}}{\partial \overline{\boldsymbol{F}}} + \boldsymbol{q}^\Delta \cdot \frac{\partial \widetilde{\boldsymbol{D}}}{\partial \overline{\boldsymbol{F}}} \right] + \boldsymbol{\Gamma}^e \quad * \left[(\boldsymbol{q}^\Delta)^T + (\boldsymbol{q}^\Delta)^T : \frac{\partial \widetilde{\boldsymbol{F}}}{\partial \overline{\boldsymbol{F}}} + \mathbb{K}^\Delta \cdot \frac{\partial \widetilde{\boldsymbol{D}}}{\partial \overline{\boldsymbol{F}}} \right],
\end{aligned}
\tag{7.83}
$$

where $(\bullet)^\Delta$ denotes the difference between the actual moduli and the constant linear reference material according to Equation (7.20). The single and double contractions appearing in Equation (7.83) correspond to the generic operator $\diamond$ introduced in the Lippmann-Schwinger-type equation

$$
- \boldsymbol{\Gamma} * \mathbb{C}^\Delta = \boldsymbol{\Gamma} * \left(\mathbb{C}^\Delta \diamond \frac{\partial \widetilde{\mathbb{G}}}{\partial \overline{\mathbb{G}}} \right) - \frac{\partial \widetilde{\mathbb{G}}}{\partial \overline{\mathbb{G}}}.
\tag{7.84}
$$

Using the explicit expression for the fluctuation sensitivities (7.83), the latter equation can now be solved by means of a direct or iterative scheme. Neglecting the coupled fluctuation sensitivities $\partial \widetilde{\boldsymbol{F}}/\partial \overline{\boldsymbol{D}} = \partial \widetilde{\boldsymbol{D}}/\partial \overline{\boldsymbol{F}} = \boldsymbol{0}$ yields the reduced system for the reduced tangent computation approach.

Homogenization and multiscale simulation of phase-field-based fracture

In this chapter, a numerical scheme for multiscale phase-field-based fracture processes is presented. As fracture and damage are locally initializing, the microstructure of a material plays a major role in when and where said initialization takes place [69]. One example is given by geometrically sharp interfaces between two material phases, which lead to a much earlier crack initiation on the microscale compared with a purely macroscopic problem. We will, therefore, first establish a variational framework for phase-field-fracture [14, 50, 139]. The rate-type-incremental variational potential will then be used to evaluate the Hill-Mandel-macrohomogeneity conditions to obtain appropriate boundary conditions and effective material properties in the presence of a fracture phase-field. Further using the operator split introduced by MIEHE ET AL. [126] then allows for the decoupling of the phase-field variable and the strains within one time step and consequently, the decoupled computation of the effective tangent operator. Finally, some numerical experiments are carried out to proof the robustness and viability of the scheme as well as to demonstrate the effect of microscopic cracks on the macroscopic response of materials.

8.1. Variational approach to phase-field fracture mechanics

We now want to use the methods for rate-type incremental variational potentials presented in Section 3.3.4 to construct a small-strain rate-type variational potential that governs brittle fracture effects as follows

$$\Pi(\dot{\boldsymbol{u}}, \dot{d}) = \int_{\mathcal{B}} \frac{d}{dt}\psi(\boldsymbol{u}, d) + \mathfrak{d}(\dot{d}) \, dV - \int_{\mathcal{B}} \boldsymbol{\gamma} \cdot \dot{\boldsymbol{u}} \, dV - \int_{\partial \mathcal{B}} \boldsymbol{t}^{\#} \cdot \dot{\boldsymbol{u}} \, dA, \qquad (8.1)$$

where a phase-field variable d indicating fracture is coupled to the displacements $\boldsymbol{u}$. In line with Section 3.3.4, $\mathfrak{d}(\dot{d})$ is a dissipation potential accounting for the dissipative process of fracture. Accounting for the mechanical external contributions, $\boldsymbol{\gamma}$ is an exterior volume force and $\boldsymbol{t}^{\#}$ are externally applied tractions. Now the question arises on how to model ψ and $\mathfrak{d}$ to describe fracture phenomena realistically. We therefore first consider a one-dimensional crack indicated by $d = 1$, whereas $d = 0$ denotes no fracture. In order
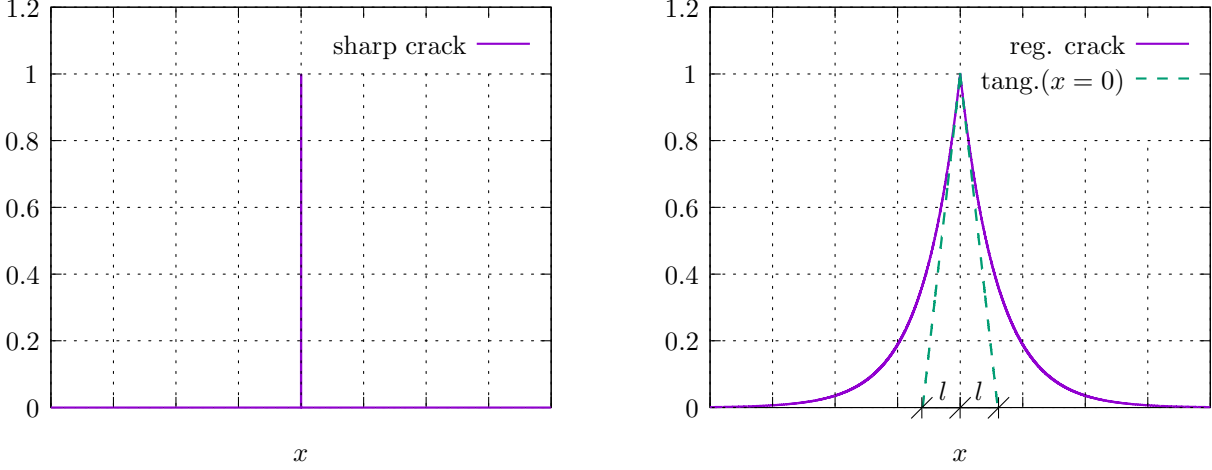
Figure 8.1: To the left, one can see the sharp crack interface as it would appear in reality. To the left, one can see the regularized crack interface $d = \exp(\frac{-|x|}{l_c})$, where l_c controls the strength of regularization, see also [126].

to describe gradient-driven phase-field fracture, we need to regularize the crack interface. One can see that this function is the solution to the following boundary value problem [126]

$$d - l_c^2 \frac{\partial^2 d}{\partial x^2} = 0 \quad \text{with} \quad d(\pm\infty) = 0 \text{ and } \frac{\partial d}{\partial x}(\pm\infty) = 0. \tag{8.2}$$

In accordance with Figure 8.1, the length scale parameter l_c controls the strength of the regularization. Carrying the concept to two- and three-dimensional problems, the differential equation becomes

$$d - l_c^2 \Delta d = 0, \tag{8.3}$$

where Δd is the Laplacian operator applied to the phase-field variable d. It is possible to retrieve the weak form of the latter differential equation from a variational formulation. We therefore first introduce the integral form

$$I(d, \nabla d) = \int_{\mathcal{B}} \frac{d^2}{2} + \frac{l_c^2}{2} |\nabla d|^2 \, dV. \tag{8.4}$$

Normalization of the latter equation by l_c yields a description of the crack surface density

$$\mathfrak{Z}(d, \nabla d) = \frac{1}{l_c} I(d, \nabla d) = \int_{\mathcal{B}} \frac{d^2}{2l} + \frac{l_c}{2} |\nabla d|^2 \, dV. \tag{8.5}$$

With the description of the crack surface at hand, we can construct the rate-type variational potential as follows

$$\begin{aligned}
\Pi(\dot{u}, \dot{d}) = &\frac{d}{dt} \int_{\mathcal{B}} (1-d)^2 \psi(\varepsilon) + g_c \left(\frac{d^2}{2l_c} + \frac{l_c}{2} |\nabla d|^2 \right) dV + \int_{\mathcal{B}} \text{In}(\dot{d}) \, dV \\
&- \int_{\mathcal{B}} \boldsymbol{\gamma} \cdot \dot{\boldsymbol{u}} \, dV - \int_{\partial\mathcal{B}} \boldsymbol{t}^\# \cdot \dot{\boldsymbol{u}} \, dA,
\end{aligned} \tag{8.6}$$

where $(1-d)^2$ is a degradation function leading to a decrease of the elastic energy density as the fracture is evolving, g_c is the Griffith constant determining the crack toughness and $\text{In}(\dot{d})$ is the indicator function defined as

$$\text{In}(\dot{d} < 0) = \infty \quad \text{and} \quad \text{In}(\dot{d} \geq 0) = 0. \tag{8.7}$$

In line with MIEHE ET AL. [132], the indicator function assures that $\dot{d} \geq 0$ is always greater or equal to zero, which is necessary to avoid thermodynamically inconsistent effects such as crack healing. To arrive at a more compact notation, we will denote the crack surface density

$$\mathfrak{z} = \frac{d^2}{2l_c} + \frac{l_c}{2}|\nabla d|^2. \tag{8.8}$$

We now want to find equilibrium in a time-incremental context. Therefore, the total energy potential is obtained through a discrete time integration

$$\Pi^{\Delta t}(\boldsymbol{u}, d) = \text{ALGO}\left\{\int_{t_n}^{t} \Pi(\dot{\boldsymbol{u}}, \dot{d})dt\right\}, \tag{8.9}$$

where quantities with index $(\bullet)_n$ denote their value at the previous time step and quantities without index $(\bullet)$ their values at the current time step. In this case, the algorithmic treatment of the time integration is performed employing an implicit Euler scheme. Applying this procedure to the global potential (8.6) gives

$$\Pi^{\Delta t} = \int_{\mathcal{B}} \frac{(1-d)^2\psi(\boldsymbol{\varepsilon}) - (1-d_n)^2\psi_n(\boldsymbol{\varepsilon}_n)}{\Delta t} + g_c\frac{\mathfrak{z}(d) - \mathfrak{z}_n(d_n)}{\Delta t}\, dV\,\Delta t$$
$$+ \int_{\mathcal{B}} \text{In}(\frac{d - d_n}{\Delta t})\, dV\Delta t - \int_{\mathcal{B}} \boldsymbol{\gamma} \cdot \frac{\boldsymbol{u} - \boldsymbol{u}_n}{\Delta t}\, dV - \int_{\partial\mathcal{B}} \boldsymbol{t}^{\#} \cdot \frac{\boldsymbol{u} - \boldsymbol{u}_n}{\Delta t}\, dA\Delta t \tag{8.10}$$

for the incremental time step Δt. We first cancel Δt where possible and then carry out the variation with respect to the current variables to determine the equilibrium state

$$\delta\Pi^{\Delta t} = \int_{\mathcal{B}} (1-d)^2\frac{\partial\psi}{\partial\boldsymbol{\varepsilon}} : \delta\boldsymbol{\varepsilon} - 2(1-d)\psi(\boldsymbol{\varepsilon})\delta d + \frac{g_c d}{l_c}\delta d + g_c l_c \nabla d\, \nabla\delta d\, dV$$
$$+ \int_{\mathcal{B}} \frac{\partial\text{In}}{\partial d}\delta d\, dV - \int_{\mathcal{B}} \boldsymbol{\gamma} \cdot \delta\boldsymbol{u}\, dV - \int_{\partial\mathcal{B}} \boldsymbol{t}^{\#} \cdot \delta\boldsymbol{u}\, dA. \tag{8.11}$$

Applying the divergence theorem, we obtain

$$\delta\Pi^{\Delta t} = \int_{\mathcal{B}} \left(-\text{div}\left[(1-d)^2\frac{\partial\psi}{\partial\boldsymbol{\varepsilon}}\right] - \boldsymbol{\gamma}\right) \cdot \delta\boldsymbol{u} - 2(1-d)\psi(\boldsymbol{\varepsilon})\delta d + \frac{g_c d}{l_c}\delta d + g_c l_c \nabla d\, \nabla\delta d\, dV$$
$$+ \int_{\mathcal{B}} \frac{\partial\text{In}}{\partial d}\delta d\, dV - \int_{\mathcal{B}} \boldsymbol{\gamma} \cdot \delta\boldsymbol{u}\, dV - \int_{\partial\mathcal{B}} \boldsymbol{t}^{\#} \cdot \delta\boldsymbol{u}\, dA. \tag{8.12}$$

As previously stated, the indicator serves to fulfill the condition $\dot{d} \geq 0$. We, therefore, follow the procedure suggested in MIEHE ET AL. [132] and introduce a local crack-driving-force

$$\mathcal{H} = \max_{t^* \in [t_0, t)} \psi(\boldsymbol{\varepsilon}). \tag{8.13}$$

as the local maximum of energy density of some point in time t^* out of all past times starting from the initial time t_0 to the current time t. In doing so, we make sure that the fracture phase field d can only grow. Applying the divergence theorem and using the local crack-driving-force gives

$$\delta\Pi^{\Delta t} = \int_{\mathcal{B}} \left(-\text{div}\left[(1-d)^2\frac{\partial\psi}{\partial\boldsymbol{\varepsilon}}\right] - \boldsymbol{\gamma}\right) \cdot \delta\boldsymbol{u} - \left(\frac{g_c}{l_c}d - g_c l_c\Delta d - 2(1-d)\mathcal{H}\right)\delta d\, dV$$
$$+ \int_{\partial\mathcal{B}} \left((1-d)^2\frac{\partial\psi}{\partial\boldsymbol{\varepsilon}} \cdot \boldsymbol{n} - \boldsymbol{t}^{\#}\right) \cdot \delta\boldsymbol{u}\, dA - \int_{\partial\mathcal{B}} (g_c l_c\nabla d \cdot \boldsymbol{n})\delta d\, dA, \tag{8.14}$$

where $\boldsymbol{n}$ is a normal vector pointing outwards of the surface of the body $\partial\mathcal{B}$. For the latter equation to hold for all displacement variations $\delta\boldsymbol{u}$ and phase-field variations δd, the following Euler-equations must be fulfilled

$$
\begin{aligned}
-\operatorname{div}\left[(1-d)^2\frac{\partial\psi}{\partial\boldsymbol{\varepsilon}}\right] - \boldsymbol{\gamma} &= \boldsymbol{0} && \text{in} && \mathcal{B}\\
\frac{g_c}{l_c}d - g_c l_c \Delta d - 2(1-d)\mathcal{H} &= 0 && \text{in} && \mathcal{B}\\
(1-d)^2\frac{\partial\psi}{\partial\boldsymbol{\varepsilon}}\boldsymbol{n} - \boldsymbol{t}^\# &= \boldsymbol{0} && \text{on} && \partial\mathcal{B}\\
g_c l_c \nabla d \cdot \boldsymbol{n} &= 0 && \text{on} && \partial\mathcal{B}.
\end{aligned}
\tag{8.15}
$$

8.2. A Hill-Mandel macrohomogeneity condition for two-scale fracture

We now want to employ a multiscale framework for brittle fracture by following the multiscale procedure introduced in Chapter 4 and *extending* it to *rate-type problems*. We therefore introduce the macroscopic strain $\overline{\boldsymbol{\varepsilon}}$. As for the strains, we assume *periodic boundary conditions* which gives in line with the Hill-Mandel assumption (4.6) and (4.28) the following decomposition on the microscale

$$
\boldsymbol{\varepsilon} = \overline{\boldsymbol{\varepsilon}} + \widetilde{\boldsymbol{\varepsilon}}(\boldsymbol{x}) = \overline{\boldsymbol{\varepsilon}} + \nabla^s\widetilde{\boldsymbol{u}},
\tag{8.16}
$$

where the macroscopic strain remains constant in the RVE while the fluctuative quantities $\widetilde{(\bullet)}$ are the variables we solve for on the microscale and where ∇^s denotes the symmetric gradient, which is the small strain simplification of the large strain theory. As for the fracture phase-field d, such decomposition on the microscale is problematic as a) a crack tip formed by the macroscopic $\overline{d}$ would be difficult to consistently incorporate into the RVE as we assume a separation of length scales and b) the interpretation of the macroscopic $\overline{d}$ is not straightforward as d is in contrast to $\boldsymbol{\varepsilon}$ not a gradient field and corresponding volume integral cannot be transferred to a surface integral. We therefore choose a decoupled approach for the phase-field and introduce a mixed variational macro-potential

$$
\overline{\Pi}^{\Delta t}(\overline{\boldsymbol{u}}) = \int_{\overline{\mathcal{B}}}\frac{\overline{\pi}^{\Delta t} - \overline{\pi}_n^{\Delta t}}{\Delta t}\,dV\,\Delta t - \int_{\overline{\mathcal{B}}}\overline{\boldsymbol{\gamma}}\cdot\frac{\overline{\boldsymbol{u}} - \overline{\boldsymbol{u}}_n}{\Delta t}\,dV - \int_{\partial\overline{\mathcal{B}}}\overline{\boldsymbol{t}}^\#\cdot\frac{\overline{\boldsymbol{u}} - \overline{\boldsymbol{u}}_n}{\Delta t}\,dA\,\Delta t,
\tag{8.17}
$$

where we followed the same theoretical thoughts that led to the micro-potential (8.10) but replaced the elastic energy contribution by

$$
\overline{\pi}^{\Delta t} = \frac{1}{|\mathcal{B}|}\inf_{\boldsymbol{u}}\inf_{d}\operatorname{ALGO}\left\{\int_{t_n}^{t}\int_{\mathcal{B}}\frac{d}{dt}\psi(\boldsymbol{u}, d) + \mathfrak{d}(\dot{d})\,dV\,dt\right\} = \frac{1}{|\mathcal{B}|}\inf_{\boldsymbol{u}}\inf_{d}\pi^{\Delta t}(\boldsymbol{u}, d),
\tag{8.18}
$$

which is the volume average of the incremental microscopic energy density and dissipation potential at equilibrium [76]. It is thus the incremental time-discrete version of the Hill-Mandel condition (4.1). The time-discrete incremental microscopic energy density and dissipation potential are obtained from Equation (8.10) as follows

$$
\pi^{\Delta t}(\boldsymbol{u}, d) = \int_{\mathcal{B}}(1-d)^2\psi(\boldsymbol{\varepsilon}) - (1-d_n)^2\psi_n(\boldsymbol{\varepsilon}_n) + g_c(\mathfrak{z}(d) - \mathfrak{z}_n(d_n))\,dV + \int_{\mathcal{B}}\operatorname{In}(\frac{d - d_n}{\Delta t})\,dV\,\Delta t
\tag{8.19}
$$

In analogy to (8.11), we now perform the variation of the macro-potential with respect to the macro-variable

$$\delta \overline{\Pi}^{\Delta t} = \int_{\overline{\mathcal{B}}} \frac{\partial \overline{\pi}^{\Delta t}}{\partial \overline{\boldsymbol{\varepsilon}}} : \delta \overline{\boldsymbol{\varepsilon}} \, dV - \int_{\overline{\mathcal{B}}} \overline{\boldsymbol{\gamma}} \cdot \delta \overline{\boldsymbol{u}} \, dV - \int_{\partial \overline{\mathcal{B}}} \overline{\boldsymbol{t}}^{\#} \cdot \delta \overline{\boldsymbol{u}} \, dA. \tag{8.20}$$

To identify macroscopic quantities, we take a closer look at the variation of the potential $\overline{\pi}^{\Delta t}$ occurring in the latter equation. According to its definition from (8.18), we will perform the variation on the microscale as follows

$$\delta_{\overline{\boldsymbol{\varepsilon}}} \overline{\pi}^{\Delta t} = \frac{\partial \overline{\pi}^{\Delta t}}{\partial \overline{\boldsymbol{\varepsilon}}} : \delta \overline{\boldsymbol{\varepsilon}} = \frac{1}{|\mathcal{B}|} \delta_{\boldsymbol{\varepsilon}} \pi^{\Delta t}, \tag{8.21}$$

where we keep in mind that $\Pi^{\Delta t}$ and thus $\pi^{\Delta t}$ according to Equation (8.18) is evaluated at equilibrium. Using the results from the previous chapter for the microscopic variation (8.11), we obtain

$$\frac{\partial \overline{\pi}^{\Delta t}}{\partial \overline{\boldsymbol{\varepsilon}}} : \delta \overline{\boldsymbol{\varepsilon}} = \frac{1}{|\mathcal{B}|} \left[\int_{\mathcal{B}} (1-d)^2 \frac{\partial \psi}{\partial \boldsymbol{\varepsilon}} : \delta \overline{\boldsymbol{\varepsilon}} \, dV + \int_{\mathcal{B}} (1-d)^2 \frac{\partial \psi}{\partial \boldsymbol{\varepsilon}} : \delta \widetilde{\boldsymbol{\varepsilon}} \, dV \right]. \tag{8.22}$$

As $\widetilde{\boldsymbol{\varepsilon}} = \nabla^s \widetilde{\boldsymbol{u}}$ is a gradient field of the fluctuative displacements, we can again use the divergence theorem for the second integral, leading to

$$\begin{aligned} \frac{\partial \overline{\pi}^{\Delta t}}{\partial \overline{\boldsymbol{\varepsilon}}} : \delta \overline{\boldsymbol{\varepsilon}} = & \frac{1}{|\mathcal{B}|} \left[\int_{\mathcal{B}} (1-d)^2 \frac{\partial \psi}{\partial \boldsymbol{\varepsilon}} : \delta \overline{\boldsymbol{\varepsilon}} \, dV + \int_{\mathcal{B}} - \operatorname{div} \left[(1-d)^2 \frac{\partial \psi}{\partial \boldsymbol{\varepsilon}} \right] \cdot \delta \widetilde{\boldsymbol{u}} \, dV \right. \\ & \left. + \int_{\partial \mathcal{B}} \left((1-d)^2 \frac{\partial \psi}{\partial \boldsymbol{\varepsilon}} \boldsymbol{n} \right) \cdot \delta \widetilde{\boldsymbol{u}} \, dA \right]. \end{aligned} \tag{8.23}$$

If we want to retrieve the macroscopic stress as the volume average over the microscopic stresses as the macroscopic stress, the last two integrals have to vanish. Comparing the second integral term with Euler equation $(8.15)_1$, we see that *in equilibrium*, the divergence becomes zero for $\boldsymbol{\gamma} = \boldsymbol{0}$, which is why we apply no volume force on the microscale. Comparing the third integral term with $(8.15)_3$ on the surface, we see that there are several methods to let the term vanish [127], see also Chapter 4. One can either prescribe Neumann boundaries with zero-tractions $\boldsymbol{t}^{\#} = \boldsymbol{0}$ or Dirichlet boundary conditions causing $\delta \widetilde{\boldsymbol{u}} = \boldsymbol{0}$. In the context of homogenization, the use of periodic Dirichlet boundary conditions has proven to give the most accurate results in terms of effective properties [189],[196]. We therefore set $\delta \widetilde{\boldsymbol{u}}(\boldsymbol{X}^+) = \delta \widetilde{\boldsymbol{u}}(\boldsymbol{X}^-)$ where $\boldsymbol{X}^+$ and $\boldsymbol{X}^-$ are opposite points on the RVE's boundary. In doing so, the boundary term

$$\left((1-d)^2 \frac{\partial \psi}{\partial \boldsymbol{\varepsilon}} \cdot \boldsymbol{n} \right)^+ = - \left((1-d)^2 \frac{\partial \psi}{\partial \boldsymbol{\varepsilon}} \cdot \boldsymbol{n} \right)^- \quad \text{on} \quad \partial \mathcal{B} \tag{8.24}$$

becomes anti-periodic on the boundary. According to the previous argumentation and choice of boundary conditions, we are left with the well known averaging rule

$$\boxed{\frac{\partial \overline{\pi}^{\Delta t}}{\partial \overline{\boldsymbol{\varepsilon}}} : \delta \overline{\boldsymbol{\varepsilon}} = \overline{\boldsymbol{\sigma}} : \delta \overline{\boldsymbol{\varepsilon}} = \frac{1}{|\mathcal{B}|} \left[\int_{\mathcal{B}} (1-d)^2 \frac{\partial \psi}{\partial \boldsymbol{\varepsilon}} \, dV \right] : \delta \overline{\boldsymbol{\varepsilon}}.} \tag{8.25}$$

We thus see that the variationally consistent macroscopic stress $\overline{\boldsymbol{\sigma}}$ is degrading with the microscopic fracture phase-field. Note that so far, the mechanical fields and the fracture

phase-field are fully coupled. When computing a consistent tangent, we would need to take this coupling between d and $\overline{\varepsilon}$ into account. In the next chapter, however, we will algorithmically decouple these fields to achieve a simpler treatment of the overall problem, including the tangent computation.

8.3. Algorithmic treatment of multiscale fracture

We now want to develop a robust algorithmic procedure for multiscale fracture. At the same time, it needs to be computationally efficient, as microscopic boundary value problems need to be fully resolved at each macroscopic iteration step. On the microscale, we thus follow the procedure suggested in MIEHE ET AL. [126] and employ an operator split when solving the time-discretized system. Consequently, given some macroscopic load $\overline{\varepsilon}$, we will use the phase-field variable of the *last time step* d_n for the solution of the microscopic mechanical boundary value problem $(8.15)_1$ and $(8.15)_3$

$$-\operatorname{div}\left[(1-d_n)^2\frac{\partial\psi}{\partial\varepsilon}\right] = \boldsymbol{0} \qquad \text{in} \quad \mathcal{B}$$
$$\widetilde{\boldsymbol{u}}(\boldsymbol{X}^+) = \widetilde{\boldsymbol{u}}(\boldsymbol{X}^-) \qquad \text{on} \quad \partial\mathcal{B}, \tag{8.26}$$

where in line with the Hill-Mandel condition, we set $\mathfrak{g} = \boldsymbol{0}$ and used periodic boundary conditions in the fluctuative displacement field $\widetilde{\boldsymbol{u}}$. The macroscopic stress can then be obtained from Equation (8.25) as follows

$$\overline{\boldsymbol{\sigma}} = \frac{1}{|\mathcal{B}|}\int_{\mathcal{B}}(1-d_n)^2\frac{\partial\psi}{\partial\varepsilon}\,dV, \tag{8.27}$$

and due to the decoupling procedure, the macroscopic tangent operator can be simply computed in line with Equation (4.40) as

$$\overline{\mathbb{A}}^{algo} = \frac{1}{|\mathcal{B}|}\int_{\mathcal{B}}(1-d_n)^2\left[\mathbb{A} + \mathbb{A}:\partial_{\widetilde{\varepsilon}}\widetilde{\varepsilon}\right]\,dV. \tag{8.28}$$

We then solve the phase-field equations in a *staggered* fashion

$$\frac{g_c}{l}d - g_c l\Delta d - 2(1-d)\mathcal{H} = 0 \qquad \text{in} \quad \mathcal{B}$$
$$d(\boldsymbol{X}^+) = d(\boldsymbol{X}^-) \qquad \text{on} \quad \partial\mathcal{B}, \tag{8.29}$$

where we use the current strain ε in the computation of the $\mathcal{H}$-field according to equation (8.13). After having found the equilibrium for the phase-field equation, we proceed with the next macroscopic *load step*. This procedure is also known as *one-pass scheme* [126].

8.3.1. FFT-based solution scheme for the mechanical problem

The FFT-based discretization and solution scheme closely follows the procedures presented before for electro-active models, which is why we keep the explanation in this subsection quite compact. However, here we will use a reformulated version of the Lippmann-Schwinger equation for the mechanical equilibrium. The aim is a compact implementation of an iterative solver, such as the conjugate gradient method. According to MOULINEC

& Suquet [137] and Vondřejc et al. [200], see also Geus et al. [36], the boundary value problem can be also formulated as follows

$$\mathbf{\Gamma}^0 * \boldsymbol{\sigma} = \boldsymbol{0}. \tag{8.30}$$

In discrete Fourier-space, the Green operator takes the same form as for the standard Lippmann-Schwinger approach (6.31). Further using a quadratic small-strain material law including the phase-field and using the decomposition (8.16) gives

$$\boldsymbol{\sigma} = ((1 - d_n)^2 + K)\mathbb{A} : \boldsymbol{\varepsilon} = ((1 - d_n)^2 + K)\mathbb{A} : (\overline{\boldsymbol{\varepsilon}} + \widetilde{\boldsymbol{\varepsilon}}). \tag{8.31}$$

In the latter equation, we added a residual stiffness K to the phase-field to obtain a numerically more stable scheme. K is usually chosen small enough to accurately approximate the zero-stiffness of a crack and large enough to have numeric stability. Equation (8.30) can then be recast into the following form

$$\mathbf{\Gamma}^0 * \left(((1 - d_n)^2 + K)\mathbb{A} : \widetilde{\boldsymbol{\varepsilon}}\right) = -\mathbf{\Gamma}^0 * \left(((1 - d_n)^2 + K)\mathbb{A} : \overline{\boldsymbol{\varepsilon}}\right), \tag{8.32}$$

which allows us to identify the right-hand side and the matrix-vector multiplication needed for iterative solvers

$$\underline{\mathbf{A}} \cdot \underline{\mathbf{x}} = \mathbf{\Gamma}^0 * \left(((1 - d_n)^2 + K)\mathbb{A} : \widetilde{\boldsymbol{\varepsilon}}\right) \quad \text{and} \quad \underline{\mathbf{b}} = -\mathbf{\Gamma}^0 * \left(((1 - d_n)^2 + K)\mathbb{A} : \overline{\boldsymbol{\varepsilon}}\right), \tag{8.33}$$

or in terms of fast Fourier transforms

$$\begin{aligned} \underline{\mathbf{A}} \cdot \underline{\mathbf{x}} &= \mathrm{fft}^{-1}\{\widehat{\underline{\mathbf{\Gamma}}}^0 : \left(\mathrm{fft}\{((1 - d_n)^2 + K)\mathbb{A} : \widetilde{\boldsymbol{\varepsilon}}\}\right)\} \quad \text{and} \\ \underline{\mathbf{b}} &= -\mathrm{fft}^{-1}\{\widehat{\underline{\mathbf{\Gamma}}}^0 : \left(\mathrm{fft}\{((1 - d_n)^2 + K)\mathbb{A} : \overline{\boldsymbol{\varepsilon}}\}\right)\}. \end{aligned} \tag{8.34}$$

The fluctuative strains are then solved employing a conjugate gradient solver

$$\widetilde{\boldsymbol{\varepsilon}}_{i+1} = \mathrm{cg}\{\underline{\mathbf{A}} \cdot \underline{\mathbf{x}}, \underline{\mathbf{b}}\}. \tag{8.35}$$

8.3.2. FFT-based solution scheme for the phase-field problem

When having found mechanical equilibrium, the fracture phase-field needs to be updated according to the new strain distribution, which gives an updated $\mathcal{H}$-field in the differential equation (8.29). Without the context of fracture mechanics, we already demonstrated in Section 5.4 how to solve such a Ginzburg-Landau type equation by means of direct methods. In two- and three spatial dimensions however, it might be costly to set up the discrete stiffness matrix, especially as it is not sparse[1]. We thus want to utilize the fast-Fourier-transform algorithm here as well within an iterative solver such as the conjugate gradient method

$$d_{i+1} = \mathrm{cg}\{\underline{\mathbf{A}}_d \cdot \underline{\mathbf{x}}, \underline{\mathbf{b}}_d\}. \tag{8.36}$$

Therefore, we do not set up the stiffness matrix explicitly, but only the matrix-vector multiplication. Using the Fourier-methods demonstrated in Section 5.3 and 5.4, the matrix-vector multiplication and the right-hand side can be computed as

$$\underline{\mathbf{A}}_d \cdot \underline{\mathbf{x}} = \frac{g_c}{l}d - g_c l\,\mathrm{fft}^{-1}\{|\boldsymbol{K}^*|^2 \mathrm{fft}\{d\}\} \quad \text{and} \quad \underline{\mathbf{b}}_d = 2(1 - d)\mathcal{H}. \tag{8.37}$$

---

[1]The non-sparsity of the overall stiffness matrix stems from the global nature of the Fourier-approximation. Naturally, nodes that are not directly connected have fewer interactions, and the further away they are from each other, the smaller their coupled entries in the stiffness matrix become.

8.3.3. FFT-based multiscale fracture scheme

We now give the algorithmic scheme for the *one-pass multiscale fracture solution scheme* as it is implemented in the code provided on the open repository [61].

1. **Macroscopic load:** Pass macroscopic strain $\overline{\varepsilon}$ from macro- to micro-boundary value problem

$$\varepsilon = \overline{\varepsilon} + \widetilde{\varepsilon}.$$

2. **Microscopic equilibrium and macroscopic stress:** Solve for equilibrated strains

$$\widetilde{\varepsilon}_{i+1} = \mathrm{cgs}\{\underline{\mathbf{A}} \cdot \underline{\mathbf{x}}, \underline{\mathbf{b}}\},$$

   where $\underline{\mathbf{A}} \cdot \underline{\mathbf{x}}$ and $\underline{\mathbf{b}}$ are obtained from Equation (8.34)

$$\underline{\mathbf{A}} \cdot \underline{\mathbf{x}} = \mathrm{fft}^{-1}\{\underline{\widehat{\mathbf{\Gamma}}}^0 : \mathrm{fft}\{((1 - d_n)^2 + K)\mathbb{A} : \widetilde{\varepsilon}\}\} \quad \text{and}$$
$$\underline{\mathbf{b}} = -\mathrm{fft}^{-1}\{\underline{\widehat{\mathbf{\Gamma}}}^0 : \mathrm{fft}\{((1 - d_n)^2 + K)\mathbb{A} : \overline{\varepsilon}\}\}.$$

3. **Macroscopic stress:** Use equilibrated strains $\varepsilon^\#$ to compute macroscopic stress

$$\overline{\sigma} = \frac{1}{|\mathcal{B}|} \int_{\mathcal{B}} ((1 - d_n)^2 + K)\frac{\partial \psi}{\partial \varepsilon} \, dV.$$

4. **Macroscopic tangent operator:** Use the modified Fourier-approach (6.16) to solve for the fluctuation sensitivities

$$(\frac{\partial \widetilde{\varepsilon}}{\partial \overline{\varepsilon}})_{i+1} = \mathrm{gmres}\{\underline{\mathbf{A}}^* \cdot \underline{\mathbf{x}}, \underline{\mathbf{b}}^*\},$$

   where $\underline{\mathbf{A}} \cdot \underline{\mathbf{x}}$ and $\underline{\mathbf{b}}$ are obtained from Equation (6.16) as follows

$$\underline{\mathbf{A}}^* \cdot \underline{\mathbf{x}} = \mathrm{fft}^{-1}\{\widehat{\mathbf{\Gamma}}^0 : \mathrm{fft}\{\left[(((1 - d_n)^2 + K)\mathbb{A} - \mathbb{A}^0) : \frac{\partial \widetilde{\varepsilon}}{\partial \overline{\varepsilon}}\right]\}\} - \frac{\partial \widetilde{\varepsilon}}{\partial \overline{\varepsilon}} \quad \text{and}$$
$$\underline{\mathbf{b}}^* = -\mathrm{fft}^{-1}\{\widehat{\mathbf{\Gamma}}^0 : \mathrm{fft}\{\left[((1 - d_n)^2 + K)\mathbb{A} - \mathbb{A}^0\right]\}\}.$$

   Use fluctuation sensitivities to compute the macroscopic tangent operator

$$\overline{\mathbb{A}}^{algo} = \frac{1}{|\mathcal{B}|} \int_{\mathcal{B}} (1 - d_n)^2 \left[\mathbb{A} + \mathbb{A} : \frac{\partial \widetilde{\varepsilon}}{\partial \overline{\varepsilon}}\right] dV.$$

5. **Macroscopic equilibrium:** Use the macroscopic stress $\overline{\sigma}$ and tangent operator $\overline{\mathbb{A}}^{algo}$ to solve the macroscopic equilibrium

$$\delta\overline{\Pi}^{\Delta t} = 0$$

   for the equilibrated macroscopic strains $\overline{\varepsilon}^\#$. If the material is non-linear, use updated $\overline{\varepsilon}^\#$ and go to step 1, else, proceed with step 6.

6. **Crack driving force:** Use equilibrated strains to compute microscopic energy density

$$\psi = \frac{1}{2}\boldsymbol{\varepsilon}^{\#} : \mathbb{A} : \boldsymbol{\varepsilon}^{\#}$$

and check if the $\mathcal{H}$-field according to Equation (8.13) needs to be updated

$$\mathcal{H} = \max_{t^* \in [t_0, t)} \psi(\boldsymbol{\varepsilon}^{\#}).$$

7. **Microscopic crack evolution:** Solve microscopic phase-field equation

$$d_{i+1} = \mathrm{pcg}\{\underline{\mathbf{A}}_d \cdot \underline{\mathbf{x}}, \underline{\mathbf{b}}_d\},$$

where $\underline{\mathbf{A}}_d \cdot \underline{\mathbf{x}}$ and $\underline{\mathbf{b}}_d$ are obtained from Equation (8.37) as follows

$$\underline{\mathbf{A}}_d \cdot \underline{\mathbf{x}} = \frac{g_c}{l}d - g_c l\,\mathrm{fft}^{-1}\{|\boldsymbol{K}^*|^2 \mathrm{fft}\{d\}\} \quad \text{and} \quad \underline{\mathbf{b}}_d = 2(1-d)\mathcal{H}.$$

Update history when tolerance of iterative solver is reached $d_n = d$.

8. **Proceed with next macroscopic load step and go to step 1.**

Without further quantitative proof, the combination of the conjugate gradient square (cgs) method for solving for the strains $\widetilde{\boldsymbol{\varepsilon}}$, the generalized minimum residual method (gmres) for solving for the fluctuation sensitivities $\dfrac{\partial \widetilde{\boldsymbol{\varepsilon}}}{\partial \overline{\boldsymbol{\varepsilon}}}$ and the preconditioned conjugate gradients method (pcg) for solving for the phase-field d appeared to be the fastest and most robust combination.

8.4. Numerical examples

In this chapter, the FFT-based phase-field implementation is tested for its robustness. First, we consider several different three-dimensional microstructure realizations and their impact on the initialization of fracture within an RVE as well as the fracture resistance. In a second step, the two-scale scheme as provided in Section 8.3 is tested for a plane-strain plate for two different microstructures.

8.4.1. Three-dimensional microscopic fracture evolution

In this first example, we want to study the numerical robustness and viability of the Fourier-based solver on the microscale based on several three-dimensional microstructures as presented in Figure 8.2. The code that produced these results is provided in a public repository [60]. Namely, a) a spherical, b) a diamond-shaped and c) a microstructure with five randomly distributed spheres are considered. The RVEs are square RVEs of unit length $l = 1$. The spherical inclusion a) has a radius of $r = 0.25l$, the diamond inclusion b) has side lengths $r = 0.6l$ from top to top in each direction, the randomly distributed spheres have a radius of $r = 1/12l$. The microstructure is discretized using $65 \times 65 \times 65$ grid points. In all cases, the inclusions are stiff, and the matrix material is soft. The small-strain energy density function governs their material behavior

$$\psi(\boldsymbol{\varepsilon}) = \frac{1}{2}\lambda(\mathrm{tr}\,\boldsymbol{\varepsilon})^2 + \mu\,\mathrm{tr}[\boldsymbol{\varepsilon}^2], \tag{8.38}$$
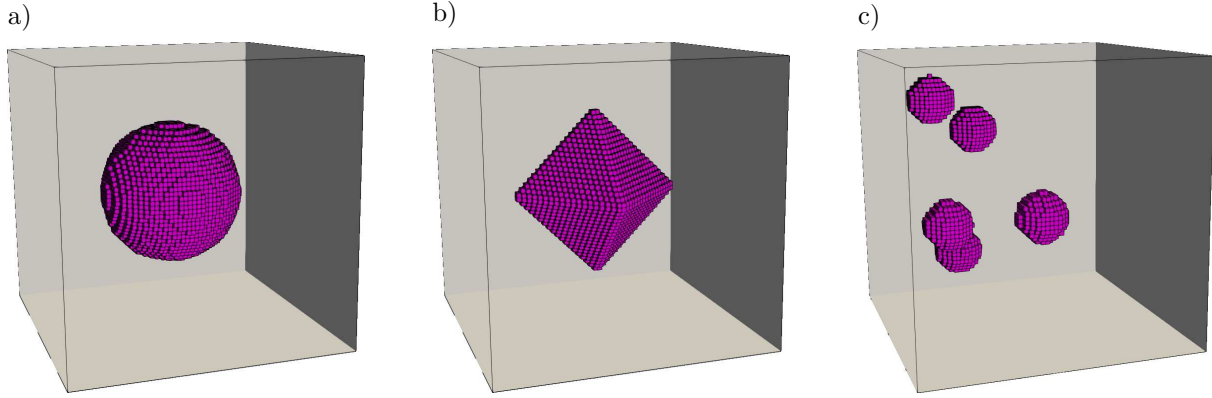
a)

b)

c)

Figure 8.2: Three different microstructure realizations for a three-dimensional fracture computation. The square RVE is of unit side length $l = 1$. a) The stiff spherical inclusion has a radius of $r = 0.25l$. b) The soft diamond inclusion has side lengths $r = 0.6l$ from top to top in each direction. c) The randomly distributed stiff spherical inclusions have a radius of $r = 1/12l$.

Table 8.1: Material parameters used for small strain three-dimensional fracture simulation for different microstructures. For the diamond inclusion, the inclusion is soft and the matrix is stiff.

no.	par.	name	unit	value
1.	μ^{matr}	shear modulus matrix	GPa	8
2.	μ^{incl}	shear modulus inclusion	GPa	80
3.	λ^{matr}	Lamés first parameter matrix	GPa	12
4.	λ^{incl}	Lamés first parameter inclusion	GPa	120
5.	g_c	fracture toughness	GN/m	0.0017
6.	l_c	length scale parameter	m	$5 \cdot 10^{-5}$
7.	K	residual stiffness	-	10^{-5}

where λ is the first Lamé constant. Through differentiation, we obtain the stress tensor

$$\boldsymbol{\sigma} = \frac{\partial \psi}{\partial \boldsymbol{\varepsilon}} = \lambda \operatorname{tr}[\boldsymbol{\varepsilon}] \mathbf{1} + 2\mu \boldsymbol{\varepsilon} \tag{8.39}$$

and the material moduli

$$\mathbb{A} = \frac{\partial^2 \psi}{\partial \boldsymbol{\varepsilon}^2} = \lambda \mathbf{1} \otimes \mathbf{1} + 2\mu \mathbb{I}^{sym}, \tag{8.40}$$

with $\mathbb{I}^{sym}$ being the fourth-order symmetric identity, which appears in index notation as

$$\mathbb{I}^{sym}_{ijkl} = \frac{1}{2}(\delta_{ik}\delta_{jl} + \delta_{il}\delta_{jk}). \tag{8.41}$$

The latter expressions are used within the algorithmic procedure presented in Section 8.3. The parameter for the matrix and the inclusion material are given in Table 8.1. The RVEs are loaded with a macroscopic strain increment of $\Delta\bar{\varepsilon}_{11} = 0.0001$ per load step while all other components of the macroscopic strain tensor are held zero. In this example, a conjugate gradient squared (cgs) solver, as implemented in MATLAB is used for the solution of the discretized mechanical equilibrium equation (8.34). The tolerance is set to $tol = 10^{-10}$ and the maximum number of iterations to 2000. For the solution of the discretized phase-field equation (8.37), a preconditioned conjugate gradient solver is used. In line with the solver for the mechanical equilibrium, the tolerance is set to $tol = 10^{-10}$ and the maximum number of iterations to 2000.

Table 8.2: Material parameters used for small strain multiscale fracture simulation. The value for g_c in brackets relates to the weakened RVE in Figure 8.4

no.	par.	name	unit	value
1.	μ^{matr}	shear modulus matrix	GPa	80
2.	μ^{incl}	shear modulus inclusion	GPa	8
3.	λ^{matr}	Lamés first parameter matrix	GPa	120
4.	λ^{incl}	Lamés first parameter inclusion	GPa	12
5.	g_c	fracture toughness	GN/m	0.0027(0.0017)
6.	l_c	length scale parameter	m	$5 \cdot 10^{-5}$
7.	K	residual stiffness	-	10^{-5}

Figure 8.3 shows the results for the different microstructures in terms of fracture surfaces at different load levels. As expected, all three RVEs fracture perpendicular to the pulling direction. However, the RVE with the soft diamond-shaped inclusion fails at a much lower macroscopic load compared with the spherical inclusions. Considering the diamond inclusion's sharp edges and the resulting stress concentration at these edges, the lower fracture toughness appears to be a likely result. One also nicely sees the symmetry of the fracture surface for the single spherical inclusion. As for the randomly distributed spherical inclusions, one can see that the crack localizes between the two spheres closest to each other and then propagates in the area of high sphere density. Such simulations might enable a controlled failure design of materials for longer durability. For example, one could think of propagating cracks into directions where a failure of the macroscopic specimen can be prevented. This procedure is also known as *crack trapping*. Brodnik et al. [17] numerically showed that the fracture toughness of materials can be enhanced by location and size of trapping inclusion.

8.4.2. Small-strain multiscale simulation

In this example, we want to demonstrate the microstructural effects on macroscopic failure in a small strain setting (8.38). We, therefore, consider a squared plane-strain plate on the macroscale that is pulled in the vertical direction as depicted in Figure 8.4. The macroscopic plate is of unit side-length $\bar{l} = 1$m and is discretized by triangular finite elements with linear shape functions and one Gauss point for the numeric integration. An RVE is attached at each of the Gauss points to compute the microscopic material response. The square RVEs are of side length $l = 1$mm $= 10^{-3}$m. In the middle of the plate, there is one weakened RVE to initiate fracture. As shown in Figure 8.4, the microstructure of the RVEs is a stiff matrix material and a soft diamond inclusion. The weakened RVE in the middle has a larger diamond inclusion and a lower fracture toughness g_c. See also Table 8.2 for the material parameters. This kind of microstructure allows for a distinct crack initialization at the notches of the soft diamond inclusion.

For the numerical experiment, the macroscopic plate is vertically pulled with $\overline{\boldsymbol{u}}^{\#}$ along the top edge. On the bottom edge, it is fixed in the vertical direction. The plate can freely move in the horizontal direction and is only fixed at the bottom-left edge. Figure 8.5 shows the result for the full multiscale simulation at load steps $\overline{u}_2^{\#} = 0.872 \cdot 10^{-2}$m, $\overline{u}_2^{\#} = 0.962 \cdot 10^{-2}$m, $\overline{u}_2^{\#} = 1.012 \cdot 10^{-2}$m and $\overline{u}_2^{\#} = 1.072 \cdot 10^{-2}$m. To the left, one sees the contour plot of the macroscopic displacement component $\overline{u}_2$ in the plate. To the right,
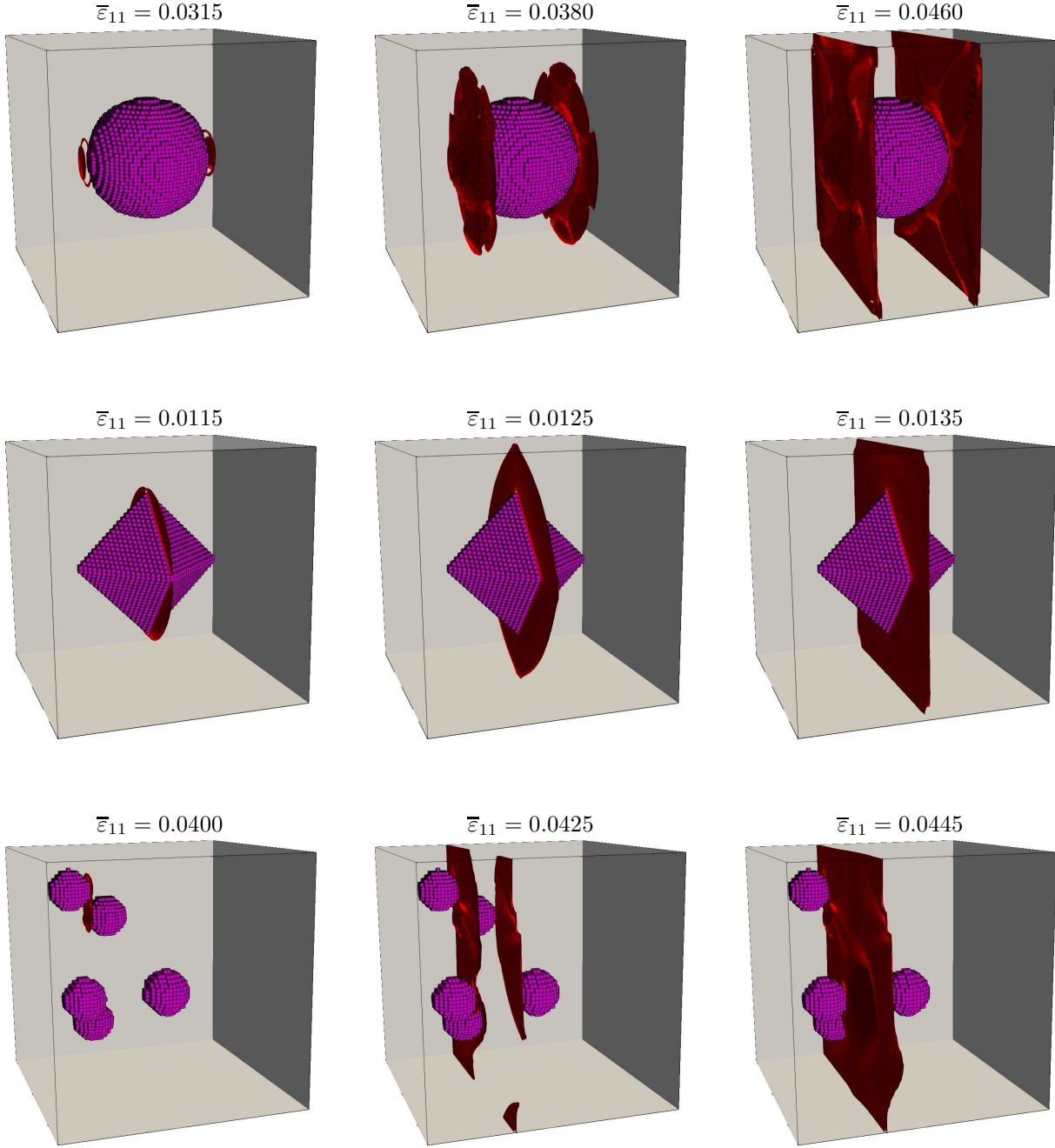
$\overline{\varepsilon}_{11} = 0.0315$ $\overline{\varepsilon}_{11} = 0.0380$ $\overline{\varepsilon}_{11} = 0.0460$

$\overline{\varepsilon}_{11} = 0.0115$ $\overline{\varepsilon}_{11} = 0.0125$ $\overline{\varepsilon}_{11} = 0.0135$

$\overline{\varepsilon}_{11} = 0.0400$ $\overline{\varepsilon}_{11} = 0.0425$ $\overline{\varepsilon}_{11} = 0.0445$

Figure 8.3: Numerical results for the fracture surface $d = 0.99$ at different load steps for different microstructures presented in Figure 8.2. Within the first RVE with a stiff spherical solution, two fracture surfaces evolve around the spherical inclusion. As the problem is fully symmetric, we also see a symmetry of the fracture phase-field. The second RVE with the soft diamond-shaped inclusion fractures at lower load steps due to the sharp edges of the microstructure geometry. Within the third RVE, the crack is localizing between the two spherical inclusions closest to each other. The fracture surface then evolves in the area of the highest sphere density.

the microscopic phase field d within the weakened element and one RVE at the plate's outer edge is visualized. As expected, one sees that fracture starts within the weakened element at the diamond inclusion notches. The crack then propagates until the RVE is completely broken, and only the resilient stiffness of the RVE is left. Macroscopically, one observes the localization of displacements in the middle of the plate where the weakened
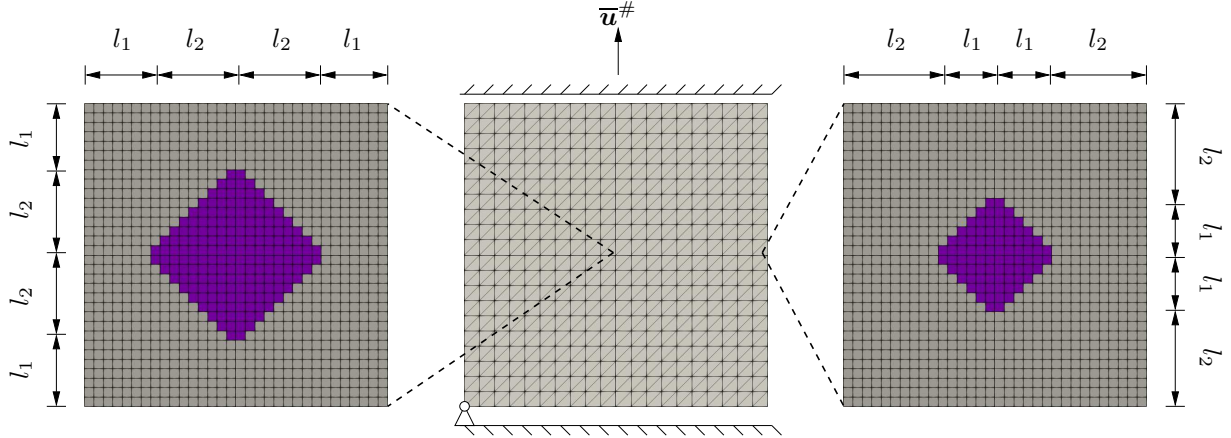
Figure 8.4: Multiscale boundary value problem for the fracture of a plane-strain plate with underlying diamond microstructure. The squared plate is of side-length $\overline{l} = 1$m, whereas the RVEs are of overall side-length $l = 1$mm $= 10^{-3}$m. The lengths occurring in the description of the diamond shape are $l_1 = 0.2l$ and $l_2 = 0.3l$. In the middle of the macroscopic plate, the RVE is geometrically and materially weakened to initiate crack propagation at that location.

RVE is placed. Further expansion of the plate leads to cracking of the standard RVEs used in the rest of the plate. The macroscopic crack moves outward in line with RVEs cracking on the microscale. Finally, the macroscopic crack reaches the outer edge, and the outer RVE is cracking as well. One sees that the phase-field in the outer RVE is more diffuse compared to the one on the middle. This might stem from shear deformations arising at the crack tip when it reaches the outer edge. One usually then needs to use smaller time steps and finer grids to allow a more localized response of the phase-field, especially in the context of the staggered scheme used here. The results presented here can be reproduced using the code provided in the open repository [61].

Next, we want to demonstrate the anisotropic crack path that can be induced by microscopic anisotropy. Again, the macroscopic problem is a plane strain plate, as shown in Figure 8.5. In this example however, the microstructure are stiff ellipsoidal inclusions that are shifted by an angle of $\pi/4$. The stiff matrix phase and the soft inclusion phase of all RVEs are distributed according to the inequality $((x_1 \cos(\pi/4) + x_2 \sin(\pi/4))/0.35l)^2 + ((x_1 \sin(\pi/4) - x_2 \cos(\pi/4))/0.15l)^2 < 1$, i.e. a nodal point with coordinate $\{x_1, x_2\}$ fulfilling the later equation is assigned to the inclusion, all others are part of the matrix material, see right RVE in Figure 8.7. The elastic and phase-field parameters are the same as in the previous computation and can be found in Table 8.2. However, in this example, the elliptic inclusion is stiff, i.e., has higher material paramaters, and the matrix material is soft. Again, in the middle of the plate, a geometrically and materially weakened RVE is attached. Its phase distribution follows the modified inequality $((x_1 \cos(\pi/4) + x_2 \sin(\pi/4))/0.4l)^2 + ((x_1 \sin(\pi/4) - x_2 \cos(\pi/4))/0.05l)^2 < 1$, which gives a sharper, flatter ellipse as visualized on the left of Figure 8.7. Consequently, the fracture is likely to localize in this RVE due to stress-peaking and lower fracture toughness.

In line with the previous simulation, the macroscopic plate is vertically pulled with $\overline{\boldsymbol{u}}^{\#}$ along the top edge and is vertically fixed on the bottom edge. The plate can freely move in horizontal direction and is only fixed at the bottom-left edge. Figure 8.7 shows the result for the full multiscale simulation at load steps $\overline{u}_2^{\#} = 5.802 \cdot 10^{-2}$m, $\overline{u}_2^{\#} = 5.822 \cdot 10^{-2}$m, $\overline{u}_2^{\#} = 5.832 \cdot 10^{-2}$m and $\overline{u}_2^{\#} = 5.840 \cdot 10^{-2}$m. One sees that the crack initializes in the weakened RVE at the edges of the sharp elliptic inclusion. In contrast to the diamond-shaped

inclusion, however, the microscopic crack in the weakened RVE is evolving in diagonal direction and merges due to the enforced periodicity of the boundary value problem. Also macroscopically, one sees the crack's initiation in the middle of the plate where the weakened RVE is located. The crack then macroscopically proceeds diagonally, indicating that the anisotropic microstructure of the underlying microstructure has an effect on the macroscopic crack path. The regular RVE located on the plate's right edge is not fully cracking, as it does not lay in the macroscopic crack's path. For future studies, the effect of the periodic boundary conditions as well as the size of the RVE on the macroscopic fracture process, needs to be investigated.
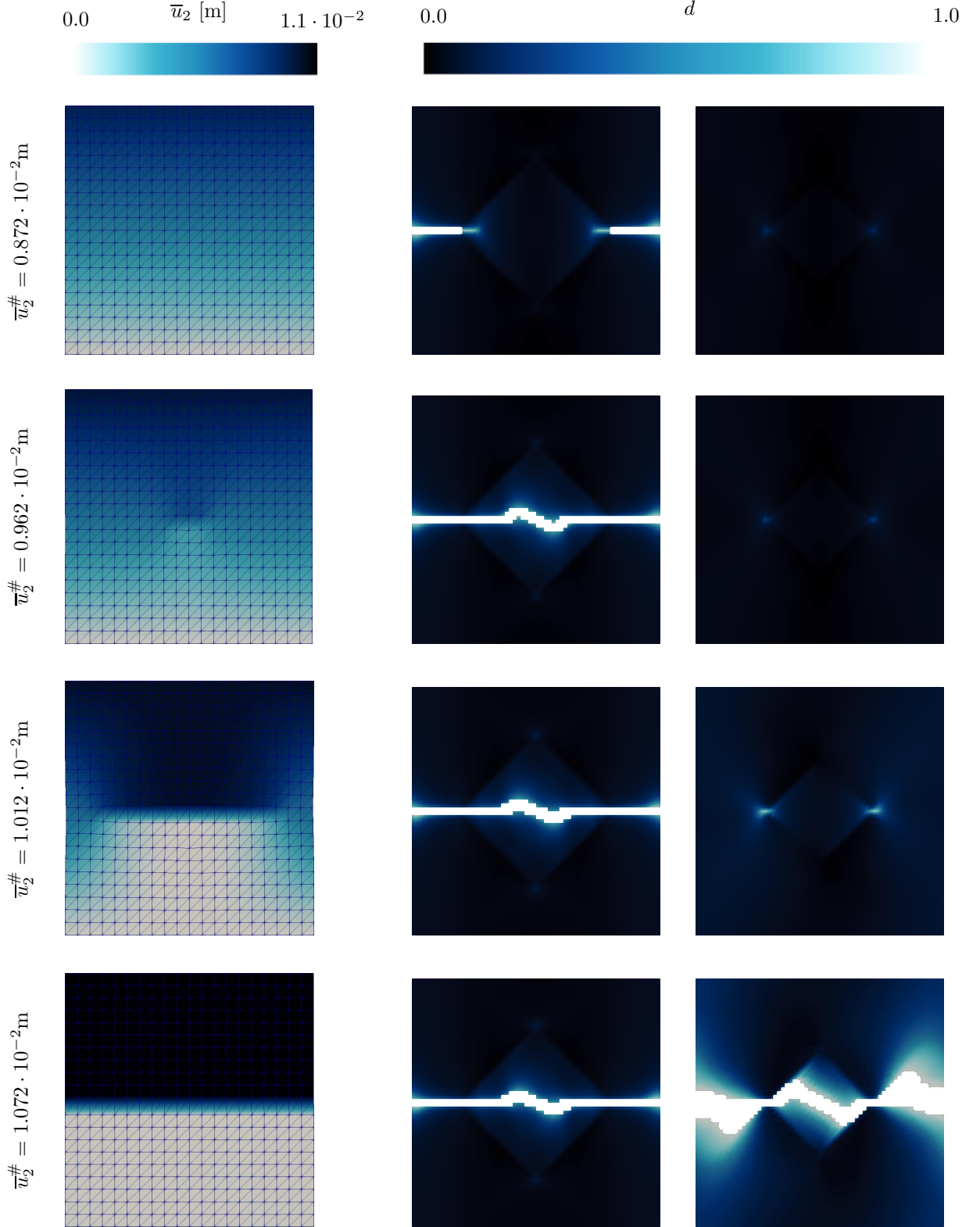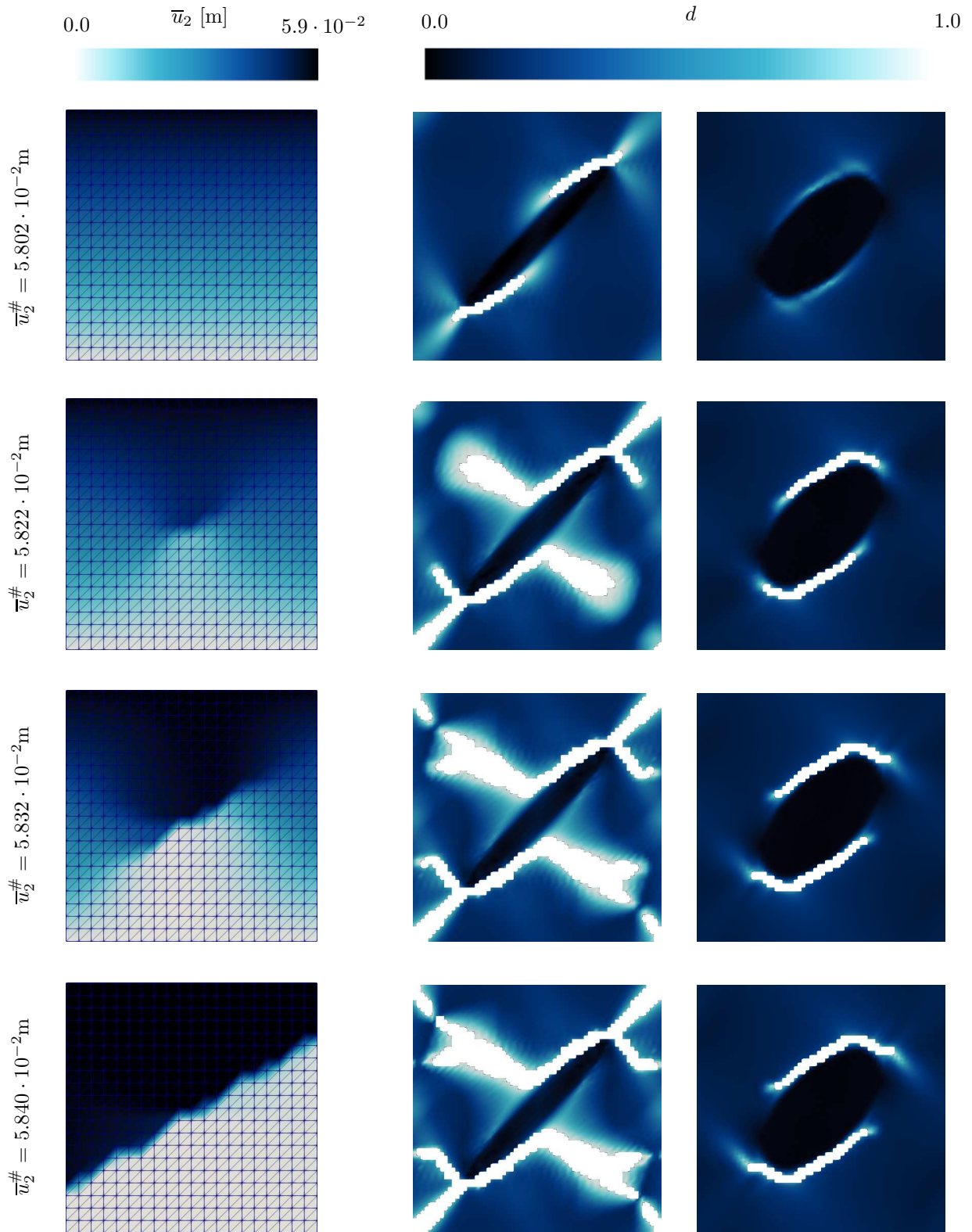
Figure 8.5: Multiscale simulation results of fracture occurring in a plane-strain plate with underlying microstructure. To the left, the macroscopic displacement component $\overline{u}_2$ is displayed at loads $\overline{u}_2^{\#} = 0.872 \cdot 10^{-2}$m, $\overline{u}_2^{\#} = 0.962 \cdot 10^{-2}$m, $\overline{u}_2^{\#} = 1.012 \cdot 10^{-2}$m and $\overline{u}_2^{\#} = 1.072 \cdot 10^{-2}$m. To the left, the microscopic fracture phase-field at the corresponding macroscopic load steps are depicted for the weakened RVE (left) in the middle of the plate and the regular RVE (right) sitting at the right edge of the RVE. One can see that the macroscopic displacements grow larger first in the area where the RVE is weakened, and the RVE is simultaneously cracking. A macrocrack – visible through the sharp change in the macroscopic displacement field – then progresses to the left and right till the whole specimen is broken.
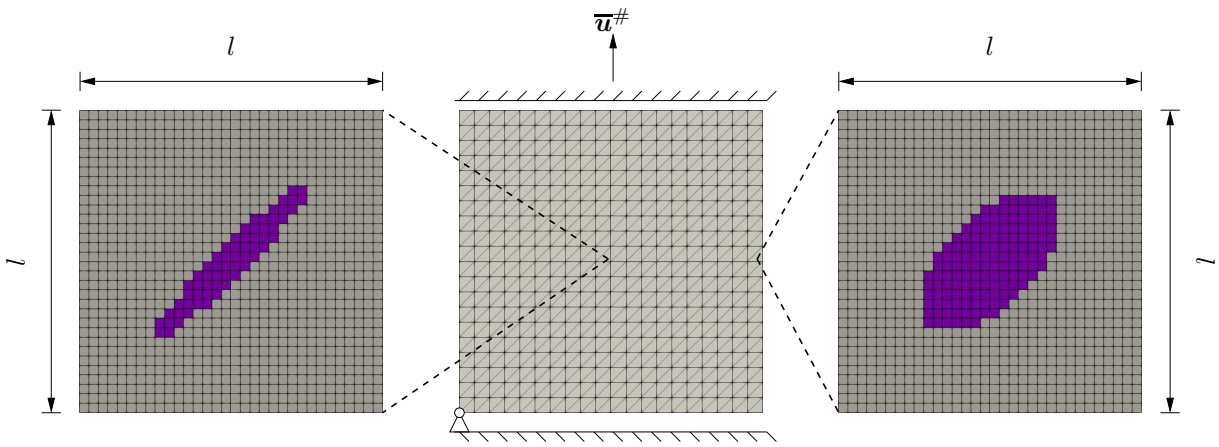
Figure 8.6: Multiscale boundary value problem for fracture of a plane-strain plate with un-derlying elliptic microstructure. The squared plate is of side-length $\bar{l} = 1$m, whereas the RVEs are of overall side-length $l = 1$mm $= 10^{-3}$m. The RVEs' microstructure obeys the following elliptic inclusion rule: If the coordinates $\{x_1, x_2\}$ of a grid point fulfill the inequality $((x_1 \cos(\pi/4) + x_2 \sin(\pi/4))/0.35l)^2 + ((x_1 \sin(\pi/4) - x_2 \cos(\pi/4))/0.15l)^2 < 1$, the point belongs to the stiff elliptic inclusion, where $\pi/4$ is the rotation angle of the ellipse, $0.15l$ its minor and $0.35l$ its major axis. The microstructure is visualized on the right. In the middle of the plate, a geometrically and materially weakened element is placed in the mid-dle of the plate, see left RVE. The microstructure follows the modified elliptic inequality $((x_1 \cos(\pi/4) + x_2 \sin(\pi/4))/0.4l)^2 + ((x_1 \sin(\pi/4) - x_2 \cos(\pi/4))/0.05l)^2 < 1$, where $\pi/4$ is the rotation angle of the ellipse, $0.05l$ its minor and $0.4l$ its major axis. The elliptic stiff inclusion is thus sharper and cracking is more likely to occur due to peaks in the stress.

Figure 8.7: Multiscale simulation results of fracture occurring in a plane-strain plate with underlying elliptic microstructure. To the left, the macroscopic displacement component $\overline{u}_2$ is displayed at loads $\overline{u}_2^{\#} = 5.802 \cdot 10^{-2}$m, $\overline{u}_2^{\#} = 5.822 \cdot 10^{-2}$m, $\overline{u}_2^{\#} = 5.832 \cdot 10^{-2}$m and $\overline{u}_2^{\#} = 5.840 \cdot 10^{-2}$m. To the left, the microscopic fracture phase-field at the corresponding macroscopic load steps are depicted for the weakened RVE (left) in the middle of the plate and the regular RVE (right) sitting at the right edge of the RVE. In contrast to the previous example, we now see an anisotropic failure of the macroscopic specimen due to the anisotropy of the underlying microstructure. Additionally, the right RVE is not completely failing, as the macro-crack has a different path now.

— **Part III** —

Artificial Neural Network-Based Approximation and Solution Schemes

Approximation of field variables and their gradients through artificial neural networks

Artificial Neural Networks (ANNs) are special kinds of approximation functions motivated by the learning processes in the human brain [71, 122]. Due to their excellent approximation of a priori unknown relations in a large amount of data, they are nowadays used in a broad range of applications [101, 183]. With the increase in applications, the number of different artificial neural network variants, such as recurrent or convolutional networks, grew. This chapter presents the neural network architecture used in this work, namely feedforward neural networks with several hidden layers. We will focus on the presentation of feedforward neural networks with one and two hidden layers to show their construction's underlying concept. The approximation properties of these ANNs are then demonstrated for a simple example and are compared to the Fourier-approximation presented in Chapter 5.

9.1. Artificial neural network variants

The basis for most of the artificial neural network variants used in recent machine learning is the perceptron [163]. In its most basic form, a perceptron consists of just one neuron with activation function $\sigma(z)$ where the argument

$$z = \sum_{j=1}^{d} w_j x_j + b \tag{9.1}$$

of the activation function is computed from the *actual input* $x_j \in \mathbb{R}^d$ multiplied with adjustable *weights* w_j and added by some adjustable *bias* b. In the beginning, the Heaviside step function was used as an activation function, mimicking a certain threshold that needs to be surpassed before the neuron is activated. However, nowadays, there are many more activation functions in use. Figure 9.1 shows three of the more popular ones and which were also used in this work. Use-case dependent choice of the activation function might lead to improved training and prediction.
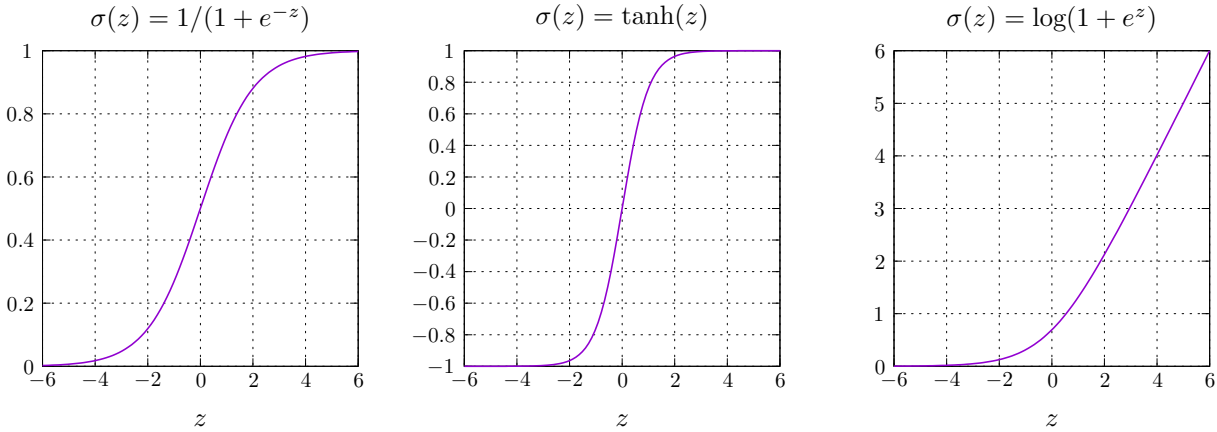Regarding the overall architecture of ANNs, there has been a major increase in different

Figure 9.1: Three possible activation functions that are popular in recent machine learning from left to right: logistic sigmoid, hyperbolic tangent and softplus function (Figure taken from [63]).

variants for different applications such as AlexNet [101] and GoogLeNet [186] for image recognition for example. However, in this work, we restrict ourselves to the basic architectures presented below.

9.1.1. Single layer perceptron (SLP)

A *single layer perceptron (SLP)* is an artificial neural network that processes the input through only one neuron. The output then appears as

$$N(\boldsymbol{x}, \mathfrak{r}) = \sigma(z) \quad \text{with} \quad z = \sum_{j=1}^{d} w_j x_j + b, \tag{9.2}$$

where we denote the vector of *all weights and biases* as $\mathfrak{r}$. Figure 9.2 shows a visualization of the SLP. Depending on the activation function, the SLP can fit linear and nonlinear functions to a certain extent. However, the approximation capabilities of the SLP have limitations. It were MINSKY & SEYMOUR [134] who proved that it is not possible to use an SLP to represent a function that is capable of performing an either-or (XOR) logical operation.

9.1.2. Multilayer perceptron

As stated above, there are some functions that SLPs are not capable of approximating. However, this restriction can be overcome by adding additional *hidden layers* of neurons in between the input and the output [134, 165]. It were CYBENKO [31] and HORNIK ET AL. [81] who first showed that ANNs of such kind using nonlinear activation functions are universal approximators, i.e., they are able to fit every function as long as they have enough internal parameters, see also [80]. Figure 9.3 shows a visualization of a densely connected multilayer perceptron. Each input x_d is multiplied with different weights for each neuron and is passed along with a bias to the individual neurons assembled in the hidden layer. The output of the neurons of one layer is then treated analogously to the input vector. They are multiplied with new weights, added by a bias, and passed to the next hidden layer. The output layer then computes the neural network's output.
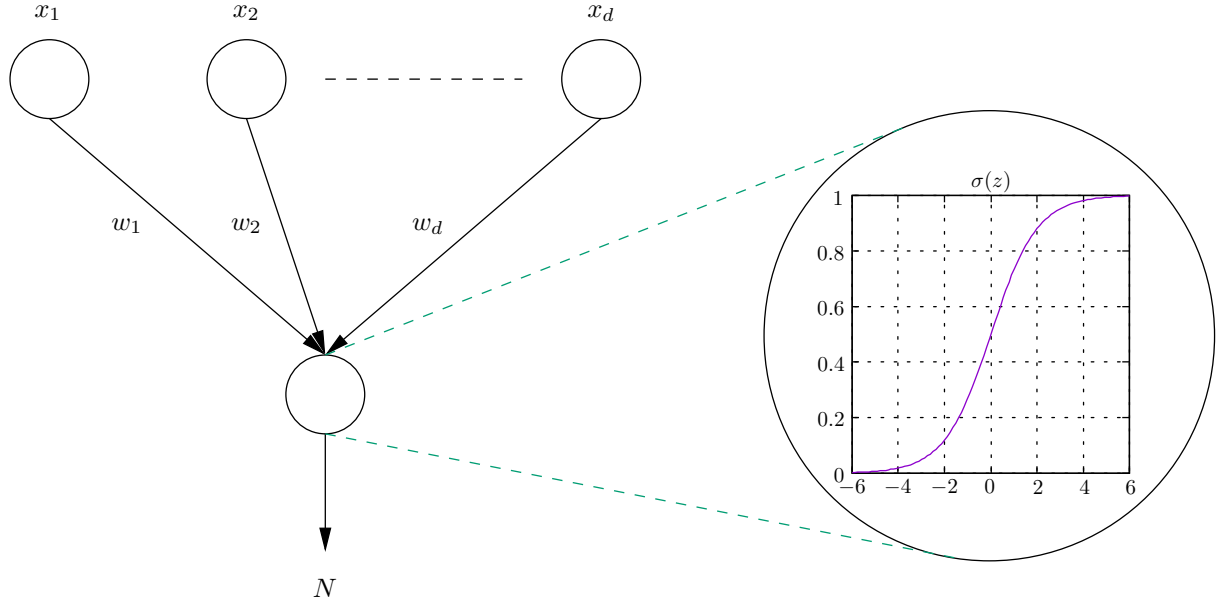
Figure 9.2: A single layer perceptron (SLP) with one input layer and an output neuron, where the activation function $\sigma(z)$ is applied.
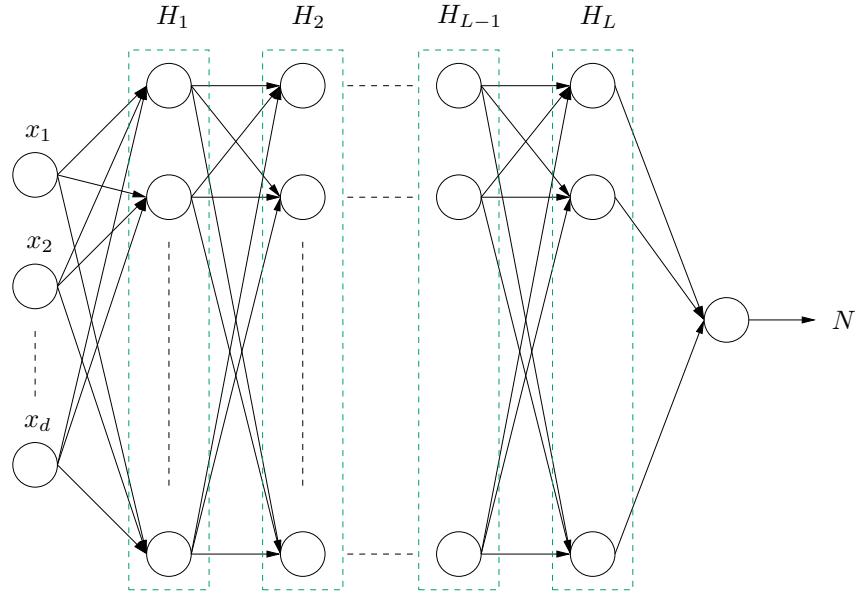

Figure 9.3: General structure of a multilayer perceptron with input $\boldsymbol{x}$, L hidden layers denoted by dotted boxes and output N. Each neuron processes its inputs through predefined activation functions according to the weights and biases.

Perceptron with one hidden layer. Casting this concept into equations, the response of a neural network with one hidden layer appears as

$$N(\boldsymbol{x}, \mathbf{r}) = \sum_{i=1}^{H} v_i \sigma(z_i) + \overline{b} \quad \text{with} \quad z_i = \sum_{j=1}^{d} w_{ij} x_j + u_i, \tag{9.3}$$

where there are the additional weights and biases v_i and $\overline{b}$ appearing and H is the number of neurons appearing in the hidden layer. Again, we assemble the weights and biases in the vector $\mathbf{r}$. To optimize a neural network through some predefined cost function, we need

the derivatives of the ANN with respect to its weights and biases. This differentiation can be done either through automatic differentiation methods [1] or analytically as follows

$$
\begin{aligned}
\frac{\partial N}{\partial u_i} &= v_i \sigma'(z_i), & \frac{\partial N_{,j}}{\partial u_i} &= v_i w_{ij} \sigma''(z_i), \\
\frac{\partial N}{\partial w_{ij}} &= v_i x_j \sigma'(z_i), & \frac{\partial N_{,j}}{\partial w_{im}} &= x_m v_i w_{ij} \sigma''(z_i) + v_i \sigma'(z_i) \delta_{jm}, \\
\frac{\partial N}{\partial \overline{b}} &= 1, & \frac{\partial N_{,j}}{\partial \overline{b}} &= 0, \\
\frac{\partial N}{\partial v_i} &= \sigma(z_i), & \frac{\partial N_{,j}}{\partial v_i} &= w_{ij} \sigma'(z_i).
\end{aligned}
\tag{9.4}
$$

In the latter equation, the indices *do not* follow Einstein's summation convention. Indices occurring twice are multiplied pointwise.

Lastly, it will be useful for later applications to have the gradient of the ANN with respect to its input x_j. In analogy to the previous derivatives, they can be either computed by the automatic differentiation or analytically as follows

$$
N_{,j} = \frac{\partial N}{\partial x_j} = \sum_{i=1}^{H} v_i w_{ij} \sigma'(z_i),
\tag{9.5}
$$

with $\sigma'(z_i)$ being the sigmoid function's derivative with respect to its input argument. We now see that the derivative of the ANN with respect to its input is itself an ANN with modified weights and biases, see also [103]. However, the modified ANN now is a gradient field and thus has the according properties such as a vanishing of the rotation.

Perceptron with two hidden layers. The concept of hidden layers in ANNs is now explained for two hidden layers. Adding further layers from this point on can then be performed in the same fashion. For two hidden layers, the ANN's response is computed according to

$$
N(\boldsymbol{x}, \mathfrak{r}) = \sum_{k=1}^{H_2} v_k \sigma(r_k) + \overline{b}, \quad r_k = \sum_{i=1}^{H_1} \theta_{ki} \sigma(z_i) + c_k \quad \text{with} \quad z_i = \sum_{j=1}^{d} w_{ij} x_j + u_i, \tag{9.6}
$$

where there are the additional weights θ_{ki} and biases c_k associated with the second hidden layer [63]. In analogy to the previous ANN, the derivatives with respect to the ANN's

weights and biases appear as

$$\frac{\partial N}{\partial u_i} = \sum_{k=1}^{H_2} v_k \sigma'(r_k)\theta_{ki}\sigma'(z_i), \qquad \frac{\partial N_{,j}}{\partial u_i} = \sum_{k=1}^{H_2}\left[v_k\sigma''(r_k)\theta_{ki}\sigma'(z_i)\sum_{i=1}^{H_1}[w_{ij}\theta_{ki}\sigma'(z_i)] \right.$$
$$\left. + v_k\sigma'(r_k)\theta_{ki}\sigma''(z_i)w_{ij}\right],$$

$$\frac{\partial N}{\partial w_{ij}} = \sum_{k=1}^{H_2} v_k\sigma'(r_k)\theta_{ki}\sigma'(z_i)x_j, \qquad \frac{\partial N_{,j}}{\partial w_{im}} = \sum_{k=1}^{H_2}\left[v_k\sigma''(r_k)\theta_{ki}\sigma'(z_i)x_m\sum_{i=1}^{H_1}[w_{ij}\theta_{ki}\sigma'(z_i)]\right.$$
$$+ v_k\sigma'(r_k)\theta_{ki}\sigma''(z_i)w_{ij}x_m$$
$$\left. + v_k\sigma'(r_k)\theta_{ki}\sigma'(z_i)\delta_{im}\right],$$

$$\frac{\partial N}{\partial c_k} = v_k\sigma'(r_k), \qquad \frac{\partial N_{,j}}{\partial c_k} = v_k\sigma''(r_k)\sum_{i=1}^{H_1}[w_{ij}\theta_{ki}\sigma'(z_i)],$$

$$\frac{\partial N}{\partial \theta_{ki}} = v_k\sigma'(r_k)\sigma(z_i), \qquad \frac{\partial N_{,j}}{\partial \theta_{ki}} = v_k\sigma''(r_k)\sigma'(z_i)\sum_{i=1}^{H_1}[w_{ij}\theta_{ki}\sigma(z_i)]$$
$$+ v_k\sigma'(r_k)\sigma'(z_i)w_{ij},$$

$$\frac{\partial N}{\partial \overline{b}} = 1, \qquad \frac{\partial N_{,j}}{\partial \overline{b}} = 0,$$

$$\frac{\partial N}{\partial v_k} = \sigma(r_k), \qquad \frac{\partial N_{,j}}{\partial v_k} = \sigma'(r_k)\sum_{i=1}^{H_1}[w_{ij}\theta_{ki}\sigma'(z_i)].$$

$$(9.7)$$

Especially in the case of more complicated problems with a large data set, the use of deeper networks potentially leads to improved training behavior and more accurate predictions [65, 166]. Even though the derivatives can still be computed analytically, they can become quite cumbersome. Especially for deeper networks, the use of automatic differentiation decreases the risk of implementation errors in experimental code.

Lastly, the derivative of the two-layered ANN is given by the following equation

$$N_{,j} = \frac{\partial N}{\partial x_j} = \sum_{k=1}^{H_2}\sum_{i=1}^{H_1} v_k\sigma'(r_k)\theta_{ki}\sigma'(z_i)w_{ij}. \tag{9.8}$$

9.2. Illustrative Example: One-Dimensional Data Fitting

We now want to demonstrate the approximation properties of ANNs based on a simple example. In analogy to the Fourier-based approximation in Chapter 5, we first generate $N = 21$ value pairs (x_N, y_N) as visualized in Figure 9.4. In this example, ANNs with one hidden layer are used. In order to optimize the response of the ANNs, a least-squares error is defined

$$\mathfrak{J} = \sum_{i=1}^{N=21} (N(x_i, \mathfrak{r}) - y_i)^2, \tag{9.9}$$

which is optimized with respect to the neural network's weights $\mathfrak{r}$. A Quasi-Newton method as implemented in [118] is used for the optimization of the objective function,
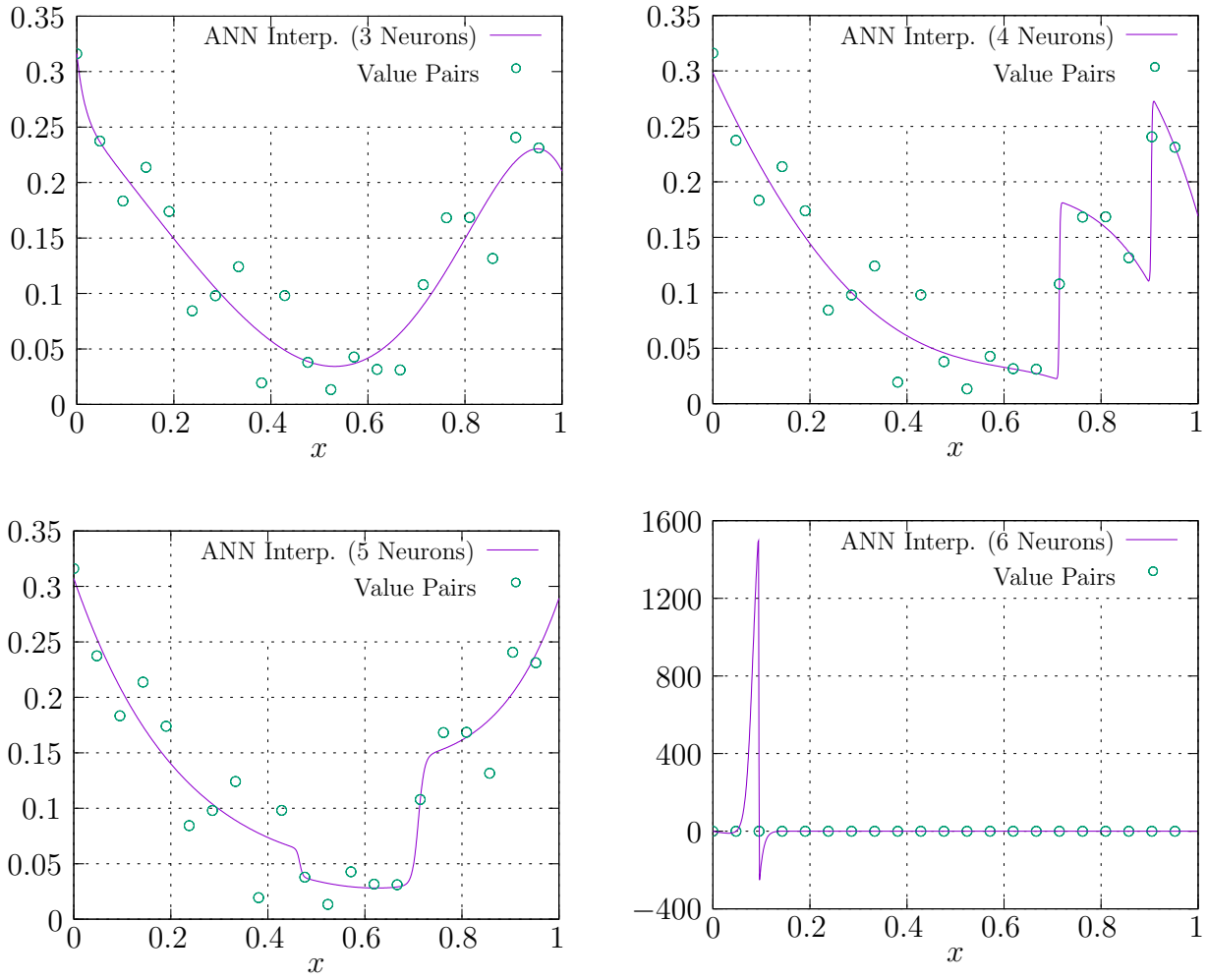
Figure 9.4: The graphs show the approximation of the $N = 21$ given value pairs with an ANN with one hidden layer according to definition (9.3) using 3, 4, 5, and 6 neurons. In contrast to the Fourier approximation 5.1, the approximated curve does not *precisely* match the value pairs as the trained ANN emerges from a least-squares optimization. Also note the localization in the last SLP, which is usually denoted as *overfitting*

where the derivatives with respect to the weights

$$\frac{\partial \mathfrak{J}}{\partial \mathbf{r}} = \sum_{i=1}^{N=21} 2(N(x_i, \mathbf{r}) - y_i)\frac{\partial N(x_i, \mathbf{r})}{\partial \mathbf{r}} \tag{9.10}$$

can be computed by using Equation (9.4). The logistic sigmoid function, as described in Figure 9.1 is chosen as an activation function for neurons in the hidden layer. All other relevant parameters for the solution process, such as tolerance and weight initialization, can be found in the MATLAB [118] code given below. Figure 9.4 shows the result for ANNs using 3, 4, 5 and 6 neurons in the hidden layer. In contrast to Fourier and finite element approximations, the approximated curve does not exactly match the value y_i at x_i. The last curve using 6 neurons shows some localization phenomenon, which is usually referred to as *overfitting*. Even though the least square error was the smallest for this ANN, the solution intuitively does not seem reasonable due to the massive peak between two data points. We conclude that, it is not trivial to construct appropriate ANNs for specific problems.

Listing 9.1: Data Fitting Matlab Implementation

```matlab
close all
clear all
rng(135,'twister')

% Number of value pairs and grid points
N = 21;
x = 0:1/N:1-(1/N);

% Create data points with random perturbation
y = (x-0.5).^2 + rand(1,N)*0.1;

% Number of hidden neurons
nn = 3;

% Initialize weights and biases
wb0 = rand(3*nn+1,1);

% Anonymous function handle for feedforward net and loss
    function
f = @(wb)neuralapprox(wb,x,y,N,nn);

% Call minimizer
opts = optimoptions(@fminunc,'Algorithm','quasi-newton',...
    'StepTolerance',1e-12,'OptimalityTolerance',1e-12,...
    'MaxFunctionEvaluations',10000,...
    'SpecifyObjectiveGradient',true,'CheckGradients',true,...
    'FiniteDifferenceType','central','MaxIterations',10000);
[wb,f] = fminunc(f,wb0,opts)

function [f, g] = neuralapprox(wb,x,y,N,nn)

% Restore weights and biases for ANN
u = wb(1:nn);
w = wb(nn+1:2*nn);
b = wb(2*nn+1);
v = wb(2*nn+2:3*nn+1);

% Input processing
z = w*x + u;
xmatr = x.*ones(size(z));

% Sigmoid activation function in each neuron
sigmoid = (1 + exp(-z)).^(-1);
ANN = sum(v.*sigmoid) + b;

% ANN derivatives w.r.t. weights and biases
```

```
46  d_sigmoid = exp(−z).∗(1 + exp(−z)).ˆ(−2);
47  ANN_du = v.∗d_sigmoid;
48  ANN_dw = v.∗d_sigmoid.∗xmatr;
49  ANN_db = ones(1,size(x,2));
50  ANN_dv = sigmoid;
51
52  % Least−squares loss function
53  JJ = (ANN − y).ˆ2;
54
55  % Derivative of least−squares loss function w.r.t. weights and
        biases
56  JJ_du = 2.0∗(ANN − y).∗ANN_du;
57  JJ_dw = 2.0∗(ANN − y).∗ANN_dw;
58  JJ_db = 2.0∗(ANN − y).∗ANN_db;
59  JJ_dv = 2.0∗(ANN − y).∗ANN_dv;
60
61  % Assemble and sum least−squares and least−squares' gradients
        over all data points
62  g1 = [JJ_du;JJ_dw;JJ_db;JJ_dv];
63  f = (1/N)∗sum(JJ);
64  g = (1/N)∗sum(g1')';
65
66  end
```

Constrained artificial neural network-based solution scheme for periodic boundary value problems

This chapter presents the idea of constrained artificial neural networks for the solution of partial differential equations. The method used here traces back to LAGARIS ET AL. [103] who introduced test functions based on artificial neural networks multiplied with constraining functions to always fulfill given boundary conditions and minimized the square norm of the strong form of different partial differential equations. In this work, the constraining functions are constructed to satisfy the periodic boundary conditions of homogenization problems, see also GÖKÜZÜM ET AL. [63]. Additionally, we will not minimize the square norm of the strong form of a partial differential equation, but the energetic potential in integral form, which is usually used in variational formulations of boundary value problems. The framework is then tested for electrostatic problems using different training methods and microstructure realizations. Wherever possible, code is provided within this chapter.

10.1. Artificial neural network-based solution scheme

In order to optimize energetic potentials such as (3.14), see also (3.16), one needs to find appropriate approximation methods for the solution fields such as the Fourier approximation discussed in Chapter 5 or the finite element method. We will now discuss a third approach tracing back to the idea of LAGARIS ET AL. [103], who suggested the multiplication of ANNs with constraining functions in order to meet given boundary conditions. Therefore, we recall that we derived periodic Dirichlet boundary conditions as one accessible solution of the Hill-Mandel equation in Section 4.3. Considering a purely electrostatic problem at hand, the energy potential (3.16) then takes the form

$$\Pi(\phi) = \int_{\mathcal{B}} \psi(\boldsymbol{x}, \boldsymbol{E}) \, dV. \tag{10.1}$$

In order to solve the latter potential under periodic boundary conditions, we now construct the trial function

$$\widetilde{\phi}_t(\boldsymbol{x}, \boldsymbol{\mathfrak{r}}) = A_0(\boldsymbol{x}) + A_1(\boldsymbol{x})N_1(\boldsymbol{x}, \boldsymbol{\mathfrak{r}}_1) + A_2(\boldsymbol{x})N_2(\boldsymbol{x}, \boldsymbol{\mathfrak{r}}_2) + \ldots + A_n(\boldsymbol{x})N_n(\boldsymbol{x}, \boldsymbol{\mathfrak{r}}_n), \tag{10.2}$$

as a combination of arbitrary ANNs $N_i(\boldsymbol{x}, \mathfrak{r}_i)$ multiplied with the constraining functions $A_i(\boldsymbol{x})$ in such a way that the trial function $\widetilde{\phi}_t(\boldsymbol{x}, \mathfrak{r})$ *a priori* fulfills the periodic boundary conditions. The trial electric field according to Equations (4.5) and (4.28) can now be computed as

$$\boldsymbol{E}_t = \overline{\boldsymbol{E}} - \nabla \widetilde{\phi}_t, \tag{10.3}$$

where the gradient of the trial function can either be obtained from Equations (9.5) and (9.8) or from automated differentiation. Insertion of the trial electric field $\boldsymbol{E}_t$ into the global potential (10.1) gives the potential in dependence of the neural network's parameters

$$\Pi(\mathfrak{r}) = \int_{\mathcal{B}} \psi(\boldsymbol{x}, \boldsymbol{E}_t(\boldsymbol{x}, \mathfrak{r})) \, dV. \tag{10.4}$$

We finally obtain our optimization objective from the Hill-Mandel condition (4.1), which states that the macroscopic potential equals the microscopic potential at equilibrium

$$\boxed{\overline{\Pi} = \sup_{\mathfrak{r}} \frac{1}{|\mathcal{B}|} \Pi(\mathfrak{r}),} \tag{10.5}$$

where the degrees of freedom are now the ANN's weights and biases $\mathfrak{r}$. These can be obtained from an unconstrained optimization as the trial function (10.2) already fulfills the periodic boundary conditions by construction.

10.2. Representative numerical examples

In this section, the validity of the aforementioned method is tested for a variety of numerical examples. First, a simple one-dimensional laminate is considered, where an analytic solution is available for comparison. For this example, the Tensorflow [1] code is given to show how the code can be set up. Second, a real microstructure is considered to show that the method can work for more complicated geometries. Lastly, a three-dimensional computation is carried out. The later examples are compared to a conventional FFT-based solution. All computations in this section are carried out with normalized units. Parts of these results can be found in GÖKÜZÜM ET AL. [63].

10.2.1. One-dimensional homogenization of a laminate

We now consider a one-dimensional laminate under a homogeneous macroscopic electric loading of $\overline{E} = 1$. The RVE of length $l = 1$ consists of two layers of electric permittivity $\kappa_1^* = 1$ and $\kappa_2^* = 2$ for $x > 0.5$. In this example, we consider a simple quadratic global potential for dielectrics of the form

$$\Pi(\phi) = \int_{\mathcal{B}} \psi(E, x) \, dx = -\int_{\mathcal{B}} \frac{1}{2} \kappa^* E^2 \, dx. \tag{10.6}$$

Comparing the latter equation with the energy density of a dielectric material (2.112), the electric permittivity used in these examples can be identified as

$$\kappa^* = \epsilon_0(1 + \chi) \tag{10.7}$$

Using the micro-macro decomposition

$$E = \overline{E} - \frac{\partial \widetilde{\phi}}{\partial x} \tag{10.8}$$

and applying the boundary conditions $\widetilde{\phi}(0) = 0$ and $\widetilde{\phi}(1) = 0$, we obtain the analytic solution for the electric field as

$$E = \begin{cases} \dfrac{2\overline{E}}{1 + \frac{\kappa_1^*}{\kappa_2^*}} & 0 \leq x < l/2 \\[4mm] \dfrac{2\overline{E}}{1 + \frac{\kappa_2^*}{\kappa_1^*}} & l/2 < x \leq l \end{cases} \tag{10.9}$$

as well as for the scalar electric potential

$$\widetilde{\phi} = \begin{cases} (\overline{E} - E)x & 0 \leq x \leq l/2 \\[2mm] (\overline{E} - E)x - (\overline{E} - E)l & l/2 \leq x \leq l \end{cases}. \tag{10.10}$$

We now want to compare an ANN-based solution to the analytic one. In order to meet the given boundary conditions, the trial function is constructed as follows

$$\widetilde{\phi}_t = A_o + A_1(x)N(x, \mathbf{r}) = x(1 - x)N(x, \mathbf{r}), \tag{10.11}$$

where N can be an arbitrary ANN, which takes the coordinate x as an input. In order to compute the electric field, we differentiate the trial function

$$\frac{\partial \widetilde{\phi}_t}{\partial x} = (1 - 2x)N(x, \mathbf{r}) + x(1 - x)\frac{\partial N(x, \mathbf{r})}{\partial x}. \tag{10.12}$$

Insertion of the latter expression into Equation (10.8) and (10.6) gives the global potential

$$\Pi(\mathbf{r}) = -\int_{\mathcal{B}} \frac{1}{2}\kappa^*(\overline{E} - \frac{\widetilde{\phi}_t}{\partial x})^2 \, dx \tag{10.13}$$

with respect to the weight parameters of the ANN. We finally need to evaluate the integral appearing in the latter equation. We therefore discretize the coordinates x in the interval $[0, 1]$ by equidistant grid points x_k of distance Δx, giving the discrete coordinates $\{\Delta x/2, 3\Delta x/2, \ldots, 1 - \Delta x/2\}$, and apply a quadrature rule at said coordinates. This procedure gives the discrete objective

$$\boxed{\overline{\Pi} = \sup_{\mathbf{r}} \sum_{0 < x_k < 1.0} -\frac{1}{2}\kappa_1^*(\overline{E} - \frac{\widetilde{\phi}_t}{\partial x})^2 \Delta x.} \tag{10.14}$$

The optimization of the objective can be carried out employing some gradient descent method.

In this example, the Adam optimizer [94] with the default training hyper-parameters is used. The ANN for the trial function has 5 hidden layers with 5 neurons each and one linear output unit. The hyperbolic tangent and the softplus function serve as activation
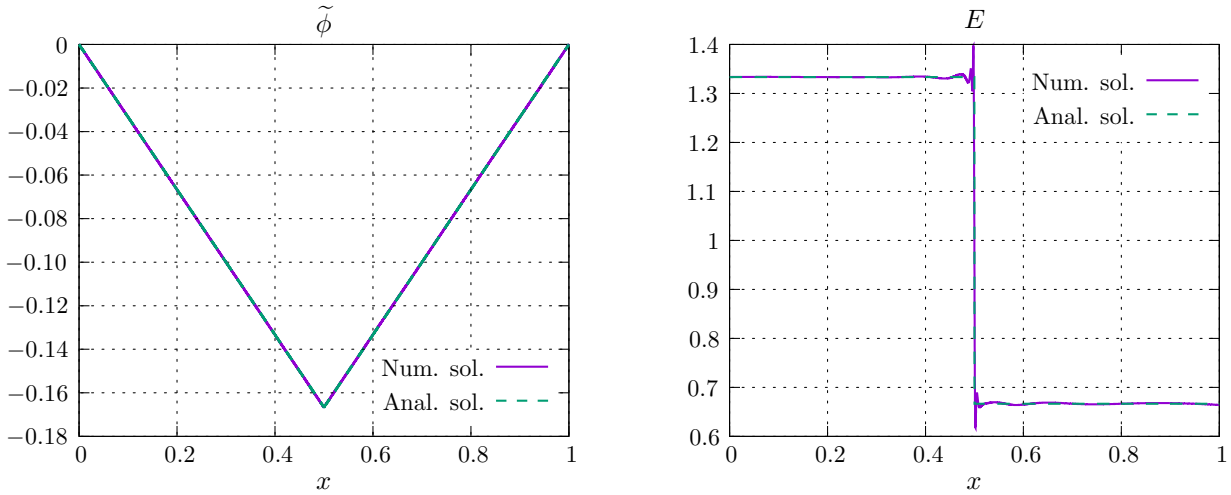
Figure 10.1: To the left, one can see a good agreement between the numerical solution to $\widetilde{\phi}$ using a modified ANN with 5 hidden layers and the analytic solution. The graph to the right for the analytic and the numeric solution of the electric field reveals oscillations at the discontinuity point.

functions in the neurons. Tensorflow's automated differentiation carries out the ANN's differentiation with respect to its input x and its weights and biases $\boldsymbol{\tau}$. The weights and biases $\boldsymbol{\tau}$ of the ANN are initialized according to the algorithm proposed by GLOROT & BENGIO [59]. Figure 10.1 shows the analytic and the numerical results for the fluctuative scalar electric potential $\widetilde{\phi}$ and the electric field E. One can see that the ANN-based solution for $\widetilde{\phi}$ is close to the analytic one. A look at the solution of the electric field reveals oscillations at the location of the discontinuity. According to CYBENKO [31] and HORNIK ET AL. [81], ANNs are able to approximate *any* function arbitrarily close. However, the training must not necessarily lead to such accurate approximations, as shown in Chapter 9. The Tensorflow code that generated this example can be found below.

Listing 10.1: One-dimensional Tensorflow Implementation

```python
import tensorflow as tf
tf.enable_eager_execution()

# Evaluation points in area
dx = 0.0001
x = tf.range(dx/2,1.0,dx)
# Stack as tf version 1.12. ANNs have a minimum input dimension
    of 2
xx = tf.stack([x,x],axis=1)
# Electric permittivity in laminate (stacked again)
kappa1 = tf.constant(1.0, shape=[(1.0/dx)/2, 2])
kappa2 = tf.constant(2.0, shape=[(1.0/dx)/2, 2])
kappa = tf.concat([kappa1, kappa2], 0)

# Build the ANN-model
class ANN(tf.keras.Model):
    def __init__(self):
        super(ANN, self).__init__()
```

```
18            # Define the layers, the neurons within the layers, the
                  neuron's activation functions and initialization
19            self.dense1 = tf.keras.layers.Dense(units = 5,
                  activation='tanh',kernel_initializer='glorot_uniform'
                  ,)
20            self.dense2 = tf.keras.layers.Dense(units = 5,
                  activation='tanh',kernel_initializer='glorot_uniform'
                  ,)
21            self.dense3 = tf.keras.layers.Dense(units = 5,
                  activation='tanh',kernel_initializer='glorot_uniform'
                  ,)
22            self.dense4 = tf.keras.layers.Dense(units = 5,
                  activation='softplus',kernel_initializer='
                  glorot_uniform',)
23            self.dense5 = tf.keras.layers.Dense(units = 5,
                  activation='softplus',kernel_initializer='
                  glorot_uniform',)
24            self.dense6 = tf.keras.layers.Dense(units = 1)
25        def call(self, inputs):
26            # Pass the input signal (x-coordinates) through the
                  layers of the ANN
27            result = self.dense1(inputs)
28            result = self.dense2(result)
29            result = self.dense3(result)
30            result = self.dense4(result)
31            result = self.dense5(result)
32            result = self.dense6(result)
33            # Multiply the response of the ANN with the constraining
                  function: (x-1)*x*N
34            return (inputs-1)*inputs*result
35
36 # Use the ADAM-optimizer with the default learning parameters
37 optimizer = tf.train.AdamOptimizer(learning_rate=0.001,beta1=
        0.9,beta2=0.999,epsilon=1e-08,use_locking=False)
38
39 # Assign the ANN-model to a function
40 phi = ANN()
41
42 # Optimization loop
43 for i in range(20000):
44     with tf.GradientTape() as tape:
45         with tf.GradientTape() as tape2:
46             tape2.watch(xx)
47             # Evaluate the fluctuative scalar potential
48             phi_t = phi(xx)
49             # Evaluate the energy potential at quadrature points
                  by using automated differentiation
```
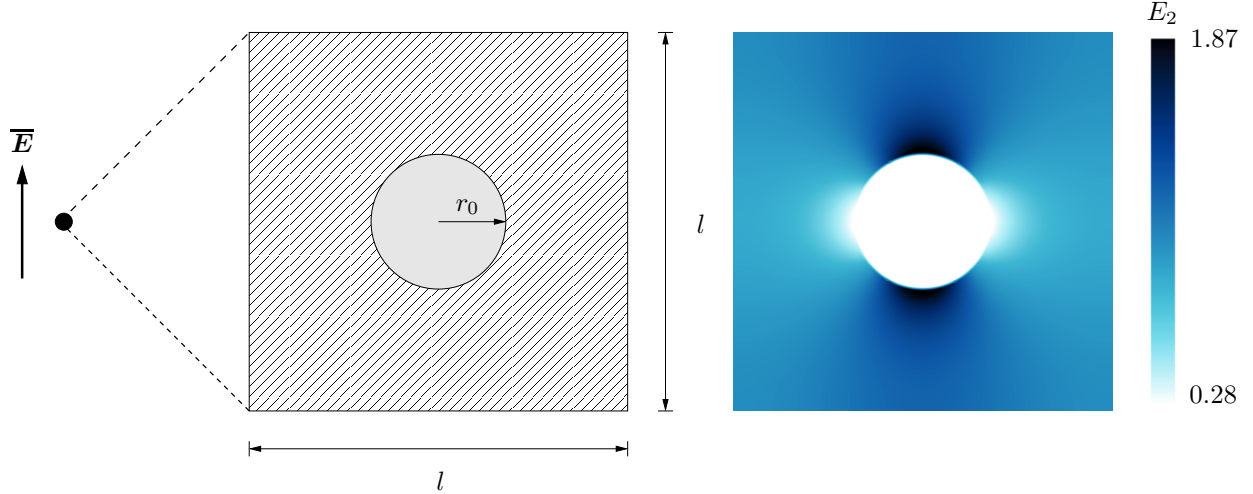
Figure 10.2: An RVE of unit length $l = 1$ consists of a matrix material with low material permittivity $\kappa = 1$ and a circular inclusion of radius $r_0 = 0.178$ of high permittivity $\kappa_2 = 10$. An electric field $\overline{E}_1 = 0$ and $\overline{E}_2 = 1$ is applied under periodic boundary conditions. To the right, one can see a FEM reference solution showing the distinct jumps at the interface.

```
50        # with respect to the x-coordinates to obtain the
             electric field
51        EnergyPotential = dx*tf.reduce_sum(0.5*kappa*(1.0 -
             tape2.gradient(phi_t,xx))**2.0)
52      # Compute gradients with respect to the weights and
           biases through automated differentiation
53      gradients = tape.gradient(EnergyPotential, phi.variables
           )
54    # Update weights and biases of the ANN using the gradients
55    optimizer.apply_gradients(zip(gradients, phi.variables),
56                              global_step=tf.train.
                                  get_or_create_global_step())
57    print(i,"%.12f"%EnergyPotential)
```

10.2.2. Periodic homogenization of RVE with two-dimensional spherical inclusion

In this example, we explore a relatively simple two-dimensional problem that allows for some numerical studies and intuitive considerations. We therefore consider an RVE of unit length $l = 1$. It consists of the matrix material of low electric permittivity $\kappa^* = 1$ and a circular inclusion of high electric permittivity $\kappa_2^* = 10$. The circular inclusion occupies approximately 10% of the overall RVE area, corresponding to a circular radius of $r_0 = 0.178$, see also Figure 10.2. The RVE is the loaded with a vertical macroscopic electric field $\overline{E}_1 = 0$ and $\overline{E}_2 = 1$ under periodic boundary conditions. The two-dimensional constitutive law and global potential then takes the form

$$\Pi = \int_{\mathcal{B}} \psi(\boldsymbol{E}) \, dV = -\int_{\mathcal{B}} \frac{1}{2}\kappa^* \boldsymbol{E} \cdot \boldsymbol{E} \, dA, \tag{10.15}$$

Figure 10.2 shows a FEM solution that will serve as a reference for the ANN-based solutions to come. The global macroscopic energy in equilibrium for the FEM simulation was computed as $\overline{\Pi}^{\mathrm{FEM}} = 0.588652$.

For an ANN-based approach, we now again need to construct a global trial function that fulfills the given set of periodic boundary conditions. For the two-dimensional case, we, therefore, need three ANNs: $N_{x_1}(X_1)$ only taking the x_1 coordinate as argument, $N_{x_2}(X_2)$ only taking the x_2 coordinate as argument and $N_{\boldsymbol{x}}$ taking both coordinates as input argument. Multiplication with the proper constraining functions yields the global trial function

$$
\begin{aligned}
\widetilde{\phi}_t(\boldsymbol{x}, \mathfrak{r}) &= A_1(x_1, x_2) N_1(\boldsymbol{x}, \mathfrak{r}_1) + A_2(x_1) N_{x_1}(x_1, \mathfrak{r}_{x_1}) + A_3(x_2) N_{x_2}(x_2, \mathfrak{r}_{x_2}) \\
&= x_1(1 - x_1) x_2(1 - x_2) N_1(\boldsymbol{x}, \mathfrak{r}_1) \\
&\quad + x_1(1 - x_1) N_{x_1}(x_1, \mathfrak{r}_{x_1}) + x_2(1 - x_2) N_{x_2}(x_2, \mathfrak{r}_{x_2}),
\end{aligned}
\tag{10.16}
$$

where we see that periodicity is always maintained due to how A_i and N_i are defined. Using the latter equation, the trial electric field can then be computed according to

$$
\boldsymbol{E}_t = \overline{\boldsymbol{E}} - \nabla \widetilde{\phi}_t.
\tag{10.17}
$$

In analogy to the one-dimensional global potential (10.13), the two-dimensional extension in terms of vectorial quantities can be obtained as

$$
\overline{\Pi} = \sup_{\mathfrak{r}} \frac{1}{|\mathcal{B}|} \Pi(\mathfrak{r}) = \sup_{\mathfrak{r}} \frac{1}{|\mathcal{B}|} \int_{\mathcal{B}} -\frac{1}{2} \kappa^*(\boldsymbol{x}) \boldsymbol{E}_t \cdot \boldsymbol{E}_t \, dA.
\tag{10.18}
$$

which needs to be optimized with respect to the ANNs' weight and bias parameters $\mathfrak{r}$. In this example, we use an MLP with two hidden layers for the neural network N_1 acting in the volume and MLPs with one hidden layer for the neural networks N_{x_1} and N_{x_2}. The hyperbolic $\sigma(z) = \tanh(z)$ serves as an activation function in all hidden layers. The gradients with respect to the input $\boldsymbol{x}$ needed for $\boldsymbol{E}_t$ as well as with respect to the weight and bias parameters $\mathfrak{r}$ needed for the optimization are now computed analytically according to Subsection 9.1.2. The optimization of $\overline{\Pi}$ is carried out utilizing the L-BFGS-B optimization algorithm [20, 213]. The integration is carried out through a regular mesh of elements using nine Gauss points for the numerical integration. In order to demonstrate the features of the method the same boundary value problem is now solved for a different combination of mesh resolution and ANN size as follows: a) 51×51 elements, 15 neurons in each of the two hidden layers of the MLP N_1 and 5 neurons each in the layer of the boundary MLPs N_{x_i}, b) 51×51 elements, 10 neurons in each of the two hidden layers of the MLP and 5 neurons each in the layer of the boundary and c) 101×101 elements, 15 neurons in each of the two hidden layers of the MLP and 5 neurons each in the layer of the boundary MLPs [63].

In classical machine learning approaches, the training behavior and response of ANNs are dependent on the initialization [59]. To show that initialization is a crucial step in this method, we will demonstrate the training result for two different initializations. First, the weight vector is initialized according to a uniform random distribution

$$
\mathfrak{r}^{(0)} \sim \mathcal{U}(-1, 1).
\tag{10.19}
$$

Figure 10.3 shows the contour plots of E_2 for the uniform distribution for the ANN and integration set-up a), b) and c) after 20 000 iterations. One can see in a) that an
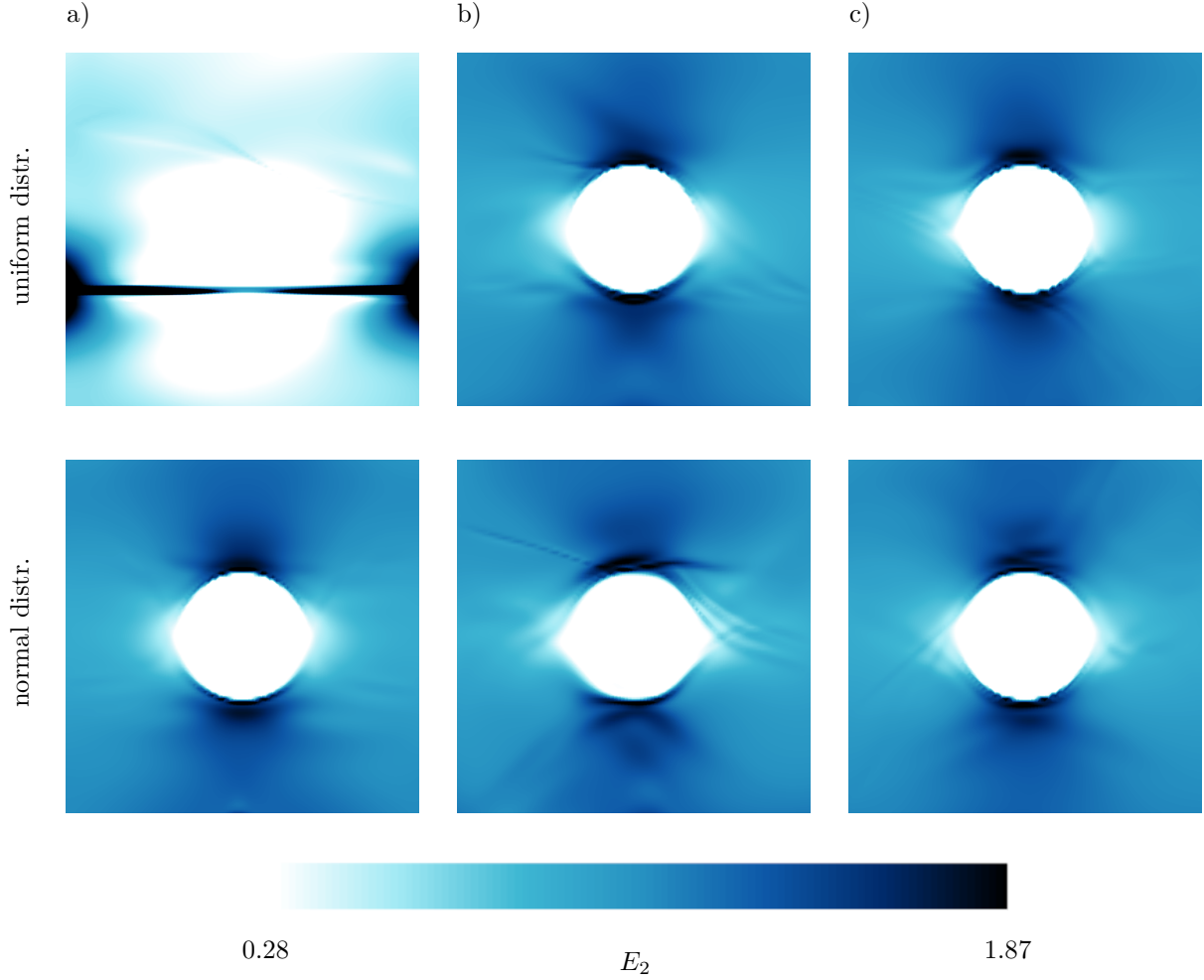
a)   b)   c)

Figure 10.3: Contour plot of E_{t1} for a set of parameters: a) 51×51 elements, 15 neurons per layer in N_1 and 5 neurons each for N_{x_1} and N_{x_2}, b) 51×51 elements, 10 neurons per layer in N_1 and 5 neurons each for N_{x_1} and N_{x_2} and c) 101×101 elements, 15 neurons per layer in N_1 and 5 neurons each for N_{x_1} and N_{x_2} ([63]).

ANN with many weight and bias parameters combined with a coarse integration leads to an unphysical equilibrium state, where the energy $\overline{\overline{\Pi}}(\mathbf{r}) = 0.213522$ is far below the energy calculated through the FEM-simulation. We suppose that this phenomenon is associated with *overfitting*. A further reason for the localization might be inaccuracies while integrating. Interestingly, such localizations did not occur when using softplus-activation functions, which might also hint to the convexity of the solution space being an influencing factor. Using the same mesh but ANNs with fewer parameters in b) gives physically more reasonable results and energy of $\overline{\overline{\Pi}}(\mathbf{r}) = 0.590266$. Using a finer grid and the larger ANN in c) also yields reasonable results with energy of c) $\overline{\overline{\Pi}}(\mathbf{r}) = 0.589887$. We now perform the same simulations but initialize the weights according to a normal distribution

$$\mathbf{r}^{(0),*} \sim \mathcal{N}(\mu, \sigma^2). \tag{10.20}$$

In Figure 10.3, the bottom pictures show the results for the normal distribution after 20 000 iterations. One can see that all three computations now yield reasonable results where we obtain the energies a) $\overline{\overline{\Pi}}(\mathbf{r}) = 0.590054$, b) $\overline{\overline{\Pi}}(\mathbf{r}) = 0.592981$ and c) $\overline{\overline{\Pi}}(\mathbf{r}) = 0.590054$.
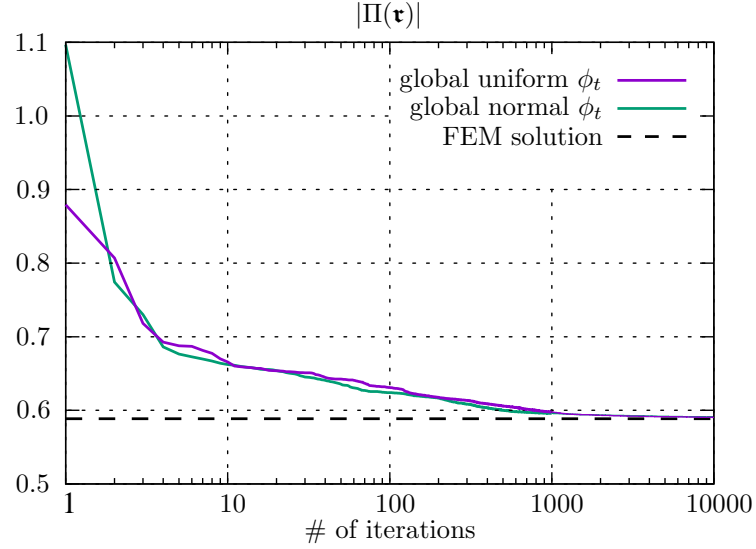
Figure 10.4: Convergence of $|\Pi(\mathbf{\tau})|$ over the iterations for a global trial function with random uniform initialization and random normal initialization for the ANN and integration set-up c) from Figure 10.3. One can see that the energies are converging towards the FEM-solution, indicated by the dashed line.

Finally, we have a look at the convergence rate of the scheme. Figure 10.4 shows the convergence of the absolute macroscopic energy $|\Pi(\mathbf{\tau})|$ for the uniform initialization using set-up c) and the normal initialization using the set-up c). One can see that the energies approach the FEM-solution, where the convergence rate slows down in the vicinity of the solution. It does not seem to make a huge difference whether one chooses the uniform or the normal initialization. The example only serves as a qualitative investigation of the choice of initial weights and bias, it, however, shows the necessity of using more sophisticated methods as presented in GLOROT & BENGIO [59] as well as preprocessing steps such as pretraining [3].

10.2.3. Two-dimensional real microstructure example

We now extend the solution scheme presented above to two dimensions and apply it to a more complex microstructure. We, therefore, consider the microstructure of meteorite NWA 2993. A three-dimensional CT-image has been produced by GHANBARZADEH & PRODANOVIC [57] and can be openly accessed through the *Digital Rocks Portal* [153]. For the two-dimensional computation, we use the middle slice of the CT-image. As the image has a pixel count of 500×500, we remove the last row and column of pixels to end up with an odd-sized grid of size 499×499 for the FFT-based comparison. The two-dimensional constitutive law and global potential then takes the form as presented in Equation (10.15) above, where the vectorial electric field $\boldsymbol{E} = \overline{\boldsymbol{E}} - \nabla \widetilde{\phi}$ can again be decomposed. We now discretize the microstructure by an equidistant grid with quadrature points and apply a macroscopic load of $\overline{E}_1 = 1$ and $\overline{E}_2 = 0$. In line with the Hill-Mandel condition, we prescribe periodic boundary conditions. We now let the microstructure only consist of two phases with a phase contrast of 10, where we set the electric permittivity in the inclusion to $\kappa_1^* = 10$ and in the matrix to $\kappa_2^* = 1$. Figure 10.5 shows an image of the meteorite as well as the result of the electric field E_1 from the FFT-based solution. Here,
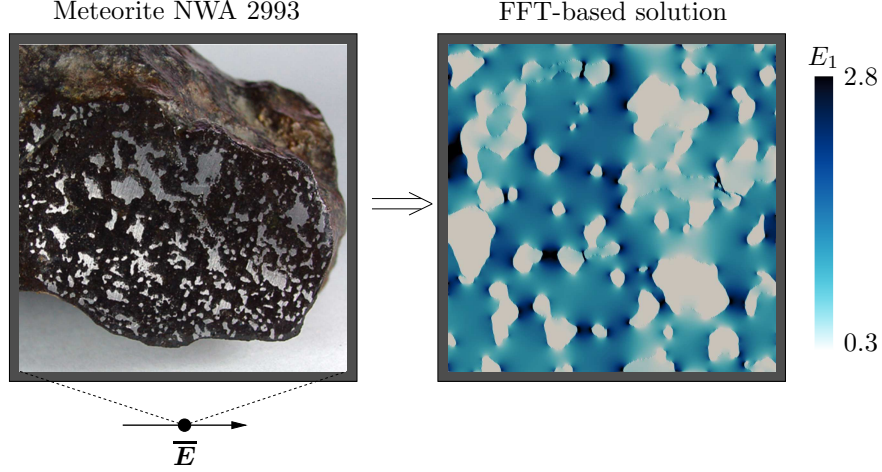
Figure 10.5: To the left, one can see an image of the meteorite NWA 2993 with its distinct microstructure (GHANBARZADEH & PRODANOVIC [57]). To the right, the FFT-based solution for E_1 under horizontal macroscopic loading and phase contrast of ten can be seen. As for the microstructure, the middle slice of the three-dimensional CT-image was taken. Characteristic peaks in the electric field at the bottlenecks between two inclusions of high permittivity can be seen.

we see the electric field's characteristic peaks at the bottlenecks between two inclusions of high permittivity. We now want to compare these results to an ANN-based solution. In order to improve training behavior and prediction accuracy, we first want to apply a method which is inspired by the idea of autoencoders [3]. Figure 10.6 shows an example of the approach used here: In a preprocessing step, a certain amount of layers of the neural network are connected to an output unit and are trained to predict the indicator function of the material phases. Therefore, the output unit uses the hyperbolic tangent to classify, if a certain location belongs to phase 1 or phase 2. The training of this network is performed through optimizing a cross-entropy loss

$$\mathfrak{J} = -y\ln(N^*(\boldsymbol{x}, \mathfrak{r}^*)) - (1 - y)\ln(1 - N^*(\boldsymbol{x}, \mathfrak{r}^*)), \tag{10.21}$$

where N^* is the trainable ANN with weights and biases $\mathfrak{r}^*$. Here, y is the phase data taking the value $y = 1$ at grid points that belong to phase 1 and $y = -1$ at ones which belong to phase 2. When the cost function falls below a certain value, the pre-training is stopped. According to Figure 10.6, the output node is then released, additional layers are added to the existing ones and are connected to a new linear output unit, creating the new ANN $N_1(\boldsymbol{x}, \mathfrak{r}_1)$. This ANN has now partially pre-trained weights and biases in $\mathfrak{r}_1$ that reflect some geometric information about the location of the inclusions. This preknowledge might make it easier for the ANN to be trained for the physical problems, as we expect jumps in physical fields to occur at phase interfaces. A similar approach has been successfully tested in [7], where the ANN used in the trial function is pre-trained to match the boundary conditions before multiplying it with a constraining function.
We now use the partially pre-trained neural network N_1 to construct a two-dimensional trial function that fulfills periodic boundary conditions

$$\begin{aligned}
\widetilde{\phi}_t(\boldsymbol{x}, \mathfrak{r}) &= A_1(x_1, x_2)N_1(\boldsymbol{x}, \mathfrak{r}_1) + A_2(x_1)N_{x_1}(x_1, \mathfrak{r}_{x_1}) + A_3(x_2)N_{x_2}(x_2, \mathfrak{r}_{x_2}) \\
&= x_1(1 - x_1)x_2(1 - x_2)N_1(\boldsymbol{x}, \mathfrak{r}_1) \\
&\quad + x_1(1 - x_1)N_{x_1}(x_1, \mathfrak{r}_{x_1}) + x_2(1 - x_2)N_{x_2}(x_2, \mathfrak{r}_{x_2}),
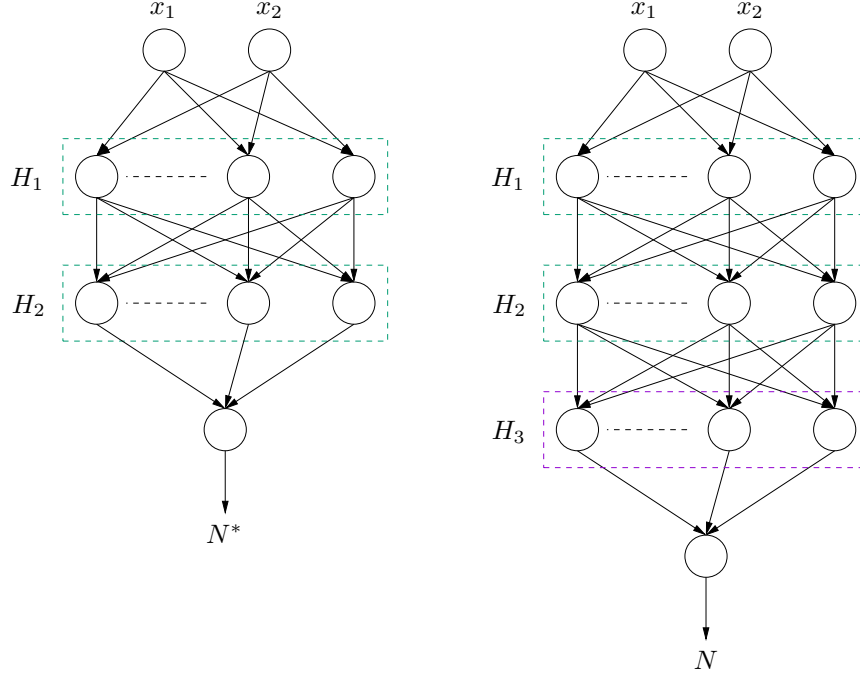\end{aligned} \tag{10.22}$$

Figure 10.6: Example for the pre-training of an ANN for homogenization problems. First, a smaller neural network N^* with, for example, two hidden layers is pretrained to predict the phase location of the microstructure. For the physical problem, the output node with its weights and bias is removed and additional layers extend the ANN. As a consequence, parts of the ANN already incorporate geometric information on the underlying microstructure problem.

where we added two more untrained ANNs N_{x_1} and N_{x_2}. These two ANNs must only be dependent on x_1 and x_2 respectively in order to satisfy periodicity at the boundaries. We can then again compute the trial electric field according to decomposition (10.17). Insertion into the global potential (10.15) finally gives the objective to optimize

$$\overline{\Pi} = \sup_{\mathfrak{r}} \frac{1}{|\mathcal{B}|} \Pi(\mathfrak{r}) = \sup_{\mathfrak{r}} \frac{1}{|\mathcal{B}|} \int_{\mathcal{B}} -\frac{1}{2} \kappa^*(\boldsymbol{x}) \boldsymbol{E}_t \cdot \boldsymbol{E}_t \, dA. \tag{10.23}$$

For the computation, we choose an ANN N_1 with three hidden layers with 100 neurons each and the hyperbolic tangent as activation function and two hidden layers with 30 neurons each and the softplus function as activation function. According to the code given below, the pre-training step is performed for the first three hidden layers before extending the ANN by the second two. The other two ANNs N_{x_1} and N_{x_2} each consist of three hidden layers with 50 neurons each. The neurons' activation function is the softplus function. This results in a total amount of 35094 trainable parameters.

Figure 10.7 shows the result for the pre-training step and for the physical equilibrium. One can see that the phases are predicted quite accurately. For the equilibrium, the results are qualitatively close to the FFT-based simulation shown in Figure 10.5, also showing characteristic peaks in between inclusions of high permittivity. In contrast to the FFT-based solution, there are still some larger oscillations appearing, and the solution seems to be smeared out, especially at the boundaries. However, the ANN-based approach works much more memory efficiently: The FFT-based scheme solves for two variables, namely the electric field components E_1 and E_2 at each grid node. For a 499×499 grid as used in this example, this results in a total amount of $499 \times 499 \times 2 = 498002$ unknowns for the FFT-based approach. The ANN-based approach however, integrates over the whole mesh,
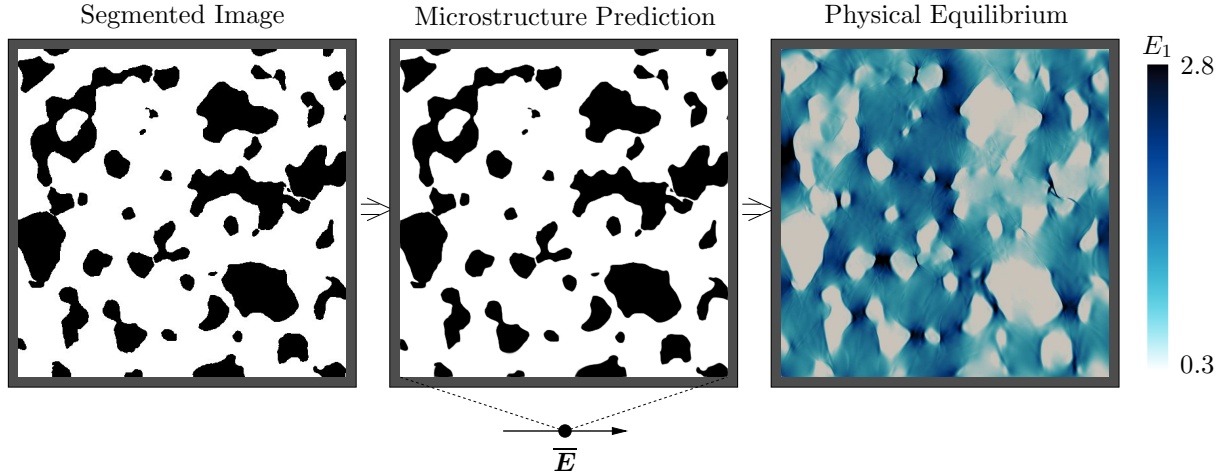
Figure 10.7: On the left one can see the segmented image of the microstructure of meteorite NWA 2993 as provided by GHANBARZADEH & PRODANOVIC [57]. The middle image shows the ANN's prediction of the microstructure after pre-training. The left image shows the ANN's prediction after extending the layers and training the physical equilibrium. Comparison with the FFT-based solution shows qualitatively good results.

but only solves for the ANNs' weights and bias. For the ANNs chosen here, these summed up to a total amount of 35094 weights and biases.

Listing 10.2: Two-dimensional Tensorflow Implementation

```
1  import tensorflow as tf
2  import numpy as np
3  tf.enable_eager_execution()
4
5  # Load segmented microstructure data (500x500x500 CT Image) as provided by
        the Digital Rocks database
6  fd = open('met_bin', 'rb')
7  pixels = 500
8  f = np.fromfile(fd, dtype=np.uint8, count=pixels**3)
9  im = f.reshape((pixels, pixels, pixels)) #notice row, column format
10 fd.close()
11
12 # Remove last row and column of image to have an odd-numbered grid and
        build two-dimensional grid
13 N1 = pixels-1
14 dx = 1/N1
15 xx = tf.range(dx/2,1.0,dx)
16 x1, x2 = tf.meshgrid(xx, xx)
17 xx1 = tf.reshape(x1,[N1*N1,])
18 xx2 = tf.reshape(x2,[N1*N1,])
19 x = tf.stack([xx1,xx2],axis=1)
20
21 # Extract the middle slice of the three-dimensional CT-image for further
        two-dimensional computations
22 # Normalize the image data between 0 and 1
23 im1 = im[249,:499,:499]/255
24
25 # Cast the material parameter from matrix into vector and stack for future
        energy calculation
26 kappaVec = tf.reshape(im1,[N1*N1,1])
27 kappa = tf.concat([kappaVec,kappaVec],axis=1)
```

```
28  # Set material parameters to be kappa = 10 in inclusion and kappa = 10 in
        inclusion
29  kappa = tf.cast(kappa, tf.float32)
30  kappa = (kappa*(-1)+1)*9+1
31
32  # Build an ANN-model that is able to distinguish between pretraining and
        physical simulation
33  class ANN(tf.keras.Model):
34      def __init__(self):
35          super(ANN, self).__init__()
36          # Build layers for pretraining and physical simulation
37          self.dense1 = tf.keras.layers.Dense(units = 100, activation='tanh',
                kernel_initializer='glorot_uniform',)
38          self.dense2 = tf.keras.layers.Dense(units = 100, activation='tanh',
                kernel_initializer='glorot_uniform',)
39          self.dense3 = tf.keras.layers.Dense(units = 100, activation='tanh',
                kernel_initializer='glorot_uniform',)
40          self.dense4 = tf.keras.layers.Dense(units = 1, activation='tanh',)
41          # Build additional layers for physical simulation
42          self.densei1 = tf.keras.layers.Dense(units = 30, activation='
                softplus',kernel_initializer='glorot_uniform',)
43          self.densei2 = tf.keras.layers.Dense(units = 30, activation='
                softplus',kernel_initializer='glorot_uniform',)
44          self.densei3 = tf.keras.layers.Dense(units = 1,)
45
46          # Build layers for one-dimensional ANN at x1-boundary
47          self.densex1_1 = tf.keras.layers.Dense(units = 50, activation='
                softplus',kernel_initializer='glorot_uniform',)
48          self.densex1_2 = tf.keras.layers.Dense(units = 50, activation='
                softplus',kernel_initializer='glorot_uniform',)
49          self.densex1_3 = tf.keras.layers.Dense(units = 50, activation='
                softplus',kernel_initializer='glorot_uniform',)
50          self.densex1_4 = tf.keras.layers.Dense(units = 1,)
51
52          # Build layers for one-dimensional ANN at x2-boundary
53          self.densex2_1 = tf.keras.layers.Dense(units = 50, activation='
                softplus',kernel_initializer='glorot_uniform',)
54          self.densex2_2 = tf.keras.layers.Dense(units = 50, activation='
                softplus',kernel_initializer='glorot_uniform',)
55          self.densex2_3 = tf.keras.layers.Dense(units = 50, activation='
                softplus',kernel_initializer='glorot_uniform',)
56          self.densex2_4 = tf.keras.layers.Dense(units = 1,)
57
58      def call(self, inputs, training=False):
59          if training:
60              # Pass input only through first layers and hyperbolic tangent
                    output neuron
61              result = self.dense1(inputs)
62              result = self.dense2(result)
63              result = self.dense3(result)
64              result = self.dense4(result)
65
66              phifield = result
67          else:
68              # Pass input whole volume ANNs
69              result = self.dense1(inputs)
70              result = self.dense2(result)
```

```
71                    result = self.dense3(result)
72                    result = self.densei1(result)
73                    result = self.densei2(result)
74                    result = self.densei3(result)
75
76                    # Extract x1-coordinate from input and pass through network
                          N_x1
77                    size = int(inputs.get_shape()[0])
78                    inputx1 = tf.reshape(inputs[:,0],[size,1])
79                    resultx1 = self.densex1_1(inputx1)
80                    resultx1 = self.densex1_2(resultx1)
81                    resultx1 = self.densex1_3(resultx1)
82                    resultx1 = self.densex1_4(resultx1)
83
84                    # Extract x2-coordinate from input and pass through network
                          N_x2
85                    inputx2 = tf.reshape(inputs[:,1],[size,1])
86                    resultx2 = self.densex2_1(inputx2)
87                    resultx2 = self.densex2_2(resultx2)
88                    resultx2 = self.densex2_3(resultx2)
89                    resultx2 = self.densex2_4(resultx2)
90
91                    # Multiply output by constraining functions (x1-1)*x1*(x2-1)*x2
                          *N_1 + (x1-1)*x1*N_x1 + (x2-1)*x2*N_x2
92                    phifield = (inputx1-1)*inputx1*(inputx2-1)*inputx2*result + (
                          inputx1-1)*inputx1*resultx1 + (inputx2-1)*inputx2*resultx2
93
94               return phifield
95
96   # Assign the modified ANNs to the phi-field
97   phi = ANN()
98
99   # Renormalize image between -1 and 1 for the hyperbolic tangent output
         classification
100  ind = (tf.cast(im1, tf.float32))*2-1
101
102  # Use the Adam-optimizer with the default learning parameters
103  optimizer0 = tf.train.AdamOptimizer(learning_rate=0.001,beta1=0.9,beta2=
         0.999,epsilon=1e-08,use_locking=False)
104
105  # Restore the indicator as vector for multiplication in loss-function
106  indVec = tf.reshape(ind,[N1*N1,1])
107
108  # Set the training flag to TRUE in order to tell model that it is in the
         pretraining stage
109  training = True
110  for i in range(100000):
111      with tf.GradientTape() as tape:
112          cross_entropy_loss = tf.reduce_mean(-(indVec+1)*0.5*tf.log((phi(x,
                 training)+1.0)*0.5+1e-12)-0.5*(1-indVec)*tf.log((1-phi(x,
                 training))*0.5+1e-12))
113          gradients0 = tape.gradient(cross_entropy_loss, phi.variables)
114      optimizer0.apply_gradients(zip(gradients0, phi.variables),
115                                  global_step=tf.train.
                                        get_or_create_global_step())
116
117      print (i,"%.12f"%cross_entropy_loss)
```

```
118
119  # Use the Adam−optimizer with the default learning parameters
120  optimizer = tf.train.AdamOptimizer(learning_rate=0.001,beta1=0.9,beta2=
         0.999,epsilon=1e−08,use_locking=False)
121
122  # Assign macroscopic loading
123  Ebar1 = tf.constant(1.0, shape=[N1*N1,])
124  Ebar2 = tf.constant(0.0, shape=[N1*N1,])
125  Ebar = tf.stack([Ebar1,Ebar2],axis=1)
126
127  # Set training parameter to FALSE to tell phi that it is in the physical
         equilibrium stage
128  training = False
129  for i in range(50000):
130      with tf.GradientTape() as tape:
131          with tf.GradientTape() as tape2:
132              tape2.watch(x)
133              phi_t = phi(x,training)
134              # Compute energy as integration over quadrature points
135              # Use automated differentiation for the computation the
                   fluctuative electric field
136              EnergyPotential = dx*dx*tf.reduce_sum(0.5*kappa*(Ebar − tape2.
                   gradient(phi_t,x))**2.0)
137          gradients = tape.gradient(EnergyPotential, phi.variables)
138      optimizer.apply_gradients(zip(gradients, phi.variables),
139                                    global_step=tf.train.
                                        get_or_create_global_step())
140      print(i,"%.12f"%EnergyPotential)
```
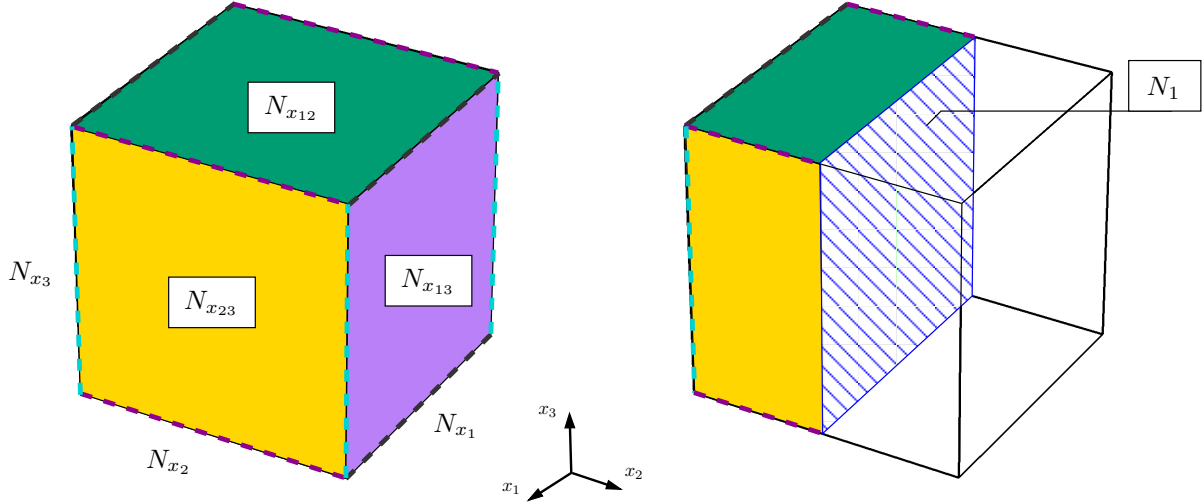
Figure 10.8: The trial function $\widetilde{\phi}_t$ is constructed using a set of seven ANNs: N_{x_1}, N_{x_2} and N_{x_3} are acting on the corresponding boundary edges, $N_{x_{12}}$, $N_{x_{13}}$ and $N_{x_{23}}$ are acting on the boundary surfaces and N_1 is acting in the volume. Finally, the seven ANNs are multiplied with the corresponding constraining functions A_i.

10.2.4. Periodic homogenization of three-dimensional RVE with spherical inclusion

Finally, we want to demonstrate that the approach is extendable to three dimensions. A cubic RVE of unit side lengths $l = 1$ is considered. The RVE consists of two phases. Material 1 forms the matrix material in which spheres of radius $r_0 = 0.178$ made of material 2 are embedded. In order to construct a trial function that a priori fulfills the periodic boundary conditions, a set of seven ANNs is needed: $N_{x_1}(x_1)$ acting in the x_1-direction, $N_{x_2}(x_2)$ acting in the x_2-direction, $N_{x_3}(x_3)$ acting in the x_3-direction, $N_{x_{12}}(x_1, x_2)$ acting in the x_1x_2-plane, $N_{x_{13}}(x_1, x_3)$ acting in the x_1x_3-plane, $N_{x_{23}}(x_2, x_3)$ acting in the x_1x_2-plane and $N_1(\boldsymbol{x})$ acting in the RVE's volume, see Figure 10.8 [63]. The trial function then takes the form

$$
\begin{aligned}
\widetilde{\phi}_t(\boldsymbol{x}, \mathbf{r}) =\ & A_1\, N_1(\boldsymbol{x}, \mathbf{r}_1) + A_2\, N_{x_{12}}(x_1, x_2, \mathbf{r}_{x_{12}}) + A_3\, N_{x_{13}}(x_1, x_3, \mathbf{r}_{x_{13}}) \\
& + A_4\, N_{x_{23}}(x_2, x_3, \mathbf{r}_{x_{23}}) + A_5\, N_{x_1}(x_1, \mathbf{r}_{x_1}) \\
& + A_6\, N_{x_2}(x_2, \mathbf{r}_{x_2}) + A_7\, N_{x_3}(x_3, \mathbf{r}_{x_3}),
\end{aligned}
\tag{10.24}
$$

where the constraining functions appear as

$$
\begin{array}{ll}
A_1 = x_1(1 - x_1)x_2(1 - x_2)x_3(1 - x_3), & A_5 = x_1(1 - x_1), \\
A_2 = x_1(1 - x_1)x_2(1 - x_2), & A_6 = x_2(1 - x_2), \\
A_3 = x_1(1 - x_1)x_3(1 - x_3), & A_7 = x_3(1 - x_3), \\
A_4 = x_2(1 - x_2)x_3(1 - x_3). &
\end{array}
\tag{10.25}
$$

From the three-dimensional trial function (10.24), the trial electric field $\boldsymbol{E}_t$ can be computed according to Equation (10.17). The trial electric field $\boldsymbol{E}_t$ is then again used in the computation of the global potential, which is optimized with respect to the weights and biases of the neural network

$$
\overline{\Pi} = \sup_{\mathbf{r}} \frac{1}{|\mathcal{B}|} \Pi^*(\mathbf{r}) = \sup_{\mathbf{r}} \frac{1}{|\mathcal{B}|} \left(-\int_{\mathcal{B}^{\mathrm{matr}}} \frac{1}{2}\kappa_1^* \boldsymbol{E}_t \cdot \boldsymbol{E}_t\, dV - \int_{\mathcal{B}^{\mathrm{incl}}} \frac{1}{2}\kappa_2^* \boldsymbol{E}_t \cdot \boldsymbol{E}_t\, dV \right).
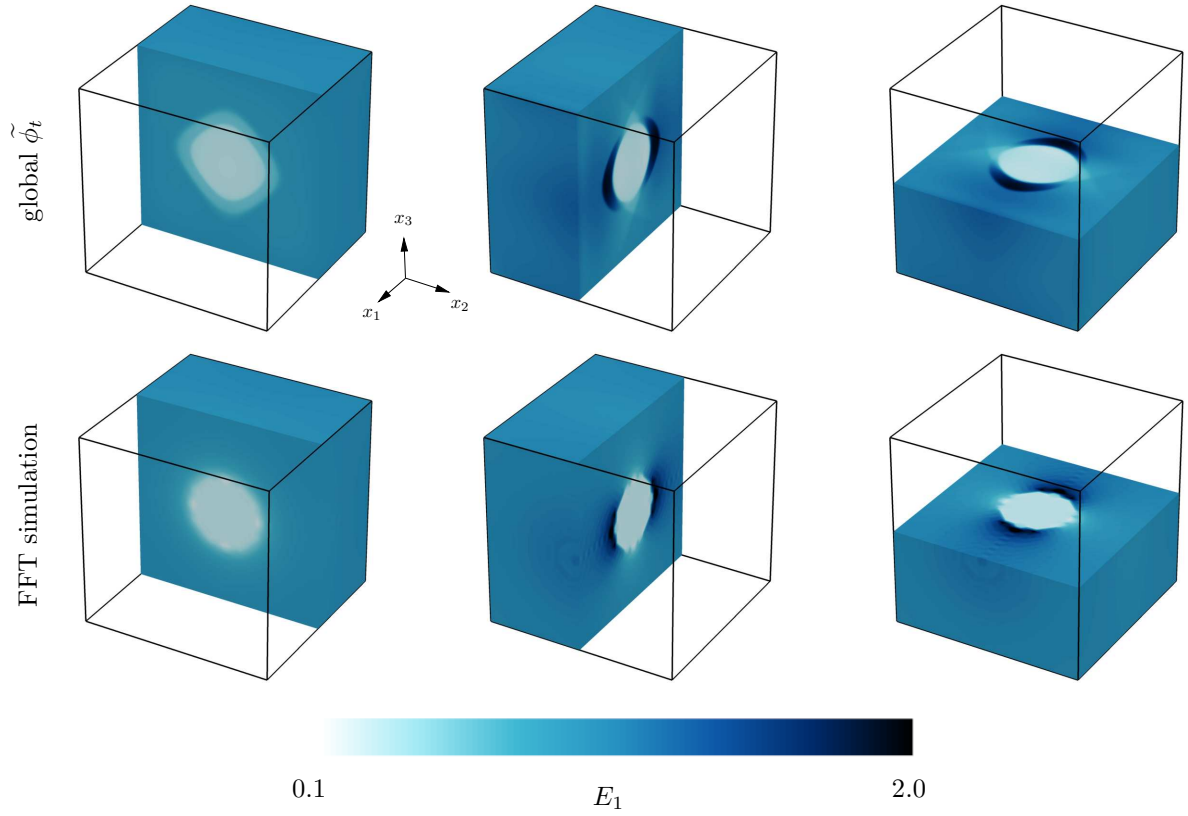\tag{10.26}
$$

Figure 10.9: On the top, the electric field E_1 as predicted by the ANN after 20000 iterations is displayed for a microstructure consisting of a matrix with low electric permittivity $\kappa_1 = 1$ and a spherical inclusion with high permittivity $\kappa_2 = 10$. The results show good agreement with an FFT-based simulation shown below.

The RVE is now loaded by the homogeneous macroscopic electric field $\overline{E}_1 = 1.0$, $\overline{E}_2 = 0.0$ and $\overline{E}_3 = 0.0$. The matrix material has an electric permittivity of $\kappa_1^* = 1$, the spherical inclusion has an electric permittivity of $\kappa_2^* = 10$. The domain is discretized using $43{\times}43{\times}43$ equidistant grid points. The ANNs covering the edges and boundary surfaces are MLPs with 4 neurons each in the hidden layer of the ANN acting on the edge and 5 neurons in the hidden layer of the ANN acting on the surface. The ANN covering the volume is an MLP with two hidden layers and 8 neurons within each layer. Summing all weights and biases gives a total of 256 optimization parameters. In this example, we use the soft-plus activation function as experience showed that it provided the most stable solutions. Using the hyperbolic tangent usually leads to higher convergence rates but increases the risk of localization behavior described in GÖKÜZÜM ET AL. [63]. The example is run on a Fortran 77 code using the L-BFGS-B optimization library [20, 213] for finding the optimal ANN parameters. As the microstructure is rather simple in this example, no pre-training is performed. Figure 10.9 shows the result of the ANN-based simulation after 20000 iterations next to an FFT-based simulation of the same boundary value problem.
 One can see that the ANN is able to qualitatively describe areas of high and low electric field as well as locations of discontinuity. However, those discontinuities are less distinct compared with the FFT-based simulation. Quantitatively, the global energy potentials $\overline{\Pi}$ of both simulations are close to each other in equilibrium, having $\overline{\Pi}(\mathbf{r}) = 0.529926$ for the ANN-based approach and $\overline{\Pi}^{FFT} = 0.52750$ for the FFT-based simulation [63].

Conclusion and outlook

Modern engineering applications and solutions push the boundaries for materials with respect to properties such as durability and weight. A major technique that allows for such progress is the smart design of the materials' microstructural properties, which can be achieved for example by means of additive manufacturing. To avoid excessive amounts of experiments for all possible microstructural configurations, there is the demand to numerically predict materials' properties based on their microstructure. Though there has been a significant increase in computational power in the past years, the difference in length-scale between a component at hand and the microstructure of its material still poses challenges with respect to computational time and efficiency.

This work provided a framework for *FFT-based multiscale simulations* with a special focus on the computation of *effective properties*, namely the *macroscopic stress* and *tangent operator*. Starting point was the Lippmann-Schwinger equation, which is characteristic for FFT-based methods and is used to solve equilibrium equations. For first-order homogenization, which allows for an additive split of field variables into a constant macroscopic contribution and a fluctuating contribution, the connection of the Lippmann-Schwinger equation and the aforementioned additive split was drawn. Having this connection at hand, an explicit expression for the fluctuation sensitivities, i.e., the differentiation of the fluctuating field variables with respect to the macrocopic field variables that is needed for the computation of the macroscopic tangent operator, could be derived. In contrast to finite difference-based approaches, the explicit expression for the fluctuation sensitivities, called a *Lippmann-Schwinger-type equation*, is linear independent of the material model used. It was shown that computing said properties utilizing the Lippmann-Schwinger-type equation, outperforms finite difference-based approaches in computational speed. Although there still needs progress to be made with respect to computational speed, the tangent computation in line with a variationally consistent framework allows for robust macroscopic convergence in multiscale simulations, including geometrical and material nonlinearity.

This robustness was shown also for electro-mechanically coupled materials at large strains. For these kind of materials, it is necessary to model and predict the interaction between mechanical deformations and electrical fields within the material. Simulations thus need to solve both the mechanical and the electrical equilibrium equation. Again, the mi-

crostructure plays a crucial role for the overall material behavior: Deformation states of a soft polymer matrix with enclosed eletrically permitive particles can be influenced by size and shape of the inclusions. In this work, we showed that the computation of the coupled macroscopic tangent operator based on the coupled *Lippmann-Schwinger-type equation* is efficient and reliable for such kind of materials. For future research, the interaction of microscopic particle shape, size, and distribution with the macroscopic deformation might be further investigated. Methods that allow local topology optimization of the microstructure in terms of desired deformation modes and stiffness might enable the smart design of macroscopic components [30, 35]. Such methods might enable improvement for applications such as artificial muscles [4] based on electroactive polymers. Further field of application might be the development of sensors, which take advantage of the coupling between mechanical deformation and electrical fields. For such applications, extending the model to include the interaction with magnetic fields as well could be beneficial [156]. Additionally, the framework was applied to phase-field-based multiscale simulation for fracture. Such simulations are of special interest in all engineering areas where there is the danger of intergranular corrosion or fracture, including pressure vessels under high pressure, temperature, radiation or chemical corrosion. In this work, we restricted ourselves to an elastic material behavior at small strains, but adding additional effects such as temperature might be a path forward. The codes for the simulation presented in this work are all made available in an open repository [60, 61]. For future investigations, a particular focus might be set on the convergence behavior of effective properties for cracked RVEs in terms of the RVEs' size. In the current work, RVEs were attached at every Gauss point of the macroscopically discretized problem. One could think of reducing computational effort by using interface elements that are adaptively integrated into the macroscopic problem and by only calculating RVE responses at those interface elements [79]. Furthermore, the extension to higher-order homogenization schemes might be necessary to include size-effects on the macroscale as well.

In the final part of this work, the use of ANNs for solving periodic boundary value problems in homogenization was explored. Hereby, the ANNs are multiplied with constraining functions to satisfy the periodic boundary conditions a priori, and an energetic potential is minimized with respect to the ANNs' weights and bias. It was shown that the method converges to results close to FFT- and FEM-based solutions and needs little memory. Recently, DONG & NI [38] presented a way of enforcing periodicity in ANNs employing trigonometric activation functions. Implementing said ANNs within the methods presented here and comparing the training behavior and accuracy to the conventional approach might give further insights and improvements. Additionally, the influence of activation functions on the convergence behavior and the quality of the solution might be further investigated. In this work, convex activation functions such as the softplus function appeared to result in a more robust convergence behavior with no localization appearing, while activation functions such as the hyperbolic tangent appeared to converge faster to the real solution but also tended to show localization effects leading to nonphysical results. However, a mathematically rigorous explanation of this observation might help choosing the appropriate activation function for a given problem.

Bibliography

[1] ABADI, M.; AGARWAL, A.; BARHAM, P.; BREVDO, E.; CHEN, Z.; CITRO, C.; CORRADO, G. S.; DAVIS, A.; DEAN, J.; DEVIN, M.; GHEMAWAT, S.; GOODFELLOW, I.; HARP, A.; IRVING, G.; ISARD, M.; JIA, Y.; JOZEFOWICZ, R.; KAISER, L.; KUDLUR, M.; LEVENBERG, J.; MANÉ, D.; MONGA, R.; MOORE, S.; MURRAY, D.; OLAH, C.; SCHUSTER, M.; SHLENS, J.; STEINER, B.; SUTSKEVER, I.; TALWAR, K.; TUCKER, P.; VANHOUCKE, V.; VASUDEVAN, V.; VIÉGAS, F.; VINYALS, O.; WARDEN, P.; WATTENBERG, M.; WICKE, M.; YU, Y.; ZHENG, X. [2015]: *TensorFlow: Large-Scale Machine Learning on Heterogeneous Systems.* Software available from tensorflow.org.

[2] ARAROMI, O. A.; GAVRILOVICH, I.; SHINTAKE, J.; ROSSET, S.; RICHARD, M.; GASS, V.; SHEA, H. R. [2015]: *Rollable Multisegment Dielectric Elastomer Minimum Energy Structures for a Deployable Microsatellite Gripper.* IEEE/ASME Transactions on Mechatronics, 20(1): 438–446.

[3] BALLARD, D. H. [1987]: *Modular Learning in Neural Networks.* In *AAAI*, pp. 279–284.

[4] BAR-COHEN, Y. (Editor) [2001]: *Electroactive Polymer (EAP) Actuators as Artificial Muscles: Reality, Potential, and Challenges.* SPIE Press.

[5] BAR-COHEN, YOSEPH; XUE, T.; JOFFE, B.; LIH, S.-S.; SHAHINPOOR, M.; HARRISON, J. S.; SMITH, J. G.; WILLIS, P. [1997]: *Electroactive polymers (EAP) low-mass muscle actuators.* Smart Structures and Materials 1997: Smart Structures and Integrated Systems, 3041: 697–701.

[6] BENSOUSSAN, A.; LIONS, J.-L.; PAPANICOLAOU, G. [2011]: *Asymptotic analysis for periodic structures*, Vol. 374. American Mathematical Soc.

[7] BERG, J.; NYSTRÖM, K. [2018]: *A unified deep artificial neural network approach to partial differential equations in complex geometries.* Neurocomputing, 317: 28–41.

[8] BERTOLDI, K.; VITELLI, V.; CHRISTENSEN, J.; VAN HECKE, M. [2017]: *Flexible mechanical metamaterials.* Nature Reviews Materials, 2(11): 1–11.

[9] BESSA, M.A.; BOSTANABAD, R.; LIU, Z.; HU, A.; APLEY, D. W.; BRINSON, C.; CHEN, W.; LIU, W. [2017]: *A framework for data-driven analysis of materials under uncertainty: Countering the curse of dimensionality.* Computer Methods in Applied Mechanics and Engineering, 320: 633 – 667.

[10] BIOT, M. A. [1955]: *Variational principles in irreversible thermodynamics with application to viscoelasticity.* Physical Review, 97(6): 1463.

[11] BOCK, F. E.; AYDIN, R. C.; CYRON, C. J.; HUBER, N.; KALIDINDI, S. R.; KLUSEMANN, B. [2019]: *A review of the application of machine learning and data mining approaches in continuum materials mechanics.* Frontiers in Materials, 6:

110.

[12] BORN, M. [1926]: *Quantenmechanik der Stoßvorgänge.* Zeitschrift für Physik, 38(11-12): 803–827.

[13] BOSE, J. C. [1898]: *On the rotation of plane of polarisation of electric wave by a twisted structure.* Proceedings of the Royal Society of London, 63(389-400): 146–152.

[14] BOURDIN, B.; FRANCFORT, G. A.; MARIGO, J.-J. [2000]: *Numerical experiments in revisited brittle fracture.* Journal of the Mechanics and Physics of Solids, 48(4): 797–826.

[15] BRISARD, S.; DORMIEUX, L. [2010]: *FFT-based methods for the mechanics of composites: A general variational framework.* Computational Materials Science, 49: 663 – 671.

[16] BRISARD, S.; DORMIEUX, L. [2012]: *Combining Galerkin approximation techniques with the principle of Hashin and Shtrikman to derive a new FFT-based numerical method for the homogenization of composites.* Computer Methods in Applied Mechanics and Engineering, 217: 197–212.

[17] BRODNIK, NEAL R; HSUEH, C.-J.; FABER, K. T.; BOURDIN, B.; RAVICHANDRAN, G.; BHATTACHARYA, K. [2020]: *Guiding and trapping cracks with compliant inclusions for enhancing toughness of brittle composite materials.* Journal of Applied Mechanics, 87(3).

[18] BÜCKMANN, T.; THIEL, M.; KADIC, M.; SCHITTNY, R.; WEGENER, M. [2014]: *An elasto-mechanical unfeelability cloak made of pentamode metamaterials.* Nature communications, 5(1): 1–6.

[19] BUDIANSKY, B. [1965]: *On the elastic moduli of some heterogeneous materials.* Journal of the Mechanics and Physics of Solids, 13: 223–227.

[20] BYRD, R. H.; LU, P.; NOCEDAL, J.; ZHU, C. [1995]: *A limited memory algorithm for bound constrained optimization.* SIAM Journal on Scientific Computing, 16(5): 1190–1208.

[21] CAO, C.; ZHAO, X. [2013]: *Tunable stiffness of electrorheological elastomers by designing mesostructures.* Applied Physics Letters, 103(4): 041901.

[22] CARPI, F.; DE ROSSI, D.; KORNBLUH, R.; PELRINE, R. E.; SOMMER-LARSEN, P. (Editors) [2011]: *Dielectric elastomers as electromechanical transducers: Fundamentals, materials, devices, models and applications of an emerging electroactive polymer technology.* Elsevier.

[23] CARPI, F.; ROSSI, D. D. [2005]: *Improvement of electromechanical actuating performances of a silicone dielectric elastomer by dispersion of titanium dioxide powder.* IEEE Transactions on Dielectrics and Electrical Insulation, 12(4): 835–843.

[24] CAVALIERE, F.; R., S.; WULFINGHOFF, S. [2020]: *Efficient two–scale simulations of engineering structures using the Hashin–Shtrikman type finite element method.* Computational Mechanics, 65(1): 159–175.

[25] CHEN, L.; CHEN, J.; LEBENSOHN, R.; JI, Y.; HEO, T.; BHATTACHARYYA, S.; CHANG, K.; MATHAUDHU, S.; LIU, Z.; CHEN, L.-Q. [2015]: *An integrated fast fourier transform-based phase-field and crystal plasticity approach to model recrystallization of three dimensional polycrystals.* Computer Methods in Applied Mechanics and Engineering, 285: 829–848.

[26] CHEN, Y.; VASIUKOV, D.; GÉLÉBART, L.; PARK, C. H. [2019]: *A FFT solver for variational phase-field modeling of brittle fracture.* Computer Methods in Applied

Mechanics and Engineering, 349: 167–190.

[27] CIARLET, P. G. [1988]: *Mathematical Elasticity: Volume I: three-dimensional elasticity.* North-Holland.

[28] CLAIRAUT, A.-C. [1754]: *Memoire sur l'orbite apparente du soleil autour de la terre, en ayant égard aux perturbations produites par les actions de la lune et des planètes principales.* Mémoires de Matématique et de Physique de l'Académie Royale des Sciences, 9: 521–564.

[29] COOLEY, J.W.; TUKEY, J. [1965]: *An Algorithm for the Machine Calculation of Complex Fourier Series.* Mathematics of Computation, 19(90): 297–301.

[30] CORNAGGIA, RÉMI; BELLIS, C. [2020]: *Tuning effective dynamical properties of periodic media by FFT-accelerated topological optimization.* International Journal for Numerical Methods in Engineering, 121(14): 3178–3205.

[31] CYBENKO, G. [1989]: *Approximation by superpositions of a sigmoidal function.* Mathematics of control, signals and systems, 2(4): 303–314.

[32] DANA, S.; WHEELER, M. F. [2020]: *A machine learning accelerated FE^2 omogenization algorithm for elastic solids.* arXiv preprint arXiv:2003.11372.

[33] DANAS, K. [2017]: *Effective response of classical, auxetic and chiral magnetoelastic materials by use of a new variational principle.* Journal of the Mechanics and Physics of Solids, 105: 25–53.

[34] DEBOTTON, G.; TEVET-DEREE, L.; SOCOLSKY, E. A. [2007]: *Electroactive heterogeneous polymers: analysis and applications to laminated composites.* Mechanics of Advanced Materials and Structures, 14(1): 13–22.

[35] DEDÈ, L.; BORDEN, M. J.; HUGHES, T. J. [2012]: *Isogeometric analysis for topology optimization with a phase field model.* Archives of Computational Methods in Engineering, 19(3): 427–465.

[36] DE GEUS, TWJ; VONDŘEJC, J.; ZEMAN, J.; PEERLINGS, R.; GEERS, M. [2017]: *Finite strain FFT-based non-linear solvers made simple.* Computer Methods in Applied Mechanics and Engineering, 318: 412–430.

[37] DENNING, D. E. [1987]: *An intrusion-detection model.* IEEE Transactions on software engineering, (2): 222–232.

[38] DONG, S.; NI, N. [2020]: *A Method for Representing Periodic Functions and Enforcing Exactly Periodic Boundary Conditions with Deep Neural Networks.* arXiv preprint arXiv:2007.07442.

[39] DORFMANN, A.; OGDEN, R. [2005]: *Nonlinear electroelasticity.* Acta Mechanica, 174(3-4): 167–183.

[40] DUFFY, D. G. [2015]: *Green's functions with applications.* Chapman and Hall/CRC.

[41] EISENLOHR, J.R.; DIEHL, M.; LEBENSOHN, R.; ROTERS, F. [2013]: *A spectral method solution to crystal-viscoplasticity at finite strains.* International Journal of Plasticity, 46: 37 – 53.

[42] ERINGEN, A. C. [1963]: *On the foundations of electroelastostatics.* International Journal of Engineering Science, 1(1): 127–153.

[43] ERINGEN, A. C.; MAUGIN, G. A. [1990]: *Electrodynamics of Continua.* Springer, New York.

[44] ESTEP, D. [2002]: *Practical analysis in one variable.* Springer Science & Business Media.

[45] EYRE, D.J.; MILTON, G. [1999]: *A fast numerical scheme for computing the re-*

sponse of composites using grid refinement. The European Physical Journal, 6: 41 – 47.

[46] Farimani, A. B.; Gomes, J.; Sharma, R.; Lee, F. L.; Pande, V. S. [2018]: *Deep Learning Phase Segregation.* arXiv preprint arXiv:1803.08993.

[47] Feyel, F.; Chaboche, J.-L. [2000]: *FE² multiscale approach for modelling the elastoviscoplastic behavior of long fibre SiC/Ti Composite materials.* Computer Methods in Applied Mechanics and Engineering, 183: 309–330.

[48] Feynmann, R.; Leighton, R. B.; Sands, M. [1965]: *The Feynman Lectures on Physics Volume II.* https://www.feynmanlectures.caltech.edu/.

[49] Fourier, J.B.J. [1822]: *Théorie analytique de la chaleur.* F. Didot.

[50] Francfort, G. A.; Marigo, J.-J. [1998]: *Revisiting brittle fracture as an energy minimization problem.* Journal of the Mechanics and Physics of Solids, 46(8): 1319–1342.

[51] Frigo, M. [1999]: *A Fast Fourier Transform Compiler.* SIGPLAN Not., 34(5): 169–180.

[52] Fritzen, F.; Fernández, M.; Larsson, F. [2019]: *On-the-fly adaptivity for nonlinear twoscale simulations using artificial neural networks and reduced order modeling.* Frontiers in Materials, 6: 75.

[53] Geers, M. G. D.; Kouznetsova, V. G.; Matouš, K.; Yvonnet, J. [2017]: *Homogenization methods and multiscale modeling: nonlinear problems.* Encyclopedia of Computational Mechanics Second Edition, pp. 1–34.

[54] Gélébart, L.; Mondon-Cancel, R. [2013]: *Non-linear extension of FFT-based methods accelerated by conjugate gradients to evaluate the mechanical behavior of composite materials.* Computational Materials Science, 77: 430 – 439.

[55] Geubelle, P.H.; Rice, J. [1995]: *A spectral method for three-dimensional elastodynamic fracture problems.* Journal of the Mechanics and Physics of Solids, 43(11): 1791 – 1824.

[56] Ghaboussi, J.; Garrett, J. H.; Wu, X. [1991]: *Knowledge-Based Modeling of Material Behavior with Neural Networks.* Journal of Engineering Mechanics, 117(1): 132–153.

[57] Ghanbarzadeh, S.; Prodanovic, M. [2016]: *Meteorite NWA 2993: A primitive achondrite.* http://www.digitalrocksportal.org/projects/64.

[58] Gitman, I. M.; Askes, H.; Sluys, L. [2007]: *Representative volume: existence and size determination.* Engineering fracture mechanics, 74(16): 2518–2534.

[59] Glorot, X.; Bengio, Y. [2010]: *Understanding the difficulty of training deep feedforward neural networks.* In Teh, Yee Whye; Titterington, M. (Editors): *Proceedings of the Thirteenth International Conference on Artificial Intelligence and Statistics*, Vol. 9 of *Proceedings of Machine Learning Research*, pp. 249–256, Chia Laguna Resort, Sardinia, Italy. PMLR.

[60] Göküzüm, F. S.: *FFT-based phase-field fracture code in 3D in Matlab.* https://bit.ly/3cEwQBz.

[61] Göküzüm, F. S.: *Small strain multiscale fracture implementation in Matlab.* https://bit.ly/2ENW18k.

[62] Göküzüm, F. S.; Keip, M.-A. [2018]: *An algorithmically consistent macroscopic tangent operator for FFT-based computational homogenization.* International Journal for Numerical Methods in Engineering, 113(4): 581–600.

[63] Göküzüm, F. S.; Nguyen, L. T. K.; Keip, M.-A. [2019]: *An Artificial Neu-*

ral Network Based Solution Scheme for Periodic Computational Homogenization of Electrostatic Problems. Mathematical and Computational Applications, 24(2): 40.

[64] GÖKÜZÜM, F. S.; NGUYEN, L. T. K.; KEIP, M.-A. [2019]: *A multiscale FE-FFT framework for electro-active materials at finite strains.* Computational mechanics, 64(1): 63–84.

[65] GOODFELLOW, I.; BENGIO, Y.; COURVILLE, A. [2016]: *Deep Learning.* MIT Press. http://www.deeplearningbook.org.

[66] GRIFFITH, A. A. [1921]: *VI. The phenomena of rupture and flow in solids.* Philosophical transactions of the royal society of london. Series A, containing papers of a mathematical or physical character, 221(582-593): 163–198.

[67] GURTIN, M. E.; FRIED, E.; ANAND, L. [2010]: *The mechanics and thermodynamics of continua.* Cambridge University Press.

[68] HACKL, K.; FISCHER, F. D. [2008]: *On the relation between the principle of maximum dissipation and inelastic evolution given by dissipation potentials.* Proceedings of the Royal Society A: Mathematical, Physical and Engineering Sciences, 464(2089): 117–132.

[69] HAHN, G.T. [1984]: *The influence of microstructure on brittle fracture toughness.* Metallurgical and Materials Transactions A, 15(6): 947–959.

[70] HASHIN, Z.; SHTRIKMAN, S. [1963]: *A variational approach to the theory of the elastic behaviour of multiphase materials.* Journal of the Mechanics and Physics of Solids, 11(2): 127 – 140.

[71] HEBB, D. O. [1949]: *The organization of behavior.* John Wiley & Sons, New York.

[72] HEIDEMAN, M. T.; JOHNSON, D.; BURRUS, C. [1984]: *Gauss and the history of the fast Fourier transform.* 1: 14–21.

[73] HEIDEMAN, M.T.; JOHNSON, D.; BURRUS, C. [1985]: *Gauss and the history of the fast Fourier transform.* Archive for History of Exact Sciences, 34: 265–277.

[74] HILDEBRAND, F. E. [2013]: *Variational multifield modeling of the formation and evolution of laminate microstructure.* Doctoral Thesis, Institute of Applied Mechanics, Stuttgart.

[75] HILL, R. [1952]: *The elastic behaviour of a crystalline aggregate.* Proceedings of the Physical Society. Section A, 65(5): 349.

[76] HILL, R. [1963]: *Elastic properties of reinforced solids: Some theoretical principles.* Journal of the Mechanics and Physics of Solids, 11(5): 357 – 372.

[77] HILL, R. [1965]: *A self-consistent mechanics of composite materials.* Journal of the Mechanics and Physics of Solids, 13: 213–222.

[78] HILL, R. [1985]: *On the micro-to-macro transition in constitutive analyses of elastoplastic response at finite strain.* Mathematical Proceedings of the Cambridge Philosophical Society, 98: 579–590.

[79] HIRSCHBERGER, C. B.; RICKER, S.; STEINMANN, P.; SUKUMAR, N. [2009]: *Computational multiscale modelling of heterogeneous material layers.* Engineering Fracture Mechanics, 76(6): 793–812.

[80] HORNIK, K. [1991]: *Approximation capabilities of multilayer feedforward networks.* Neural networks, 4(2): 251–257.

[81] HORNIK, K.; STINCHCOMBE, M.; WHITE, H.; OTHERS [1989]: *Multilayer feedforward networks are universal approximators.* Neural networks, 2(5): 359–366.

[82] HUANG, C.; ZHANG, Q. M.; DEBOTTON, G.; BHATTACHARYA, K. [2004]: *All-organic dielectric-percolative three-component composite materials with high elec-*

tromechanical response. Applied Physics Letters, 84: 4391–4393.

[83] HUBER, N.; TSAKMAKIS, C. [2001]: *A neural network tool for identifying the material parameters of a finite deformation viscoplasticity model with static recovery.* Computer Methods in Applied Mechanics and Engineering, 191(3): 353 – 384.

[84] IRWIN, G.R. [1958]: *Elasticity and plasticity.* Encyclopaedia of physics, 6: 551–590.

[85] JAVILI, A.; CHATZIGEORGIOU, G.; STEINMANN, P. [2013]: *Computational homogenization in magneto-mechanics.* International Journal of Solids and Structures, 50: 4197–4216.

[86] KABEL, M.; BÖHLKE, T.; SCHNEIDER, M. [2014]: *Efficient fixed point and Newton-Krylov solvers for FFT-based homogenization of elasticity at large deformations.* Computational Mechanics, 54: 1497 – 1514.

[87] KABEL, M.; FLIEGENER, S.; SCHNEIDER, M. [2016]: *Mixed boundary conditions for FFT-based homogenization at finite strains.* Computational Mechanics, 57: 193 – 210.

[88] KADIC, M.; BÜCKMANN, T.; SCHITTNY, R.; WEGENER, M. [2013]: *Metamaterials beyond electromagnetism.* Reports on Progress in physics, 76(12): 126501.

[89] KANOUTE, P.; BOSO, D.; CHABOCHE, J.; SCHREFLER, B. [2009]: *Multiscale methods for composites: a review.* Archives of Computational Methods in Engineering, 16(1): 31–75.

[90] KEIP, M.-A.; RAMBAUSEK, M. [2016]: *A multiscale approach to the computational characterization of magnetorheological elastomers.* International Journal for Numerical Methods in Engineering, 107: 338–360.

[91] KEIP, M.-A.; RAMBAUSEK, M. [2017]: *Computational and analytical investigations of shape effects in the experimental characterization of magnetorheological elastomers.* International Journal of Solids and Structures, 121: 1–20.

[92] KEIP, M.-A.; STEINMANN, P.; SCHRÖDER, J. [2014]: *Two-scale computational homogenization of electro-elasticity at finite strains.* Computer Methods in Applied Mechanics and Engineering, 278: 62–79.

[93] KIM, K. J.; TADOKORO, S. [2007]: *Electroactive polymers for robotics applications: artificial muscles and sensors.* Springer.

[94] KINGMA, D. P.; BA, J. [2014]: *Adam: A method for stochastic optimization.* arXiv preprint arXiv:1412.6980.

[95] KOCHMANN, J.; WULFINGHOFF, S.; REESE, S.; MIANROODI, J. R.; SVENDSEN, B. [2016]: *Two-scale FE-FFT- and phase-field-based computational modeling of bulk microstructural evolution and macroscopic material behavior.* Computer methods in applied mechanics and engineering, 305: 89 – 110.

[96] KOCHMANN, J.; WULFINGHOFF, S.; EHLE, L.; MAYER, J.; SVENDSEN, B.; REESE, S. [2018]: *Efficient and accurate two-scale FE-FFT-based prediction of the effective material behavior of elasto-viscoplastic polycrystals.* Computational Mechanics, 61(6): 751–764.

[97] KOSMANN-SCHWARZBACH, YVETTE [2011]: *The Noether Theorems.* In *The Noether Theorems*, pp. 55–64. Springer.

[98] KOUZNETSOVA, V.; GEERS, M. G. D.; BREKELMANS, W. A. M. [2002]: *Multiscale constitutive modelling of heterogeneous materials with a gradient-enhanced computational homogenization scheme.* International Journal for Numerical Methods in Engineering, 54(8): 1235–1260.

[99] KOVACS, G.; LOCHMATTER, P.; WISSLER, M. [2007]: *An arm wrestling robot*

driven by dielectric elastomer actuators. Smart Materials and Structures, 16(2): S306.

[100] KOVETZ, A. [2000]: *Electromagnetic theory*, Vol. 975. Oxford University Press Oxford.

[101] KRIZHEVSKY, A.; SUTSKEVER, I.; HINTON, G. E. [2012]: *ImageNet Classification with Deep Convolutional Neural Networks.* In PEREIRA, F.; BURGES, C. J. C.; BOTTOU, L.; WEINBERGER, K. Q. (Editors): *Advances in Neural Information Processing Systems 25*, pp. 1097–1105. Curran Associates, Inc.

[102] KRÖNER, E. [1977]: *Bounds for effective elastic moduli of disordered materials.* Journal of the Mechanics and Physics of Solids, 2(25): 137 – 155.

[103] LAGARIS, I. E.; LIKAS, A.; FOTIADIS, D. I. [1998]: *Artificial neural networks for solving ordinary and partial differential equations.* IEEE Transactions on Neural Networks, 9(5): 987–1000.

[104] LAGRANGE, J. L. [1762]: *Solution de différents problémes de calcul integral.* Miscellanea Taurinensia ou Mélanges de Turin,, 3.

[105] LAHELLEC, N.; SUQUET, P. [2007]: *On the effective behavior of nonlinear inelastic composites: I. Incremental variational principles.* Journal of the Mechanics and Physics of Solids, 55(9): 1932–1963.

[106] LANDAU, L.D.; LIFSCHITZ, E. [1984]: *Lehrbuch der Theoretischen Physik. Band 1: Mechanik.* Akademie Verlag Berlin.

[107] LE, B. A.; YVONNET, J.; HE, Q.-C. [2015]: *Computational homogenization of nonlinear elastic materials using neural networks.* International Journal for Numerical Methods in Engineering, 104(12): 1061–1084.

[108] LEBENSOHN, R. A. [2001]: *N-site modeling of a 3D viscoplastic polycrystal using fast Fourier transform.* Acta Materialia, 49: 2723 – 2737.

[109] LEBENSOHN, R. A.; LIU, Y.; CASTAÑEDA, P. [2004]: *Macroscopic properties and field fluctuations in model power-law polycrystals: full-field solutions versus self-consistent estimates.* Proceedings of the Royal Society of London, 460: 1381 – 1405.

[110] LEFÈVRE, V.; LOPEZ-PAMIES, O. [2017]: *Nonlinear electroelastic deformations of dielectric elastomer composites: II – Non-Gaussian elastic dielectrics.* Journal of the Mechanics and Physics of Solids, 99: 438–470.

[111] LEUSCHNER, M.; FRITZEN, F. [2017]: *Fourier-Accelerated Nodal Solvers (FANS) for homogenization problems.* Computational Mechanics, doi: 10.1007/s00466–017–1501–5.

[112] LINDMAN, K. F. [1920]: *Über eine durch ein isotropes System von spiralförmigen Resonatoren erzeugte Rotationspolarisation der elektromagnetischen Wellen.* Annalen der Physik, 368(23): 621–644.

[113] LIPPMANN, B. A.; SCHWINGER, J. [1950]: *Variational principles for scattering processes. I.* Physical Review, 79: 469–480.

[114] LIU, Z.; BESSA, M.; LIU, W. K. [2016]: *Self-consistent clustering analysis: an efficient multi-scale scheme for inelastic heterogeneous materials.* Computer Methods in Applied Mechanics and Engineering, 306: 319–341.

[115] MA, R.; SUN, W. [2020]: *FFT-based solver for higher-order and multi-phase-field fracture models applied to strongly anisotropic brittle materials.* Computer Methods in Applied Mechanics and Engineering, 362: 112781.

[116] MA, R.; TRUSTER, T. J. [2019]: *FFT-based homogenization of hypoelastic plas-*

ticity at finite strains. Computer Methods in Applied Mechanics and Engineering, 349: 499–521.

[117] MARSDEN, J. E.; HUGHES, T. J. [1994]: *Mathematical foundations of elasticity.* Courier Corporation.

[118] MATLAB [2017]: *version 9.3.0 (R2017b).* The MathWorks Inc., Natick, Massachusetts.

[119] MAUGIN, G. A. [1992]: *The thermomechanics of plasticity and fracture*, Vol. 7. Cambridge University Press.

[120] MAUGIN, G. A. [2013]: *Continuum mechanics of electromagnetic solids.* Elsevier.

[121] MAXWELL, J. C. [1873]: *A treatise on electricity and magnetism*, Vol. 1. Oxford: Clarendon Press.

[122] MCCULLOCH, W. S.; PITTS, W. [1943]: *A logical calculus of the ideas immanent in nervous activity.* The bulletin of mathematical biophysics, 5(4): 115–133.

[123] MCMEEKING, R. M.; LANDIS, C. M. [2005]: *Electrostatic forces and stored energy for deformable dielectric materials.* Journal of Applied Mechanics, 72(4): 581–590.

[124] MICHEL, J.-C.; SUQUET, P. [2016]: *A model-reduction approach to the micromechanical analysis of polycrystalline materials.* Computational Mechanics, 57(3): 483–508.

[125] MIEHE, C. [2002]: *Strain-driven homogenization of inelastic microstructures and composites based on an incremental variational formulation.* International Journal for numerical methods in engineering, 55(11): 1285–1322.

[126] MIEHE, C.; HOFACKER, M.; WELSCHINGER, F. [2010]: *A phase field model for rate-independent crack propagation: Robust algorithmic implementation based on operator splits.* Computer Methods in Applied Mechanics and Engineering, 199(45-48): 2765–2778.

[127] MIEHE, C.; KOCH, A. [2002]: *Computational micro-to-macro transitions of discretized microstructures undergoing small strains.* Archive of Applied Mechanics, 72(4): 300–317.

[128] MIEHE, C.; ROSATO, D.; KIEFER, B. [2011]: *Variational principles in dissipative electro-magneto-mechanics: A framework for the macro-modeling of functional materials.* International Journal for Numerical Methods in Engineering, 86(10): 1225–1276.

[129] MIEHE, C.; SCHRÖDER, J.; SCHOTTE, J. [1999]: *Computational homogenization analysis in finite plasticity. Simulation of texture development in polycrystalline materials.* Computer Methods in Applied Mechanics and Engineering, 171: 387–418.

[130] MIEHE, C.; TEICHTMEISTER, S. [2019]: *Geometrical methods of nonlinear continuum mechanics and continuum thermodynamics.* Lecture Notes (University of Stuttgart).

[131] MIEHE, C.; VALLICOTTI, D.; TEICHTMEISTER, S. [2016]: *Homogenization and multiscale stability analysis in finite magneto-electro-elasticity. Application to soft matter EE, ME and MEE composites.* Computer Methods in Applied Mechanics and Engineering, 300: 294 – 346.

[132] MIEHE, C.; WELSCHINGER, F.; HOFACKER, M. [2010]: *Thermodynamically consistent phase-field models of fracture: Variational principles and multi-field FE implementations.* International journal for numerical methods in engineering, 83(10): 1273–1311.

[133] MILTON, G. W. [2002]: *The Theory of Composites.* Cambridge University Press.

[134] MINSKY, M.; PAPERT, S. A. [2017]: *Perceptrons: An introduction to computational geometry.* MIT press.

[135] MORI, T.; TANAKA, K. [1973]: *Average stress in matrix and average elastic energy of materials with misfitting inclusions.* Acta Mechanica, 21: 571–574.

[136] MOULINEC, H.; SUQUET, P. [1994]: *A fast numerical method for computing the linear and nonlinear mechanical properties of composites.* Académie des Sciences, 2: 1417 – 1423.

[137] MOULINEC, H.; SUQUET, P. [1998]: *A numerical method for computing the overall response of nonlinear composites with complex microstructure.* Computer methods in applied mechanics and engineering, 157: 69 – 94.

[138] MÜLLER, R.; XU, B.-X.; GROSS, D.; LYSCHIK, M.; SCHRADE, D.; KLINKEL, S. [2010]: *Deformable dielectrics – optimization of heterogeneities.* International Journal of Engineering Science, 48(7): 647–657.

[139] MUMFORD, D. B.; SHAH, J. [1989]: *Optimal approximations by piecewise smooth functions and associated variational problems.* Communications on pure and applied mathematics.

[140] NABIAN, M. A.; MEIDANI, H. [2018]: *A deep neural network surrogate for high-dimensional random partial differential equations.* arXiv preprint arXiv:1806.02957.

[141] NOETHER, EMMY [1918]: *Invarianten beliebiger differentialausdrücke.* Nachrichten von der Gesellschaft der Wissenschaften zu Göttingen, mathematisch-physikalische Klasse, 1918: 37–44.

[142] NORRIS, A. N. [1985]: *A differential scheme for the effective moduli of composites.* Mechanics of Materials, 4(1): 1–16.

[143] ORTIZ, M.; REPETTO, E. [1999]: *Nonconvex energy minimization and dislocation structures in ductile single crystals.* Journal of the Mechanics and Physics of Solids, 47(2): 397–462.

[144] OTERO, F.; OLLER, S.; MARTINEZ, X. [2018]: *Multiscale computational homogenization: review and proposal of a new enhanced-first-order method.* Archives of Computational Methods in Engineering, 25(2): 479–505.

[145] ÖZDEMIR, I; BREKELMANS, W.; GEERS, M. G. [2008]: *FE² computational homogenization for the thermo-mechanical analysis of heterogeneous solids.* Computer Methods in Applied Mechanics and Engineering, 198(3-4): 602–613.

[146] ÖZDEMIR, I.; BREKELMANS, W. A. M.; GEERS, M. G. D. [2008]: *Computational homogenization for heat conduction in heterogeneous solids.* International journal for numerical methods in engineering, 73(2): 185–204.

[147] PAO, YIH-HSING; HUTTER, K. [1975]: *Electrodynamics for moving elastic solids and viscous fluids.* Proceedings of the IEEE, 63(7): 1011–1021.

[148] PEACOCK, J. [2014/15]: *Junior Honours Fourier Analysis.* Lecture Notes, pp. 66–67.

[149] PELRINE, R.; KORNBLUH, R.; PEI, Q.; JOSEPH, J. [2000]: *High-Speed Electrically Actuated Elastomers with Strain Greater Than 100%.* Science, 287(5454): 836–839.

[150] PELTERET, J.-P.; STEINMANN, P. [2019]: *Magneto-Active Polymers: Fabrication, characterisation, modelling and simulation at the micro-and macro-scale.* Walter de Gruyter GmbH & Co KG.

[151] PONTE CASTAÑEDA, P. [1991]: *The effective mechanical properties of nonlinear isotropic composites.* Journal of the Mechanics and Physics of Solids, 39(1): 45 –

71.

[152] PONTE CASTAÑEDA, P.; SIBONI, M. H. [2012]: *A finite-strain constitutive theory for electro-active polymer composites via homogenization.* International Journal of Non-Linear Mechanics, 47(2): 293–306.

[153] PRODANOVIC, M.; ESTEVA, M.; HANLON, M.; NANDA, G.; AGARWAL, P. [2015]: *Digital Rocks Portal: a repository for porous media images.* https://www.digitalrocksportal.org/.

[154] RAISSI, M.; YAZDANI, A.; KARNIADAKIS, G. E. [2018]: *Hidden Fluid Mechanics: A Navier-Stokes Informed Deep Learning Framework for Assimilating Flow Visualization Data.* CoRR, abs/1808.04327.

[155] RAMBAUSEK, M.; GÖKÜZÜM, F. S.; NGUYEN, L. T. K.; KEIP, M.-A. [2019]: *A two-scale FE-FFT approach to nonlinear magneto-elasticity.* International Journal for Numerical Methods in Engineering, 117(11): 1117–1142.

[156] RAMBAUSEK, M; KEIP, M.-A. [2018]: *Analytical estimation of non-local deformation-mediated magneto-electric coupling in soft composites.* Proceedings of the Royal Society A: Mathematical, Physical and Engineering Sciences, 474(2216): 20170803.

[157] REBHAN, E. [1999]: *Theoretische Physik.* Elsevier, Spektrum, Akad. Verlag.

[158] RENARD, J.; MARMONIER, M. F. [1987]: *Etude de l'initiation de l'endommagement dans la matrice d'un matériau composite par une méthode d'homogénéisation.* La Recherche aérospatiale, (6): 43–51.

[159] REUSS, A. [1929]: *Berechnung der Fließgrenze von Mischkristallen auf Grund der Plastizitätsbedingung für Einkristalle.* ZAMM-Journal of Applied Mathematics and Mechanics/Zeitschrift für Angewandte Mathematik und Mechanik, 9(1): 49–58.

[160] RICE, J. R. [1968]: *A path independent integral and the approximate analysis of strain concentration by notches and cracks.*

[161] RILEY, K. F.; HOBSON, M. P.; BENCE, S. J. [2006]: *Mathematical methods for physics and engineering: a comprehensive guide.* Cambridge university press.

[162] RÖNTGEN, W. C. [1880]: *Ueber die durch Electricität bewirkten Form-und Volumenänderungen von dielectrischen Körpern.* Annalen der Physik, 247(13): 771–786.

[163] ROSENBLATT, F. [1958]: *The perceptron: a probabilistic model for information storage and organization in the brain.* Psychological review, 65(6): 386.

[164] RUDYKH, S.; LEWINSTEIN, A.; UNER, G.; DEBOTTON, G. [2013]: *Analysis of microstructural induced enhancement of electromechanical coupling in soft dielectrics.* Applied Physics Letters, 102(15): 151905.

[165] RUMELHART, D. E.; HINTON, G. E.; WILLIAMS, R. J. [1985]: *Learning internal representations by error propagation.* Technical report, California Univ San Diego La Jolla Inst for Cognitive Science.

[166] RUMELHART, D. E.; McCLELLAND, J. L. [1986]: *Parallel distributed processing: explorations in the microstructure of cognition. volume 1. foundations.*

[167] SACHS, G. [1928]: *Zur ableitung einer fliessbedingung.* Zeitschrift des Vereins Deutscher Ingenieure, 72: 734–736.

[168] SÁNCHEZ-PALENCIA, E. [1980]: *Non-homogeneous media and vibration theory.* Lecture notes in physics, 127.

[169] SAVVAS, D.; STEFANOU, G.; PAPADRAKAKIS, M. [2016]: *Determination of RVE size for random composites with local volume fraction variation.* Computer Methods in Applied Mechanics and Engineering, 305: 340–358.

[170] Schaedler, T. A.; Jacobsen, A. J.; Torrents, A.; Sorensen, A. E.; Lian, J.; Greer, J. R.; Valdevit, L.; Carter, W. B. [2011]: *Ultralight metallic microlattices.* Science, 334(6058): 962–965.

[171] Schneider, M. [2015]: *Convergence of FFT-based homogenization for strongly heterogeneous media.* Mathematical Methods in the Applied Sciences, 38(13): 2761–2778.

[172] Schneider, M.; Merkert, D.; Kabel, M. [2017]: *FFT-based homogenization for microstructures discretized by linear hexahedral elements.* International Journal for Numerical Methods in Engineering, 109(10): 1461–1489.

[173] Schneider, M.; Ospald, F.; Kabel, M. [2016]: *Computational homogenization of elasticity on a staggered grid.* International Journal for Numerical Methods in Engineering, 105(9): 693–720. nme.5008.

[174] Schröder, J. [2009]: *Derivation of the localization and homogenization conditions for electro-mechanically coupled problems.* Computational Materials Science, 46(3): 595–599.

[175] Schröder, J. [2014]: *A numerical two-scale homogenization scheme: the FE^2–method.* In Schröder, J.; Hackl, K. (Editors): *Plasticity and Beyond*, Vol. 550 of *CISM Courses and Lectures*, pp. 1–64. Springer.

[176] Schröder, J.; Keip, M.-A. [2012]: *Two-scale homogenization of electromechanically coupled boundary value problems.* Computational Mechanics, 50: 229–244.

[177] Seol, D.J.; Hu, S.; Li, Y.; Shen, J.; Oh, K.; Chen, L.-Q. [2003]: *Computer simulation of spinodal decomposition in constrained films.* Acta materialia, 51(17): 5173–5185.

[178] Siboni, H. M.; Ponte Castañeda, P. [2013]: *Dielectric elastomer composites: small-deformation theory and applications.* Philosophical Magazine, 93(21): 2769–2801.

[179] Siboni, M. H.; Ponte Castañeda, P. [2014]: *Fiber-constrained, dielectric-elastomer composites: Finite-strain response and stability analysis.* Journal of the Mechanics and Physics of Solids, 68: 211–238.

[180] Šilhavỳ, M. [2013]: *The mechanics and thermodynamics of continuous media.* Springer Science & Business Media.

[181] Smit, R.J.M.; Brekelmans, W.; Meijer, H. [1998]: *Prediction of the mechanical behavior of nonlinear heterogeneous systems by multi-level finite element modeling.* Computer Methods in Applied Mechanics and Engineering, 155: 181–192.

[182] Spahn, J.; Andrä, H.; Kabel, M.; Müller, R. [2014]: *A multiscale approach for modeling progressive damage of composite materials using fast Fourier transforms.* Computer methods in applied mechanics and engineering, 268: 871 – 883.

[183] Srivastava, N.; Hinton, G.; Krizhevsky, A.; Sutskever, I.; Salakhutdinov, R. [2014]: *Dropout: a simple way to prevent neural networks from overfitting.* The Journal of Machine Learning Research, 15(1): 1929–1958.

[184] Steinwart, I.; Christmann, A. [2008]: *Support vector machines.* Springer Science & Business Media.

[185] Suquet, P. M. [1986]: *Elements of homogenization for inelastic solid mechanics.* In Sanchez-Palenzia, E.; Zaoui, A. (Editors): *Homogenization Techniques for Composite Materials*, Vol. 272 of *Lecture Notes in Physics*, pp. 193–278. Springer.

[186] Szegedy, C.; Liu, W.; Jia, Y.; Sermanet, P.; Reed, S.; Anguelov, D.; Erhan, D.; Vanhoucke, V.; Rabinovich, A. [2015]: *Going Deeper with Con-*

volutions. In *Computer Vision and Pattern Recognition (CVPR)*.

[187] TAYLOR, G. I. [1938]: *Plastic strain in metals.* Journal of the Institute of Metals, 62: 307–324.

[188] TAYLOR, R. L. [2017]: *FEAP - Finite Element Analysis Program.* University of California, Berkeley.

[189] TERADA, K.; HORI, M.; KYOYA, T.; KIKUCHI, N. [2000]: *Simulation of the multi-scale convergence in computational homogenization approaches.* International Journal of Solids and Structures, 37(16): 2285–2311.

[190] TERADA, K.; KIKUCHI, N. [2001]: *A class of general algorithms for multi-scale analyses of heterogeneous media.* Computer methods in applied mechanics and engineering, 190(40-41): 5427–5464.

[191] TIERSTEN, H. F. [1971]: *On the nonlinear equations of thermo-electroelasticity.* International Journal of Engineering Science, 9(7): 587–604.

[192] TOUPIN, R. A. [1956]: *The elastic dielectric.* Journal of Rational Mechanics and Analysis, 5(6): 849–915.

[193] TREFETHEN, L. N. [2000]: *Spectral methods in MATLAB*, Vol. 10. Siam.

[194] VALLICOTTI, D. [2019]: *Magneto-electro-mechanical coupling phenomena across multiple length scales: variational framework and stability analysis.* Doctoral Thesis, Institute of Applied Mechanics, Stuttgart.

[195] VALLICOTTI, D.; SRIDHAR, A.; KEIP, M.-A. [2018]: *Variationally consistent computational homogenization of micro-electro-mechanics at finite deformations.* International Journal for Multiscale Computational Engineering, 16(4): 377–395.

[196] VAN DER SLUIS, O.; SCHREURS, P. J. G.; BREKELMANS, W. A. M.; MEIJER, H. E. H. [2000]: *Overall behaviour of heterogeneous elastoviscoplastic materials: effect of microstructural modelling.* Mechanics of Materials, 32(8): 449–462.

[197] VATANKHAH-VARNOOSFADERANI, M.; DANIEL, W. F.; ZHUSHMA, A. P.; LI, Q.; MORGAN, B. J.; MATYJASZEWSKI, K.; ARMSTRONG, D. P.; SPONTAK, R. J.; DOBRYNIN, A. V.; SHEIKO, S. S. [2017]: *Bottlebrush elastomers: A new platform for freestanding electroactuation.* Advanced Materials, 29(2): 1604209.

[198] VOIGT, W. [1887]: *Theoretische Studien über die Elastizitastsverhältnisse der Kristalle.* Königliche Gesellschaft der Wissenschaften zu Göttingen, 34.

[199] VONDŘEJC, J. [2016]: *Improved guaranteed computable bounds on homogenized properties of periodic media by the Fourier-Galerkin method with exact integration.* International Journal for Numerical Methods in Engineering, 107(13): 1106–1135. nme.5199.

[200] VONDŘEJC, J.; ZEMAN, J.; MAREK, I. [2014]: *An FFT-based Galerkin method for homogenization of periodic media.* Computers & Mathematics with Applications, 68(3): 156 – 173.

[201] VON GOETHE, J. W. [1879]: *Faust: eine tragödie*, Vol. 2. G. Hempel.

[202] VU, D. K.; STEINMANN, P.; POSSART, G. [2007]: *Numerical modelling of nonlinear electroelasticity.* International Journal for Numerical Methods in Engineering, 70(6): 685–704.

[203] WANG, J.J.; MA, X.; LI, Q.; BRITSON, J.; CHEN, L.-Q. [2013]: *Phase transitions and domain structures of ferroelectric nanoparticles: Phase field model incorporating strong elastic and dielectric inhomogeneity.* Acta Materialia, 61(20): 7591–7603.

[204] WILLIS, J.R. [1977]: *Bounds and self-consistent estimates for the overall properties of anisotropic composites.* Journal of the Mechanics and Physics of Solids, 25: 185

– 202.

[205] WILLOT, F.; ABDALLAH, B.; PELLEGRINI, Y. [2014]: *Fourier-based schemes with modified Green operator for computing the electrical response of heterogeneous media with accurate local fields.* International Journal for Numerical Methods in Engineering, 98(7): 518–533.

[206] WONG, M. W. [2011]: *Discrete fourier analysis*, Vol. 5. Springer Science & Business Media.

[207] YAN, W.; LIN, S.; KAFKA, O. L.; LIAN, Y.; YU, C.; LIU, Z.; YAN, J.; WOLFF, S.; WU, H.; NDIP-AGBOR, E.; OTHERS [2018]: *Data-driven multi-scale multi-physics models to derive process–structure–property relationships for additive manufacturing.* Computational Mechanics, 61(5): 521–541.

[208] ZABIHYAN, R.; MERGHEIM, J.; JAVILI, A.; STEINMANN, P. [2018]: *Aspects of computational homogenization in magneto-mechanics: Boundary conditions, RVE size and microstructure composition.* International Journal of Solids and Structures, 130: 105–121.

[209] ZÄH, D. [2014]: *Variational homogenization in electro-mechanics: from micro-electro-elasticity to electroactive polymers.* Doctoral Thesis, Institute of Applied Mechanics, Stuttgart.

[210] ZEMAN, J.; GEUS, T. W. J. DE ; VONDŘEJC, J.; PEERLINGS, R. H. J.; GEERS, M. G. D. [2016]: *A finite element perspective on non-linear FFT-based micromechanical simulations.* International Journal for Numerical Methods in Engineering, 111: 903–926.

[211] ZEMAN, J.; VONDŘEJC, J.; NOVAK, J.; MAREK, I. [2010]: *Accelerating a FFT-based solver for numerical homogenization of periodic media by conjugate gradients.* Journal of Computational Physics, 229: 8065–8071.

[212] ZHANG, Q. M.; LI, H.; POH, M.; XIA, F.; CHENG, Z.-Y.; XU, H.; HUANG, C. [2002]: *An all-organic composite actuator material with a high dielectric constant.* Nature, 419(6904): 284–287.

[213] ZHU, C.; BYRD, R. H.; LU, P.; NOCEDAL, J. [1997]: *Algorithm 778: L-BFGS-B: Fortran subroutines for large-scale bound-constrained optimization.* ACM Transactions on Mathematical Software (TOMS), 23(4): 550–560.

Institute of Applied Mechanics (IAM)
Chair for Continuum Mechanics

The goal of numerics based science is the replication of our tangible reality within computer-aided simulations at least possible deviation from relevant experiments. An ever-growing hardware capability led to an ever-growing resolution of simulations. This increase starts to enable the simulation of material behavior on several length scales and their interaction in computational solid mechanics. From a material physics point of view, the analysis of several lengths scales is of high interest, as many macroscopically observable effects are of microscopic origin.

However, despite the massive increase in computational power, full-field simulations across several scales are still uneconomic and time-consuming, preventing them from being applied to a wide range of realistic engineering problems. To relieve said problem, researchers developed homogenization methods and the concept of representative volume elements. The present work deals with numerical homogenization approaches and applies them to several material effects. Particular focus is put on the computation of effective properties as well as their embedding into multiscale simulations.